

Stochastic (thermo)dynamics of molecular coupled processes

Dissertation for the award of the degree
“Doctor rerum naturalium” (Dr. rer. nat.)
of the Georg-August-Universität Göttingen

within the doctoral program Physics
of the Georg-August University School of Science
(GAUSS)

submitted by Michalis Chatzittofi

from Limassol, Cyprus

Göttingen, 2024

Thesis Advisory Committee

Prof. Dr. Ramin Golestanian

Living Matter Physics Department

Max Planck Institute for Dynamics and Self Organization, Göttingen

Prof. Dr. Jörg Enderlein

III. Institute of Physics-Biophysics

Georg-August University, Göttingen

Prof. Dr. Marcus Müller

Institute for Theoretical Physics,

Georg-August University, Göttingen

Members of the examination board

Reviewer: Prof. Dr. Ramin Golestanian

Living Matter Physics Department

Max Planck Institute for Dynamics and Self Organization, Göttingen

Second Reviewer: Prof. Dr. Marcus Müller

Institute for Theoretical Physics, Georg-August University, Göttingen

Prof. Dr. Jörg Enderlein

III. Institute of Physics-Biophysics Georg-August University, Göttingen

Dr. Aljaz Godec

Research Group Mathematical Biophysics,

Max Planck Institute for Multidisciplinary Sciences, Göttingen

Prof. Dr. Matthias Krüger

Institute for Theoretical Physics, Georg-August University, Göttingen

Prof. Dr. Stefan Klumpp

Institute for Nonlinear Dynamics, Georg-August University, Göttingen

Prof. Dr. Helmut Grubmüller

Theoretical and Computational Biophysics Department

Max Planck Institute for Multidisciplinary Sciences, Göttingen

Date of oral examination: 23rd of October 2024

Abstract

Out of equilibrium biological processes are the key for life. From large animals to the smallest proteins, life is sustained by a continuous throughput of free energy. This happens through the exchange of some form of energy to another. Interestingly, the properties of a broad class of these different systems can be described by simple models in the language of non-equilibrium statistical physics.

In this thesis, we focus on the smallest existing machines; these are enzymes, molecular motors and microswimmers, which can either be biological or synthetic. At the simplest level these machines convert chemical energy into mechanical work. Our goal is to provide a minimal description of molecular processes and to study the impact of the mechanical degrees of freedom on the chemical dynamics. We consider both single particle as well as multiple interacting processes. Our study leads to some new results including mechanisms for the coordination of stochastic dynamics, simple models for designing bio-inspired systems, inference protocols of non-equilibrium driving forces and the importance of external forces in the internal dynamics of nano-machines.

We begin with a short introduction to provide some background information from statistical and biological physics including some examples and models from the literature.

We then set out on our journey and first examine the collective dynamics described by thermally activated identical coupled phase oscillators and establish a new model of synchronization. This becomes possible via a mobility matrix that couples the chemical forces of the different processes, referred as the dissipative coupling.

Following this, we study the effect of the dissipative coupling in the case of non-identical processes. Strikingly, this leads to topological phase locking and boosted stochastic dynamics.

Using the same principles, we consider an out-of-equilibrium process of an enzyme mechanically coupled to a passive molecule, and study the steady-state dynamics of the whole system and how the non-equilibrium conformational changes affect the molecule state. We demonstrate that the coupling in this case is controlled by the geometry of the enzyme which promotes the thermodynamically unfavorable state of the passive molecule to become favorable.

These lead to three golden rules for designing an enzyme.

To model relevant biological processes we need to respect thermodynamics. To this end, we utilize tools from the literature of stochastic thermodynamics and suggest a simple way of inferring correlations in non-equilibrium coupled systems. This is achieved by applying thermodynamic uncertainty relations to problems of many coupled processes.

We then provide a framework to describe the total entropy production rate of stochastic microswimmers and we propose an experimental protocol which allows for the exact inference of the chemical driving force that generates the active-swimming of the swimmer.

Finally, focusing on the individual processes, we construct a nonlinear response theory for molecular machines. We find that their activity changes in a non-monotonic way when subjected to external forces.

We conclude with a summary, discussion and future perspectives.

Acknowledgements

I would like to thank Ramin Golestanian for giving me the chance to work under his supervision in the Living Matter Physics department at the Max Planck Institute for Dynamics and Self-Organization. With him, I have been exposed to many new ideas, and I have expanded my knowledge in the field of theoretical physics and active matter. His continuous support and our evening discussions about work or other general topics are some of the things that I will always carry with me.

I would also like to thank Jaime Agudo-Canalejo. From the very first day he has been by my side helping me with any kind of questions that I had. Especially, at the beginning, our everyday discussions were essential. His supervision was of great importance and equipped me with many new skills and ideas.

Hopefully, the three-body collaboration between Ramin, Jaime and I is reflected in this thesis.

In addition, I would like to thank the thesis advisory committee members Prof. Dr. Jörg Enderlein and Prof. Dr. Marcus Müller, and the other members of the examination board, Dr. Aljaz Godec, Prof. Dr. Matthias Krügger, Prof. Dr. Stefan Klumpp, and Prof. Dr. Helmut Grubmüller.

I would like to thank Navdeep Rana, Jakob Metson, Luca Cocconi, and Charlotte Myin for reading and giving constructive feedback regarding the present work.

The last three years here in Göttingen were incredible both from the scientific and social point of view. This was due to the amazing colleagues and friends inside our institute. In addition, it was a great pleasure to share a house with my three flatmates. Therefore, I would like to thank all of those who made the time in Göttingen enjoyable and fulfilled; full of beautiful memories. I am really lucky that I had the chance to meet all of you.

Finally, I would like to thank my family and friends back home who provided me with support and encouragement.

Contents

1	Introduction	8
1.1	Enzymes and molecular motors	9
1.1.1	Enzyme enhanced diffusion	11
1.2	Microswimmers	11
1.3	Models of synchronization	13
1.4	Stochastic dynamics	15
1.4.1	Brownian dynamics	15
1.4.2	Overdamped Langevin and Fokker-Planck equations	17
1.4.3	Discrete Markov processes	20
1.5	Stochastic thermodynamics	22
1.5.1	Entropy production rate	22
1.5.2	Local detailed balance	24
1.5.3	Thermodynamic uncertainty relation	25
1.6	Cooperation between coupled enzymes	27
1.7	Outline	29
1.8	References	31
2	Collective synchronization of dissipatively-coupled noise-activated processes	46
2.1	Abstract, results and discussion	47
2.2	References	60
2.3	Supplemental material	62
3	Topological phase locking in molecular oscillators	64
3.1	Abstract, results and discussion	65
3.2	References	73
3.3	Supplementary Information	75

4	Universal mechanistic rules for de novo design of enzymes	80
4.1	Abstract, results and discussion	81
4.2	Appendix	91
4.3	References	94
5	Thermodynamic inference of correlations in nonequilibrium collective dynamics	96
5.1	Abstract, results and discussion	97
5.2	Appendix	101
5.3	References	102
6	Entropy production and thermodynamic inference for stochastic microswimmers	103
6.1	Abstract, results and discussion	104
6.2	Appendix	108
6.3	References	109
6.4	Supplemental material	111
7	Nonlinear response theory of molecular machines	120
7.1	Abstract, results and discussion	121
7.2	References	127
8	Discussion and conclusions	128

Chapter 1

Introduction

Fundamental questions regarding the origin of life puzzle many scientists around the globe. In particular, it is spectacular how biological systems operate in a well defined and self-organized way [1]. Even though this still remains an open question, there is clear evidence regarding mechanisms that operate life as it is. From a physics perspective, life consumes energy and is intrinsically out-of equilibrium [2]. This results in the emergence of new physical phenomena which are of primary interest for various scientific groups from the field of active matter [3, 4].

For a better insight into the biological phenomena, let us consider some examples from our everyday lives. For instance, one can easily say that human beings are good at dancing and in many cases this appears as a form of coordinated motion. Of course, such behavior is possible because humans have brains. On the microscopic scale, simple microswimmers like bacteria which do not have brains, are able to self-propel by simply receiving and processing chemical signals, or in other words to chemotax towards their food [5]. On a collective level this leads to pattern formation. Another very fascinating observation is that some micro-organisms exhibit self-organizing or coordinating features. An evident examples of a mechanism for self-organization in living cells is liquid-liquid phase-separation [6, 7]. A different example of an out-of equilibrium phenomenon for self-organization at the sub-cellular level is the formation of mitotic spindles [8]. Therefore, it is reasonable to ask if at even smaller scales -at the scale of proteins where diffusion and thermal fluctuations dominate- is it possible to also achieve new emergent dynamics. At those scales the out-of equilibrium systems are enzymes, which stochastically per-

form reactions, releasing Gibbs free energy. Can enzymes achieve coordination or increase their performance?

Biological systems as previously mentioned convert energy into motion. From a statistical physics perspective it is also interesting to study this mechanochemical interplay and how the work done by a mechanical force might affect the chemical cycle of an out-of-equilibrium process.

In this introduction, we summarize some background information regarding enzymes, molecular machines and microswimmers, all of which are microscale non-equilibrium systems. We then discuss stochastic dynamics, the framework used to describe these systems. We also cover briefly some important tools from the framework of stochastic thermodynamics. All these are important and basic ingredients used for the presented work in this thesis.

1.1 Enzymes and molecular motors

Enzymes are the biological catalysts which appear in many biochemical reactions in our body, and also in everyday processes like fermentation. From 20th century and onward, a theoretical and experimental framework was developed to understand how enzymes operate. An example of this development is the work by Michaelis and Menten which relates the enzymatic activity with the surrounding concentration of substrate, through a simple formula [9]. A further contribution is Kramers' pioneering work which was crucial in developing a framework for kinetic rate theory [10] which gives a well described picture on how enzymes work [11, 12, 13, 14].

Fig. 1.1(a) describes a typical schematic of the enzymatic cycle where the enzyme binds the substrate molecules and after catalysis it releases the products. This cycle occurs more rapidly compared to a cycle without the presence of the enzyme [15]. The schematic plot in Fig. 1.1(b), shows an energetic free landscape that drives the reaction. Sometimes, the substrate might spontaneously get converted into products (if the reaction is energetically favored). This happens at some characteristic rate proportional to $e^{-E_{\text{ba}}/k_B T}$, with k_B being the Boltzmann constant and T the temperature. This exponential factor is known as the Arrhenius law, with E_{ba} being the energy barrier or activation energy (see black dashed line) of the process [16]. In the one-dimensional picture presented in Fig. 1.1(b), the presence of the enzyme lowers the energy barrier (solid purple line) and hence, it accelerates the rate of the process.

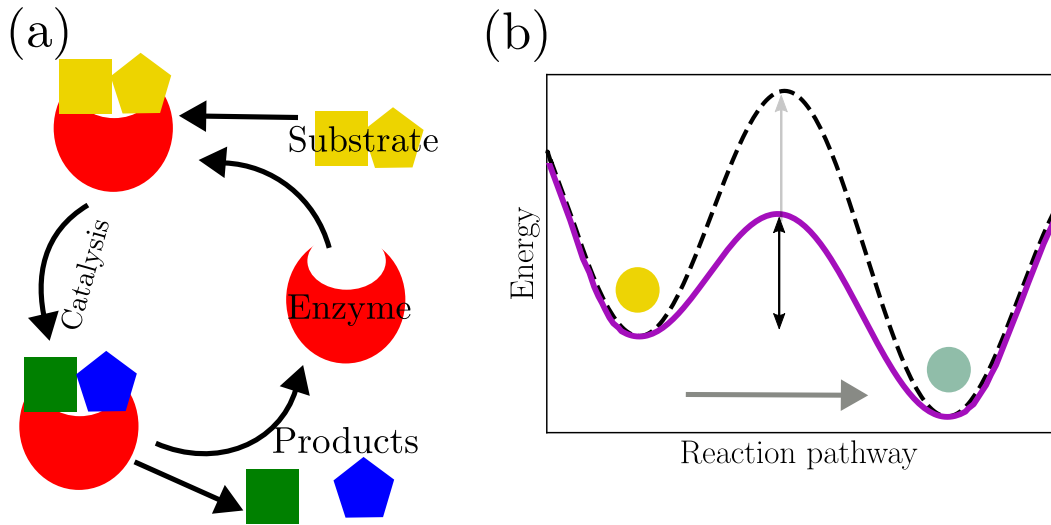


Figure 1.1: (a) An illustration of an enzymatic cycle. The free enzyme binds a substrate molecule and after the catalytic reaction it releases the resulting products. (b) An example of a potential that drives the reaction coordinate. The yellow dot represents the initial state of the reaction and green dot the final state. The energy barrier in between the two states defines a characteristic time scale for the reaction. The difference in height between the two minima is related to the difference in the Gibbs free energy released after the reaction. The presence of an enzyme lowers the energy barrier of the process.

Employing this single coordinate picture, in which thermal-noise activations cause barrier crossing reactions [13], leads to the Kramers' rate expression,

$$k_{\text{Kr}} = \frac{\sqrt{|\lambda|\lambda_0}k_B T}{2\pi\gamma} \exp\left(-\frac{E_{\text{ba}}}{k_B T}\right), \quad (1.1)$$

where γ is the friction coefficient of the reaction, λ and λ_0 are constants related to the second derivative of the free energy landscape. This expression agrees with the Arrhenius equation exponential factor and also determines its prefactor.

In biological cells another example of molecular machines are known as molecular motors. These motors perform reactions through the conversion of fuel into useful work or a different form of mechanical energy [17, 18]. The most used molecule in these processes is ATP. Hydrolyzing ATP to ADP releases energy which is used by the motor for useful work or motion [15]. This process is known as ATP-hydrolysis [19]. Some classical examples that utilize this mechanism are myosins and kinesins [17, 20].

Another example is the ATP Synthase enzyme which consists of different protein units having the overall characteristic of mini rotor [21]. It catalyzes ATP from ADP [22, 23] and is found in chloroplasts or mitochondria [24]. In the biophysics literature numerous models exist to describe the dynamics of these motors and enzymes, from minimal models [25, 26, 27, 28] to large scale molecular dynamics simulations [29, 30, 31, 32] to deal with their complex structure.

1.1.1 Enzyme enhanced diffusion

The idea of describing enzymatic reactions via a cycle that converts substrates into products is not the end of the story. Enzymes have complicated structures and might deliver mechanical work and energy. Hence, mechanical properties of the enzyme have to be considered. One of the important aspects which is observed experimentally is that enzymes change their conformation during their catalytic activity [33]. A well established technique for this type of experiments is fluorescent microscopy, which became a powerful tool in studying the properties of proteins [34]. In recent experimental studies, enhancement in the spatial diffusion of enzymes was reported during their catalysis [35, 36, 37].

In recent theories, the mechanical properties of the enzyme are included through a dumbbell like description of the enzyme [38, 39]. In this way the complicated macromolecular structure is projected into two unequal sub-units. This picture enables the enzyme to freely change its conformation and it includes any relevant hydrodynamic fluctuations that might affect its conformational state. By performing systematic moment expansions and by including an equilibrium mechanochemical cycle, it can be deduced that the hydrodynamic fluctuations are reduced during the chemical cycle, leading to enhancement in diffusion [38, 40].

In what follows, we discuss microswimmers, another form of active matter.

1.2 Microswimmers

In this section, we focus on microswimmers, a topic of interest for physicists, mathematicians and biologists [41]. Inside our body, we meet some examples of these systems, e.g sperms and bacteria equipped with different mechanisms for self-propulsion [42]. For instance, bacteria have rotating flagella, whilst

sperms swim by beating their tails [41].

Swimming at low Reynolds number is considered to be difficult since there is no inertia or the notion of time. Therefore, there needs to be a particular pattern of motion that the swimmer performs to achieve locomotion. This is related to the famous Scallop theorem by Purcell which states that a swimmer with one degree of freedom is not able to swim [43]. Therefore, swimmers need at least two degrees of freedom, such that a periodic and specific sequence of moves would enclose an area in the phase-space and cause swimming [44].

Microswimmers or artificially designed nanomotors are of major interest these days, in particular for drug delivery research [45, 46, 47]. A synthetic example of microswimmers are phoretic swimmers which are driven by gradients of some chemical scalar field that generate interactions with the body surface [48, 49] causing motion along the chemical gradients [50, 51]. A direct application of this are the Janus particles [52] or colloids with surface asymmetries [53, 54], where the integrated induced slip velocity over the swimmer's surface generates the propulsion [55, 56].

A classical model of a microswimmer is the Najafi-Golestanian swimmer, also known as the three-sphere swimmer [57]. This swimmer is a minimal example of locomotion where propulsion arises through the expansion-contraction of its arms through a simple cyclic sequence of deformations [58].

To illustrate this, we summarize how to construct the equations of motion of this swimmer. We start from the Oseen tensor which is the Green function of the incompressible Stokes equation,

$$\eta \nabla^2 \mathbf{v} - \nabla p = \mathbf{F} \delta(\mathbf{x}) \quad (1.2)$$

$$\nabla \cdot \mathbf{v} = 0, \quad (1.3)$$

where \mathbf{v} , p are velocity and the pressure of the fluid respectively, \mathbf{F} is a point force and η is the fluid viscosity. The Green function is,

$$G_{ij} = \frac{1}{8\pi\eta r} \left(\delta_{ij} + \frac{x_i x_j}{r^2} \right), \quad (1.4)$$

with x_i being the position vector and $r^2 = x_i x_i$ assuming Einstein summation convention [59]. We consider three spheres linked in a straight line whose motion is controlled by two arms that expand and contract. The axial symmetry of the problem implies that there are forces only along the body axis which

causes one-dimensional motion. Fixing the swimming direction to be in the x -axis, and the spheres to have radius a , the equations of motion take the form,

$$\dot{x}_\alpha = K_{\alpha\beta} f_\beta , \quad (1.5)$$

with $\alpha, \beta = 1, 2, 3$ the index of each sphere and $K_{\alpha\beta}$,

$$K_{\alpha\beta} \equiv \frac{\delta_{\alpha\beta}}{6\pi\eta a} + \frac{1 - \delta_{\alpha\beta}}{4\pi\eta|x_\alpha - x_\beta|} . \quad (1.6)$$

Here, the first term is the Stokes law on a sphere and the second one is due to the hydrodynamic interactions. Eq. (1.5) is a velocity-force relation which connects the forces and $K_{\alpha\beta}$ is a hydrodynamic mobility tensor. We define $x_2 - x_1 \equiv L_{\text{left}}$ and $x_3 - x_2 \equiv L_{\text{right}}$, and if we further assume that the left and right arms expand with some time amplitude variations such that $L_i = L^{(0)} + u_i(t)$ with, $L^{(0)}$ being constant, $u_{\text{left}}(t)$ and $u_{\text{right}}(t)$ are some time periodic functions, then the average velocity of the swimmer is,

$$\langle \dot{x}_i \rangle = C_g \langle \dot{u}_{\text{right}} u_{\text{left}} - \dot{u}_{\text{left}} u_{\text{right}} \rangle , \quad (1.7)$$

with C_g being a geometric factor [60]. This expression highlights what we mentioned earlier, that the swimming velocity is proportional to the enclosed area in the phase-space [41, 61]. This simple swimming mechanism has given the opportunity for further analytical and numerical studies of this swimmer in different situations and scenarios [62, 63, 64, 65, 64, 66].

So far, we have introduced different systems that can be either biological or synthetic. Now we move on to explore descriptions of synchronization for oscillators.

1.3 Models of synchronization

Synchronization is observed and studied long ago with one brilliant example, the Huygens experiment with the clocks. These days, it has become a very well understood subject which attracts the attention of people working in the field of non-linear dynamical systems [67, 68]. A popular model of synchronization in the literature is the Kuramoto model. [69, 70]. This model describes the

dynamics of coupled oscillators denoted by θ_i through a potential and driven by some constant force. The two-dimensional problem is expressed as,

$$\dot{\theta}_1 = \omega_1 + \frac{K}{2} \sin(\theta_2 - \theta_1) \quad (1.8)$$

$$\dot{\theta}_2 = \omega_2 + \frac{K}{2} \sin(\theta_1 - \theta_2) , \quad (1.9)$$

where ω_i is a constant driving and K is the coupling strength. The above equations can be trivially extended to the case of an arbitrary number of N oscillators. Intuitively, the synchronization arises because there is an alignment interaction force, and therefore, the oscillators synchronize above a critical K_c . To demonstrate this, we consider the rotating frame of reference of the system where $\omega_1 = -\omega_2 = \omega$ and we define $\Delta\theta \equiv \theta_1 - \theta_2$. This leads to,

$$\Delta\dot{\theta} = 2\omega - K \sin(\Delta\theta) . \quad (1.10)$$

For $K > K_c = 2\omega$ there is a stable fixed point where the two phases are locked. For larger number of oscillators, it is more convenient to introduce an order parameter and work with mean-field descriptions [71]. In addition, the Kuramoto model has been of major interest in the past because number of problems are effectively mapped into these dynamics or might effectively described by similar underlying equations. Some of these are problems of classical metronomes [72], chemical oscillators [73], time delayed interactions, [74] density waves [75, 76], semiconductor laser arrays [77, 78], Josephson junctions [79], noise-activated rotors [80], dynamics of swarms [81] and many others.

In biological systems, synchronization emerges in various systems via different mechanisms. These phenomena were experimentally observed in cardiac cells [82] (by mechanical stimulation), in green algae [83, 84], beating cilia [85, 86], microorganism flagella [87, 88], sperms [89] (by hydrodynamic coupling) and other relevant theoretical works propose hydrodynamic interactions as a mediator for synchronization [90, 91, 92, 93, 94]. Thus, it becomes evident that there is not universal model for synchronization and various mechanisms might give rise to these coordinated dynamics.

As already discussed in the first section, here we are interested in molecular size machines, therefore a stochastic description is suitable for these systems which are affected by thermal fluctuations. The Secs. 1.4-1.5 give a very brief introduction to methods, equations and theoretical tools that are used from

non-equilibrium statistical physics literature in the present work.

1.4 Stochastic dynamics

1.4.1 Brownian dynamics

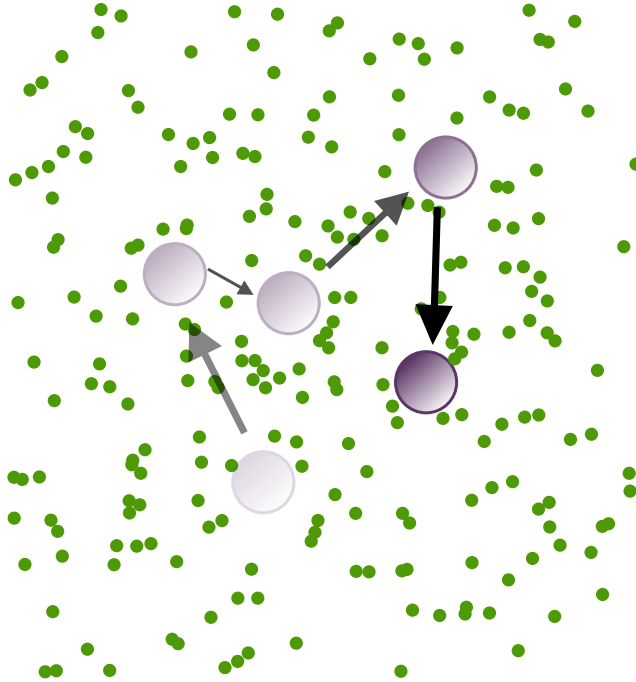


Figure 1.2: A particle undergoing Brownian motion by receiving random kicks from the surrounding medium at different instances of time.

A classical example of a stochastic process is the dynamics of a Brownian particle [95, 96, 97]. Consider a particle of mass m inside a fluid at a certain temperature T . Due to the friction from the surrounding fluid we expect a damping force to act on the particle which is assumed to be proportional to its velocity, $-\gamma v_i$, where the subscript index represents a spatial component. In addition, we assume that the particle receives random forces $\xi_i(t)$ from the surrounding medium during its motion. Over time, from symmetry arguments, the average force would be zero, $\langle \xi_i(t) \rangle = 0$, since it receives this force from any direction with any magnitude. Here, $\langle \dots \rangle$ indicates the average over the noise. We further assume that the forces at two different instants and along different directions are uncorrelated, $\langle \xi_i(t) \xi_j(t') \rangle = C \delta_{ij} \delta(t - t')$. The factor C is the force strength and will be determined in what follows. This additional stochas-

tic force converts the equation to a stochastic differential equation known as the Langevin equation. We start by writing the underdamped equations of motion of the particle using the momentum description for the velocity such that,

$$\dot{p}_i = -\gamma p_i/m + \xi_i \quad (1.11)$$

$$\dot{x}_i = p_i/m , \quad (1.12)$$

where $v_i = p_i/m$ and x_i is the position of the particle. We can predict the average behavior of the particle, by integrating over time and calculating the equal time correlator of $\langle p^2/m \rangle$ ($p^2 = p_i p_i$ assuming summation convention). We find that,

$$\left\langle \frac{p^2}{m} \right\rangle = e^{-2\gamma t/m} \left\langle \frac{p^2(0)}{m} \right\rangle + \frac{Cd}{2\gamma} (1 - e^{-2\gamma t/m}) , \quad (1.13)$$

where d is the number of dimensions of the system. In the long time limit, and using equipartition theorem, we find that $C = k_B T \gamma$ with k_B being the Boltzmann constant, T the temperature.

If the particle starts from the origin, due to its random motion it is expected that the average displacement of the particle will be zero. A non-zero quantity of interest is the mean-square displacement of the particle. By integrating and taking the long time limit one finds that,

$$\lim_{t \rightarrow \infty} \langle (x_i - \langle x_i \rangle)^2 \rangle \equiv 2Dt , \quad (1.14)$$

where we define the diffusion coefficient of the random walk to be D . This leads to the famous Einstein relation,

$$D = \frac{k_B T}{\gamma} = \mu k_B T . \quad (1.15)$$

In the second equality in Eq. (1.15), we define the particle mobility $\mu \equiv \gamma^{-1}$. The Einstein relation is a special case of the fluctuation-dissipation theorem [98] and it demonstrates the connections between the particle mobility (or its size) and the thermal fluctuations are linked with its diffusion. As an example a Janus colloid (see Sec. 1.2) is much larger than the surrounding solute particles, hence, by employing the Einstein relation (in combination with Stokes' law)

one can assume that the diffusion of the solute particles is much faster than the dynamics of the colloid [52].

In the limit of $m/\gamma \rightarrow 0$ where the viscous forces dominate over the inertial forces, we can neglect the inertial contributions and obtain the overdamped version of the equations. A typical example of overdamped Langevin equations in active matter is active Brownian particles (ABPs), where the particles are assumed to have a constant self-propulsion speed and random orientational dynamics [99, 100].

The equivalent description of an overdamped Langevin equation is a Fokker-Planck equation which is a partial differential equation of the probability distribution that describes the stochastic dynamics of the system. In what follows, we focus on the dynamics in the overdamped limit since such description is more suitable for describing stochastic dynamics at small scales, due to the large viscous forces.

1.4.2 Overdamped Langevin and Fokker-Planck equations

We have seen the passive stochastic dynamics of a particle inside a fluid medium that is subjected to stochastic forces. Now, we would like to add more ingredients to the mathematical description inspired by biological systems, and consider the dynamics of a bacterium near a solid surface. Experiments were performed using *E. Coli* bacteria which show that these micro organisms perform circular motion near a wall [101]. This behaviour has also been explained theoretically [102].

As a first step, we consider the friction forces of this problem in the underdamped picture. Because *E. Coli* bacteria have elongated shape the friction forces will be unequal along different axes of the swimmer, which leads to anisotropic friction. To describe this effect we are going to use the friction tensor Γ_{ij} . In the case of a Brownian particle in Sec. 1.4.1, $\Gamma_{ij} = \gamma\delta_{ij}$. Furthermore, the hydrodynamic interactions of the swimmer with the wall induces some off-diagonal forces and torques which imply that Γ_{ij} will also have off-diagonal components. Another aspect which might be present are inhomogeneities in the fluid or viscosity gradients that surround the microswimmer [103, 104]. Conceptually, this implies that at different regions the swimmer might experience different frictional forces, which results in a spatially dependent friction tensor $\Gamma_{ij}(x_k)$. Notice that here we focus for simplicity on the

translational dynamics of the swimmer but it is also possible to include the rotational dynamics of the swimmer. In that case, the generic friction tensor is known as the resistance tensor in hydrodynamics and it includes all the possible couplings of force/torques with translational/angular velocities [41, 44, 59]. Therefore, a suggested description of the underdamped translational dynamics is,

$$\dot{p}_i = F_i - \Gamma_{ij}p_j/m \quad (1.16)$$

$$\dot{x}_i = p_i/m, \quad (1.17)$$

where F_i models the self-propelled force that generates the swimming and possible other forces from potentials. However, in this regime it is safe to use the overdamped description since at low Reynolds number the inertial forces are negligible. Therefore, in this limit an overdamped description is more suitable and convenient given by,

$$\dot{x}_i = M_{ij}(x_k)F_j + \xi_i, \quad (1.18)$$

where $M_{ij}(x_k) \equiv \Gamma_{ij}^{-1}(x_k)$ is the mobility tensor of the dynamics, and ξ_i is the noise [97]. The mobility tensor is a generalization of the scalar μ in Eq. (1.15). Here in the deterministic part of the equation, we see another type of a force velocity relation similar to what is discussed in Sec. 1.2. We now describe the

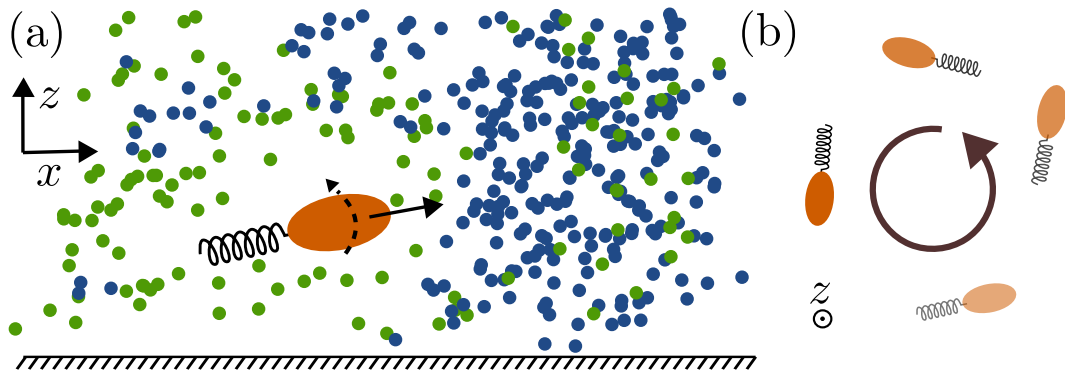


Figure 1.3: (a) A bacterium near a solid surface inside a fluid with inhomogeneous fluid density which self-propels due to the rotation of its head and helical shape flagellum. (b) The emerging hydrodynamic interaction causes the bacterium to move in circles.

noise. For example, if the bacterium's flagellum stop rotating the bacterium will exhibit a diffusive motion due to the random forces from the medium.

As already demonstrated the Einstein relation relates the diffusion with the particle's mobility. This must be taken into account in the noise strength. In particular, the spatial dependence of the mobility needs to be treated carefully to include the spatial dependencies in the noise-strength. The complete overdamped Langevin equation for the Eq. (1.18) in the Ito interpretation is,

$$\dot{x}_i = M_{ij}F_j + k_B T \partial_j M_{ij} + \sqrt{2k_B T} \Sigma_{ij} \xi_j, \quad (1.19)$$

where $\langle \xi_i \rangle = 0$ and $\langle \xi_i \xi_j \rangle = \delta_{ij} \delta(t-t')$ [105]. This equation falls in the category of Langevin equations with multiplicative noise and this is due to the space dependence of $M_{ij}(x_k)$. The first term in Eq. (1.19) is the deterministic part and a velocity-force relation via the mobility tensor. The last term in the equation above is the term related to the thermal noise where the tensor Σ_{ij} satisfies $\Sigma_{ik} \Sigma_{jk} = M_{ij}$. The second term is known as the spurious drift term and is required (in Ito's convention) for the Langevin equation in combination with the third term to respect the fluctuation-dissipation theorem and give consistent thermodynamics [106]. In the case that the mobility is constant the spurious drift term vanishes.

Another example of multiplicative noise is the stochastic version of the three-sphere swimmer model (see $K_{\alpha\beta}$ Eq. (1.5)), where due to the expansion/contraction of the arms the mobility of the swimmer continuously changes and in the presence of fluctuation this will give rise to multiplicative noise [66, 107].

Solving the stochastic equations of motion for different trajectories (noise realizations) and initial conditions allows us to obtain statistics of relevant observables of the system and construct probability distributions. Such a probability distribution, denoted as $P(x_i, t)$, is expected to evolve in time and space and to describe the same stochastic dynamics as the Langevin one. This leads to the classical equation known as the Fokker-Planck equation which for Eq. (1.19) corresponds to [97, 105],

$$\partial_t P = \partial_i [M_{ij} (k_B T \partial_j P - F_j P)] . \quad (1.20)$$

The term inside the square brackets is equal to the negative value of the prob-

ability current J_i defined as,

$$J_i = M_{ij} (F_j P - k_B T \partial_j P) . \quad (1.21)$$

It is worth noting that in Eq. (1.20) the mobility tensor in the probability current is factored out, thus, in the absence of any non-equilibrium driving (when then dynamics are governed by an equilibrium potential i.e. $F_i = -\partial_i U$), at the stationary state, one recovers Boltzmann equilibrium. This happens independently of the form of the friction and by solving the case $J_i = 0$ we find

$$P_{\text{eq}} \propto \exp\left(-\frac{U}{k_B T}\right) , \quad (1.22)$$

which is the standard Boltzmann weight.

1.4.3 Discrete Markov processes

A different framework for studying the evolution of stochastic dynamics is through discrete Markov processes [97, 108]. Markov processes are processes where the probability of an event depends only on the previous state, i.e. there is no memory in the evolution of the dynamics of the system. This is also the case for the Langevin dynamics. In this formalism, we assume that the system can be found in a discrete state i from a set of possible states with some probability P_i . As the time evolves, the system will explore other states, through kinetic transitions from the state $i \rightarrow j$. This implies that the rate of change of the probabilities can be described by a linear system of equations known as the master equation which is given by,

$$\frac{dP_i}{dt} = \sum_j k_{ij} P_j , \quad (1.23)$$

where k_{ji} is the rate jumping from i to j with the conservation of probability constraint being $\sum_i P_i = 1$ (demanding conservation of probability $k_{jj} = -\sum_i k_{ij}$) [108]. To demonstrate the relation of these transition rates with a physical picture, one can consider the Kramer potential in Fig. 1.1(b) and map that problem into a discrete one. The left and right minima might be assumed to be two discrete states where the system can jump between them through the kinetic rates. Using the Kramer rate expression in Eq. (1.1) one

might link the rates with that energy landscape. Notice that for the backward rate the energy barrier is effectively higher because the right minimum is at lower energy level. Therefore, without going to further mathematical details, it is expected at the long time limits to find the process on the right side of the potential since the escape times are higher.

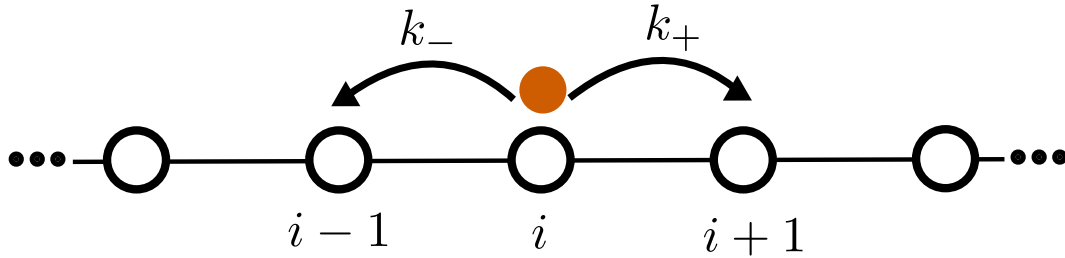


Figure 1.4: An infinite lattice of discrete states. The orange circle represents a particle hopping towards the right with probability rate k_+ and to the left with some probability rate k_- .

Another way to demonstrate a connection with overdamped Langevin dynamics is by considering a particle hopping in an one-dimensional lattice model. This might be a very simple model for a molecular motor stepping with directed motion [27, 109]. The particle at every position has a transition rate k_+ (k_-) to jump towards the right (left) direction. Therefore, if the particle is located at the i th position there is an inward and outward probability flux from the left and the right which by using master equation is expressed as,

$$\frac{dP_i}{dt} = \sum_i k_+(P_{i-1} - P_i) + k_-(P_{i+1} - P_i) . \quad (1.24)$$

By assuming that the lattice has infinitely many states, a continuum limit assumption holds such that the probability $P_i(t) \rightarrow P(x, t)$. This allows us to Taylor expand for P_{i+1} as,

$$P_{i+1}(t) = P(x + \Delta x, t) = P(x, t) + \Delta x \partial_x P(x, t) + \frac{\Delta x^2}{2} \partial_x^2 P(x, t) + \mathcal{O}(\Delta x^3) , \quad (1.25)$$

and similarly for P_{i-1} . Δx is defined as the space between the sites. Substituting back into Eq. (1.24) we get the one dimensional Fokker-Planck equation,

$$\partial_t P = -\partial_x (vP - D\partial_x P) , \quad (1.26)$$

with,

$$v \equiv (k_+ - k_-)\Delta x \quad (1.27)$$

$$D \equiv (k_+ + k_-)\frac{\Delta x^2}{2} . \quad (1.28)$$

The parameter v is the non-equilibrium drift velocity and D is the diffusion coefficient of the process. This shows an effective connection between the discrete and continuous picture. To complete the stochastic descriptions we need to include thermodynamics in the picture.

1.5 Stochastic thermodynamics

1.5.1 Entropy production rate

In the 18th century, the first steam engines inspired physicists of those times to create what today we call classical thermodynamics. In a similar way, for microscopic non-equilibrium systems we need a framework to quantify the measure of dissipation and irreversibility. First, we revisit the stochastic version of the first law of thermodynamics related to the trajectory of a particle which states that,

$$\vec{d}w = \vec{d}q + dU , \quad (1.29)$$

where $U(x_i, \lambda)$ is the internal energy which depends on space and on a time-dependent control parameter λ such that $dU = -\partial_i U dx_i + \partial_\lambda U d\lambda$ [106]. x_i represents the stochastic trajectory of a process. When the particle is subject to an external driving force F_i then the heat dissipated into the medium is $\vec{d}q = F_i dx_i = F_i^{\text{neq}} dx_i - \partial_i U dx_i$. Therefore, by integrating, the work increment splits into two contributions,

$$w(t) = q(t) + U(\lambda(t)) - U(\lambda(0)) , \quad (1.30)$$

where we identify the dissipated heat in the medium as,

$$q[x_i(t)] = \int_0^t d\tau \dot{x}_i \circ F_i . \quad (1.31)$$

This is a trajectory dependent quantity and the \circ is to emphasize that for the inner product Stratonovitch product is assumed [110].

Perhaps a more mathematical way to construct the definition of heat dissipation is through path integral probabilities. Non-equilibrium systems break time-reversal symmetry, therefore, the path probability of a trajectory going forward in time has a different weight from the one that goes backward. This probability is defined as $\mathcal{P}[(x_i(t))] \propto e^{-\mathcal{S}}$ where by using a Martin-Siggia-Rose treatment for the path integrals and without going into derivation details, the Onsager-Machlup action \mathcal{S} is [111],

$$\mathcal{S}[x_i(\tau)] = \int_0^t d\tau \left[(\dot{x}_i - M_{ij}F_j) (4D)_{ik}^{-1} (\dot{x}_k - M_{kl}F_l) + \frac{1}{2} \partial_i M_{ij} F_j \right], \quad (1.32)$$

with $D_{ij} = M_{ij}k_B T$ satisfying the Einstein relation. In the time reverse trajectories $\tilde{x}_i(\tau) = x_i(t - \tau)$ the velocities flip sign and thus,

$$q[x_i(t)] = k_B T \ln \left(\frac{\mathcal{P}_{\text{forw}}}{\mathcal{P}_{\text{back}}} \right) = \int_0^t d\tau \dot{x}_i F_i, \quad (1.33)$$

as in Eq. (1.31) the product is odd in time reverse transformation [106].

The rate of of heat dissipation inside the medium will increase the entropy where the corresponding contribution is defined as $T\dot{s}_{\text{med}} \equiv \dot{q} = \dot{x}_i F_i$. The other contribution to the entropy comes from the Gibbs entropy S ,

$$S = -k_B \int d^d x P(x_i, t) \ln P(x_i, t). \quad (1.34)$$

In stochastic thermodynamics, a quantity of interest is the total average entropy production rate (EPR). Combining the two contributions leads to $\dot{S}_{\text{tot}}(t) = \dot{S}_{\text{med}} + \dot{S}$, with $\dot{S}_{\text{med}} = \langle \dot{s}_{\text{med}} \rangle$. After algebraic manipulations this leads to [110],

$$T\dot{S}_{\text{tot}}(t) = k_B T \int d^d x \frac{J_i(x_k, t) (D(x_i)^{-1})_{ij} J_j(x_k, t)}{P(x_k, t)}, \quad (1.35)$$

with J_i being the probability current defined by Eq. (1.21). It is worth emphasizing that the bilinear structure of the entropy production in combination with the positive definite D_{ij} imply that the entropy production is non-negative which manifests the second law of thermodynamics [112]. At the non-equilibrium steady state, where $\partial_t P_{\text{ss}}(x_k) = 0$, the contribution from \dot{S} vanishes and hence, only the heat dissipation contributes towards the entropy

production rate. As a result, the combination of Eqs. (1.21) and (1.35) leads to the EPR at the steady state $T\dot{\sigma}$,

$$T\dot{\sigma} = \int d^d x J_i^{\text{ss}} F_i^{\text{neq}}, \quad (1.36)$$

where J_i^{ss} stands for the steady-state current. Notice that the force from the potential U becomes a boundary term after integration and vanishes. This expression highlights that any contribution in the EPR is a product between currents and corresponding non-equilibrium forces which disappear when the drivings become zero.

1.5.2 Local detailed balance

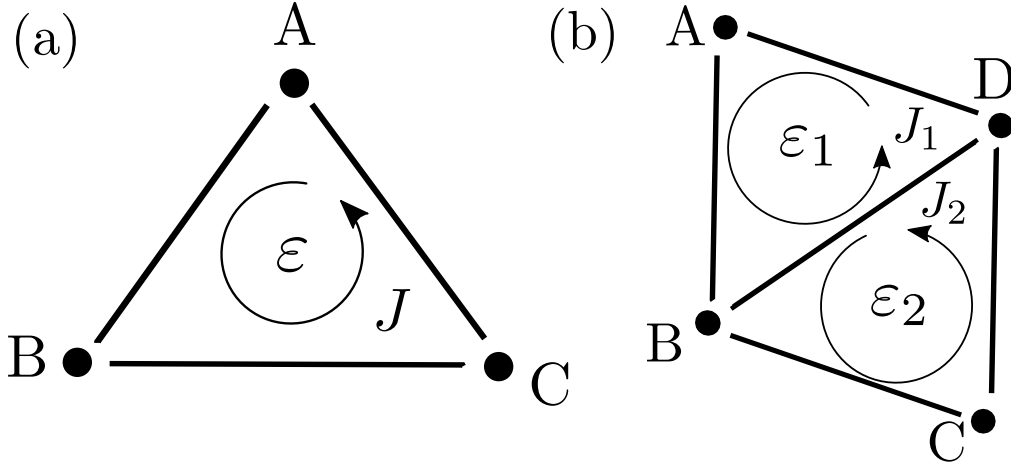


Figure 1.5: Two examples of discrete lattice networks. (a) A unicyclic network with three states, where J is the steady state current and ε the non-equilibrium affinity. (b) A network of four states and two cycles with different currents and affinities.

The consistent thermodynamic description in the discrete case arises via a relation between the kinetic rates k_{ij} . In particular, the ratio between the forward and backward rates during the transition $i \rightarrow j$ needs to satisfy,

$$\frac{k_{ji}}{k_{ij}} = \exp(\Delta\sigma_{ji}/k_B), \quad (1.37)$$

with $\Delta\sigma_{ji}$ being the total dissipation of the system during that transition. This is known as the local-detailed balance condition [106] and typically has two contributions, the chemical energy ε_{ji} which is the energy dissipated for

the process to happen and the mechanical one which is related to some work done W_{ji} by an external force [113]. Then by starting from Eq. (1.23), one can deduce that the entropy production rate at the steady-state for the discrete dynamics is,

$$T\dot{\sigma} = \frac{k_B T}{2} \sum_{i,j} (k_{ij} P_j^{\text{ss}} - k_{ji} P_i^{\text{ss}}) \ln \frac{k_{ji}}{k_{ij}}, \quad (1.38)$$

where P_i^{ss} is the probability of finding the system in the i th state at the stationary state [114]. We define the affinity of a cycle a as,

$$T\Delta\sigma_a = k_B T \sum_{\{ij\}} \ln \frac{k_{ji}^a}{k_{ij}^a}, \quad (1.39)$$

where k_{ji}^a (k_{ij}^a) are the forward (backward) rates of cycle a [115]. In Fig. 1.5, we include two simple examples of cyclic networks, which might minimally model biomolecular processes [26, 27, 116]. For example in the triangular unicyclic network in Fig. 1.5(a), the affinity is, $\varepsilon = \ln \frac{k_{CB}k_{BA}k_{AC}}{k_{BC}k_{CA}k_{AB}}$. Solving the master equation gives the steady-state velocity current $J = P_B^{\text{ss}}k_{BA} - P_A^{\text{ss}}k_{AB}$ [117]. In a similar way, for the network with four states in Fig. 1.5(b), the affinities are $\varepsilon_1 = \ln \frac{k_{DB}k_{BA}k_{AD}}{k_{BD}k_{DA}k_{AB}}$ and $\varepsilon_2 = \ln \frac{k_{BD}k_{CB}k_{DC}}{k_{BC}k_{CD}k_{DB}}$, with $J_1 = P_B^{\text{ss}}k_{BA} - P_A^{\text{ss}}k_{AB}$ and $J_2 = P_C^{\text{ss}}k_{CB} - P_B^{\text{ss}}k_{BC}$. The EPR of the network with two cycles is the sum of the energy dissipated by the two and thus, $T\dot{\sigma} = J_1\varepsilon_1 + J_2\varepsilon_2$, agreeing as expected with Eq. (1.38). More generically, the expression at steady-state for the EPR reduces to [115],

$$T\dot{\sigma} = \sum_i J_i \varepsilon_i, \quad (1.40)$$

which is equivalent to the continuous description.

1.5.3 Thermodynamic uncertainty relation

In Sec. 1.4.3, we introduced a simple model of a particle hopping on an infinite lattice. However, that model is not complete in the thermodynamic sense since the transition rates are arbitrary at the moment. If we imagine that the particle is related to some realistic process then every time that it performs a step, it must consume some energy ε . The local-detailed balance condition

implies that,

$$\varepsilon = k_B T \ln \left(\frac{k_+}{k_-} \right) , \quad (1.41)$$

which is the affinity of the process. The velocity of the process, or the average current which we denote as $v = J = k_+ - k_-$ (where we assume $\Delta x = 1$), and the diffusion coefficient is $2D = k_+ + k_-$. Intuitively, the rate of energy dissipation is the product between the velocity current J and the affinity ε and thus, $T\dot{\sigma} = J\varepsilon$ as in the case of the unicyclic network. Notice also that if the rates are equal then the affinity $\varepsilon = 0$. At the same time the non-equilibrium current J vanishes, and the system recovers equilibrium.

We would like to define a dimensionless precision quality factor that measures the trade-off between the precision of the stochastic current J and the dissipation of the system. One possible choice is the following [118],

$$\mathcal{Q} \equiv \frac{k_B J^2}{D \dot{\sigma}} , \quad (1.42)$$

where applying this to the hopping problem we get,

$$\mathcal{Q} = \frac{2k_B T}{\varepsilon} \tanh \frac{\varepsilon}{2k_B T} \leq 1 . \quad (1.43)$$

This inequality holds for any values of $\varepsilon/k_B T$ and it is saturated at $\varepsilon \rightarrow 0$. The quality factor \mathcal{Q} was conjectured to be bounded from above by one for any discrete stochastic system independent of its topology, and some time later this was mathematically proven to be correct and also extended to overdamped Langevin equations. This is known as the thermodynamic uncertainty relation (TUR) [118] a very powerful inequality of stochastic thermodynamics, analogous to the Heisenberg uncertainty principle in quantum mechanics. Following this work, different approaches were employed to prove [119, 120, 121] this inequality. Moreover, TUR has inspired studies for numerous other uncertainty relations in stochastic thermodynamics [122, 123, 124, 125, 126, 127, 128]. A direct generalization of the single TUR, is a multidimensional version of it which includes multiple currents of the non-equilibrium system and their correlation, the multidimensional TUR (MTUR) [129] which is given by,

$$J_i(\mathcal{D})_{ij}^{-1} J_j \leq \frac{\dot{\sigma}}{k_B} , \quad (1.44)$$

with \mathcal{D}_{ij} being the correlation matrix at the steady state with its diagonal components to correspond to the diffusion coefficients of each current and the off-diagonal ones are the steady state correlations between the i th and j th currents of the dynamics. This inequality is useful in systems in which there are couplings between the non-equilibrium currents.

1.6 Cooperation between coupled enzymes

In Sec. 1.1.1 we have discussed a minimal description of enzymes using a dumb-bell like shape. Here, an important ingredient is added to that picture related to the fact that enzymes are out of equilibrium. To include this feature, a phase coordinate ϕ is introduced which describes the internal state of the enzyme during a chemical reaction. The potential that describes the dynamics

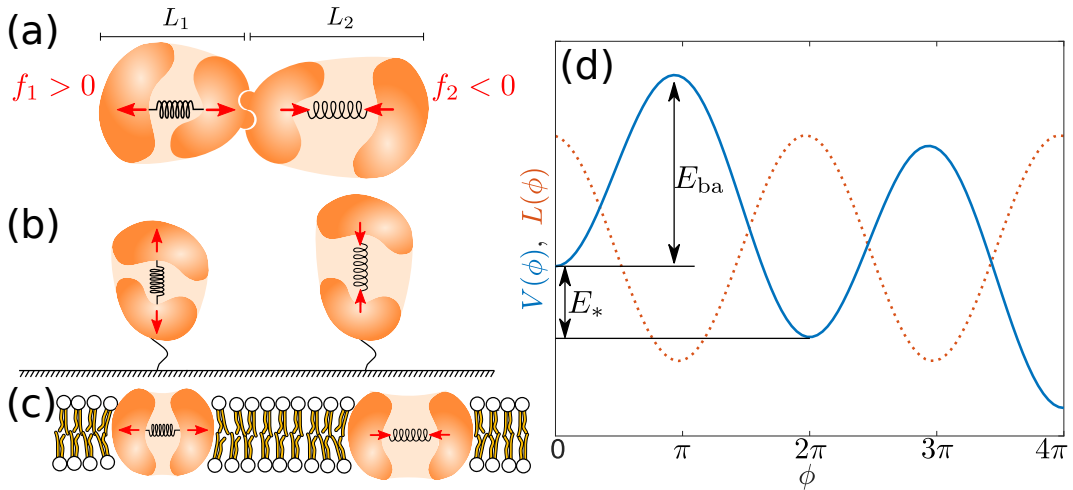


Figure 1.6: Examples of mechanical interactions: (a) Two enzymes bound to each other forming a complex. Each enzyme has elongation L_α and experiences an internal force f_α . (b) Two enzymes interact with each other hydrodynamically through the surrounding viscous fluid medium. (c) Two enzymes embedded in a lipid membrane interact elastically. (d) The catalytic cycle of each enzyme is represented by a phase ϕ_α evolving in a biased free energy landscape $V(\phi_\alpha)$ (solid blue). The enzyme elongation L_α tries to adapt to a phase-dependent rest length $L(\phi_\alpha)$ (dotted red). Reprinted with permission from “Synchronization and enhanced catalysis of mechanically coupled enzymes.”, Jaime Agudo-Canalejo, Tunrayo Adeleke-Larodo, Pierre Illien, Ramin Golestanian, Physical Review Letters, 127, 208103. Copyright 2021 American Physical Society [130].

of an enzyme of length L with internal coordinate ϕ is given by,

$$U(L, \phi) = \frac{k}{2}(L - L(\phi))^2 + V(\phi) , \quad (1.45)$$

where k is the spring constant, $L(\phi)$ is the preferential length of the enzyme and $V(\phi)$ is the non-equilibrium potential of the chemical dynamics [130]. A possible choice for $V(\phi)$ is the washboard potential, denoted as $V(\phi) = -F\phi - v \cos(\phi + \delta)$, with F being the chemical driving force and δ is an arbitrary phase factor (see Fig 1.6(d)). A cycle corresponds to the phase advancing by 2π and corresponds to a chemical reaction. F is related to the difference in Gibbs free energy consumed after a complete cycle which is denoted by E_* . The preferential length has ϕ dependence which is responsible for the conformational changes induced by the chemical reaction. In addition, the function form of $L(\phi)$ must be periodic.

The question is the following; what would happen if one enzyme gets attached to another forming a complex (Fig. 1.6(a))? How will the conformational changes of one affect the chemical dynamics of the other and vice-versa? To answer this question first we write the equations of motion for the lengths and the chemical cyclic coordinates. Considering the overdamped scenario the equations are,

$$\dot{L}_\alpha = \mu(f_\alpha + hf_\beta) \quad (1.46)$$

$$\dot{\phi}_\alpha = -\mu_\phi[-k(L_\alpha - L(\phi_\alpha))L'(\phi_\alpha) + V'(\phi_\alpha)] , \quad (1.47)$$

where $\alpha = 1, 2$, μ is hydrodynamic mobility, μ_ϕ is the chemical mobility and $f_\alpha = -\partial_{L_\alpha}U$. Then, assuming the enzymes are stiff ($k \gg 1$) allows us to project to slow dynamics which are the internal coordinates. In particular, the dynamics of the two phases become coupled through the following relation (in Ito convention),

$$\dot{\phi}_\alpha = M_{\alpha\beta}(-\partial_\beta V) + k_B T \partial_\beta M_{\alpha\beta} + \sqrt{2k_B T} \Sigma_{\alpha\beta} \xi_\beta , \quad (1.48)$$

with, $M_{\alpha\beta}$ being the mobility matrix that couples the forces $\partial_\beta V$. In the third term ξ_β is the white noise with $\langle \xi_\beta \rangle = 0$ and $\langle \xi_\alpha(t) \xi_\beta(t') \rangle = \delta_{\alpha\beta} \delta(t - t')$. $\Sigma_{\alpha\beta}$ is the principal square root of the mobility matrix $M_{\alpha\beta}$ such that $\Sigma_{\alpha\gamma} \Sigma_{\beta\gamma} = M_{\alpha\beta}$. These terms are similar to what have been introduced in Eq. (1.19). However,

here the subscripts indicate the enzymes whereas in the previous example they were vector indices.

Importantly, $M_{\alpha\beta}$ has non-zero off-diagonal components which depend on the geometry of the enzyme. In the special case in which the enzymes have negligible conformational oscillation, they do not affect each other mechanically and hence, the off-diagonal terms vanish. This implies that the chemical dynamics of the enzymes become uncoupled. In the case where the off-diagonal mobility terms are non-zero, surprisingly, not only synchronization in the phase dynamics, but also enhancement in the activity of the enzymes is observed [130].

This behaviour is understood by focusing on the deterministic dynamics using phase-portraits. By varying the off-diagonal coupling strength the dynamics exhibit a novel global bifurcation. This bifurcation leads to the formation of periodic band which is a region with trajectories that do not reach the fixed point. When the noise is present, it eventually kicks the system into this band which leads to running trajectories and therefore, to a synchronization and increase in the speed of the reactions [130]. An enhancement in the activity of enzymes is observed experimentally when enzymes form oligomeric structures. Importantly, this is a new model of synchronization since the coupling in this case comes from the mobility matrix. The physical reason is the formation of the complex and the conformational changes of the enzymes. This leads to the distinct difference with the Kuramoto model where the coupling arises from the forces (i.e. $\sin(\theta_1 - \theta_2)$). In principle, Eq. (1.48) has a generic structure and it can be applicable to other problems of coupled processes.

1.7 Outline

In this introductory chapter, we have explored various topics and simple examples related to biological and statistical physics. After defining and presenting different notions and ideas, we reached a minimal model of coupled enzymes exhibiting synchronization and enhancement in the catalytic activity. These concepts can be viewed as the starting point and the main ingredients that we use for what follows in this thesis.

Chapter 2 of this work deals with a generalization from two coupled processes to an arbitrary number. This is a natural extension of Eq. (1.48). As a first step, we consider that the phase oscillators ϕ_α are coupled via an

all-to-all constant coupling, which gives a mean-field realization of the problem. Through this work we have shown that indeed the mean-field description leads to collective synchronization. By performing numerical integration of the stochastic differential equations, this becomes evident especially at low number of oscillators and high off-diagonal coupling. At the limit of a large number of processes, the situation changes and the collective dynamics reach a deterministic behavior. We explain these simulation results through a mean-field theory which exhibits a great agreement with the numerics. Using the TUR we calculate the performance factor of the system which increases in the deterministic phase.

In Chapter 3, we focus on the scenario of two processes but with different energetic landscapes. The simplest way to establish this asymmetry is by varying the Gibbs free energy consumed by each enzyme after each reaction. In this work we use the same type of dissipative coupling. It can be shown that, this serves as a minimal model of two mechanically or hydrodynamically coupled interacting rotors. The dynamics in this work exhibit a rich structure and a hierarchy of bifurcations takes place. The phase-oscillators now undergo phase-locked multi-steps, and at certain regions in the parameter space there is the appearance of topological phase-locked states. States are called topological phase-locked states, where there is an emergence of periodic asymmetric bands that do not reach the fixed points of the dynamics. As confirmed by stochastic simulations, it leads to enhancement in speed and diffusion of the coupled processes.

Another class of coupled processes that we consider is when one is driven but the other is passive. In Chapter 4 we introduce a model to describe a catalyzed chemical reaction. In this work, we show that a non-equilibrium process can cause an energetically unfavorable process to become favorable through the dissipative coupling. This is demonstrated directly through the example of an enzyme that binds to a molecule.

Then, we consider applications of the thermodynamic uncertainty relations in problems of coupled non-equilibrium processes. In Chapter 5, we focus on examples of coupled oscillators, models of gears, and coupled discrete networks where we propose a protocol on how one can experimentally infer the correlations between processes through a measurement of a single process.

In Chapter 6, we introduce a thermodynamically consistent framework for stochastic microswimmers. By distinguishing the active swimming mechanism

and the mechanical external forces exerted on the swimmer, the swimming velocity and the structure of its total dissipation is determined. We employ this framework on a stochastic version of the three-sphere swimmer (introduced in Sec. 1.2) which allows us to tract the problem analytically. This exact description reveals the importance of the mechanochemical coupling far from equilibrium. Furthermore, by utilizing the MTUR on the spatial and chemical currents of the swimmer we propose an experimental strategy for inference of the chemical driving force of the stochastic swimmers.

The mechanistic descriptions of the nano-machines introduced in the previous chapters in combination with the effect of external applied forces on them is studied in Chapter 7 where a nonlinear response framework for these molecular machines is developed. It is shown that the speed and the diffusion of the processes exhibit a non monotonic behavior with the external mechanical force.

References

- [1] Eric Karsenti. Self-organization in cell biology: a brief history. *Nature Review Molecular Cell Biology*, 9:255–262, March 2008.
- [2] Mark J. Bowick, Nikta Fakhri, M. Cristina Marchetti, and Sriram Ramaswamy. Symmetry, thermodynamics, and topology in active matter. *Physical Review X*, 12:010501, February 2022.
- [3] Gerhard Gompper, Roland G Winkler, Thomas Speck, Alexandre Solon, Cesare Nardini, Fernando Peruani, Hartmut Löwen, Ramin Golestanian, U Benjamin Kaupp, Luis Alvarez, et al. The 2020 motile active matter roadmap. *Journal of Physics: Condensed Matter*, 32(19):193001, 2020.
- [4] Sriram Ramaswamy. The mechanics and statistics of active matter. *Annual Review of Condensed Matter Physics*, 1(1):323–345, 2010.
- [5] George H. Wadhams and Judith P. Armitage. Making sense of it all: bacterial chemotaxis. *Nature Review Molecular Cell Biology*, 5:1024–1037, December 2004.
- [6] Anthony A Hyman, Christoph A Weber, and Frank Jülicher. Liquid-liquid phase separation in biology. *Annual Review of Cell and Developmental Biology*, 30(1):39–58, 2014.
- [7] Clifford P. Brangwynne, Christian R. Eckmann, David S. Courson, Agata Rybarska, Carsten Hoege, Jöbin Gharakhani, Frank Jülicher, and Anthony A. Hyman. Germline P Granules Are Liquid Droplets That Localize by Controlled Dissolution/Condensation. *Science*, 324(5935):1729–1732, June 2009.
- [8] Kenneth E Sawin, Katherine LeGuellec, Michel Philippe, and Timothy J Mitchison. Mitotic spindle organization by a plus-end-directed microtubule motor. *Nature*, 359(6395):540–543, 1992.

- [9] Kenneth A Johnson and Roger S Goody. The original Michaelis constant: translation of the 1913 Michaelis–Menten paper. *Biochemistry*, 50(39):8264–8269, 2011.
- [10] Hans Kramers. Brownian motion in a field of force and the diffusion model of chemical reactions. *Physica*, 7(4):284–304, April 1940.
- [11] Athel Cornish-Bowden. One hundred years of michaelis–menten kinetics. *Perspectives in Science*, 4:3–9, 2015.
- [12] Peter K Robinson. Enzymes: principles and biotechnological applications. *Essays in biochemistry*, 59:1, 2015.
- [13] Peter Hänggi, Peter Talkner, and Michal Borkovec. Reaction-rate theory: fifty years after kramers. *Reviews of modern physics*, 62(2):251, 1990.
- [14] Joseph Kraut. How do enzymes work? *Science*, 242(4878):533–540, 1988.
- [15] Bruce Alberts, Dennis Bray, Julian Lewis, Martin Raff, Keith Roberts, James D Watson, et al. *Molecular biology of the cell*, volume 3. Garland New York, 1994.
- [16] Keith J Laidler. The development of the arrhenius equation. *Journal of chemical Education*, 61(6):494, 1984.
- [17] Frank Jülicher, Armand Ajdari, and Jacques Prost. Modeling molecular motors. *Review of Modern Physics*, 69:1269–1282, October 1997.
- [18] David Keller and Carlos Bustamante. The mechanochemistry of molecular motors. *Biophysical Journal*, 78(2):541–556, February 2000.
- [19] Reinhard Lipowsky and Steffen Liepelt. Chemomechanical coupling of molecular motors: Thermodynamics, network representations, and balance conditions. *Journal of Statistical Physics*, 130:39–67, 2008.
- [20] Wei Hua, Edgar C Young, Margaret L Fleming, and Jeff Gelles. Coupling of kinesin steps to atp hydrolysis. *Nature*, 388(6640):390–393, 1997.
- [21] Hiroyuki Noji, Ryohei Yasuda, Masasuke Yoshida, and Kazuhiko Kinoshita. Direct observation of the rotation of f1-atpase. *Nature*, 386(6622):299–302, March 1997.

- [22] D. Okuno, R. Iino, and H. Noji. Rotation and structure of fof1-atp synthase. *Journal of Biochemistry*, 149(6):655–664, April 2011.
- [23] Wolfgang Junge and Nathan Nelson. Atp synthase. *Annual Review of Biochemistry*, 84(1):631–657, June 2015.
- [24] Alastair G Stewart, Elise M Laming, Meghna Sobti, and Daniela Stock. Rotary atpases—dynamic molecular machines. *Current opinion in structural biology*, 25:40–48, 2014.
- [25] Jacques Prost, Jean-François Chauwin, Luca Peliti, and Armand Ajdari. Asymmetric pumping of particles. *Physical Review Letters*, 72(16):2652, 1994.
- [26] Stefan Klumpp and Reinhard Lipowsky. Cooperative cargo transport by several molecular motors. *Proceedings of the National Academy of Sciences*, 102(48):17284–17289, 2005.
- [27] Reinhard Lipowsky and Stefan Klumpp. ‘life is motion’: multiscale motility of molecular motors. *Physica A: Statistical Mechanics and its Applications*, 352(1):53–112, 2005.
- [28] Steffen Liepelt and Reinhard Lipowsky. Kinesin’s network of chemomechanical motor cycles. *Physical Review Letters*, 98:258102, June 2007.
- [29] Martin Karplus. Molecular Dynamics Simulations of Biomolecules. *Acc. Chem. Res.*, 35(6):321–323, June 2002.
- [30] Rainer A Böckmann and Helmut Grubmüller. Conformational dynamics of the F1-ATPase β -subunit: a molecular dynamics study. *Biophysical Journal*, 85(3):1482–1491, 2003.
- [31] Michał Badocha, Miłosz Wieczór, Antoni Marciniak, Cyprian Kleist, Helmut Grubmüller, and Jacek Czub. Molecular mechanism and energetics of coupling between substrate binding and product release in the f1-atpase catalytic cycle. *Proceedings of the National Academy of Sciences*, 120(8):e2215650120, 2023.
- [32] Sarah L. Lovelock, Rebecca Crawshaw, Sophie Basler, Colin Levy, David Baker, Donald Hilvert, and Anthony P. Green. The road to fully programmable protein catalysis. *Nature*, 606(7912):49–58, June 2022.

- [33] Robert Callender and R. Brian Dyer. The dynamical nature of enzymatic catalysis. *Accounts of Chemical Research*, 48(2):407–413, December 2014.
- [34] Eilon Sherman, Anna Itkin, Yosef Yehuda Kuttner, Elizabeth Rhoades, Dan Amir, Elisha Haas, and Gilad Haran. Using fluorescence correlation spectroscopy to study conformational changes in denatured proteins. *Biophysical journal*, 94(12):4819–4827, 2008.
- [35] Hari S Muddana, Samudra Sengupta, Thomas E Mallouk, Ayusman Sen, and Peter J Butler. Substrate catalysis enhances single-enzyme diffusion. *Journal of the American Chemical Society*, 132(7):2110–2111, 2010.
- [36] Clement Riedel, Ronen Gabizon, Christian AM Wilson, Kambiz Hamadani, Konstantinos Tsekouras, Susan Marqusee, Steve Pressé, and Carlos Bustamante. The heat released during catalytic turnover enhances the diffusion of an enzyme. *Nature*, 517(7533):227–230, 2015.
- [37] Samudra Sengupta, Michelle M Spiering, Krishna K Dey, Wentao Duan, Debabrata Patra, Peter J Butler, R Dean Astumian, Stephen J Benkovic, and Ayusman Sen. Dna polymerase as a molecular motor and pump. *ACS nano*, 8(3):2410–2418, 2014.
- [38] Pierre Illien, Tunrayo Adeleke-Larodo, and Ramin Golestanian. Diffusion of an enzyme: The role of fluctuation-induced hydrodynamic coupling. *Europhysics Letters*, 119(4):40002, 2017.
- [39] Jaime Agudo-Canalejo, Pierre Illien, and Ramin Golestanian. Phoresis and enhanced diffusion compete in enzyme chemotaxis. *Nano letters*, 18(4):2711–2717, 2018.
- [40] Jaime Agudo-Canalejo and Ramin Golestanian. Diffusion and steady state distributions of flexible chemotactic enzymes. *The European Physical Journal Special Topics*, 229(17):2791–2806, 2020.
- [41] Eric Lauga and Thomas R Powers. The hydrodynamics of swimming microorganisms. *Reports on progress in physics*, 72(9):096601, 2009.
- [42] Jens Elgeti, Roland G Winkler, and Gerhard Gompper. Physics of microswimmers—single particle motion and collective behavior: a review. *Reports on progress in physics*, 78(5):056601, 2015.

- [43] Edward M Purcell. Life at low reynolds number. In *Physics and our world: reissue of the proceedings of a symposium in honor of Victor F Weisskopf*, pages 47–67. World Scientific, 2014.
- [44] Eric Lauga. Life around the scallop theorem. *Soft Matter*, 7(7):3060–3065, 2011.
- [45] Wei Gao and Joseph Wang. Synthetic micro/nanomotors in drug delivery. *Nanoscale*, 6(18):10486–10494, August 2014.
- [46] Byung-Wook Park, Jiang Zhuang, Oncay Yasa, and Metin Sitti. Multifunctional bacteria-driven microswimmers for targeted active drug delivery. *ACS nano*, 11(9):8910–8923, 2017.
- [47] Samuel Sánchez, Lluís Soler, and Jaideep Katuri. Chemically powered micro-and nanomotors. *Angewandte Chemie International Edition*, 54(5):1414–1444, 2015.
- [48] John L Anderson. Colloid Transport by Interfacial Forces. *Annual Review of Fluid Mechanics*, 21(Volume 21, 1989):61–99, January 1989.
- [49] Frank Jülicher and Jacques Prost. Generic theory of colloidal transport. *The European Physical Journal E*, 29:27–36, 2009.
- [50] John L Anderson, ME Lowell, and DC Prieve. Motion of a particle generated by chemical gradients part 1. non-electrolytes. *Journal of Fluid Mechanics*, 117:107–121, 1982.
- [51] Jonathan R Howse, Richard AL Jones, Anthony J Ryan, Tim Gough, Reza Vafabakhsh, and Ramin Golestanian. Self-motile colloidal particles: from directed propulsion to random walk. *Physical Review Letters*, 99(4):048102, 2007.
- [52] Ramin Golestanian, Tanniemola Liverpool, and Armand Ajdari. Designing phoretic micro-and nano-swimmers. *New Journal of Physics*, 9(5):126, 2007.
- [53] Ramin Golestanian, Tanniemola B Liverpool, and Armand Ajdari. Propulsion of a molecular machine by asymmetric distribution of reaction products. *Physical Review Letters*, 94(22):220801, 2005.

- [54] Ramin Golestanian. Anomalous diffusion of symmetric and asymmetric active colloids. *Physical Review Letters*, 102(18):188305, 2009.
- [55] Howard A Stone and Aravinthan DT Samuel. Propulsion of microorganisms by surface distortions. *Physical Review Letters*, 77(19):4102, 1996.
- [56] Hassan Masoud and Howard A Stone. The reciprocal theorem in fluid dynamics and transport phenomena. *Journal of Fluid Mechanics*, 879:P1, 2019.
- [57] Ali Najafi and Ramin Golestanian. Simple swimmer at low reynolds number: Three linked spheres. *Physical Review E—Statistical, Nonlinear, and Soft Matter Physics*, 69(6):062901, 2004.
- [58] Ali Najafi and Ramin Golestanian. Propulsion at low reynolds number. *Journal of Physics: Condensed Matter*, 17(14):S1203, 2005.
- [59] Sangtae Kim and Seppo J Karrila. *Microhydrodynamics: principles and selected applications*. Butterworth-Heinemann, Oxford, England, UK, 2013.
- [60] Ali Najafi and Ramin Golestanian. Simple swimmer at low reynolds number: Three linked spheres. *Physical Review E*, 69:062901, June 2004.
- [61] Ramin Golestanian and Armand Ajdari. Stochastic low reynolds number swimmers. *Journal of Physics: Condensed Matter*, 21(20):204104, 2009.
- [62] Ramin Golestanian and Armand Ajdari. Mechanical response of a small swimmer driven by conformational transitions. *Physical Review Letters*, 100(3):038101, 2008.
- [63] Ramin Golestanian. Three-sphere low-reynolds-number swimmer with a cargo container. *The European Physical Journal E*, 25:1–4, 2008.
- [64] Abdallah Daddi-Moussa-Ider, Maciej Lisicki, Christian Hoell, and Hartmut Löwen. Swimming trajectories of a three-sphere microswimmer near a wall. *The Journal of Chemical Physics*, 148(13), 2018.
- [65] Mark P Curtis and Eamonn A Gaffney. Three-sphere swimmer in a non-linear viscoelastic medium. *Physical Review E—Statistical, Nonlinear, and Soft Matter Physics*, 87(4):043006, 2013.

- [66] Kento Yasuda, Yuto Hosaka, and Shigeyuki Komura. Generalized three-sphere microswimmers. *Journal of the Physical Society of Japan*, 92(12):121008, 2023.
- [67] Arkady Pikovsky, Michael Rosenblum, and Jürgen Kurths. Synchronization. *Cambridge university press*, 12, 2001.
- [68] Steven H Strogatz. *Sync: How order emerges from chaos in the universe, nature, and daily life*. Hyperion Books, New York, 2012.
- [69] Yoshiki Kuramoto and Ikuko Nishikawa. Statistical macrodynamics of large dynamical systems. case of a phase transition in oscillator communities. *Journal of Statistical Physics*, 49(3–4):569–605, November 1987.
- [70] Juan A. Acebrón, L. L. Bonilla, Conrad J. Pérez Vicente, Félix Ritort, and Renato Spigler. The Kuramoto model: A simple paradigm for synchronization phenomena. *Review of Modern Physics*, 77:137–185, April 2005.
- [71] Steven H. Strogatz. From Kuramoto to Crawford: exploring the onset of synchronization in populations of coupled oscillators. *Physica D: Nonlinear Phenomena*, 143(1–4):1–20, September 2000.
- [72] James Pantaleone. Synchronization of metronomes. *American Journal of Physics*, 70(10):992–1000, September 2002.
- [73] Yoshiki Kuramoto. *Chemical Oscillations, Waves, and Turbulence*. Springer Berlin Heidelberg, 1984.
- [74] M. K. Stephen Yeung and Steven H. Strogatz. Time delay in the Kuramoto model of coupled oscillators. *Physical Review Letters*, 82:648–651, January 1999.
- [75] M. Marcus, Charles, H. Strogatz, Steven, and M. Westervelt, Robert. Delayed switching in a phase-slip model of charge-density-wave transport. *Physical Review B*, 40:5588–5592, September 1989.
- [76] H. Strogatz, Steven, M. Marcus, Charles, M. Westervelt, Robert, and Renato Mirollo. Simple model of collective transport with phase slippage. *Physical Review Letters*, 61:2380–2383, November 1988.

- [77] Gregory Kozyreff, Adrei Vladimirov, and Paul Mandel. Global coupling with time delay in an array of semiconductor lasers. *Physical Review Letters*, 85:3809–3812, October 2000.
- [78] G. Kozyreff, A. G. Vladimirov, and Paul Mandel. Dynamics of a semiconductor laser array with delayed global coupling. *Physical Review E*, 64:016613, June 2001.
- [79] Kurt Wiesenfeld, Pere Colet, and Steven H. Strogatz. Synchronization transitions in a disordered josephson series array. *Physical Review Letters*, 76:404–407, January 1996.
- [80] Shigeru Shinomoto and Yoshiki Kuramoto. Phase transitions in active rotator systems. *Progress of Theoretical Physics*, 75(5):1105–1110, May 1986.
- [81] Kevin P. O’Keeffe, Hyunsuk Hong, and Steven H. Strogatz. Oscillators that sync and swarm. *Nature Communications*, 8(1), November 2017.
- [82] Ido Nitsan, Stavit Drori, Yair E. Lewis, Shlomi Cohen, and Shelly Tzlil. Mechanical communication in cardiac cell synchronized beating. *Nature Physics*, 12(5):472–477, January 2016.
- [83] Greta Quaranta, Marie-Eve Aubin-Tam, and Daniel Tam. Hydrodynamics versus intracellular coupling in the synchronization of eukaryotic flagella. *Physical Review Letters*, 115:238101, November 2015.
- [84] Kirsty Y. Wan and Raymond E. Goldstein. Coordinated beating of algal flagella is mediated by basal coupling. *Proceedings of the National Academy of Sciences*, 113(20), May 2016.
- [85] Andrej Vilfan and Frank Jülicher. Hydrodynamic flow patterns and synchronization of beating cilia. *Physical Review Letters*, 96:058102, February 2006.
- [86] Armando Maestro, Nicolas Bruot, Jurij Kotar, Nariya Uchida, Ramin Golestanian, and Pietro Cicuta. Control of synchronization in models of hydrodynamically coupled motile cilia. *Communications Physics*, 1(1):28, 2018.

- [87] Raymond E Goldstein, Marco Polin, and Idan Tuval. Noise and synchronization in pairs of beating eukaryotic flagella. *Physical Review Letters*, 103(16):168103, 2009.
- [88] Douglas R Brumley, Kirsty Y Wan, Marco Polin, and Raymond E Goldstein. Flagellar synchronization through direct hydrodynamic interactions. *eLife*, 3:e02750, 2014.
- [89] Ingmar H Riedel, Karsten Kruse, and Jonathon Howard. A self-organized vortex array of hydrodynamically entrained sperm cells. *Science*, 309(5732):300–303, 2005.
- [90] Geoffrey Ingram Taylor. Analysis of the swimming of microscopic organisms. *Proceedings of the Royal Society of London. Series A. Mathematical and Physical Sciences*, 209(1099):447–461, 1951.
- [91] Ramin Golestanian, Julia M Yeomans, and Nariya Uchida. Hydrodynamic synchronization at low reynolds number. *Soft Matter*, 7(7):3074–3082, 2011.
- [92] Nariya Uchida. Many-body theory of synchronization by long-range interactions. *Physical Review Letters*, 106:064101, February 2011.
- [93] Nariya Uchida and Ramin Golestanian. Generic conditions for hydrodynamic synchronization. *Physical Review Letters*, 106(5):058104, 2011.
- [94] Raymond E Goldstein, Eric Lauga, Adriana I Pesci, and Michael RE Proctor. Elastohydrodynamic synchronization of adjacent beating flagella. *Physical Review Fluids*, 1(7):073201, 2016.
- [95] Don S Lemons and Paul Langevin. *An introduction to stochastic processes in physics*. JHU Press, 2002.
- [96] Grigorios A Pavliotis. Stochastic processes and applications. *Texts in applied mathematics*, 60, 2014.
- [97] Nicolaas Godfried Van Kampen. *Stochastic processes in physics and chemistry*, volume 1. Elsevier, Oxford, England, UK, 1992.
- [98] Ryogo Kubo. The fluctuation-dissipation theorem. *Reports on Progress in Physics*, 29(1):255, 1966.

- [99] Pawel Romanczuk, Markus Bär, Werner Ebeling, Benjamin Lindner, and Lutz Schimansky-Geier. Active brownian particles: From individual to collective stochastic dynamics. *The European Physical Journal Special Topics*, 202:1–162, 2012.
- [100] Alexandre P Solon, Michael E Cates, and Julien Tailleur. Active brownian particles and run-and-tumble particles: A comparative study. *The European Physical Journal Special Topics*, 224(7):1231–1262, 2015.
- [101] H. C. Berg and L. Turner. Chemotaxis of bacteria in glass capillary arrays. *Escherichia coli*, motility, microchannel plate, and light scattering. *Biophysical Journal*, 58(4):919, October 1990.
- [102] Eric Lauga, Willow R DiLuzio, George M Whitesides, and Howard A Stone. Swimming in circles: motion of bacteria near solid boundaries. *Biophysical journal*, 90(2):400–412, 2006.
- [103] Charu Datt and Gwynn J Elfring. Active particles in viscosity gradients. *Physical Review Letters*, 123(15):158006, 2019.
- [104] Benno Liebchen, Paul Monderkamp, Borge Ten Hagen, and Hartmut Löwen. Viscotaxis: Microswimmer navigation in viscosity gradients. *Physical Review Letters*, 120(20):208002, 2018.
- [105] Hannes Risken. *Fokker-Planck equation*. Springer, 1996.
- [106] Udo Seifert. Stochastic thermodynamics, fluctuation theorems and molecular machines. *Reports on progress in physics*, 75(12):126001, 2012.
- [107] Akira Kobayashi, Kento Yasuda, Li-Shing Lin, Isamu Sou, Yuto Hosaka, and Shigeyuki Komura. Simulations of odd microswimmers. *Journal of the Physical Society of Japan*, 92(3):034803, 2023.
- [108] Crispin Gardiner. *Stochastic Methods*. Springer, Berlin, Germany, 2009.
- [109] Anatoly B Kolomeisky and Michael E Fisher. Molecular motors: a theorist’s perspective. *Annual Review of Physical Chemistry*, 58(1):675–695, 2007.
- [110] Udo Seifert. Entropy production along a stochastic trajectory and an integral fluctuation theorem. *Physical Review Letters*, 95(4):040602, 2005.

- [111] Lars Onsager and Stefan Machlup. Fluctuations and irreversible processes. *Physical Review*, 91:1505–1512, September 1953.
- [112] Sybren Ruurds De Groot and Peter Mazur. *Non-equilibrium thermodynamics*. Dover Publications, Mineola, NY, USA, 2013.
- [113] Patrick Pietzonka, Andre C. Barato, and Udo Seifert. Universal bound on the efficiency of molecular motors. *Journal of Statistical Mechanics: Theory and Experiment*, 2016(12):124004, December 2016.
- [114] Luca Cocconi, Rosalba Garcia-Millan, Zigan Zhen, Bianca Buturca, and Gunnar Pruessner. Entropy production in exactly solvable systems. *Entropy*, 22(11):1252, 2020.
- [115] Jürgen Schnakenberg. Network theory of microscopic and macroscopic behavior of master equation systems. *Reviews of Modern physics*, 48(4):571, 1976.
- [116] John D Chodera and Frank Noé. Markov state models of biomolecular conformational dynamics. *Current opinion in Structural Biology*, 25:135–144, 2014.
- [117] Bernard Derrida. Velocity and diffusion constant of a periodic one-dimensional hopping model. *Journal of statistical physics*, 31:433–450, 1983.
- [118] Andre C Barato and Udo Seifert. Thermodynamic uncertainty relation for biomolecular processes. *Physical Review Letters*, 114(15):158101, 2015.
- [119] Yoshihiko Hasegawa and Tan Van Vu. Fluctuation theorem uncertainty relation. *Physical Review Letters*, 123:110602, September 2019.
- [120] Cai Dieball and Aljaž Godec. Direct route to thermodynamic uncertainty relations and their saturation. *Physical Review Letters*, 130(8):087101, 2023.
- [121] Todd R. Gingrich, Jordan M. Horowitz, Nikolay Perunov, and Jeremy L. England. Dissipation bounds all steady-state current fluctuations. *Physical Review Letters*, 116:120601, March 2016.

- [122] Jordan M. Horowitz and Todd R. Gingrich. Thermodynamic uncertainty relations constrain non-equilibrium fluctuations. *Nature Physics*, 16:15–20, January 2020.
- [123] Jordan M. Horowitz and Todd R. Gingrich. Proof of the finite-time thermodynamic uncertainty relation for steady-state currents. *Phys. Rev. E*, 96(2):020103, August 2017.
- [124] Naruo Ohga, Sosuke Ito, and Artemy Kolchinsky. Thermodynamic bound on the asymmetry of cross-correlations. *Physical Review Letters*, 131(7):077101, 2023.
- [125] Timur Koyuk and Udo Seifert. Thermodynamic uncertainty relation for time-dependent driving. *Physical Review Letters*, 125(26):260604, 2020.
- [126] Katarzyna Macieszczak, Kay Brandner, and Juan P Garrahan. Unified thermodynamic uncertainty relations in linear response. *Physical Review Letters*, 121(13):130601, 2018.
- [127] Patrick P Potts and Peter Samuelsson. Thermodynamic uncertainty relations including measurement and feedback. *Physical Review E*, 100(5):052137, 2019.
- [128] Matteo Polettini, Alexandre Lazarescu, and Massimiliano Esposito. Tightening the uncertainty principle for stochastic currents. *Physical Review E*, 94(5):052104, November 2016.
- [129] Andreas Dechant. Multidimensional thermodynamic uncertainty relations. *Journal of Physics A: Mathematical and Theoretical*, 52(3):035001, 2018.
- [130] Jaime Agudo-Canalejo, Tunrayo Adeleke-Larodo, Pierre Illien, and Ramin Golestanian. Synchronization and Enhanced Catalysis of Mechanically Coupled Enzymes. *Physical Review Letters*, 127(20):208103, November 2021.
- [131] M. Chatzittofi, R. Golestanian, and J. Agudo-Canalejo. Collective synchronization of dissipatively-coupled noise-activated processes. *New Journal of Physics*, 25(9):093014, September 2023.

- [132] Michalis Chatzittofi, Ramin Golestanian, and Jaime Agudo-Canalejo. Topological phase locking in molecular oscillators. *arXiv:2310.11788*, 2024.
- [133] Michalis Chatzittofi, Jaime Agudo-Canalejo, and Ramin Golestanian. Universal mechanistic rules for de novo design of enzymes. *arXiv:2408.16639*, 2024.
- [134] Michalis Chatzittofi, Ramin Golestanian, and Jaime Agudo-Canalejo. Thermodynamic inference of correlations in nonequilibrium collective dynamics. *Physical Review Research*, 6(4):L042012, 2024.
- [135] Michalis Chatzittofi, Jaime Agudo-Canalejo, and Ramin Golestanian. Entropy production and thermodynamic inference for stochastic microswimmers. *Physical Review Research*, 6(2):L022044, May 2024.
- [136] Michalis Chatzittofi, Jaime Agudo-Canalejo, and Ramin Golestanian. Nonlinear response theory of molecular machines. *Europhysics Letters*, 147(2):21002, August 2024.
- [137] Michael J. Hehir, Jennifer E. Murphy, and Evan R. Kantrowitz. Characterization of Heterodimeric Alkaline Phosphatases from *Escherichia coli*: An Investigation of Intragenic Complementation. *Journal of Molecular Biology*, 304(4):645–656, December 2000.
- [138] Anna-Katharina Pumm, Wouter Engelen, Enzo Kopperger, Jonas Isensee, Matthias Vogt, Viktorija Kozina, Massimo Kube, Maximilian N. Honemann, Eva Bertosin, Martin Langecker, Ramin Golestanian, Friedrich C. Simmel, and Hendrik Dietz. A DNA origami rotary ratchet motor. *Nature*, 607:492–498, July 2022.
- [139] Xin Shi, Anna-Katharina Pumm, Christopher Maffeo, Fabian Kohler, Elija Feigl, Wenxuan Zhao, Daniel Verschueren, Ramin Golestanian, Aleksei Aksimentiev, Hendrik Dietz, and Cees Dekker. A DNA turbine powered by a transmembrane potential across a nanopore. *Nature Nanotechnology*, 19:338–344, March 2024.
- [140] Seung-Bo Shim, Matthias Imboden, and Pritiraj Mohanty. Synchronized Oscillation in Coupled Nanomechanical Oscillators. *Science*, 316(5821):95–99, April 2007.

- [141] Bertrand Ottino-Löffler and Steven H Strogatz. Comparing the locking threshold for rings and chains of oscillators. *Physical Review E*, 94(6):062203, 2016.
- [142] Tommaso Castellani and Andrea Cavagna. Spin-glass theory for pedestrians. *Journal of Statistical Mechanics: Theory and Experiment*, 2005(05):P05012, 2005.
- [143] Hyunsuk Hong, Kevin P. O’Keeffe, and Steven H. Strogatz. Correlated disorder in the Kuramoto model: Effects on phase coherence, finite-size scaling, and dynamic fluctuations. *Chaos: An Interdisciplinary Journal of Nonlinear Science*, 26(10), October 2016.
- [144] Nonlinear Phenomena in Complex Systems, 2002, Vol.5, No.4, pp.380-385, January 2003. [Online; accessed 2. Aug. 2024].
- [145] Mark R Tinsley, Simbarashe Nkomo, and Kenneth Showalter. Chimera and phase-cluster states in populations of coupled chemical oscillators. *Nature Physics*, 8(9):662–665, 2012.
- [146] Yulia Sokolov, Derek Frydel, David G. Grier, Haim Diamant, and Yael Roichman. Hydrodynamic pair attractions between driven colloidal particles. *Physical Review Letters*, 107:158302, October 2011.
- [147] Sergi Garcia-Manyes and Amy EM Beedle. Steering chemical reactions with force. *Nature Review Chemistry*, 1(11):0083, 2017.

Chapter 2

Collective synchronization of dissipatively-coupled noise-activated processes

This chapter is reproduced from M Chatzittofi *et al* 2023 New J. Phys. **25** 093014 [[131](#)]. In this article, I contributed in designing the research and the numerical code in Julia for integrating the Langevin equations of motion. I have performed numerical, and analytical calculations, contributed in the analysis of the results and in writing/editing the paper.



PAPER

Collective synchronization of dissipatively-coupled noise-activated processes

OPEN ACCESS

RECEIVED

14 March 2023

REVISED

17 August 2023

ACCEPTED FOR PUBLICATION

22 August 2023

PUBLISHED

6 September 2023

Original Content from
this work may be used
under the terms of the
[Creative Commons
Attribution 4.0 licence](#).

Any further distribution
of this work must
maintain attribution to
the author(s) and the title
of the work, journal
citation and DOI.

M Chatzitofi¹ , R Golestanian^{1,2,*}  and J Agudo-Canalejo^{1,*} ¹ Living Matter Physics, Max Planck Institute for Dynamics and Self-Organisation, D-37077 Goettingen, Germany² Rudolf Peierls Centre for Theoretical Physics, University of Oxford, Oxford OX1 3PU, United Kingdom

* Authors to whom any correspondence should be addressed.

E-mail: ramin.golestanian@ds.mpg.de and jaime.agudo@ds.mpg.de**Keywords:** stochastic dynamics, synchronization, mean-field theory, dynamical systemsSupplementary material for this article is available [online](#)

Abstract

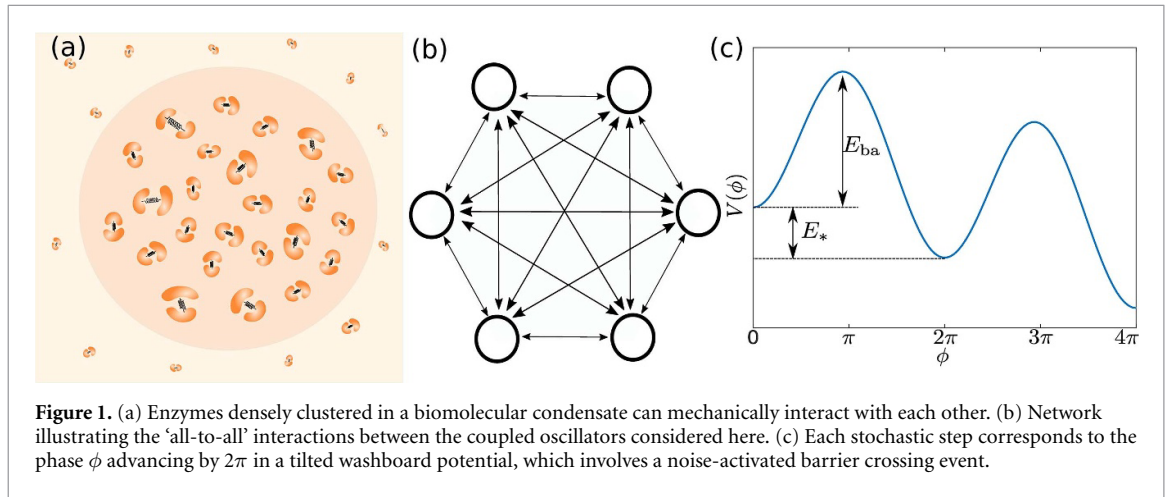
We study the stochastic dynamics of an arbitrary number of noise-activated cyclic processes, or oscillators, that are all coupled to each other via a dissipative coupling. The N coupled oscillators are described by N phase coordinates driven in a tilted washboard potential. At low N and strong coupling, we find synchronization as well as an enhancement in the average speed of the oscillators. In the large N regime, we show that the collective dynamics can be described through a mean-field theory, which predicts a great enhancement in the average speed. In fact, beyond a critical value of the coupling strength, noise activation becomes irrelevant and the dynamics switch to an effectively deterministic ‘running’ mode. Finally, we study the stochastic thermodynamics of the coupled oscillators, in particular their performance with regards to the thermodynamic uncertainty relation.

1. Introduction

A system of driven, nonlinear coupled oscillators is nontrivial and can quickly lead to complex and unexpected situations when these oscillators synchronize, like in the famous case of the Millennium bridge [1]. Generic features of synchronization have been widely studied using minimal models such as the Kuramoto model [2–5]. Networks of such oscillators give rise to fascinating phenomena such as states displaying coexistence of synchronization and incoherence, known as chimera states [6].

In biological systems, at the microscopic scale, the interactions are usually mediated by a viscous medium. For instance, hydrodynamic interactions can cause beating cilia or flagella to become synchronised [7, 8] displaying emergent phenomena such as metachronal waves [9]. At an even smaller scale, on the scale of enzymes and molecular motors, many relevant processes are stochastic and thermally-activated: thermal noise is required to push the system over free energy barriers, e.g. during chemical reactions inside enzymes or during the mechanical steps of molecular motors. These cyclic processes convert chemical energy into mechanical energy and heat [10–12].

Enzymes and other catalytically active particles can self-organize in space thanks to the gradients generated by their nonequilibrium chemical activity [13, 14]. Additionally, the catalytic activity of the enzymes may be associated to conformational changes or oscillations in the enzyme shape [15, 16]. The effect of such conformational changes on the spatial dynamics and the rheology of enzyme-rich solutions has been a topic of great recent interest [17–20]. In this context, a new mechanism for synchronization between two enzymes was recently reported, for enzymes that undergo conformational changes during their noise-activated catalytic steps, and which are coupled to each other through a viscous medium [21]. The model for coupled phase dynamics that emerges after coarse graining the microscopic degrees of freedom in this system has some very peculiar features and emergent properties that are entirely different from those in conventional models for synchronization such as the Kuramoto model. In particular, interactions between phases are *dissipative*, in the sense that they are mediated not by interaction potentials but rather by the



mobility tensor (inverse to a friction tensor) that couples forces to velocities in the system. The same mobility tensor determines the stochastic noise in the system through the fluctuation-dissipation relation, making the model thermodynamically-consistent. Additionally, the transition to synchronization with increasing coupling was found to be due to a global bifurcation in the underlying dynamical system, defined on the torus.

Inspired by these observations on the behavior of two coupled enzymes, here we generalize the model to a system composed of an arbitrary number of stochastic oscillators, which interact with each other through a constant coupling of the dissipative kind. This could for example represent the interactions between enzymes in an enzyme-rich biomolecular condensate or metabolon [22, 23], see figure 1(a); but also any generic collection of noise-activated processes that are dissipatively coupled to each other. For simplicity, and in the spirit of minimal models of synchronization such as the original Kuramoto model [2], we neglect the spatial structure and consider that each phase coupled with all other phases with equal strength, see figure 1(b). The individual dynamics of each process is governed by a tilted washboard potential, see figure 1(c). The resulting equations are rather generic and thus may find application as minimal models of not only catalytic processes but also other excitable systems [24], such as Josephson junctions [25–28] or firing neurons [29–31].

Because the model studied here is thermodynamically-consistent, it allows us to examine detailed features of its thermodynamic performance. A theoretical framework to understand the thermodynamics of fluctuating systems has been developed in recent years [32]. Of particular interest is a bound on the precision achievable by driven processes, determined by their entropy production, or equivalently their heat dissipation, known as the thermodynamic uncertainty relation (TUR) [33, 34]. There is a growing interest in understanding how synchronization affects such thermodynamic measures of precision or efficiency, with applications to e.g. beating cilia [35], generic Kuramoto oscillators [36], or molecular clocks [37].

The paper is organized as follows. We begin by presenting the model of dissipatively coupled oscillators in its most general form, followed by its particularization to the minimal model studied here of N identical oscillators with global (all-to-all) coupling. We then present the results of stochastic simulations for small and large numbers of oscillators. Next, we focus on the large N limit, for which we show that the dynamics can be well understood using a mean-field theory. Finally, we study the stochastic thermodynamics of precision in the presence of coupling in our system.

2. Model

2.1. Dissipative coupling

We consider stochastic cyclic processes (oscillators) that are coupled to each other not through interaction forces, but through a mobility tensor that has nonzero off-diagonal components. That is, we will consider phases ϕ_α with $\alpha = 1, \dots, N$ which evolve according to the coupled overdamped Langevin equations

$$\dot{\phi}_\alpha = -M_{\alpha\beta} \partial_\beta U + k_B T \Sigma_{\alpha\nu} \partial_\beta \Sigma_{\beta\nu} + \sqrt{2k_B T} \Sigma_{\alpha\beta} \xi_\beta \quad (1)$$

where $\partial_\beta \equiv \frac{\partial}{\partial \phi_\beta}$, the Einstein summation convention for repeated indices is used, and the stochastic equation is to be interpreted in the Stratonovich sense. Here, the first term represents the deterministic velocity of the phases. The mobility tensor $M_{\alpha\beta}(\phi_1, \dots, \phi_N)$ can in principle be phase-dependent. For the dynamics to be thermodynamically consistent, this mobility tensor must be symmetric and positive definite [38, 39]. Because there are no interaction forces between the phases, the potential U is separable and may be

written as $U(\phi_1, \dots, \phi_N) = V_1(\phi_1) + \dots + V_N(\phi_N)$. The third term represents the noise where, in order to satisfy the fluctuation-dissipation relation, Σ is the square root of the mobility tensor defined via $M_{\alpha\beta} = \Sigma_{\alpha\nu} \Sigma_{\beta\nu}$, and ξ_β is unit white noise such that $\langle \xi_\beta(t) \rangle = 0$ and $\langle \xi_\alpha(t) \xi_\beta(t') \rangle = \delta_{\alpha\beta} \delta(t - t')$. This structure necessarily introduces correlations between the noise experienced by different oscillators. The second term represents a spurious drift term that is only present when the noise is multiplicative, i.e. when the mobility tensor is phase-dependent.

The stochastic dynamics given by (1) may equivalently be written in the Fokker-Planck representation for the evolution of the probability distribution $P(\phi_1, \dots, \phi_N; t)$ as

$$\partial_t P = \partial_\alpha \{ M_{\alpha\beta} [k_B T \partial_\beta P + (\partial_\beta U) P] \}, \quad (2)$$

which highlights that, when the choice of potential allows it, the system will relax to a steady state corresponding to thermodynamic equilibrium such that we recover the Boltzmann distribution $P(\phi_1, \dots, \phi_N) \propto \exp[-U(\phi_1, \dots, \phi_N)/k_B T]$, independently of the choice of mobility tensor $M_{\alpha\beta}$. In fact, because the potential U is separable, we may write $P(\phi_1, \dots, \phi_N) = \prod_{\alpha=1}^N P_\alpha(\phi_\alpha)$, with each phase independently satisfying the Boltzmann distribution $P_\alpha(\phi_\alpha) \propto \exp[-V_\alpha(\phi_\alpha)/k_B T]$.

Importantly, when the choice of potential does not allow thermodynamic equilibrium, as in driven but periodic systems such as the ones that we will consider in the following, the system relaxes to a nonequilibrium steady state which (i) does depend on the choice of the mobility tensor $M_{\alpha\beta}$ and therefore on the strength of the coupling between oscillators determined by its off-diagonal components; and (ii) is no longer separable, so that there are correlations between the different phases.

A coupling of the form given by (1) or equivalently (2) arises naturally in processes that are coupled to each other through mechanical interactions at the nano- and microscale, as these are mediated by viscous, overdamped fields described by low Reynolds number hydrodynamics [39]. It represents a form of *dissipative* coupling, as it can be understood as arising from taking the overdamped limit of full Langevin dynamics in the presence of a friction force on phase ϕ_α going as $f_\alpha = -B_{\alpha\beta} \dot{\phi}_\beta$, where $B \equiv M^{-1}$ is a friction tensor.

2.2. Noise-activated processes with global coupling

As anticipated, we will consider here N identical driven, noise-activated oscillators. This implies that the potentials for each phase are chosen to be identical, i.e. $U(\phi_1, \dots, \phi_N) = V(\phi_1) + \dots + V(\phi_N)$, and $V(\phi)$ is chosen to be a tilted washboard potential of the form $V(\phi) = -F\phi - \nu \cos(\phi + \delta)$, with $F < \nu$ and $\delta = \arcsin(F/\nu)$ so that the minima are located at multiple integers of 2π . The maxima of the potential are in turn located at $\phi_{\max} \equiv \pi - \arcsin(F/\nu) \pmod{2\pi}$. The values of ν and the driving force F can be related to the energy barrier E_{ba} of the noise-activated step and to the energy E_* released in each step, see figure 1(c), through $E_{\text{ba}} = [2\sqrt{1 - (F/\nu)^2} - (F/\nu)(\pi - 2\delta)]\nu$ and $E_* = 2\pi F$ [21]. For an uncoupled oscillator, the height of the energy barrier relative to the thermal energy $k_B T$ controls the typical waiting time between stochastic steps, which scales as $e^{E_{\text{ba}}/k_B T}$ for $E_{\text{ba}} \gg k_B T$ [40]. Note that, when $F > \nu$, the potential no longer displays energy barriers and becomes monotonically decreasing, so that the dynamics are no longer noise-activated.

We will consider the simplest possible dissipative coupling between the oscillators, where each of them interacts equally with all others via a mobility matrix $M_{\alpha\beta} = \mu_\phi \tilde{M}_{\alpha\beta}$ with constant diagonal coefficients $\tilde{M}_{\alpha\alpha} = 1$, and constant off-diagonal coefficients $\tilde{M}_{\alpha\beta} = h/(N-1)$ for $\alpha \neq \beta$. Here, μ_ϕ sets the mobility scale, and h is a dimensionless parameter that determines the strength of the coupling. This can be seen as an N -dimensional generalization of the two-dimensional problem studied in [21], with the additional simplification that the off-diagonal coefficients are constant, as it was shown in that work that this simplification does not affect the observed phenomenology. For the mobility matrix to be positive definite, the coupling strength must satisfy $-1 < h < N-1$. We will focus on positive values of h , for which the synchronization phenomenology is observed. Note that, since we choose the mobility matrix to be constant, the spurious drift term in the Langevin dynamics (1) vanishes.

With these choices, the equations of motion (1) become

$$\dot{\phi}_\alpha = \sum_{\beta=1}^N \left\{ \mu_\phi \tilde{M}_{\alpha\beta} [F - \nu \sin(\phi_\beta + \delta)] + \sqrt{2\mu_\phi k_B T} \tilde{\Sigma}_{\alpha\beta} \xi_\beta \right\} \quad (3)$$

with $\tilde{\Sigma}$ defined by $\tilde{M}_{\alpha\beta} = \tilde{\Sigma}_{\alpha\nu} \tilde{\Sigma}_{\beta\nu}$. We remind that the parameter δ does not affect the dynamics, and is only used to ensure that the minima of the potential are located at integer multiples of 2π . Choosing $(\mu_\phi \nu)^{-1}$ as a unit of time, the dynamics then depend only on the number of oscillators N , as well as three dimensionless parameters: the shape of the potential is determined by F/ν , the strength of the noise by $k_B T/\nu$, and the strength of the coupling by h . Note that, to facilitate comparison with the experimentally

measurable characteristics of the driving potential E_{ba} and E_* (figure 1(c)), F/ν and $k_B T/\nu$ can be mapped onto the dimensionless ratios E_{ba}/E_* and $k_B T/E_{\text{ba}}$, which we will report in all figures.

The deterministic ($T = 0$) version of the Langevin equation (3) can, with the redefinitions $\omega \equiv (1 + h)F\mu_\phi$, $a \equiv \mu_\phi \nu(1 - \frac{h}{N-1})$, $K \equiv h\mu_\phi \nu \frac{N}{N-1}$, and $\theta_\alpha \equiv \phi_\alpha - \delta + \pi$, be rewritten as $\dot{\theta}_\alpha = \omega + a \sin \theta_\alpha + \frac{K}{N} \sum_{\beta=1}^N \sin \theta_\beta$. It is worth noting that this dynamical system has been previously studied in the context of superconducting Josephson junction arrays [25–28]. These studies however focused mostly in the barrier-free regime where no fixed points exist ($F > \nu$ or equivalently $\omega > a + K$), and mostly in its deterministic behavior, with a few exceptions in which an ad-hoc white noise was added [25, 27]. Here, on the other hand, we will focus on the stochastic dynamics of the system in the noise-activated regime ($F < \nu$ or equivalently $\omega < a + K$) where fixed points exist, and in the presence of a thermodynamically-consistent noise (satisfying the fluctuation-dissipation theorem, which introduces correlations in the noise experienced by different oscillators). Furthermore we will focus on quantifying its collective, nonequilibrium stochastic dynamics (average speed, phase diffusion coefficient, phase correlations, and thermodynamic costs of precision), rather than on the properties of the underlying dynamical system. Our model is also distinct from the ‘active rotator’ model for the synchronization of excitable units previously studied [41–43], as the latter is based on a Kuramoto-type coupling and uncorrelated noise, with the two models showing distinct phenomenologies.

A particularly interesting feature of our dissipative coupling is that the location and the nature of the fixed points of the underlying deterministic dynamics are by construction unaffected by the strength of the coupling h , and always located at the points at which the forces vanish, i.e. at the minima or maxima of the potential. In particular, within the unit cell $-\pi < \phi_\alpha < \pi$ there is always a stable fixed point located at the origin ($\phi_\alpha = 0$ for all $\alpha = 1, \dots, N$) corresponding to all phases being at the minimum of the potential; an unstable fixed point (located at $\phi_\alpha = \phi_{\text{max}}$ for all $\alpha = 1, \dots, N$) corresponding to all phases being at the maximum of the potential; and $2^N - 2$ saddle points located at all other vertices of the N -dimensional hypercube spanned by 0 and ϕ_{max} , corresponding to some phases being at the minimum and others at the maximum of the potential. As a consequence, any bifurcation in the deterministic dynamics occurring as a function of the coupling strength h must be a *global* bifurcation.

2.3. Quantitative measures of the stochastic dynamics

In order to quantitatively assess synchronization, we must construct an order parameter. The usual order parameter in traditional synchronization problems, such as the Kuramoto model [2], is $r \equiv |\frac{1}{N} \sum_{\alpha=1}^N e^{i\phi_\alpha}|$. However, in the context of noise-activated oscillators such as those studied here, the oscillators tend to spend a major fraction of the time in the stable fixed point corresponding to the minima of the driving potential (here at integer multiples of 2π), independently of the strength of the coupling. The order parameter r is thus not suitable in this context, as it would give $r \approx 1$ even for uncoupled oscillators.

Following Agudo-Canalejo *et al* [21], we will use the correlations between the stochastic dynamics of the oscillators as an order parameter. In particular, defining $\delta\phi_\alpha(\tau; t) \equiv \phi_\alpha(t + \tau) - \phi_\alpha(t)$, we may define the diffusion coefficient D_ϕ of an individual oscillator as

$$\langle [\delta\phi_\alpha(\tau; t) - \langle \delta\phi_\alpha(\tau; t) \rangle_{\alpha, t}]^2 \rangle_{\alpha, t} \underset{\tau \rightarrow \infty}{\sim} 2D_\phi \tau \quad (4)$$

where the operator $\langle \dots \rangle_{\alpha, t}$ denotes a combined average over the N oscillators and over time. The \sim symbol indicates that the equality is achieved asymptotically as $\tau \rightarrow \infty$. We may also define the diffusion coefficient D_δ of the phase difference between a pair of oscillators, as

$$\langle [\delta\phi_\alpha(\tau; t) - \delta\phi_\beta(\tau; t)]^2 \rangle_{\alpha\beta, t} \underset{\tau \rightarrow \infty}{\sim} 2D_\delta \tau \quad (5)$$

where the operator $\langle \dots \rangle_{\alpha\beta, t}$ denotes a combined average over the $N(N-1)/2$ pairs of oscillators and over time. Finally, we can define the correlation C as the long τ limit of the correlation function (dimensionless covariance) between pairs of oscillators, i.e.

$$\frac{\langle [\delta\phi_\alpha(\tau; t) - \langle \delta\phi_\alpha(\tau; t) \rangle_{\alpha, t}] [\delta\phi_\beta(\tau; t) - \langle \delta\phi_\beta(\tau; t) \rangle_{\beta, t}] \rangle_{\alpha\beta, t}}{\langle [\delta\phi_\alpha(\tau; t) - \langle \delta\phi_\alpha(\tau; t) \rangle_{\alpha, t}]^2 \rangle_{\alpha, t}} \underset{\tau \rightarrow \infty}{\sim} C \quad (6)$$

which we will use as our order parameter for synchronization. It is straightforward to show that C is related to the two diffusion coefficients defined above through

$$C = 1 - \frac{D_\delta}{2D_\phi}. \quad (7)$$

In particular, for uncorrelated oscillators we have $D_\delta = 2D_\phi$ and thus $C = 0$, whereas for perfectly correlated oscillators we have $D_\delta = 0$ and thus $C = 1$. Anticorrelations would correspond to $C < 0$, with a lower bound

$C = -1/(N - 1)$ for maximally anticorrelated oscillators. Note that this measure of correlations can be easily generalized to the case of non-identical processes. Lastly, we will define the average speed Ω of the oscillators as

$$\langle \delta\phi_\alpha(\tau; t) \rangle \underset{\tau \rightarrow \infty}{\sim} \Omega\tau. \quad (8)$$

We note that, in these definitions, combined ensemble and time averages were performed to make optimal use of our simulation data. This combined averaging is justified by the ergodicity of our stochastic dynamics together with the symmetry inherent to the global coupling, and we verified the equivalence between time averages and ensemble averages in our simulations. Ergodicity necessarily arises in the finite N stochastic dynamics because the Langevin dynamics (1) are equivalent to the Fokker–Planck equation (2), which has a unique steady state to which all solutions relax at sufficiently long times [44, 45]. This is true even if the corresponding deterministic dynamics may show chaotic behavior, as has been shown for small number of oscillators in the context of Josephson junctions [28]. An example of how the quantitative measures above are extracted from simulations is shown in the supplementary material.

3. Results

3.1. Stochastic simulations

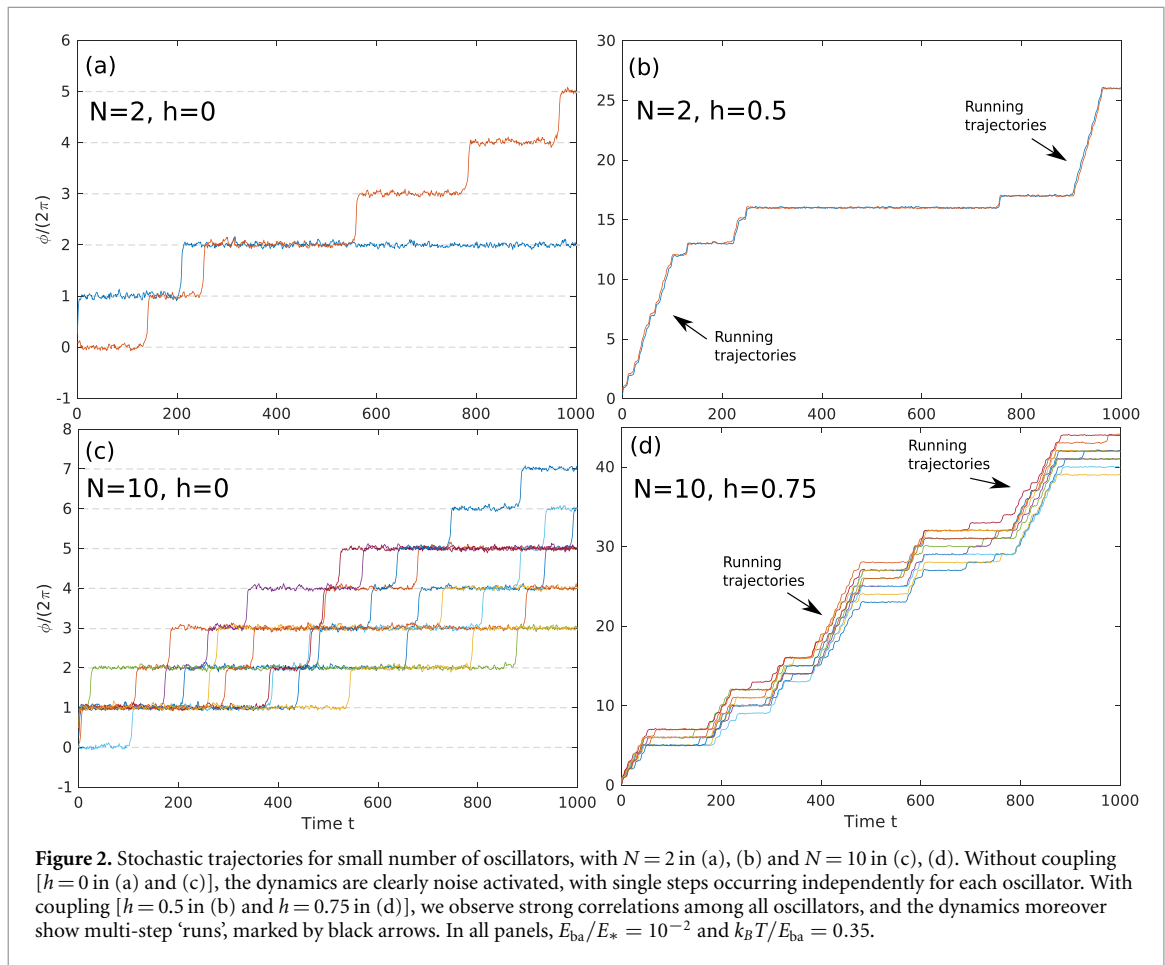
3.1.1. Small number of oscillators

For the case $N = 2$ [21], we previously found that the system exhibits synchronization and an enhanced average speed above a critical h . Examples of stochastic trajectories resulting from numerical solution of the Langevin dynamics (1) for $N = 2$ are shown in figures 2(a) and (b), where the steps (jumps) correspond to a complete oscillatory cycle, in which the phase advances by 2π by crossing over the energy barrier (see figure 1(c)). Note that, here and throughout the text, time is given in units of $(\mu_\phi \nu)^{-1}$. One clearly observes how, at zero or low coupling (figure 2(a)), the trajectories appear independent, whereas at high coupling (figure 2(b)) the two oscillators are strongly correlated. Moreover, the average speed increases: within the same timescale, a much larger number of steps is observed in the presence of coupling, and long ‘runs’ of several consecutive steps are observed, as indicated by the black arrows.

A similar behavior is observed for a larger, but still small, number of oscillators ($2 < N \lesssim 25$). As seen in figures 2(c) and (d), with increasing coupling the oscillators become correlated, the average speed increases, and long runs become apparent (black arrows).

The dynamics are quantified in figure 3 as a function of number of oscillators N and strength of the coupling h . The average speed increases with increasing coupling for all N , see figure 3(a), although this increase is significantly more pronounced at higher N . On the other hand, synchronization as measured by C increases monotonically with h at small N , while it appears to peak at intermediate h for larger N , see figure 3(b). The minimal value of h required to observe synchronization (large C) is also smaller for small N . Interestingly, for sufficiently large values of N the phase diffusion coefficient D_ϕ appears to peak at a specific, N -dependent value of the coupling, see figure 3(c). The phase-difference diffusion coefficient D_δ also appears to peak at intermediate h (figure 3(d)) for sufficiently large values of N , but to a much smaller extent than D_ϕ , so that all in all the order parameter C still peaks at an intermediate h for larger values of N .

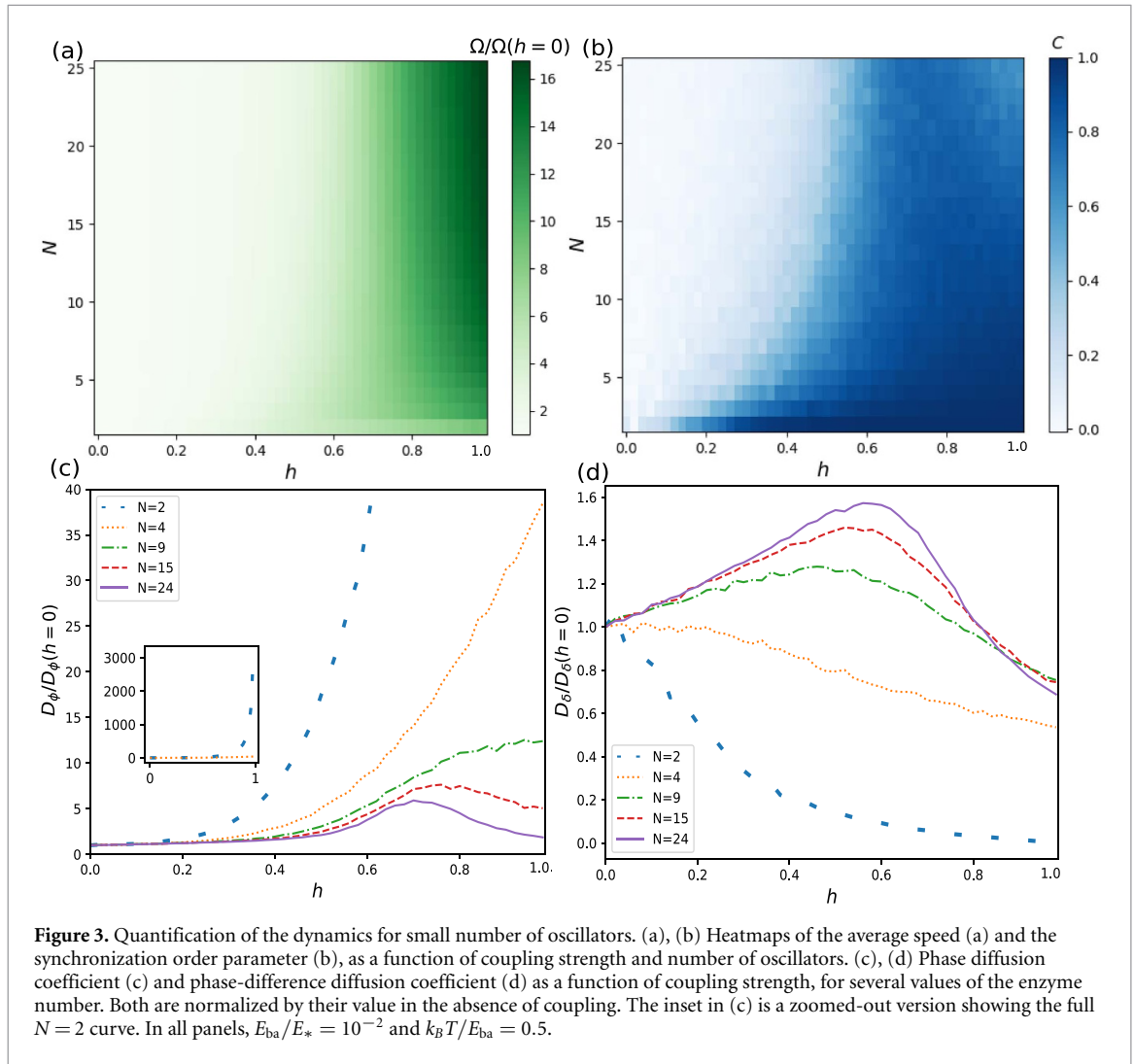
It is worth noting that enhanced phase diffusion in a tilted washboard potential has been previously reported for the motion of a single phase in such a potential [46, 47], in which case it was related to the transition from noise-activated dynamics to deterministic dynamics mediated by the saddle-node bifurcation of the system at $F = \nu$. However, in our case we have $F < \nu$ in all cases, i.e. the dynamics remain noise-activated and integer values of 2π always correspond to stable fixed point of the ϕ_α 's, independently of the strength of the coupling h . A relation between these two distinct systems can still be established (and will be further clarified when we study the large N limit in section 3.2). In [21], exploring the case $N = 2$, it was found that at a critical value of h a global bifurcation of the underlying deterministic dynamical system ($k_B T = 0$) occurs, giving rise to a splitting of the (ϕ_1, ϕ_2) phase space, which corresponds modulo 2π to a torus, into two disconnected regions, see figures 4(a)–(c). In all three panels, the whole blue region corresponds to the basin of attraction of the $(\phi_1, \phi_2) = (0, 0)$ stable fixed point. This region is further subdivided into four subregions with different shades of blue marked $(0, 0)$, $(1, 0)$, $(0, 1)$, and $(1, 1)$, which indicate the winding of trajectories around the torus as they reach the fixed point, i.e. whether when unwrapping the torus the trajectories would reach the fixed point at $(0, 0)$, $(2\pi, 0)$, $(0, 2\pi)$, or $(2\pi, 2\pi)$, respectively. These subregions are initially (figure 4(a)) separated by heteroclinic orbits joining the unstable fixed point [in red, located at $(\phi_{\max}, \phi_{\max})$ as described in section 2.2] and the saddle points [in blue, located at $(\phi_{\max}, 0)$ and $(0, \phi_{\max})$]. At the global bifurcation, these orbits collide and form a heteroclinic cycle. Beyond the bifurcation (figures 4(b) and (c)), we find two homoclinic cycles connecting the saddle points to



themselves, in between which a new region (in yellow) corresponding to a band of periodic orbits emerges, along which ϕ_1 and ϕ_2 increase deterministically. We refer the reader to [21] for further details on the $N = 2$ bifurcation. This bifurcation had also been previously reported in a study of two coupled Josephson junctions [26]. Our work further shows that this bifurcation is responsible for the emergence of synchronization, enhanced average speed, and the ‘running trajectories’ in the stochastic system [$k_B T > 0$, figures 2(b) and (d)]. The enhancement in the phase and phase-difference diffusion coefficients observed at intermediate h is therefore likely related to the transition from purely noise-activated dynamics before the bifurcation, to a mixture of noise-activated and deterministic dynamics once the periodic orbits have emerged.

Indeed, an analysis of the deterministic dynamics for $N > 2$ shows that a similar splitting of the phase space (now an N -torus) into disconnected regions occurs beyond an N -dependent critical value of h , one region corresponding to the basin of attraction of the fixed point, the others to periodic orbits along which all ϕ_α increase deterministically. The regions containing periodic orbits in the case $N = 3$ can be seen in figure 4(d). In this case, there are two distinct ‘tubes’ corresponding to periodic orbits in which ϕ_1, ϕ_2 , and ϕ_3 advance in the order $(\dots 1 2 3 1 2 3 \dots)$ and $(\dots 1 3 2 1 3 2 \dots)$, respectively. For arbitrary N , the number of higher-dimensional ‘tubes’ containing periodic orbits therefore is $(N - 1)!$, the number of circular permutations of N distinct objects, as previously reported in the context of Josephson junction arrays [25].

A global measure of the dominance of a given basin of attraction in the dynamics of a system is the volume fraction of the phase space occupied by said basin, also known as ‘basin stability’ [48, 49]. We have measured the volume fraction of the phase space that is occupied by periodic bands as a function of h , for several values of N , see figure 4(e). For this purpose, we scanned a N -dimensional grid of 30^N equally spaced points in the unit cell $-\pi < \phi_\alpha < \pi$ for all α , and determined whether the trajectory starting from each point was periodic, or reached the stable fixed point. To improve the performance of this calculation we used the symmetries of the equations ($\phi_\alpha \leftrightarrow \phi_\beta$), where the exact number of points used was $\binom{L+N-1}{N}$, with $L = 30$. Periodic trajectories were operationally defined as trajectories that reach $\phi_\alpha = 6\pi$ for any α at some $t > 0$, which implies that they do not end at the stable fixed point of the starting unit cell or any of its nearest neighbors. Beyond the critical h , the volume fraction grows from zero and saturates towards a limiting value as h increases. Interestingly, with increasing N , the growth of this volume fraction beyond the critical h becomes sharper, and the limiting value at large h becomes closer to one. Extrapolating this trend we may

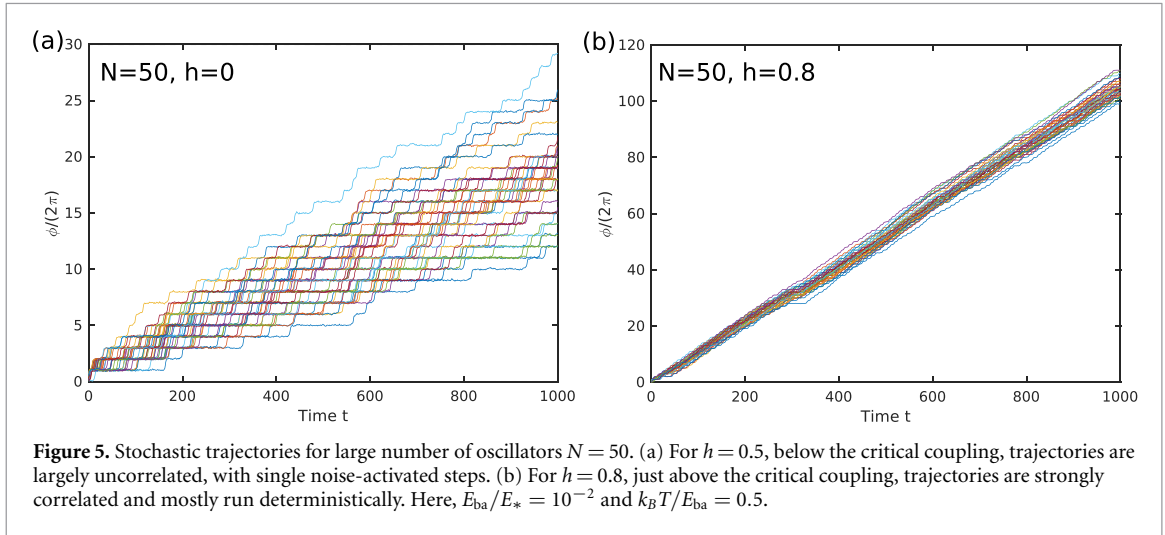
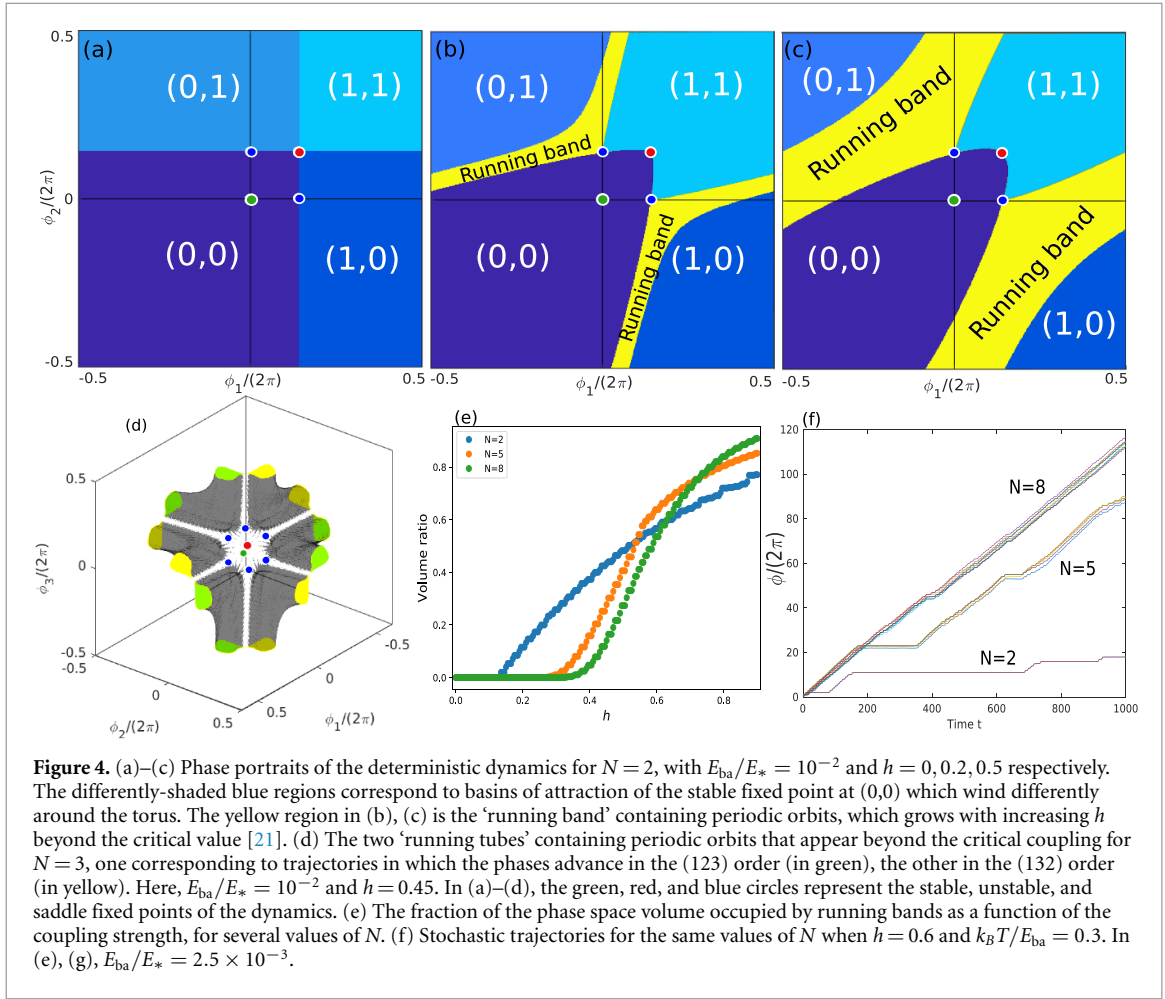


speculate that, for large N , a sharp transition occurs at a critical h at which the phase space becomes almost entirely occupied, or ‘crowded’ [25], by periodic orbits. In figure 4(f), some stochastic trajectories are shown, for h beyond the critical value and several values of N . For $N = 2$ we see longer periods in which the system is ‘resting’ at the fixed point and the phases do not advance, interspersed with short deterministic runs. As N is increased, the resting periods become shorter while the runs become longer, as one may expect from the considerations just described regarding the phase space volume occupied by periodic orbits.

3.1.2. Large number of oscillators

As the number of oscillators increases, the behavior observed in stochastic simulations becomes largely independent of this number. We observe that, beyond an N -independent critical value of h , trajectories mostly run deterministically, without barely any resting periods at which the oscillators visit the fixed point of the dynamics, see figure 5. The stochastic dynamics are quantified for various values of N in figure 6. All relevant quantities Ω , D_ϕ , and D_δ depend only very weakly on N and approach an asymptotic limit as $N \rightarrow \infty$, with D_ϕ showing the slowest approach towards this limit.

Interestingly, however, the synchronization order parameter becomes strongly nonmonotonic as a function of the coupling h , see figure 6(b): while synchronization is absent at low h , it rises sharply as we approach the critical h , but then quickly decreases back to zero (uncorrelated trajectories) as h is further increased. Intuitively, in light of the results described in the previous section, this implies that the oscillators are most correlated the phase space volume fraction occupied by periodic orbits is intermediate, neither too small (in which case trajectories are predominantly noise-activated, with independent steps by each oscillator) not too large (in which case trajectories are effectively deterministic and uncoupled).

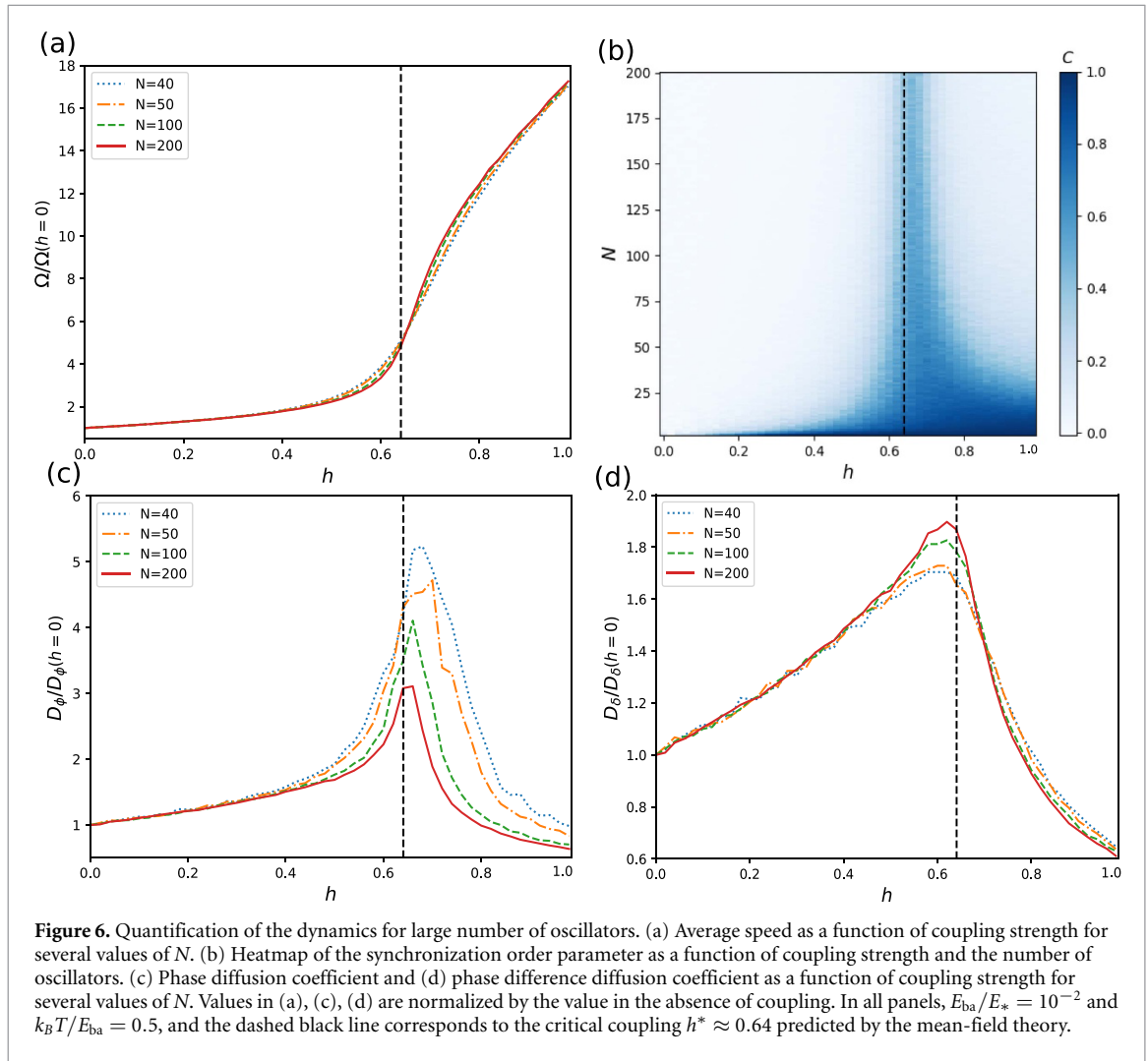


3.2. Mean-field theory in the large N limit

3.2.1. General case

The fact that the oscillators become uncorrelated in the large N limit suggests that we may describe the behavior of the system through a mean-field theory. Then we begin from the Fokker-Planck equation of this model which, following (2), is given by

$$\partial_t P(\phi_1, \dots, \phi_N; t) = \partial_\alpha \left\{ \mu_\phi \tilde{M}_{\alpha\beta} [k_B T \partial_\beta P + (\partial_\beta V(\phi_\beta)) P] \right\}. \quad (9)$$



To study the large N limit we first coarse grain over $(N - 1)$ degrees of freedom to get an equation for the one-particle distribution $\rho(\phi; t)$,

$$\rho(\phi; t) = \int d\phi_2 \dots d\phi_N P(\phi, \dots, \phi_N; t). \quad (10)$$

By assuming that the processes are uncorrelated, so that the two-particle distribution reads $P_2(\phi, \phi_1; t) = \rho(\phi; t)\rho(\phi_1; t)$, we close the hierarchy of equations and obtain an equation for the one-particle distribution,

$$\partial_t \rho(\phi; t) = \mu_\phi \partial_\phi \{k_B T \partial_\phi \rho - [F + h f_{\text{ave}} - v \sin(\phi + \delta)] \rho\}, \quad (11)$$

where

$$f_{\text{ave}} = - \int_0^{2\pi} d\phi \rho(\phi; t) \frac{\partial V(\phi)}{\partial \phi} \quad (12)$$

is the average force experienced by an oscillator. Therefore, in the mean-field approximation each oscillator feels an effective driving force $F_{\text{eff}} = F + h f_{\text{ave}}$, independent of the number of enzymes, with the strength of the deviation from the true driving force F governed by h . Notice that the equation of motion becomes nonlinear and nonlocal in ϕ , due to the presence of ρ in the definition of f_{ave} .

Nonlinear partial differential equations such as equation (11) can have many solutions, including solutions that oscillate at long times and chaotic solutions [28, 41, 43]. Because we want to understand the results of the stochastic simulations at large but finite N described above, however, we will focus only on

stationary (steady state) solutions satisfying $\partial_t \rho(\phi; t) = 0$, which are of particular relevance. The steady state(s) $\rho_{ss}(\phi)$ of equation (11) can be found by imposing the condition of constant flux

$$-J/\mu_\phi = k_B T \partial_\phi \rho_{ss} - [F + hf_{ave} - v \sin(\phi + \delta)] \rho_{ss}, \quad (13)$$

where J corresponds to the flux. This problem is identical to that of finding the steady state distribution of a single particle in a washboard potential with driving force $F_{eff} = F + hf_{ave}$, which is well studied and easily solved using standard methods [50], except that here one must additionally solve for f_{ave} in the implicit equation $f_{ave} = \int_0^{2\pi} d\phi \rho_{ss}(\phi) [F - v \sin(\phi + \delta)]$ (note that ρ_{ss} depends on f_{ave}), required for self-consistency, see (12). Armed with this self-consistent value of f_{ave} and thus of F_{eff} , which is a function of all parameters of the system and in particular of the coupling h , we can then obtain the average speed Ω and the phase diffusion coefficient D_ϕ (which corresponds to $D_\delta/2$ given the absence of correlations) using the known results for a single particle in a tilted washboard potential [46, 47, 50]. Additionally, we may calculate a critical value of the coupling $h = h^*$ at which $F_{eff} = v$, i.e. the value of the coupling for which the energy barriers of the effective washboard potential vanish and the dynamics become deterministic (downhill). This further showcases the analogy between the giant diffusion observed at $F = v$ for a single particle in a washboard potential, and that seen at $h = h^*$ for both the phase and phase-difference diffusion coefficients in the present work.

The values for Ω , D_ϕ , and D_δ obtained from this mean-field theory are compared to those obtained from stochastic simulations with $N = 200$ in figure 7, for three different values of the noise $k_B T$. We observe an excellent match, except for D_ϕ at the critical coupling, which is underestimated particularly for low temperatures (as described above, the limit $N \rightarrow \infty$ is approached slowly for D_ϕ). Interestingly, we find that whether the transition to a running state with increasing h is continuous or discontinuous in the mean field theory depends on whether the temperature is above or below a critical temperature, which for $E_{ba}/E_* = 10^{-2}$ as used in figure 7 we find to be $k_B T/E_{ba} \simeq 0.48$. Above the critical temperature, a single branch of solutions exists, with monotonically increasing average speed, see figures 7(a)–(d). Below the critical temperature, on the other hand, three different branches of stationary solutions exist: a slow or arrested stable branch, a fast or running stable branch, and an unstable branch marking the transition state between the two, see figures 7(e) and (f). The transition from the arrested to the running state is discontinuous, with both states coexisting at an intermediate range of h -values. In this coexistence region, the stochastic simulations at finite but large N show that the average speed interpolates between that of the arrested and the running states of the mean field theory, see figure 7(f), whereas the phase diffusion coefficient is greatly enhanced, see figure 7(e). This is consistent with the system stochastically switching between the arrested and running states.

In figure 8, the critical coupling h^* at which $F_{eff} = v$ and the dynamics become effectively deterministic is shown as a function of the shape of the washboard potential [E_{ba}/E_* , see figure 1(c), which is in one-to-one correspondence with F/v], for various values of the noise strength. This line divides the parameter plane into two regions corresponding to noise-activated and deterministic dynamics. Additionally, the critical coupling h^* obtained from the mean-field theory is plotted as the vertical line in figure 6, again with excellent agreement. As expected, it marks the transition between noise-activated and deterministic dynamics.

3.2.2. Limit of vanishing noise

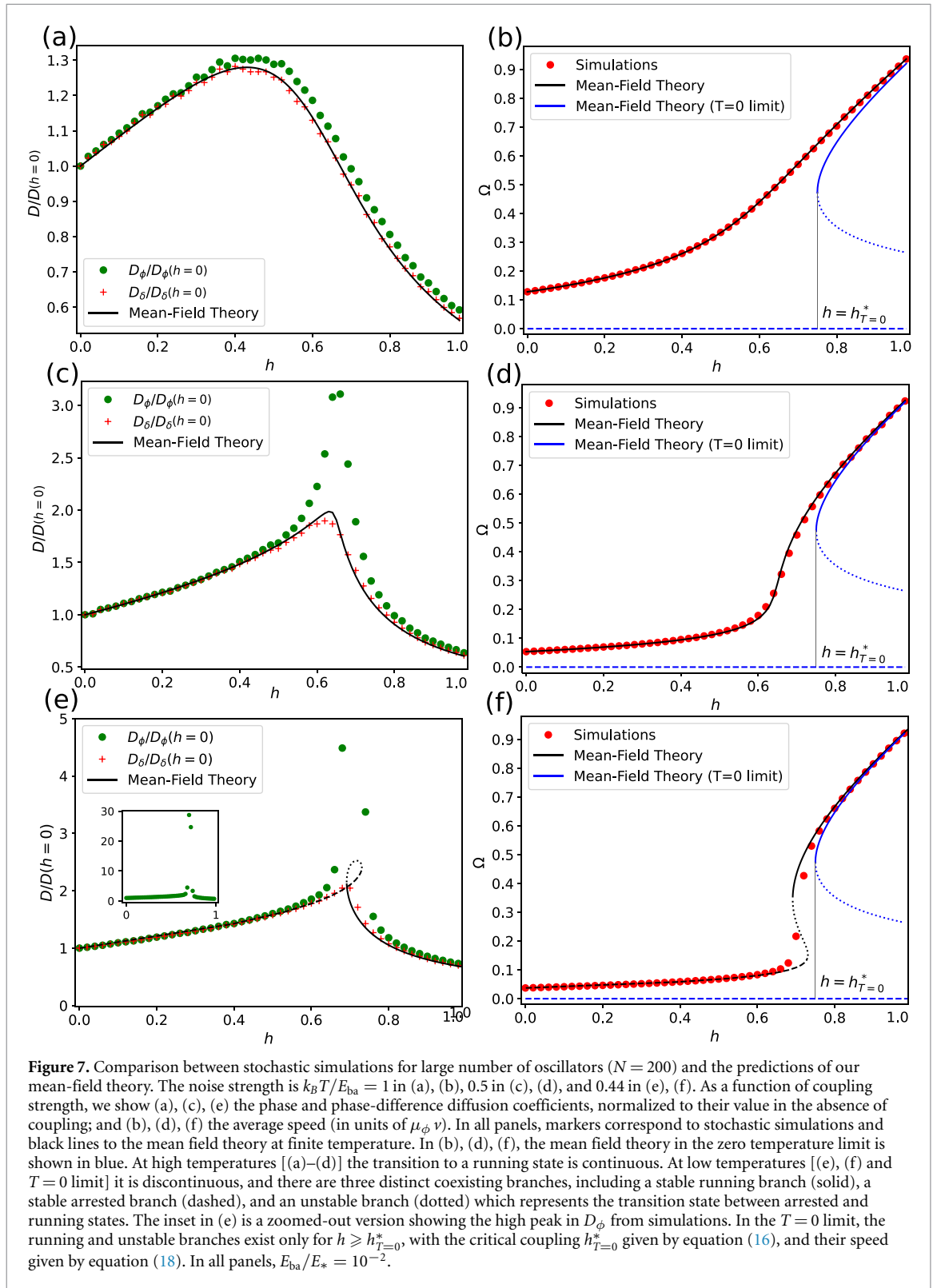
Further analytical progress is possible in the limit of vanishing noise $T \rightarrow 0$. Like in the case of small but finite temperatures, there are several steady state solutions satisfying (13). One trivial solution, independent of all parameters, is the arrested solution ($J = 0$) in which all oscillators are located at the stable fixed point $\phi = 0$ of the dynamics, with a Dirac delta distribution $\rho_{ss}(\phi) = \delta(\phi)$. The non-trivial solutions ($J > 0$) corresponding to the running state and the unstable branch are obtained by directly solving for ρ_{ss} in (13), giving

$$\rho_{ss}(\phi) = \frac{1}{2\pi} \frac{\sqrt{(F + hf_{ave})^2 - v^2}}{F + hf_{ave} - v \sin(\phi + \delta)} \quad (14)$$

where J has been used to enforce normalization $\int_0^{2\pi} \rho_{ss} d\phi = 1$. Note that these steady states are only well-defined when $F_{eff} > v$, so that the effective potential admits deterministic dynamics. Using (14) in the self-consistency condition gives $f_{ave} = \sqrt{(F + hf_{ave})^2 - v^2} - hf_{ave}$ and, solving for f_{ave} , we obtain two solutions given by

$$f_{ave}^\pm = \frac{Fh \pm \sqrt{F^2(1+h)^2 - (1+2h)v^2}}{1+2h}. \quad (15)$$

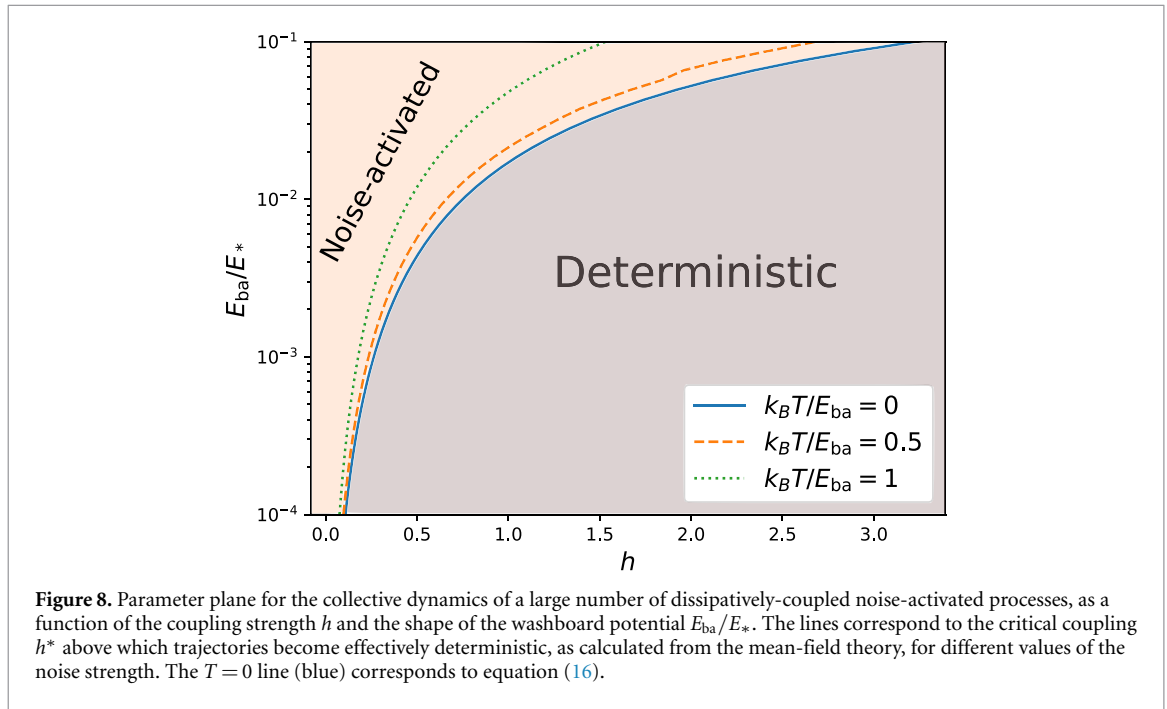
The solution with the plus sign corresponds to the stable running steady state, whereas the solution with the minus sign corresponds to the unstable branch. Like in the case of small but finite temperatures, this



unstable branch corresponds to the transition state between the arrested state and the running state. These two solutions are real only when the term inside the square root is positive, which is possible when

$$h > \frac{v^2 - F^2 + \sqrt{v^2 - F^2}}{F^2} \equiv h_{T=0}^* \quad (16)$$

and serves to define the critical value of the coupling $h_{T=0}^*$ above which deterministic, ‘running’ trajectories exist in the vanishing noise limit. Naturally, such a critical coupling is only well-defined when energy barriers are present in the true washboard potential ($F < v$), and $h_{T=0}^* \rightarrow 0$ from above as $F \rightarrow v$ from below. The



critical coupling given by equation (16) is shown as a function of E_{ba}/E_* (which is in one-to-one correspondence with F/ν) as the $T=0$ line in figure 8; and as the vertical lines in figures 7(b), (d) and (f)).

Interestingly, at the critical coupling we do not find $F_{\text{eff}}(h_{T=0}^*) = \nu$ as one might have naively expected, but rather

$$F_{\text{eff}}(h_{T=0}^*) = F + h_{T=0}^* f_{\text{ave}}(h_{T=0}^*) = \frac{\nu^2}{F} \quad (17)$$

which implies that $F_{\text{eff}}(h_{T=0}^*) > \nu$ when $F < \nu$, i.e. the effective washboard potential is already beyond the critical tilt, and the dynamics are therefore fully deterministic, when the critical coupling is reached. This is a reflection of the fact that the transition to the running state is discontinuous and noise-activated, as for $h > h_{T=0}^*$ the running state still coexists with the arrested state. This also implies that, at the critical coupling, there is already a finite, non-vanishing average speed Ω of the oscillators in the running state. Indeed, the average speed for the running and unstable branches may be calculated as

$$\Omega^\pm = 2\pi J^\pm = \mu_\phi (1+h) f_{\text{ave}}^\pm. \quad (18)$$

At the critical coupling, both branches coincide and we find

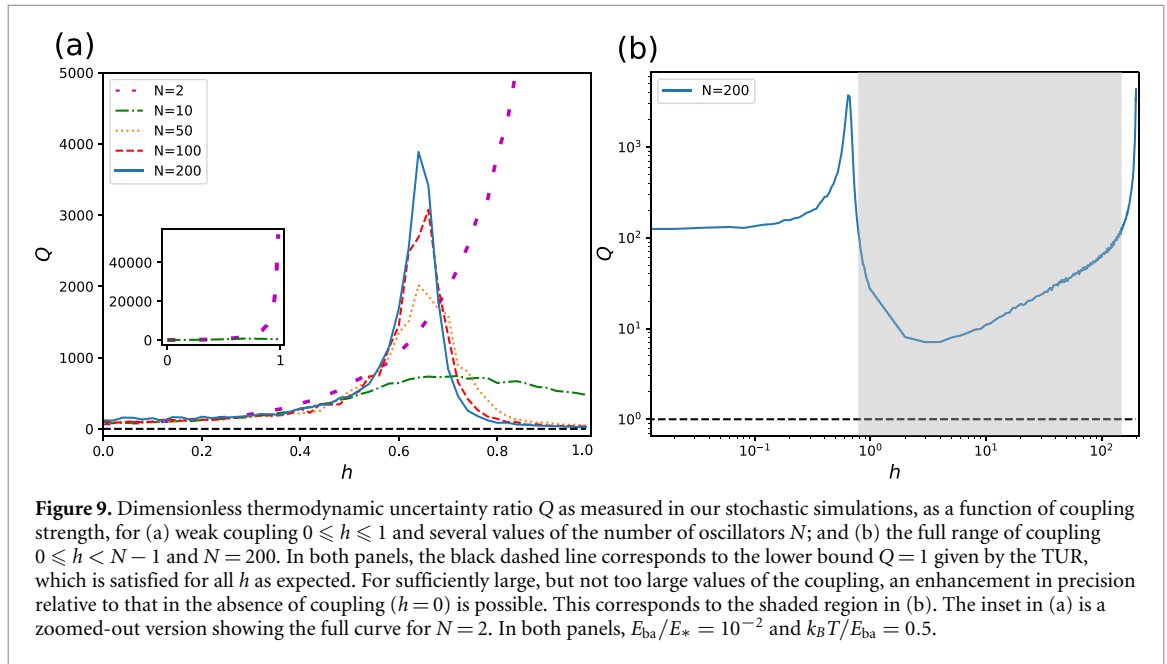
$$\Omega(h_{T=0}^*) = \mu_\phi (1+h_{T=0}^*) f_{\text{ave}}(h_{T=0}^*) = \mu_\phi \nu \frac{\sqrt{\nu^2 - F^2}}{F} \quad (19)$$

which is real and positive for any $F < \nu$. The zero temperature average speed of the running (resp. unstable) branch as given by Ω^+ (resp. Ω^-) in equation (18) is plotted as the blue solid (resp. dotted) lines in figures 7(b), (d) and (f)). As discussed above, these two branches exist only for $h \geq h_{T=0}^*$. Additionally, the arrested branch is plotted as the dashed blue line ($\Omega = 0$), and exists for all h . The running branch in this $T=0$ limit is in very good agreement with both the stochastic simulations and the mean-field theory at finite temperature, serving as further confirmation that the dynamics beyond the critical coupling are largely deterministic.

3.3. Stochastic thermodynamics of precision

The coupling-induced transition marks a very strong change in the dynamics of the system, from noise-activated to deterministic. It is thus interesting to explore how does the transition affect the precision of the oscillators, which is bounded from below by the entropy production rate in the system [32]. Specifically, the TUR states the bound [33]

$$\dot{\sigma} \tau \epsilon^2 \geq 2k_B, \quad (20)$$



where $\dot{\sigma}$ is the entropy production rate, and ϵ^2 is the relative uncertainty defined as

$$\epsilon^2 = \frac{\langle X^2 \rangle - \langle X \rangle^2}{\langle X \rangle^2}, \quad (21)$$

where X is the observable of interest. This inequality is crucial, since it implies that a higher precision in the catalytic rate (smaller ϵ) requires higher entropy production or equivalently heat dissipation (higher $\dot{\sigma}$). In our model the observable of interest is the total amount of phase advanced by the oscillators

$$X = \sum_i^N \phi_i. \quad (22)$$

The entropy production rate $\dot{\sigma}$ is easily calculated as

$$\dot{\sigma} T = F \langle \dot{X} \rangle, \quad (23)$$

and is directly related to the free energy $E_* = 2\pi F$ released in each noise-activated step, see figure 1(c).

In figure 9, we plot the dimensionless thermodynamic uncertainty ratio $Q \equiv \dot{\sigma} t \epsilon^2 / (2k_B)$ as a function of the coupling h , as measured in our stochastic simulations for several values of N . According to the TUR (20), satisfies $Q \geq 1$. A process satisfying $Q = 1$ is performing optimally from a thermodynamic perspective (as precisely as possible given its energy dissipation). We see that, as expected, the TUR is always respected. The behavior of Q with increasing h is strongly non-monotonic (with the exception of the case $N = 2$). Starting from the uncoupled case $h = 0$, Q first increases with increasing h , in the regime of noise-activated dynamics. After peaking around the critical $h = h^*$, however, Q sharply decreases as h is further increased and we venture further into the deterministic regime. Values of Q smaller than the value $Q(h = 0)$ are observed in this regime, implying that the coupling can enhance the thermodynamic performance of the oscillators. Finally, as we approach the upper bound of $h < N - 1$ required by the positive definiteness of the mobility, Q is observed to rise again. We note, however, that the regime $1 \ll h < N - 1$ is somewhat artificial, as it corresponds to cases where the effects of cross-interactions between oscillators are much stronger than those of self-interactions. Moreover, this regime only exists for finite N and becomes inaccessible in the thermodynamic limit $N \rightarrow \infty$.

4. Conclusions

We have studied a minimal model describing the collective dynamics of noise-activated cyclic processes, or stochastic oscillators, that are coupled to each other through a dissipative coupling. That is, the processes are not coupled to each other through an interaction potential (or interaction force), but through the mobility tensor that connects forces to velocities in the overdamped dynamics. This mobility tensor also defines the

properties of the stochastic noise through the fluctuation-dissipation relation, ensuring that the dynamics are thermodynamically-consistent and relax to thermodynamic equilibrium when such an equilibrium is available. Previously, we have shown how this kind of coupling arises naturally for processes that are mechanically coupled (e.g. physically or through hydrodynamic interactions) in an overdamped, viscous medium [21].

For low N , where N is the number of coupled oscillators, we found results analogous to those previously obtained for $N = 2$ in [21]. Beyond a critical coupling h^* , strong synchronization (as measured by the correlation function) and an enhancement in the average speed of the processes is observed. This transition can be understood as arising from a global bifurcation of the underlying dynamical system, defined on the N -torus, which leads to the emergence of periodic orbits that represent ‘running’ trajectories, along which the phases of all the oscillators increase deterministically.

For large N , synchronization becomes confined to a narrow region near the critical coupling h^* . Below h^* , the dynamics are uncorrelated and stochastic (noise-activated). Above h^* , they are uncorrelated and effectively deterministic, and the average phase speed becomes greatly enhanced. We can understand this effect in two complementary ways: (i) analysis of the underlying dynamical system shows that, at large N , the volume fraction of the phase space occupied by periodic orbits increases very sharply at the bifurcation; and (ii) a mean-field theory shows that the energy barriers in the effective potential landscape experienced by each oscillator vanish at the critical coupling, and the dynamics become deterministic (downhill). The mean-field theory provides a great match to the results of stochastic simulations at large N and allows for analytical prediction of the critical coupling and the average speed of the oscillators, particularly in the limit of low noise.

Finally, we have shown that the oscillator dynamics can become more optimal in the presence of coupling, in the context of the trade-off between precision and entropy production described by the TUR. This occurs within the deterministic regime of the dynamics, beyond the critical coupling h^* . Over the full range of coupling strengths, the behavior relative to the thermodynamic bound on precision is rather complex, and signatures of the stochastic-to-deterministic transition at the critical coupling are clearly apparent in the precision.

Due to its simplicity, its general applicability to the description of coupled microscopic processes [21], and its intriguing features in the context of nonequilibrium statistical physics and dynamical systems theory, we believe that the model presented here merits significant further investigation. Future work may consider local interactions between the nearest neighbours rather than all-to-all interactions as studied here, endowing the model with a spatial structure, as well as the role of quenched disorder [51]. Of great interest would also be the interactions between non-identical oscillators, as only the synchronization between identical oscillators has been studied so far. Lastly, one may explore connections to Bose–Einstein-like condensation in driven scalar active matter [52] when interactions among particles are non-negligible.

Data availability statement

All data that support the findings of this study are included within the article (and any supplementary files).

ORCID iDs

M Chatzittofi  <https://orcid.org/0009-0007-3898-3638>

R Golestanian  <https://orcid.org/0000-0002-3149-4002>

J Agudo-Canalejo  <https://orcid.org/0000-0001-9677-6054>

References

- [1] Strogatz S H, Abrams D M, McRobie A, Eckhardt B and Ott E 2005 *Nature* **438** 43–44
- [2] Kuramoto Y 1984 *Chemical Oscillations, Waves and Turbulence* (Springer)
- [3] Pikovsky A, Rosenblum M and Kurths J 2001 *Synchronization: A Universal Concept in Nonlinear Sciences (Cambridge Nonlinear Science Series)* (Cambridge University Press)
- [4] Acebrón J A, Bonilla L L, Vicente C J P, Ritort F and Spigler R 2005 *Rev. Mod. Phys.* **77** 137
- [5] Gupta S, Campa A and Ruffo S 2014 *J. Stat. Mech.: Theory Exp.* **2014** R08001
- [6] Panaggio M J and Abrams D M 2015 *Nonlinearity* **28** R67
- [7] Golestanian R, Yeomans J M and Uchida N 2011 *Soft Matter* **7** 3074
- [8] Vilfan A and Jülicher F 2006 *Phys. Rev. Lett.* **96** 058102
- [9] Meng F, Bennett R R, Uchida N and Golestanian R 2021 *Proc. Natl Acad. Sci. USA* **118** e2102828118
- [10] Magnasco M O 1994 *Phys. Rev. Lett.* **72** 2656–9
- [11] Golubeva N, Imparato A and Peliti L 2012 *Europhys. Lett.* **97** 60005
- [12] Malgaretti P, Pagonabarraga I and Frenkel D 2012 *Phys. Rev. Lett.* **109** 168101
- [13] Ouazan-Reboul V, Agudo-Canalejo J and Golestanian R 2021 *Eur. Phys. J. E* **44** 113

- [14] Cotton M W, Golestanian R and Agudo-Canalejo J 2022 *Phys. Rev. Lett.* **129** 158101
- [15] Glowacki D R, Harvey J N and Mulholland A J 2012 *Nat. Chem.* **4** 169–76
- [16] Callender R and Dyer R B 2015 *Acc. Chem. Res.* **48** 407–13
- [17] Golestanian R 2015 *Phys. Rev. Lett.* **115** 108102
- [18] Hosaka Y, Komura S and Mikhailov A S 2020 *Soft Matter* **16** 10734–49
- [19] Agudo-Canalejo J, Adeleke-Larodo T, Illien P and Golestanian R 2018 *Acc. Chem. Res.* **51** 2365–72
- [20] Agudo-Canalejo J and Golestanian R 2020 *Eur. Phys. J. Spec. Top.* **229** 2791–806
- [21] Agudo-Canalejo J, Adeleke-Larodo T, Illien P and Golestanian R 2021 *Phys. Rev. Lett.* **127** 208103
- [22] Sweetlove L J and Fernie A R 2018 *Nat. Commun.* **9** 2136
- [23] O’Flynn B G and Mittag T 2021 *Curr. Opin. Cell Biol.* **69** 70–79
- [24] Lindner B, Garcia-Ojalvo J, Neiman A and Schimansky-Geier L 2004 *Phys. Rep.* **392** 321–424
- [25] Wiesenfeld K and Hadley P 1989 *Phys. Rev. Lett.* **62** 1335
- [26] Tsang K Y, Mirollo R E, Strogatz S H and Wiesenfeld K 1991 *Physica D* **48** 102–12
- [27] Golomb D, Hansel D, Shraiman B and Sompolinsky H 1992 *Phys. Rev. A* **45** 3516
- [28] Watanabe S and Strogatz S H 1994 *Physica D* **74** 197–253
- [29] Hodgkin A L and Huxley A F 1952 *J. Physiol.* **117** 500
- [30] FitzHugh R 1961 *Biophys. J.* **1** 445–66
- [31] Nagumo J, Arimoto S and Yoshizawa S 1962 *Proc. IRE* **50** 2061–70
- [32] Seifert U 2005 *Phys. Rev. Lett.* **95** 040602
- [33] Barato A C and Seifert U 2015 *Phys. Rev. Lett.* **114** 158101
- [34] Skinner D J and Dunkel J 2021 *Phys. Rev. Lett.* **127** 198101
- [35] Hong H, Jo J, Hyeon C and Park H 2020 *J. Stat. Mech.: Theory Exp.* **2020** 074001
- [36] Lee S, Hyeon C and Jo J 2018 *Phys. Rev. E* **98** 032119
- [37] Zhang D, Cao Y, Ouyang Q and Tu Y 2019 *Nat. Phys.* **16** 95–100
- [38] De Groot S R and Mazur P 2013 *Non-Equilibrium Thermodynamics* (Courier Corporation)
- [39] Kim S and Karrila S J 2013 *Microhydrodynamics: Principles and Selected Applications* (Courier Corporation)
- [40] Kramers H A 1940 *Physica* **7** 284–304
- [41] Shinomoto S and Kuramoto Y 1986 *Prog. Theor. Phys.* **75** 1105–10
- [42] Sakaguchi H, Shinomoto S and Kuramoto Y 1988 *Prog. Theor. Phys.* **79** 600–7
- [43] Klinshov V V, Kirillov S Y, Nekorkin V I and Wolfrum M 2021 *Chaos* **31** 083103
- [44] Zeeman E 1988 *Nonlinearity* **1** 115
- [45] Huang W, Ji M, Liu Z and Yi Y 2015 *J. Dyn. Differ. Equ.* **27** 721–42
- [46] Reimann P, Van den Broeck C, Linke H, Hänggi P, Rubi J M and Pérez-Madrid A 2001 *Phys. Rev. Lett.* **87** 010602
- [47] Reimann P, Van den Broeck C, Linke H, Hänggi P, Rubi J M and Pérez-Madrid A 2002 *Phys. Rev. E* **65** 031104
- [48] Wiley D A, Strogatz S H and Girvan M 2006 *Chaos* **16** 015103
- [49] Menck P J, Heitzig J, Marwan N and Kurths J 2013 *Nat. Phys.* **9** 89–92
- [50] Risken H 1996 *Fokker-Planck Equation (The Fokker-Planck Equation)* (Springer) pp 63–95
- [51] Uchida N and Golestanian R 2010 *Europhys. Lett.* **89** 50011
- [52] Berx J, Bose A, Golestanian R and Mahault B 2023 *Europhys. Lett.* **142** 67004

Collective synchronization of dissipatively-coupled noise-activated processes

Supplementary material

M Chatzittofi¹, R Golestanian^{1,2} and J Agudo-Canalejo¹

¹ Living Matter Physics, Max Planck Institute for Dynamics and Self-Organisation, D-37077, Goettingen, Germany

² Rudolf Peierls Centre for Theoretical Physics, University of Oxford, Oxford OX1 3PU, United Kingdom

E-mail: ramin.golestanian@ds.mpg.de; jaime.agudo@ds.mpg.de

1. Example: Analysis of simulations

We restate here the definitions of the phase mean square displacement $[\text{MS}\phi(\tau)]$, phase difference mean square displacement $[\text{MS}\delta(\tau)]$, and pair correlation function $[\text{corr}(\tau)]$, see equations (4)–(6) from the main text:

$$\text{MS}\phi(\tau) = \langle [\delta\phi_\alpha(\tau; t) - \langle \delta\phi_\alpha(\tau; t) \rangle_{\alpha,t}]^2 \rangle_{\alpha,t} \quad (1)$$

$$\text{MS}\delta(\tau) = \langle [\delta\phi_\alpha(\tau; t) - \delta\phi_\beta(\tau; t)]^2 \rangle_{\alpha\beta,t} \quad (2)$$

$$\text{corr}(\tau) = \frac{\langle [\delta\phi_\alpha(\tau; t) - \langle \delta\phi_\alpha(\tau; t) \rangle_{\alpha,t}] [\delta\phi_\beta(\tau; t) - \langle \delta\phi_\beta(\tau; t) \rangle_{\beta,t}] \rangle_{\alpha\beta,t}}{\langle [\delta\phi_\alpha(\tau; t) - \langle \delta\phi_\alpha(\tau; t) \rangle_{\alpha,t}]^2 \rangle_{\alpha,t}} \quad (3)$$

The τ -dependence of these three functions is shown in figure 1 for the example parameters $E_{\text{ba}}/E_* = 10^{-2}$, $k_B T/E_{\text{ba}} = 0.5$, $N = 4$, $h = 0.4$. The time step used is $dt = 10^{-2}$, where time is given in units of $(\mu_\phi v)^{-1}$. The total number of simulation steps is 10^9 (so that the total time of the simulation is $t_{\text{tot}} = 10^7$), and the number of equally spaced samples recorded and used for the analysis is 5×10^6 .

As expected, $\text{MS}\phi(\tau)$ and $\text{MS}\delta(\tau)$ show linear behavior at long times, where the respective slopes correspond to $2D_\phi$ and $2D_\delta$. Lastly, as also expected, $\text{corr}(\tau)$ tends to a constant which corresponds to the correlation C .

The slopes can be estimated by choosing two sufficiently large values of τ , for example $\tau_1 = 5 \times 10^4$ and $\tau_2 = 10^5$. We can then calculate D_ϕ as $D_\phi = (1/2)(\text{MS}\phi(\tau_2) - \text{MS}\phi(\tau_1))/(\tau_2 - \tau_1) \simeq 0.0092$ and similarly D_δ as $D_\delta = (1/2)(\text{MS}\delta(\tau_2) - \text{MS}\delta(\tau_1))/(\tau_2 - \tau_1) \simeq 0.0062$. As described in the main text, these two diffusion coefficients are related to the correlation coefficient by $C = 1 - \frac{D_\delta}{2D_\phi}$, which gives $C \simeq 0.66$.

Alternatively, we may directly calculate C from its definition, i.e. from the $\tau \rightarrow \infty$ asymptote of $\text{corr}(\tau)$. To this end, we calculate the average value of $\text{corr}(\tau)$ between τ_1 and τ_2 . This gives $C \simeq 0.66$, which as expected agrees with the above value. In practice, we always obtain C from $C = 1 - \frac{D_\delta}{2D_\phi}$.

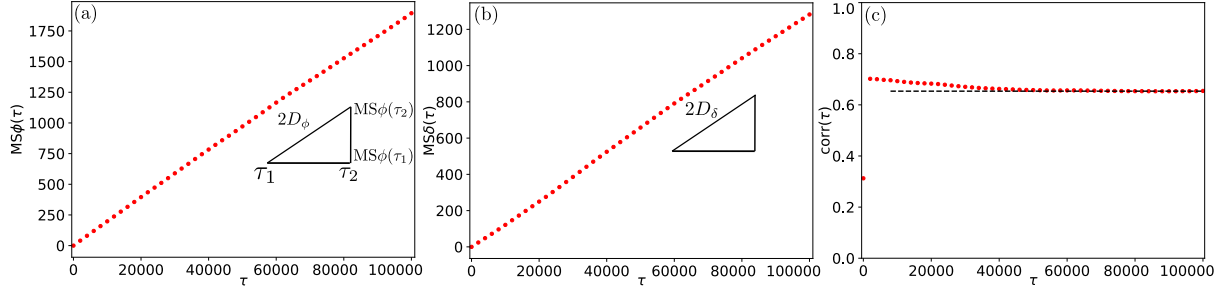


Figure 1: Examples of (a) $MS\phi(\tau)$, (b) $MS\delta(\tau)$, and (c) $corr(\tau)$, for a simulation with $E_{ba}/E_* = 10^{-2}$, $k_B T/E_{ba} = 0.5$, $N = 4$, $h = 0.4$. In (c), the black dashed line corresponds to the asymptotic value of $corr(\tau)$ which defines the correlation C , here calculated from averaging $corr(\tau)$ between $\tau_1 = 5 \times 10^4$ and $\tau_2 = 10^5$.

Chapter 3

Topological phase locking in molecular oscillators

This chapter is reproduced from a revised version of the preprint Chatzittofi M. et al arXiv:2310.11788 [[132](#)] which is under review in Nature Communications. In this work, I contributed in designing the research and in deriving the equations of motion. I also developed the numerical code in Matlab for generating the phase-portraits. I have performed numerical calculations, contributed in the analysis of the results and writing/editing the paper.

Topological phase locking in molecular oscillators

Michalis Chatzittofi,¹ Ramin Golestanian,^{1,2,*} and Jaime Agudo-Canalejo^{1,3,†}

¹Max Planck Institute for Dynamics and Self-Organization (MPI-DS), D-37077 Göttingen, Germany

²Rudolf Peierls Centre for Theoretical Physics, University of Oxford, Oxford OX1 3PU, United Kingdom

³Department of Physics and Astronomy, University College London, London WC1E 6BT, United Kingdom

(Dated: May 14, 2024)

The dynamics of molecular-scale enzymes and molecular motors are activated by thermal noise, and driven out-of-equilibrium by local energy dissipation. Because the energies dissipated in these systems are comparable to the thermal energy, one would generally expect their dynamics to be highly stochastic. Here, by studying a thermodynamically-consistent model of two coupled noise-activated oscillators, we show that this is not always the case. Thanks to a novel phenomenon that we term topological phase locking (TPL), the coupled dynamics become quasi-deterministic, resulting in a greatly enhanced average speed of the oscillators. TPL is characterized by the emergence of a band of periodic orbits that form a torus knot in phase space, along which the two oscillators advance in rational multiples of each other. The effectively conservative dynamics along this band coexists with the basin of attraction of the dissipative fixed point. We further show that TPL arises as a result of a complex, infinite hierarchy of global bifurcations. Our results have implications for understanding the dynamics of a wide range of systems, from biological enzymes and molecular motors to engineered nanoscale electronic, optical, or mechanical oscillators.

Enzymes and molecular motors are pivotal in catalyzing biochemical reactions and converting chemical energy into mechanical work [1, 2]. By dissipating energy at the molecular scale, they play a crucial role in the maintenance of life’s out-of-equilibrium dynamics. However, because the dynamics in these systems tend to involve noise-activated barrier-crossing processes with energy scales comparable to the thermal energy, $k_B T$, their dynamics tend to be highly stochastic. To be more reliable, biological systems have developed various strategies that trade off energy dissipation for increased precision [3–5], as exemplified by e.g. proofreading [6, 7] or noise buffering strategies [8, 9].

One possible strategy for reducing stochasticity and in turn increasing reliability lies in many-body interactions, i.e. synchronization [10, 11]. For example, in the case of the KaiABC circadian clock, the collective oscillations of many interacting KaiABC protein complexes are significantly more coherent than those of a single complex [12, 13]. In the KaiABC system, interactions are “chemical”, in the sense that they are mediated by monomer exchange among the complexes. However, because enzymes and molecular motors transduce chemical energy into motion, they also experience “physical”, or mechanical, interactions with each other through the viscous medium in which they are embedded, see Fig. 1(a–d). The viscous nature of the medium leads to interactions mediated by hydrodynamic friction, or *dissipative* interactions.

Due to the key role that the interplay between thermal fluctuations and nonequilibrium driving energies plays in these systems, one must be particularly careful when modelling their dynamics. Thermodynamic consistency, in particular the requirement that local detailed balance and a fluctuation-dissipation relation be

satisfied, strongly constrain the form of the dynamics [14]. Recently, using a minimal thermodynamically-consistent model for two identical enzymes that are mechanically-coupled to each other and undergo conformational changes during their reaction cycle, we showed that the mechanochemical coupling in these systems can cause synchronization and enhanced reaction speeds [15]. A generalization of this model to arbitrary numbers of coupled identical noise-activated oscillators shows synchronization at low number of oscillators, and enhanced speeds independent of the number of oscillators [16]. Interestingly, the transition to the synchronized state in this model was shown to occur as a result of a global bifurcation in the underlying dynamical system, which transitions from purely dissipative, noise-activated dynamics (where all trajectories lead to the fixed point) to a mixture of dissipative and conservative dynamics (where some trajectories are periodic and avoid the fixed point) beyond a critical coupling strength [15, 16]. This very intriguing bifurcation has also been reported in the context of coupled superconducting Josephson junctions [17].

While fascinating, the latter results have limited applicability, as they only concern coupled identical oscillators. Here, we study the dynamics of two non-identical noise-activated oscillators that are dissipatively coupled. Crucially, our model is generic enough that it may serve as a minimal model for a wide variety of cyclic nanoscale systems. Examples include dissimilar enzymes [see Fig. 1(a) and (b)] [18] or gating nano-pores [19], nanoscale rotary motors [see Fig. 1(c) and (d)] (either biological, such as ATP synthase [20], or synthetic, such as those recently made from DNA-origami [21–23]), circadian clocks [24, 25], superconducting Josephson junction arrays [Fig. 1(e)] [17, 26], firing neurons [Fig. 1(f)]

[27, 28], artificial systems like magnetic rotors [29], laser cavities [30, 31], opto-mechanical devices [32, 33], mechanical oscillators [34, 35], or any other suitably-reduced description of an excitable system [36, 37].

We find that, instead of a single bifurcation occurring with increasing coupling strength as for identical oscillators, non-identical oscillators undergo an infinite number of bifurcations as the coupling is increased. The oscillators are generically phase-locked, such that noise activation leads to a finite number of oscillations for each oscillator, with a fixed ratio between them. Moreover, for sufficiently strong asymmetry in the nonequilibrium driving forces, a finite number of “resonant” modes emerges at specific values of the coupling strength. For these resonant modes, we find periodic trajectories that avoid the fixed point and maintain a fixed ratio between the number of steps advanced by each oscillator. To reach (or move away from) these resonant modes, an infinite ladder of bifurcations must be climbed (or descended). We find that the resonant modes correspond to very special topologies of the deterministic phase portraits of the system, defined on the torus, in which the phase space splits into a band of periodic orbits which form torus knots [38] with a specific winding number. We thus refer to this novel phenomenon as *topological phase locking* (TPL). In the stochastic dynamics, TPL results in a greatly enhanced average speed as well as giant diffusion [39], which together create strong signatures in the stochastic thermodynamics of the precision of the coupled oscillators [4, 40].

Dissipative coupling of noise-activated processes

We consider two processes, each defined by a phase ϕ_α with $\alpha = 1, 2$, which evolve along two washboard potentials $V_\alpha(\phi_\alpha)$, see Fig. 1(g). The key parameters of the potential are the height of the energy barrier $E_{\text{ba}\alpha}$, which determines the noise-activated dynamics, and the energy released per transition $E_{*\alpha}$, which acts as the nonequilibrium driving force. The two phases are coupled not through an interaction force or potential, but through the off-diagonal components of the mobility tensor that connects forces to velocities in the overdamped dynamics. That is, the phases evolve according to the following coupled Langevin equations

$$\dot{\phi}_\alpha = \sum_{\beta=1}^2 \left[M_{\alpha\beta} \left(-\frac{\partial V_\beta(\phi_\beta)}{\partial \phi_\beta} \right) + \sqrt{2k_B T} \Sigma_{\alpha\beta} \xi_\beta \right], \quad (1)$$

where $M_{\alpha\beta}$ is the mobility tensor, described below, $\Sigma_{\alpha\beta}$ is the principal square root of $M_{\alpha\beta}$ such that $M_{\alpha\beta} = \Sigma_{\alpha\gamma} \Sigma_{\beta\gamma}$, and $\xi_\alpha(t)$ is a Gaussian white noise satisfying $\langle \xi_\alpha(t) \rangle = 0$, $\langle \xi_\alpha(t) \xi_\beta(t') \rangle = \delta_{\alpha\beta} \delta(t - t')$. Moreover, k_B is the Boltzmann constant and T is the temperature of the medium, so that $k_B T$ is the thermal energy controlling

the strength of thermal fluctuations. For non-thermal systems, $k_B T$ may be taken as the strength of the effective noise. For the dynamics to be thermodynamically consistent, the mobility tensor must be symmetric and positive definite [41, 42]. We take the components of the mobility tensor to be $M_{11} = \mu_1$, $M_{22} = \mu_2$, and $M_{12} = M_{21} = \sqrt{\mu_1 \mu_2} h$. Thus, the dimensionless parameter h controls the strength of the coupling, and the condition of positive definiteness implies that it is constrained to the range $-1 < h < 1$. Through $\Sigma_{\alpha\beta}$, the mobility tensor also controls the form of the additive noise, so that the fluctuation-dissipation theorem is satisfied. This further implies that, independently of the strength of the coupling, the system is guaranteed to equilibrate to the Boltzmann distribution $P_{\text{eq}}(\phi_1, \phi_2) \propto \exp(-[V_1(\phi_1) + V_2(\phi_2)]/k_B T)$ when such an equilibrium is possible (e.g. in the absence of nonequilibrium driving forces, $E_{*1} = E_{*2} = 0$).

A coupling of the form in (1) arises naturally in processes that are coupled to each other through mechanical interactions at the nano- and microscale, as these are mediated by viscous, overdamped fields described by low Reynolds number hydrodynamics [42]. It represents a form of dissipative coupling, as it can be understood as arising from taking the overdamped limit of full Langevin dynamics in the presence of a friction force on phase ϕ_α going as $f_\alpha = -\sum_{\beta=1}^2 Z_{\alpha\beta} \dot{\phi}_\beta$, where $Z \equiv M^{-1}$ is a friction tensor. As an example, we show in the Supplemental Material how (1) can be derived from a microscopic model of two rotors that are hydrodynamically coupled (see Fig. 1(c-d)) [43]. In this case, the coupling h is exactly constant, and its magnitude and sign are governed by the rotation rate and chirality of the rotors. In a similar way, one can derive coupled phase equations for enzymes that undergo conformational changes (Fig. 1(a-b)), where they reduce to exactly the same form but with a phase-dependent coupling constant $h(\phi_1, \phi_2)$ which moreover leads to multiplicative noise [15].

The potentials are chosen to be tilted washboard potentials of the form $V_\beta(\phi_\beta) = -F_\beta \phi_\beta - v_\beta \cos(\phi_\beta + \delta_\beta)$, where the shift $\delta_\beta = \arcsin(F_\beta/v_\beta)$ ensures that the minima of the potential are located at multiples of 2π and does not otherwise affect the phase dynamics. The maxima of the potential are located at $\phi_\beta^{\text{max}} \equiv \pi - \arcsin(F_\beta/v_\beta) \pmod{2\pi}$. The parameters F_β and v_β can be mapped to the energy barrier and the energy released per step [Fig. 1(d)] as $E_{\text{ba}\beta} = [2\sqrt{1 - (F_\beta/v_\beta)^2} - (F_\beta/v_\beta)(\pi - 2\delta_\beta)]v_\beta$ and $E_{*\beta} = 2\pi F_\beta$. In the following, except where noted, we focus on the case of equal self-mobilities $\mu_1 = \mu_2 = \mu$, equal energy barriers $E_{\text{ba}1} = E_{\text{ba}2} = E_{\text{ba}}$, and strongly driven dynamics $E_{*1} \gg E_{\text{ba}}$ (we fix $E_{\text{ba}}/E_{*1} = 3 \cdot 10^{-4}$). Choosing a mobility scale μ_0 and an energy scale E_0 , which together define a timescale $(\mu_0 E_0)^{-1}$, only three dimensionless parameters remain: E_{*2}/E_{*1} , which governs the asymmetry in the nonequilibrium driving of the two processes

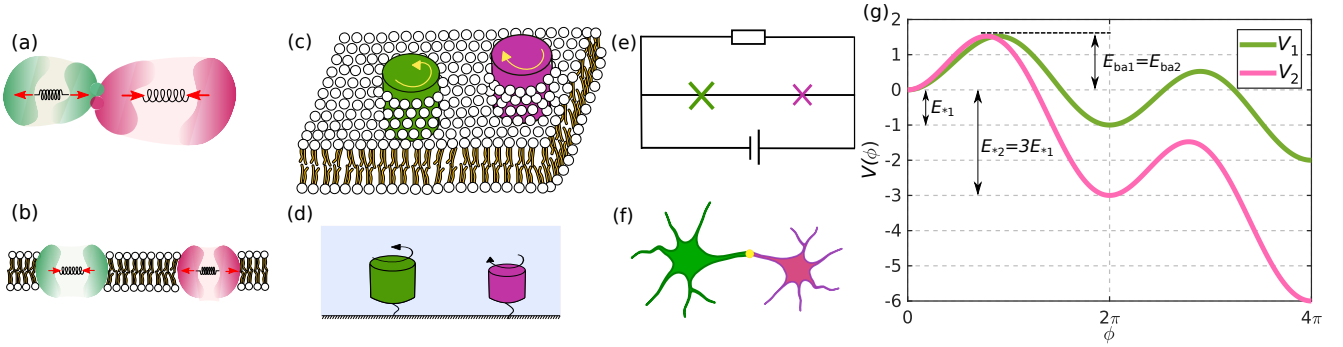


FIG. 1. (a–f) Examples of coupled noise-activated oscillators: (a) Two enzymes attached to each other forming an oligomeric complex, (b) Two membrane channels interacting with each other via the intervening viscous medium, (c) Two rotating inclusions in a membrane, (d) Two molecular rotors interacting hydrodynamically, (e) A circuit with two Josephson junctions, (f) Two excitable neurons interacting through a synapse. (g) The internal phase ϕ of each oscillator experiences a driving force represented by a tilted washboard potential, with a noise-activated oscillation corresponding to the phase advancing by the amount of 2π by crossing the energy barrier. In the case of enzymes, the potential represents the free energy of a (repeated) catalytic reaction.

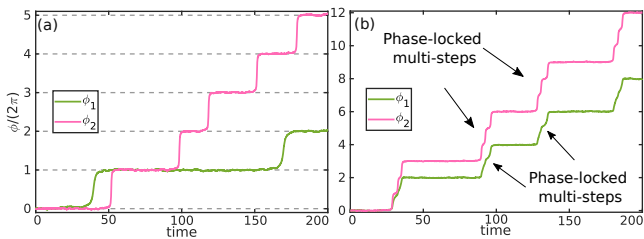


FIG. 2. Examples of stochastic trajectories for asymmetry $E_{*2}/E_{*1} = 5$ and noise strength $k_B T/E_{ba} = 1$. (a) In the absence of coupling, $h = 0$, only a few, independent single steps are observed. (b) With coupling, $h = 0.33$, a much larger overall number of steps is observed in the same time period, and moreover both phases move in tandem, in phase-locked, multi-step bursts. Time is given in units of $(\mu\nu_1)^{-1}$.

and we take to be ≥ 1 (i.e. oscillator 2 is more strongly driven than oscillator 1); h , which defines the strength of the dissipative coupling; and $k_B T/E_{ba}$, which defines the strength of the noise.

Stochastic trajectories

We briefly present the phenomenology observed in stochastic simulations of the equations of motion, (1), when the dissipative coupling is switched on (Fig. 2). In the absence of coupling, as expected, the trajectories are independent, and consist of single steps representing noise-activated crossings of the energy barriers in the potential, separated by long periods of time in which the phases are resting at the minima of the potential [see Fig. 1(d)]. With sufficiently large positive coupling, on the other hand, we observe that when the system is pushed out of the resting state, both oscillators advance at the same time, and moreover multiple steps occur as

a result of a single fluctuation. This results in an overall enhanced average speed of the oscillators. In contrast to what was observed for identical oscillators [15, 16], the oscillators here do not appear to be synchronized, but there are signatures of phase locking, where ϕ_1 advances n_1 steps while ϕ_2 advances n_2 steps with a reproducible ratio $n_1 : n_2$, in this example 2:3.

Importantly, this behavior is apparent even at very low values of the noise. This suggests that, as in the case of identical oscillators [15, 16], the phase locking phenomenology may be a consequence of bifurcations occurring in the underlying deterministic dynamical system.

Finite phase locking

We start by analyzing the phase portraits in (ϕ_1, ϕ_2) space corresponding to the deterministic part of (1). Because the dynamics are 2π -periodic, this dynamical system is defined on the torus. Notice that the system always has four fixed points: a stable fixed point at $(0,0)$, corresponding to both oscillators being at a minimum of their potential energy; an unstable fixed point, at $(\phi_1^{\max}, \phi_2^{\max})$ when both are at a maximum; and two saddle points at $(\phi_1^{\max}, 0)$ and $(0, \phi_2^{\max})$, when one oscillator is at a minimum and the other at a maximum. Because of the structure of (1), the location and character of these fixed points is independent of the strength of the coupling. In particular, this means that local bifurcations (where fixed points split or merge and change character) are impossible. Any bifurcation in this system must be *global*, arising from a change in topology of the network of heteroclinic and homoclinic orbits connecting these four fixed points [44].

Phase portraits for weak driving force asymmetry $E_{*2}/E_{*1} = 5$ and several values of the coupling h are

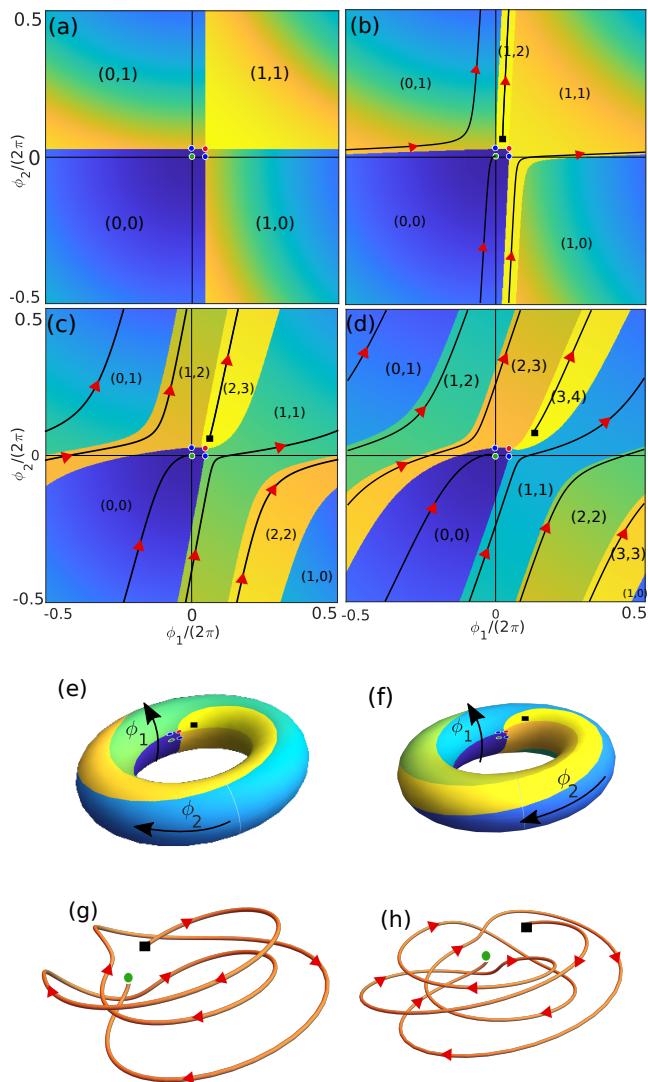


FIG. 3. Phase portraits of the deterministic dynamics for weak asymmetry $E_{*2}/E_{*1} = 5$ and various values of the coupling h . (a) (1,1) topology for $h = 0$. (b) (1,2) topology for $h = 0.05$. (c) (2,3) topology for $h = 0.19$. (d) (3,4) topology for $h = 0.33$. In all panels the green, red, and blue circles respectively correspond to the stable, unstable, and saddle fixed points of the dynamics. An example trajectory, starting at the black square and finishing at the stable fixed point, is shown in (b)–(d). The phase portraits in (c,d) are represented on the torus in (e,f). The example trajectories in (c,d) are represented as three-dimensional trajectories around the torus in (g,h). The colormap in (a)–(f) and the labels (m, n) in (a)–(d) are explained in the text.

shown in Fig. 3. The labels (m, n) are *winding number pairs*, describing how many times a trajectory starting in that region will wind around the torus along each dimension before reaching the stable fixed point. Equivalently, if the torus were to be unwrapped and tiled onto

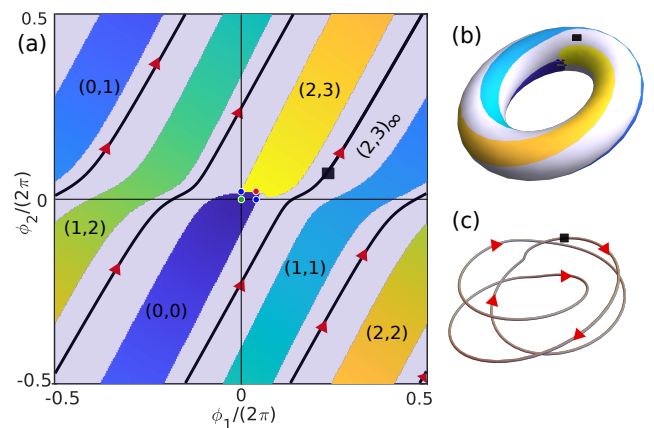


FIG. 4. (a) Phase portrait for strong asymmetry $E_{*2}/E_{*1} = 19.15$ and $h = 0.51$, demonstrating a $(2, 3)_\infty$ TPL state, and (b) its projection on a torus. The running band is shown in gray. The black line crossing through the black square (shown as a reference point) is an example of a periodic orbit within the running band, and is depicted in (c) as a three-dimensional loop around the torus, which forms a trefoil knot.

the plane, the stable fixed point reached when starting from that region in the phase portrait would be located at $(\phi_1, \phi_2) = (2\pi m, 2\pi n)$. In the same vein, every point of the phase portrait (except those at heteroclinic orbits, which connect the unstable fixed point to the saddle points) has been colored according to the Euclidean distance between the point in question and the fixed point (for an unwrapped torus) that a trajectory starting at that point would reach. Thus, yellow corresponds to longer trajectories towards the fixed point, whereas blue corresponds to shorter trajectories.

In the planar phase portraits [Fig. 3(a)–(d)], regions with different winding number appear separated from each other by the heteroclinic orbits. However, on the surface of the torus [Fig. 3(e)–(f)], one can appreciate that the region enclosed by the heteroclinic orbits is still simply connected, covers the whole torus, and corresponds to the basin of attraction of the stable fixed point. With increasing coupling, we observe a series of global bifurcations in the heteroclinic network, which change the maximal winding numbers that are possible from e.g. (1,1) in the absence of coupling [Fig. 3(a)] to (3,4) for coupling $h = 0.33$ [Fig. 3(d)]. This higher winding implies that the basin of attraction becomes a narrower and narrower strip, which winds around the torus an increasing number of times given by the highest winding number pair.

These bifurcations are responsible for the phenomenology observed in the stochastic simulations of Fig. 2, which we term *finite phase locking*. Indeed, let us take the phase portraits in Fig. 3(a,d) as an example. In the presence of fluctuations, a system initially located at the stable fixed point will typically be kicked by noise over either of the

saddle points. In the absence of coupling, Fig. 3(a), this implies that the system enters either the (1,0) or the (0,1) basin, so that just one of the oscillators undergoes a single step. With coupling, Fig. 3(d), the system instead enters the (2,3) or the (1,1) basin, resulting in a finite number of steps taken in tandem by the two enzymes. Note that, typically, one of the two saddle points will be more easily reachable and thus traversed much more frequently than the other [45, 46]. It is also important to note that, although the maximal winding number pair in Fig. 3(d) is (3,4), observing a (3,4) transition in the stochastic system should be rare, as the system will typically escape the stable fixed point through one of the saddle points, and not through the unstable point. In this particular case, the stochastic simulations in Fig. 2(b) confirm that the $(0, \phi_2^{\max})$ saddle point is preferred, as all the stochastic transitions observed lead to a (2,3) transition. The time-course of a (2,3) stochastic transition is shown on top of the corresponding deterministic phase portrait in Movie S1.

Topological phase locking

For sufficiently strong driving force asymmetry, at specific values of the parameters belonging to a subset of codimension 1 in parameter space, we find phase portraits that are qualitatively different, see Fig. 4. The topology of the heteroclinic network changes, resulting in the formation of two homoclinic orbits that connect each of the two saddle points to itself. As a consequence, the phase space becomes disconnected into two regions: the basin of attraction of the stable fixed point, and a band of periodic orbits (in grey in Fig. 4). We refer to this phenomenon as topological phase locking (TPL).

Importantly, a nontrivial winding number pair can also be assigned to the running band region. In the particular example of Fig. 4, we observe that a periodic orbit (and, by extension, the running band region as a whole) winds two times along the ϕ_1 direction and three times along the ϕ_2 direction before closing in on itself, implying a winding number pair which we denote as $(2, 3)_\infty$ in analogy with the notation for winding number pairs introduced above, where the ∞ subscript indicates that the trajectories are periodic and never reach a fixed point.

An example of a periodic trajectory within the running band is shown in Fig. 4(a), with the three-dimensional view of its projection on a torus shown in Fig. 4(c). It is interesting to note that the loop formed by the trajectory corresponds to a trefoil knot which, naturally, belongs to the class of torus knots (knots that lie on the surface of a torus) [38].

TPL has very strong consequences in the stochastic dynamics. In the presence of fluctuations, a system initially located at the stable fixed point will now be kicked by noise over either of the saddle points and fall into the

running band. The phases ϕ_1 and ϕ_2 will then advance deterministically, in the ratio given by the corresponding winding number pair, until a sufficiently strong fluctuation kicks the system out of the running band and back into the stable fixed point. The average speed of the oscillations can therefore be greatly enhanced by the presence of a running band. The time-course of a stochastic multi-step run in a $(2, 3)_\infty$ TPL state is shown on top of the corresponding deterministic phase portrait in Movie S2.

Phase-locking diagram

To understand how and where these different phase portrait topologies emerge in parameter space, as well as the global bifurcations that connect them, we scanned the parameter space as a function of driving force asymmetry E_{*2}/E_{*1} and coupling strength h . The topologies of phase portraits with finite phase locking were identified by means of the highest winding number pair (m, n) , whereas those corresponding to TPL were identified using the winding number pair $(m, n)_\infty$ of their running band.

The resulting phase-locking diagram, shown in Fig. 5, demonstrates an incredibly rich structure of bifurcations in the system. Note that the colors in the diagram correspond to the logarithmic value of the second number n in the winding number pair (m, n) , with blue corresponding to low numbers and red to high numbers. We find a variety of regions corresponding to phase portraits with finite phase locking with different winding numbers. Most interestingly, however, we observe a number of dark red branches or resonances at which the winding numbers very sharply peak as we vary E_{*2}/E_{*1} and/or h and cross through the resonance. At the very center of these resonances, in a lower-dimensional manifold of codimension 1, we find the phase portraits with TPL (TPL states).

To better understand the bifurcation structure, let us focus on the $(1, 2)_\infty$ TPL state, which is the first one to appear as the coupling h is increased. Suppose we begin at the dot marked (2, 5) to the left of the TPL state in Fig. 5, which corresponds to finite phase locking. As we increase h , we first observe a bifurcation to (3, 7), i.e. the maximal winding numbers increase by (1, 2). With a further increase of h , we observe a bifurcation to (4, 9), again by an increment of (1, 2). As we increase h further, we keep undergoing more and more of these bifurcations, effectively climbing up an infinite ladder of the form $(2, 5) + n \times (1, 2)$ with $n = 0, 1, 2, \dots, \infty$. After only a finite increase in h up to a critical value h_∞ , the system has undergone an infinite number of these bifurcations and reaches a TPL state $\lim_{n \rightarrow \infty} [(2, 5) + n \times (1, 2)] = (1, 2)_\infty$, i.e. a phase portrait with running band emerges. When h is further increased beyond h_∞ , we now descend down a different infinite ladder, out of step with the first one, of the form $(4, 7) + n \times (1, 2)$ with $n = \infty, \dots, 2, 1, 0$. The

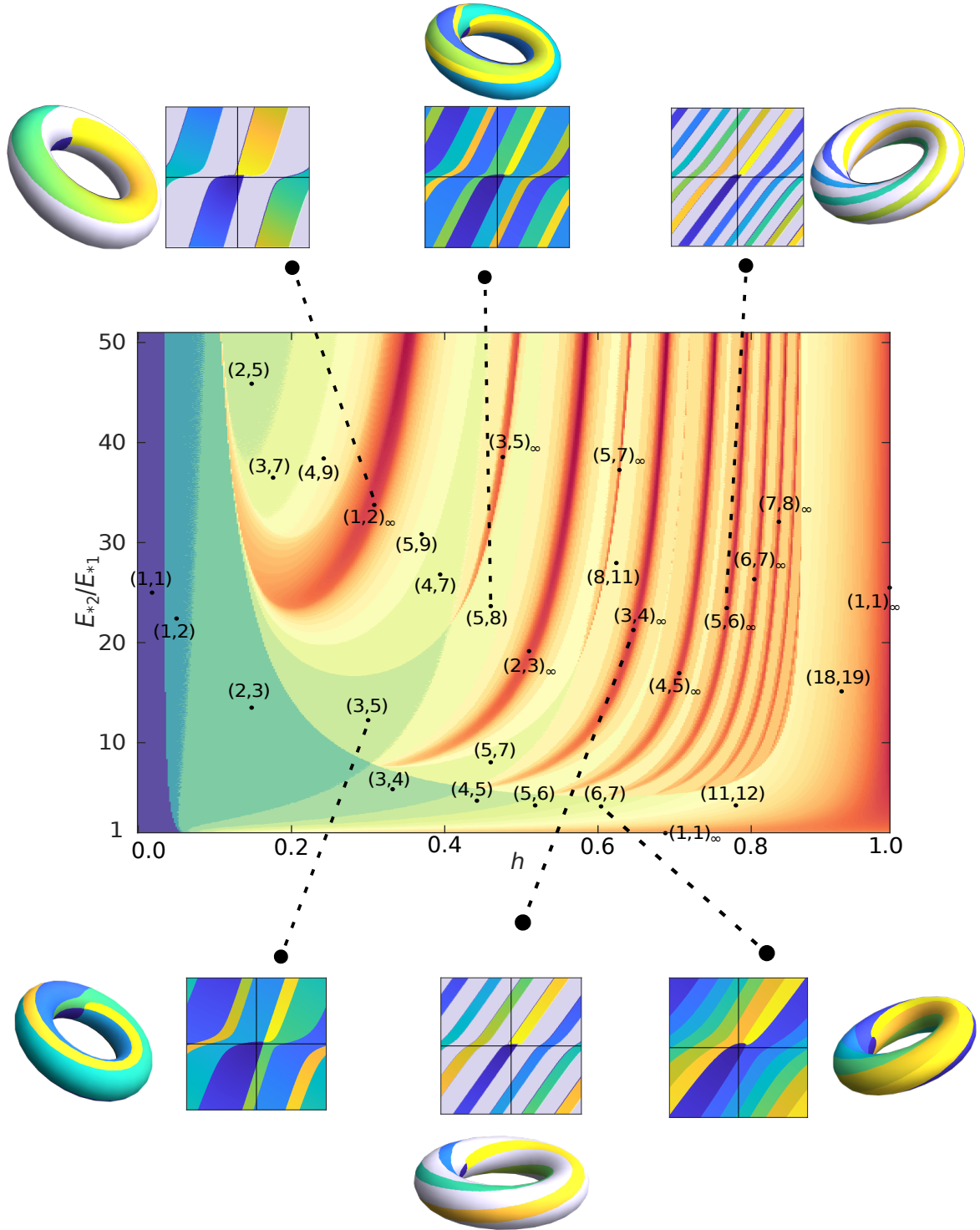


FIG. 5. Phase-locking diagram as a function of the coupling strength h and the driving force asymmetry E_{*2}/E_{*1} . The logarithmic colormap indicates the maximum winding of the second oscillator, and is used to differentiate the different phase portrait topologies that emerge. The labels indicate the topology in the region marked by the black dots. Selected examples of phase portraits are shown on a two-dimensional projection and on the torus.

system thus ultimately reaches the finite phase locking topology (4, 7). A further increase of h now takes us into the range of influence of the $(3, 5)_\infty$ TPL state, so that the system begins to climb up a new ladder and bifurcates to a $(4, 7) + (3, 5) = (7, 12)$ topology, and so on and so forth. An example of how the phase portraits change as one moves across the $(2, 3)_\infty$ TPL state is shown in SI Fig. S1.

A number of phase portraits for different points on the phase-locking diagram is shown in the insets of Fig. 5, and more examples are shown in SI Fig. S2 and SI Fig. S3. In particular, a number of phase portraits displaying TPL are included. Just like the $(2, 3)_\infty$ trajectory in Fig. 4, periodic trajectories inside these running bands form torus knots. Such knots are defined by a tuple (q, p) where q, p are coprime to each other and characterize the winding along the two axis of the torus [38]. For all $(m, n)_\infty$ topologies that we have observed, m and n were indeed coprime, suggesting that the TPL states correspond to various torus knots. Torus-knot trajectories have been found in the past in soliton equations, for instance in the non-linear Schrödinger equation [47]. Our system provides a new example of a non-linear dynamical system which can give rise to such mathematical structures.

The phase-locking diagram in Fig. 5 bears some resemblance to the well-known Arnold tongues describing phase locking in a number of other systems [34, 48–50]. However, the resemblance is only superficial: in fact, while in the case of Arnold tongues the key parameter controlling phase-locking ratios is the frequency asymmetry and the coupling merely acts to broaden the phase-locking regions, here the opposite is true. The main parameter controlling the phase-locking ratios is the coupling h , and the very limited amount of broadening of the phase-locking regions originates from the driving asymmetry E_{*2}/E_{*1} . Besides this clear operational difference, the context here is entirely different, as we are still dealing with noise-activated dynamics – although the coexistence of a running band and a stable fixed point leads to a coexistence of dissipative and effectively conservative/deterministic dynamics [17].

Lastly, it is worth commenting on the role of symmetry. Interestingly, the TPL state $(1, 1)_\infty$ occurs in two very particular lower dimensional manifolds, namely on the manifold defined by $E_{*2}/E_{*1} = 1$ and $h > h_*$, and on the manifold defined by $h = 1$ (maximum coupling allowed by positive-definiteness of the mobility matrix). This explains the results of Ref. 15 and Ref. 16, which dealt with symmetric oscillators and observed $(1, 1)_\infty$ topologies for all values of the coupling above a critical value h_* . This appears to be a special feature of the symmetric case, as in the general case studied here we find that TPL states only occur at discrete values of the coupling strength.

For the sake of completeness, we have calculated analogous phase-locking diagrams for other choices of system parameters, see SI Fig. S4 and SI Fig. S5. The overall

qualitative features are unchanged.

Signatures of TPL in the stochastic dynamics

In order to ascertain whether the TPL states in Fig. 5 have an effect on the stochastic dynamics in the presence of noise, we now quantify the long-time behavior of our stochastic simulations. In particular, we will measure the average speed Ω_α and diffusion coefficient D_α of each oscillator ($\alpha = 1, 2$), and the correlation C between the two oscillators. Defining $\delta\phi_\alpha(\tau; t) \equiv \phi_\alpha(t + \tau) - \phi_\alpha(t)$, we calculate the average speed of oscillator α as

$$\langle \delta\phi_\alpha(\tau; t) \rangle_t \underset{\tau \rightarrow \infty}{\sim} \Omega_\alpha \tau, \quad (2)$$

where the operator $\langle \dots \rangle_t$ denotes a time average over a long simulation. The diffusion coefficient is similarly calculated as

$$\langle [\delta\phi_\alpha(\tau; t) - \langle \delta\phi_\alpha(\tau; t) \rangle_t]^2 \rangle_t \underset{\tau \rightarrow \infty}{\sim} 2D_\alpha \tau. \quad (3)$$

Finally, the correlation between oscillators is calculated as

$$\frac{\langle \prod_{\alpha=1,2} [\delta\phi_\alpha(\tau; t) - \langle \delta\phi_\alpha(\tau; t) \rangle_t] \rangle_t}{\sqrt{\prod_{\alpha=1,2} \langle [\delta\phi_\alpha(\tau; t) - \langle \delta\phi_\alpha(\tau; t) \rangle_t]^2 \rangle_t}} \underset{\tau \rightarrow \infty}{\sim} C, \quad (4)$$

and is bounded between -1 and 1 for perfectly anticorrelated and perfectly correlated processes, respectively.

We first considered the average speed Ω_α as a function of coupling strength for fixed values of the driving asymmetry [Fig. 6(a)], corresponding to horizontal cuts in the phase-locking diagram of Fig. 5. For small asymmetry, where there are no TPL states, the average speed of both oscillators increases monotonically with increasing coupling. The phenomenology is very different for strong asymmetry, where increasing the coupling strength takes the system through a series of TPL states. At each of these, we find that the average speed of the coupled slow-fast oscillators sharply peaks. Thus, the presence of a running band strongly enhances the average speed of the oscillators.

An analogous behavior is observed for the diffusion coefficients D_α , with a monotonic increase in the absence of TPL states at weak driving force asymmetry, and very sharp peaks when TPL states are crossed at strong driving force asymmetry [Fig. 6(b)]. In analogy with the standard giant diffusion observed for single oscillators at the threshold of noise-activated and deterministic dynamics [39], the giant diffusion for TPL states can be understood as a consequence of the bistability that arises in systems with a running band, which stochastically switch between dissipative dynamics that keep the system at the stable fixed point, and quasi-deterministic dynamics when the system is within the running band [16].

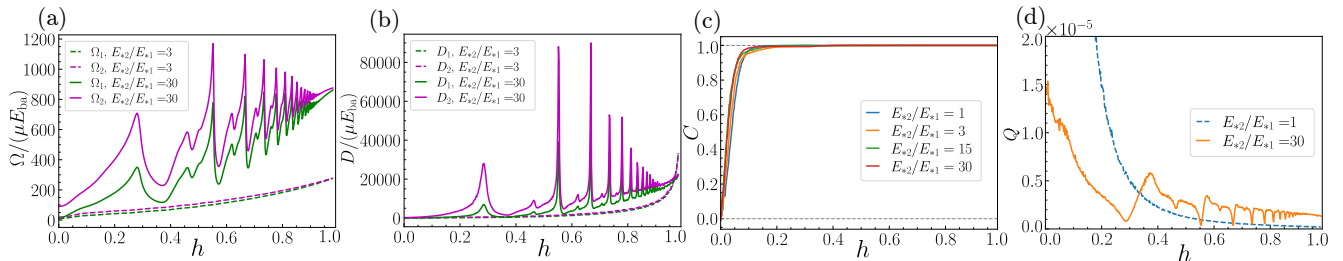


FIG. 6. Signatures of TPL states in the stochastic simulations, appearing as a function of the coupling strength h . (a) Average speed and (b) diffusion coefficient of the oscillators for weak and strong driving force asymmetry. Peaks are observed as the resonances are crossed for strong asymmetry. (c) The correlation between oscillators rapidly grows independently of the driving force asymmetry. (d) Quality factor quantifying the stochastic thermodynamics of precision (Eq. (5)). The quality factor drops as the resonances are crossed.

We also note that, independently of the amount of driving force asymmetry, the correlation C quickly grows with increasing coupling, and for $h \gtrsim 0.1$ saturates to $C \approx 1$ indicating perfect correlation between the oscillators, see Fig. 6(c). Indeed, from the topology of the deterministic phase portraits, we expect the dynamics of the oscillators to become correlated for any topology other than the trivial topology (1,1), which is present only at very low h independently of the driving force asymmetry.

Lastly, we consider the stochastic thermodynamics of the two coupled processes [51]. In particular, the thermodynamic uncertainty relation (TUR) [4] shows that energy dissipation (or entropy production) puts a fundamental lower bound to the precision of a nonequilibrium process. More precisely, the multidimensional TUR (MTUR) provides the bound $\mathcal{J}^T \mathcal{D}^{-1} \mathcal{J} \leq \dot{\sigma}/k_B$ at steady state, where $\dot{\sigma}$ is the entropy production rate, \mathcal{J} is any vectorial current, and \mathcal{D} is the diffusion matrix describing the fluctuations of the current [40].

In our two-oscillator system, we have $\mathcal{J}_\alpha = \Omega_\alpha$ and $\mathcal{D}_{\alpha\alpha} = D_\alpha$ for $\alpha = 1, 2$, as well as $\mathcal{D}_{12} = \mathcal{D}_{21} = C\sqrt{D_1 D_2}$. The MTUR can then be rewritten explicitly as

$$Q \equiv \frac{1}{1 - C^2} \left(\frac{\Omega_1^2}{D_1} - \frac{2C\Omega_1\Omega_2}{\sqrt{D_1 D_2}} + \frac{\Omega_2^2}{D_2} \right) \frac{k_B}{\dot{\sigma}} \leq 1 \quad (5)$$

where Q is a *quality factor*, equal to 1 when the bound is saturated (the precision is as high as thermodynamically allowed) and 0 for a purely diffusive process. The entropy production $\dot{\sigma}$ can be calculated from the steady state dissipation $\dot{\sigma}T = F_1\Omega_1 + F_2\Omega_2$.

The behavior of the quality factor Q as a function of the coupling strength h for both weak and strong driving force asymmetries is shown in Fig. 6(d). The fact that for strong asymmetry the system crosses through various TPL states with increasing h is clearly signalled in the stochastic thermodynamics of precision. In particular, we see that Q strongly decreases at each TPL state, which may be counter-intuitive considering that the average speed peaks at these states [Fig. 6(a)]. However,

note that the diffusion coefficient also strongly peaks at the TPL states [Fig. 6(b)], more sharply than the average speed, so that the quality factor ultimately decreases at the TPL states.

Outlook

Besides the obvious interest from the point of view of dynamical systems theory, we anticipate that our results may find practical applications in a variety of systems. In particular, we previously showed how a dissipative coupling arises when two enzymes that undergo conformational changes during their chemical reactions are in proximity of, or mechanically linked to, each other [15]. We hypothesize that the rate enhancements afforded by TPL states could be exploited by enzymes that form heterodimers (that is, complexes of two distinct enzymes) in order to boost the catalytic activity of the slower enzyme. Indeed, some heterodimeric enzymes show higher activity than what could be achieved by the two individual enzymes alone [52, 53]. The same kind of rate enhancement could be present in clusters of transmembrane protein channels [19] and rotors [20–23], as well as in groups of kinesins and dyneins walking on the same microtubule [54], or different myosins exerting contractile forces on nearby actin filaments [55]. Alternatively, TPL states may be targeted in engineered systems whose dissipative coupling and driving force asymmetry can be experimentally controlled, such as superconducting Josephson junction arrays [17, 26], laser cavities [30, 31] or optomechanical devices [32, 33].

METHODS

Stochastic simulations

To integrate the stochastic differential equations, Eq. (1), we employed the Euler-Maruyama method using a custom code written in the Julia language [56].

Time was nondimensionalized as $\tilde{t} = \mu_1 v_1 t$. For the results in Fig. 6, a time step $d\tilde{t} = 10^{-2}$ was used, with the total number of steps equal to 10^9 and the number of samples equal to 10^6 . We also averaged over 10 different runs. More detailed information on how the observables in Eqs. (2)–(4) were calculated can be found in the supplementary information of Ref. 16.

Phase portraits

To generate phase portraits, we integrated the deterministic equations of motion (corresponding to Eq. (1) without the noise term) using the built-in *ode45* integrator in MATLAB [57], which employs a 4th order Runge-Kutta method. A 301×301 grid of initial points in the interval $-\pi < \phi_{1,2} < \pi$ was used, and we integrated the trajectories up to a maximum integration time $t_{\max} = 100$. The final points were then used to identify the winding number (m, n) if the trajectory reached a stable fixed point, or $(m, n)_\infty$ if the trajectory was found to be periodic and thus to lie on a running band.

ACKNOWLEDGEMENTS

We acknowledge support from the Max Planck School Matter to Life and the MaxSynBio Consortium which are jointly funded by the Federal Ministry of Education and Research (BMBF) of Germany and the Max Planck Society.

* ramin.golestanian@ds.mpg.de

† j.agudo-canalejo@ucl.ac.uk

- [1] M. O. Magnasco, Molecular combustion motors, *Phys. Rev. Lett.* **72**, 2656 (1994).
- [2] F. Jülicher, A. Ajdari, and J. Prost, Modeling molecular motors, *Reviews of Modern Physics* **69**, 1269 (1997).
- [3] Y. Cao, H. Wang, Q. Ouyang, and Y. Tu, The free-energy cost of accurate biochemical oscillations, *Nat. Phys.* **11**, 772–778 (2015).
- [4] A. C. Barato and U. Seifert, Thermodynamic uncertainty relation for biomolecular processes, *Phys. Rev. Lett.* **114**, 158101 (2015).
- [5] J. M. Horowitz and T. R. Gingrich, Thermodynamic uncertainty relations constrain non-equilibrium fluctuations, *Nat. Phys.* **16**, 15–20 (2019).
- [6] J. J. Hopfield, Kinetic proofreading: A new mechanism for reducing errors in biosynthetic processes requiring high specificity, *Proc. Natl. Acad. Sci. U.S.A* **71**, 4135–4139 (1974).
- [7] A. Murugan, D. A. Huse, and S. Leibler, Speed, dissipation, and error in kinetic proofreading, *Proc. Natl. Acad. Sci. U.S.A* **109**, 12034–12039 (2012).
- [8] A. Klosin, F. Oltsch, T. Harmon, A. Honigmann, F. Jülicher, A. A. Hyman, and C. Zechner, Phase separation provides a mechanism to reduce noise in cells, *Science* **367**, 464–468 (2020).
- [9] D. Deviri and S. A. Safran, Physical theory of biological noise buffering by multicomponent phase separation, *Proc. Natl. Acad. Sci. U.S.A* **118** (2021).
- [10] J. A. Acebrón, L. L. Bonilla, C. J. Pérez Vicente, F. Ritort, and R. Spigler, The Kuramoto model: A simple paradigm for synchronization phenomena, *Rev. Mod. Phys.* **77**, 137 (2005).
- [11] J. Halatek and E. Frey, Rethinking pattern formation in reaction–diffusion systems, *Nat. Phys.* **14**, 507–514 (2018).
- [12] J. S. van Zon, D. K. Lubensky, P. R. H. Altena, and P. R. ten Wolde, An allosteric model of circadian KaiC phosphorylation, *Proc. Natl. Acad. Sci. U.S.A* **104**, 7420–7425 (2007).
- [13] D. Zhang, Y. Cao, Q. Ouyang, and Y. Tu, The energy cost and optimal design for synchronization of coupled molecular oscillators, *Nat. Phys.* **16**, 95–100 (2019).
- [14] R. Kubo, The fluctuation-dissipation theorem, *Rep. Prog. Phys.* **29**, 255–284 (1966).
- [15] J. Agudo-Canalejo, T. Adeleke-Larodo, P. Illien, and R. Golestanian, Synchronization and enhanced catalysis of mechanically coupled enzymes, *Phys. Rev. Lett.* **127**, 208103 (2021).
- [16] M. Chatzittofi, R. Golestanian, and J. Agudo-Canalejo, Collective synchronization of dissipatively-coupled noise-activated processes, *New J. Phys.* **25**, 093014 (2023).
- [17] K. Y. Tsang, R. E. Mirollo, S. H. Strogatz, and K. Wiesenfeld, Dynamics of a globally coupled oscillator array, *Phys. D* **48**, 102–112 (1991).
- [18] F. Hinzpeter, F. Tostevin, A. Buchner, and U. Gerland, Trade-offs and design principles in the spatial organization of catalytic particles, *Nat. Phys.* **18**, 203–211 (2021).
- [19] D. J. Bonthuis and R. Golestanian, Mechanosensitive channel activation by diffusio-osmotic force, *Phys. Rev. Lett.* **113**, 148101 (2014).
- [20] W. Junge and N. Nelson, ATP Synthase, *Annu. Rev. Biochem.* **84**, 631–657 (2015).
- [21] A.-K. Pumm, W. Engelen, E. Kopperger, J. Isensee, M. Vogt, V. Kozina, M. Kube, M. N. Honemann, E. Bertolin, M. Langecker, R. Golestanian, F. C. Simmel, and H. Dietz, A DNA origami rotary ratchet motor, *Nature* **607**, 492–498 (2022).
- [22] X. Shi, A.-K. Pumm, J. Isensee, W. Zhao, D. Verschuere, A. Martin-Gonzalez, R. Golestanian, H. Dietz, and C. Dekker, Sustained unidirectional rotation of a self-organized DNA rotor on a nanopore, *Nat. Phys.* **18**, 1105–1111 (2022).
- [23] X. Shi, A.-K. Pumm, C. Maffeo, F. Kohler, E. Feigl, W. Zhao, D. Verschuere, R. Golestanian, A. Aksimentiev, H. Dietz, and C. Dekker, A DNA turbine powered by a transmembrane potential across a nanopore, *Nat. Nanotechnol.* (2023).
- [24] C. Feillet, P. Krusche, F. Tamanini, R. C. Janssens, M. J. Downey, P. Martin, M. Teboul, S. Saito, F. A. Lévi, T. Bretschneider, G. T. J. van der Horst, F. Delaunay, and D. A. Rand, Phase locking and multiple oscillating attractors for the coupled mammalian clock and cell cycle, *Proc. Natl. Acad. Sci. U.S.A* **111**, 9828–9833 (2014).
- [25] M. Fang, A. G. Chavan, A. LiWang, and S. S. Golden, Synchronization of the circadian clock to the environment tracked in real time, *Proc. Natl. Acad. Sci. U.S.A* **120** (2023).

- [26] S. Watanabe and S. H. Strogatz, Constants of motion for superconducting josephson arrays, *Phys. D* **74**, 197–253 (1994).
- [27] E. Montbrió, D. Pazó, and A. Roxin, Macroscopic description for networks of spiking neurons, *Phys. Rev. X* **5**, 021028 (2015).
- [28] M. J. Grabowska, R. Jeans, J. Steeves, and B. van Swinderen, Oscillations in the central brain of drosophila are phase locked to attended visual features, *Proc. Natl. Acad. Sci. U.S.A* **117**, 29925–29936 (2020).
- [29] D. Matsunaga, J. K. Hamilton, F. Meng, N. Bukin, E. L. Martin, F. Y. Ogrin, J. M. Yeomans, and R. Golestanian, Controlling collective rotational patterns of magnetic rotors, *Nat. Commun.* **10** (2019).
- [30] A. Politi, G. L. Oppo, and R. Badii, Coexistence of conservative and dissipative behavior in reversible dynamical systems, *Phys. Rev. A* **33**, 4055 (1986).
- [31] J. Ding and M.-A. Miri, Mode discrimination in dissipatively coupled laser arrays, *Opt. Lett.* **44**, 5021 (2019).
- [32] Q. Zhang, C. Yang, J. Sheng, and H. Wu, Dissipative coupling-induced phonon lasing, *Proc. Natl. Acad. Sci. U.S.A* **119** (2022).
- [33] C. Yang, J. Sheng, and H. Wu, Anomalous thermodynamic cost of clock synchronization, arXiv preprint arXiv:2309.01974 (2023).
- [34] S.-B. Shim, M. Imboden, and P. Mohanty, Synchronized oscillation in coupled nanomechanical oscillators, *Science* **316**, 95–99 (2007).
- [35] E. A. Martens, S. Thutupalli, A. Fourrière, and O. Hallatschek, Chimera states in mechanical oscillator networks, *Proc. Natl. Acad. Sci. U.S.A* **110**, 10563–10567 (2013).
- [36] B. Lindner, Effects of noise in excitable systems, *Phys. Rep.* **392**, 321–424 (2004).
- [37] F. Dörfler, M. Chertkov, and F. Bullo, Synchronization in complex oscillator networks and smart grids, *Proc. Natl. Acad. Sci. U.S.A* **110**, 2005–2010 (2013).
- [38] C. C. Adams, *The knot book* (American Mathematical Soc., 1994).
- [39] P. Reimann, C. Van den Broeck, H. Linke, P. Hänggi, J. M. Rubi, and A. Pérez-Madrid, Giant acceleration of free diffusion by use of tilted periodic potentials, *Phys. Rev. Lett.* **87**, 010602 (2001).
- [40] A. Dechant, Multidimensional thermodynamic uncertainty relations, *J. Phys. A Math. Theor.* **52**, 035001 (2018).
- [41] S. R. De Groot and P. Mazur, *Non-equilibrium thermodynamics* (Courier Corporation, 2013).
- [42] S. Kim and S. J. Karrila, *Microhydrodynamics: principles and selected applications* (Courier Corporation, 2013).
- [43] S. K. Richter and A. M. Menzel, Mediated interactions between rigid inclusions in two-dimensional elastic or fluid films, *Phys. Rev. E* **105**, 014609 (2022).
- [44] S. Wiggins, *Global bifurcations and chaos: analytical methods*, Vol. 73 (Springer Science & Business Media, 2013).
- [45] J. Langer, Statistical theory of the decay of metastable states, *Ann. Phys. (N. Y.)* **54**, 258–275 (1969).
- [46] P. Hänggi, P. Talkner, and M. Borkovec, Reaction-rate theory: fifty years after kramers, *Rev. Mod. Phys.* **62**, 251 (1990).
- [47] R. L. Ricca, Torus knots and polynomial invariants for a class of soliton equations, *Chaos* **3**, 83–91 (1993).
- [48] A. Pikovsky, M. Rosenblum, and J. Kurths, *Synchronization: A Universal Concept in Nonlinear Sciences*, Cambridge Nonlinear Science Series (Cambridge University Press, 2001).
- [49] V. I. Arnold, Small denominators. I. Mapping the circle onto itself, *Izv. Akad. Nauk SSSR Ser. Mat* **25**, 21 (1961).
- [50] M. P. Juniper, A. V. Straube, R. Besseling, D. G. Aarts, and R. P. Dullens, Microscopic dynamics of synchronization in driven colloids, *Nat. Commun.* **6** (2015).
- [51] U. Seifert, Stochastic thermodynamics, fluctuation theorems and molecular machines, *Rep. Prog. Phys.* **75**, 126001 (2012).
- [52] M. J. Hehir, J. E. Murphy, and E. R. Kantrowitz, Characterization of Heterodimeric Alkaline Phosphatases from *Escherichia coli*: An Investigation of Intragenic Complementmentation, *J. Mol. Biol.* **304**, 645–656 (2000).
- [53] S. Lu, S. Li, and J. Zhang, Harnessing allostery: A novel approach to drug discovery, *Med. Res. Rev.* **34**, 1242–1285 (2014).
- [54] M. J. I. Müller, S. Klumpp, and R. Lipowsky, Tug-of-war as a cooperative mechanism for bidirectional cargo transport by molecular motors, *Proc. Natl. Acad. Sci. U.S.A* **105**, 4609–4614 (2008).
- [55] M. A. Hartman and J. A. Spudich, The myosin superfamily at a glance, *J. Cell Sci.* **125**, 1627–1632 (2012).
- [56] J. Bezanson, S. Karpinski, V. B. Shah, and A. Edelman, Julia: A fast dynamic language for technical computing, arXiv preprint arXiv:1209.5145 (2012).
- [57] T. M. Inc., *Matlab version: 9.14.0 (r2023a)* (2023).

Supplementary Information

DERIVATION OF THE PHASE EQUATIONS

We consider two non-identical rotors that are close to each other or even attached. To describe their rotating dynamics, we use the angle θ_1 and θ_2 which correspond to the angle of rotor 1 and 2. These rotors can self-rotate thanks to a driven internal cyclic process, representing a chemical reaction. The dynamics of this internal process is described using the phases ϕ_1 and ϕ_2 which are the phases that appear in the main text.

Firstly, to describe the dynamics of a single rotor ($i = 1, 2$) we consider the potential

$$U_i(\theta_i, \phi_i) = -k_i \cos(n_i \theta_i - \phi_i) + V_i(\phi_i) \quad (6)$$

with $V_i(\phi_i)$ being the washboard potential described in the main text, $V_i(\phi_i) = -F_i \phi_i - v_i \cos(\phi_i + \delta_i)$. The first term represents a “toothed gear” potential which provides the mechanochemical coupling, with strength k_i , between the rotation angle θ_i and the chemical process described by ϕ_i . We remind that a chemical reaction corresponds to ϕ advancing by 2π . The integer n_i thus describes how many reactions it takes to complete a full turn of the rotor, with its sign defining the direction or chirality of the rotation (clockwise or anticlockwise). For example, for a typical ATP synthase which rotates 120° per reaction [20], we have $n_i = \pm 3$.

The surrounding medium or substrate causes hydrodynamic interactions between the two rotors and this induces a coupling between the two. Therefore the dynamical equations in terms of the torques τ_1 and τ_2 are,

$$\dot{\theta}_1 = \mu_{\theta 1} \tau_1 + g \tau_2 \quad (7)$$

$$\dot{\theta}_2 = g \tau_1 + \mu_{\theta 2} \tau_2 \quad (8)$$

where $\mu_{\theta i}$ are rotational hydrodynamic self-mobilities, and g is the coupling from hydrodynamic interactions (cross-mobility) or from friction due to direct contact. For example, for a rotating disk, $\mu_{\theta} = 1/(4\pi\eta a^2)$, with a the radius of the disk and η the hydrodynamic viscosity. Typically, the value g is negative, and in the case of two interacting rotating disks is $g = -1/(8\pi\eta r)$ with r the distance between the two rotors [43]. The torques τ_i are derived directly from the potential $U_i(\theta_i, \phi_i)$, as $\tau_i = -\partial_{\theta_i} U_i(\theta_i, \phi_i) = -k_i n_i \sin(n_i \theta_i - \phi_i)$.

The equations for the internal phases are also derived directly from the potential, as

$$\dot{\phi}_i = -\mu_{\phi i} \partial_{\phi_i} U_i(\theta_i, \phi_i) = \mu_{\phi i} k_i \sin(n_i \theta_i - \phi_i) - \mu_{\phi i} V_i'(\phi_i) \quad (9)$$

where $\mu_{\phi i}$ is the mobility governing the overdamped dynamics of the reaction coordinate ϕ_i . Let us denote $\delta\theta_i \equiv n_i \theta_i - \phi_i$. By assuming strong mechanochemical coupling, i.e. that the timescale of angle relaxation $(k_i \mu_{\theta i})^{-1}$ is much shorter than the timescale for the changes in internal phase velocity, we simplify the dynamics since the angles will relax quickly and the dynamics will be dictated by the dynamics of the phases ϕ_i , which are the slow variables. Mathematically, this is equivalent to $\delta\dot{\theta}_i \simeq 0$, which implies that $\dot{\theta}_i \simeq \dot{\phi}_i / n_i$. Substituting this into (7)-(8), we can solve for $k_1 \sin \delta\theta_1$ and $k_2 \sin \delta\theta_2$ and introduce them into (9). Further solving for $\dot{\phi}_1$ and $\dot{\phi}_2$, we finally obtain the deterministic part of Eq. (1) in the main text, i.e.

$$\dot{\phi}_1 = \mu_1 [-V'(\phi_1)] + \sqrt{\mu_1 \mu_2} h [-V'(\phi_2)] \quad (10a)$$

$$\dot{\phi}_2 = \sqrt{\mu_1 \mu_2} h [-V'(\phi_1)] + \mu_2 [-V'(\phi_2)] \quad (10b)$$

with the coefficients

$$\mu_1 \equiv \mu_{\phi 1} \left(1 + \frac{\mu_{\theta 1} \mu_{\phi 2}}{n_1 n_2 (\mu_{\theta 1} \mu_{\theta 2} - g^2)} \right) \left(1 + \frac{\mu_{\theta 1} \mu_{\phi 2} + \mu_{\phi 1} \mu_{\theta 2} + \frac{\mu_{\phi 1} \mu_{\phi 2}}{n_1 n_2}}{n_1 n_2 (\mu_{\theta 1} \mu_{\theta 2} - g^2)} \right)^{-1}, \quad (11)$$

$$\mu_2 \equiv \mu_{\phi 2} \left(1 + \frac{\mu_{\phi 1} \mu_{\theta 2}}{n_1 n_2 (\mu_{\theta 1} \mu_{\theta 2} - g^2)} \right) \left(1 + \frac{\mu_{\theta 1} \mu_{\phi 2} + \mu_{\phi 1} \mu_{\theta 2} + \frac{\mu_{\phi 1} \mu_{\phi 2}}{n_1 n_2}}{n_1 n_2 (\mu_{\theta 1} \mu_{\theta 2} - g^2)} \right)^{-1}, \quad (12)$$

$$h \equiv \frac{g}{n_1 n_2} \frac{\sqrt{\mu_{\phi 1} \mu_{\phi 2}}}{\mu_{\theta 1} \mu_{\theta 2} - g^2} \left(1 + \frac{\mu_{\theta 1} \mu_{\phi 2}}{n_1 n_2 (\mu_{\theta 1} \mu_{\theta 2} - g^2)} \right)^{-\frac{1}{2}} \left(1 + \frac{\mu_{\phi 1} \mu_{\theta 2}}{n_1 n_2 (\mu_{\theta 1} \mu_{\theta 2} - g^2)} \right)^{-\frac{1}{2}}. \quad (13)$$

The corresponding noise term in Eq. (1) of the main text follows directly from requiring a fluctuation-dissipation relation.

Additionally making the reasonable assumptions that the mobility of the internal phase is smaller than the hydrodynamic mobility of the angle ($\mu_{\phi_i}/\mu_{\theta_i} \ll 1$), and that the hydrodynamic coupling is small ($g/\sqrt{\mu_{\theta_1}\mu_{\theta_2}} \ll 1$) we find that the coefficients to leading order in these ratios are

$$\mu_1 \simeq \mu_{\phi 1}, \quad \mu_2 \simeq \mu_{\phi 2}, \quad h \simeq \frac{g}{n_1 n_2} \frac{\sqrt{\mu_{\phi 1} \mu_{\phi 2}}}{\mu_{\theta 1} \mu_{\theta 2}}. \quad (14)$$

The sign of h depends on the signs of g , n_1 , and n_2 . Since in the case of hydrodynamic interactions g is negative, in order to obtain $h > 0$ we find that n_1 and n_2 must have opposite signs, that is, the rotors must rotate in opposite directions (with opposite chirality).

DESCRIPTION OF THE SUPPLEMENTARY MOVIES

We provide the following movies:

- **Movie 1:** An example of a stochastic $(2, 3)$ transition in a $(3, 4)$ finite phase locking topology. On the left panel, the evolution of the trajectory is shown on top of the phase portrait. On the right panel, the completed cycles are shown as a function of simulation time.
- **Movie 2:** An example of the stochastic dynamics on a $(2, 3)_\infty$ TPL topology. On the left panel, the evolution of the trajectory is shown on top of the phase portrait. On the right panel, the completed cycles are shown as a function of simulation time.

SUPPLEMENTARY FIGURES

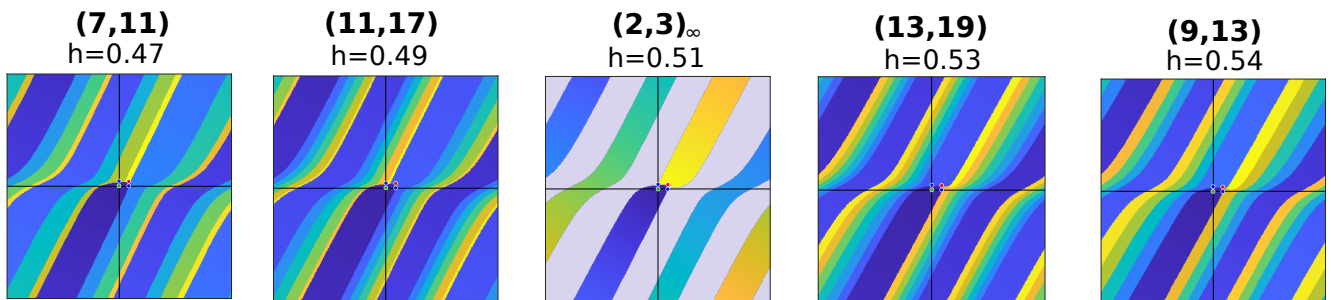


FIG. S1. Phase portraits as the system crosses through the $(2, 3)_\infty$ TPL state with increasing h . The driving force asymmetry is $E_{*2}/E_{*1} = 19.15$. In all cases, $E_{\text{ba}1}/E_{*1} = 3 \cdot 10^{-4}$.

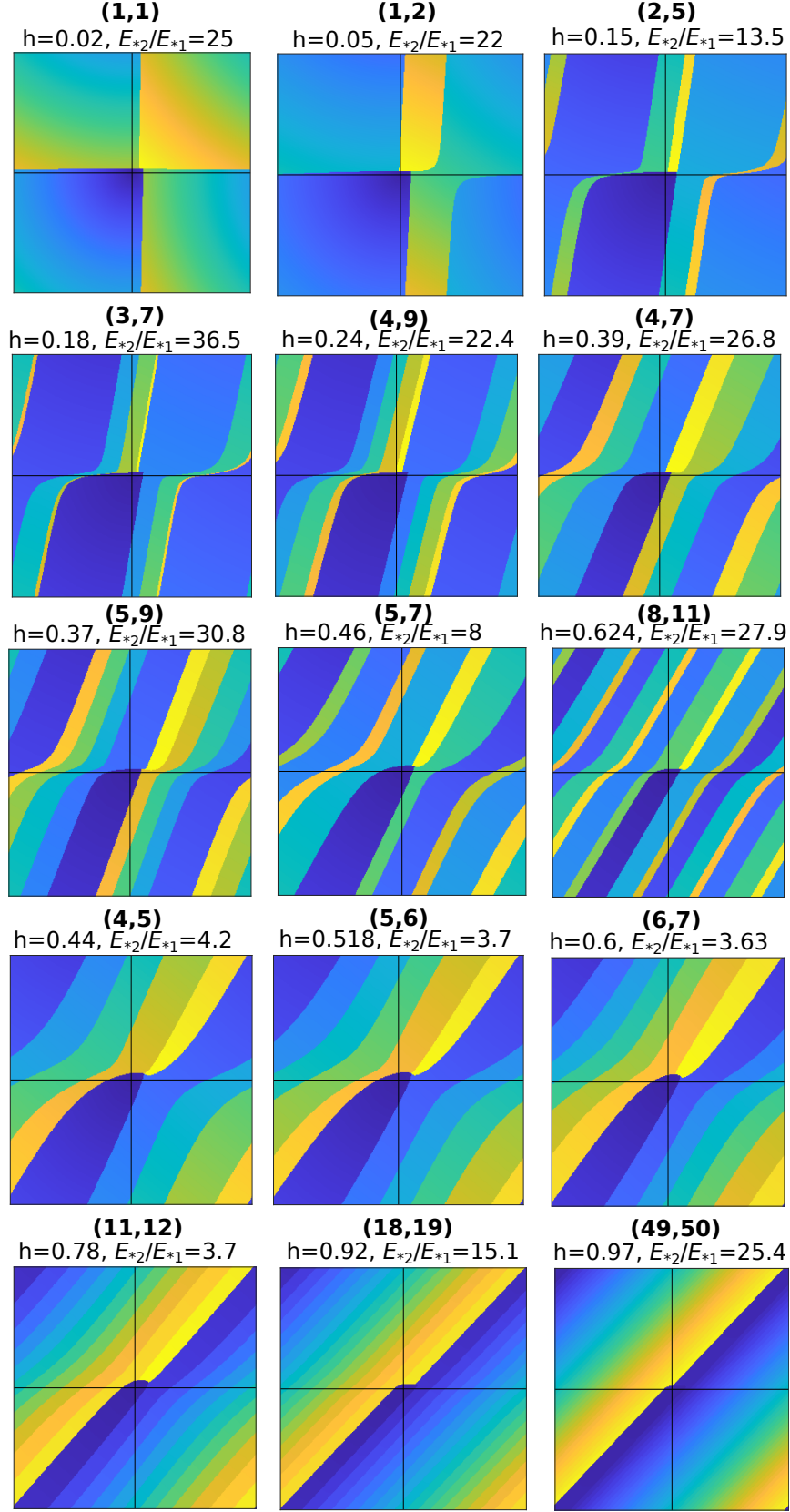


FIG. S2. Various phase portraits with finite phase locking. In all cases, $E_{ba1}/E_{*1} = 3 \cdot 10^{-4}$.

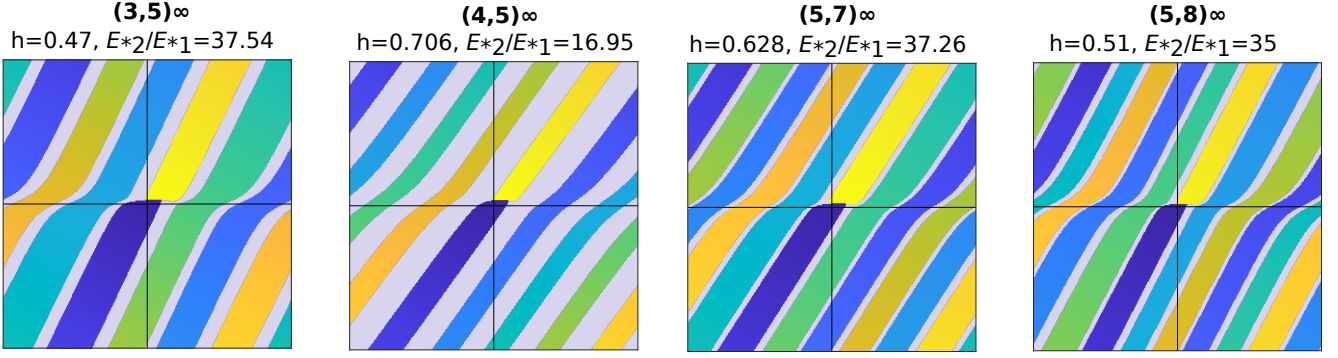


FIG. S3. Various TPL phase portraits. For the topologies $(3,5)_\infty$, $(4,5)_\infty$ and $(5,7)_\infty$, we used $E_{ba1}/E_{*1} = 3 \cdot 10^{-4}$. For the portrait $(5,8)_\infty$, we used $E_{ba1}/E_{*1} = 1 \cdot 10^{-4}$.

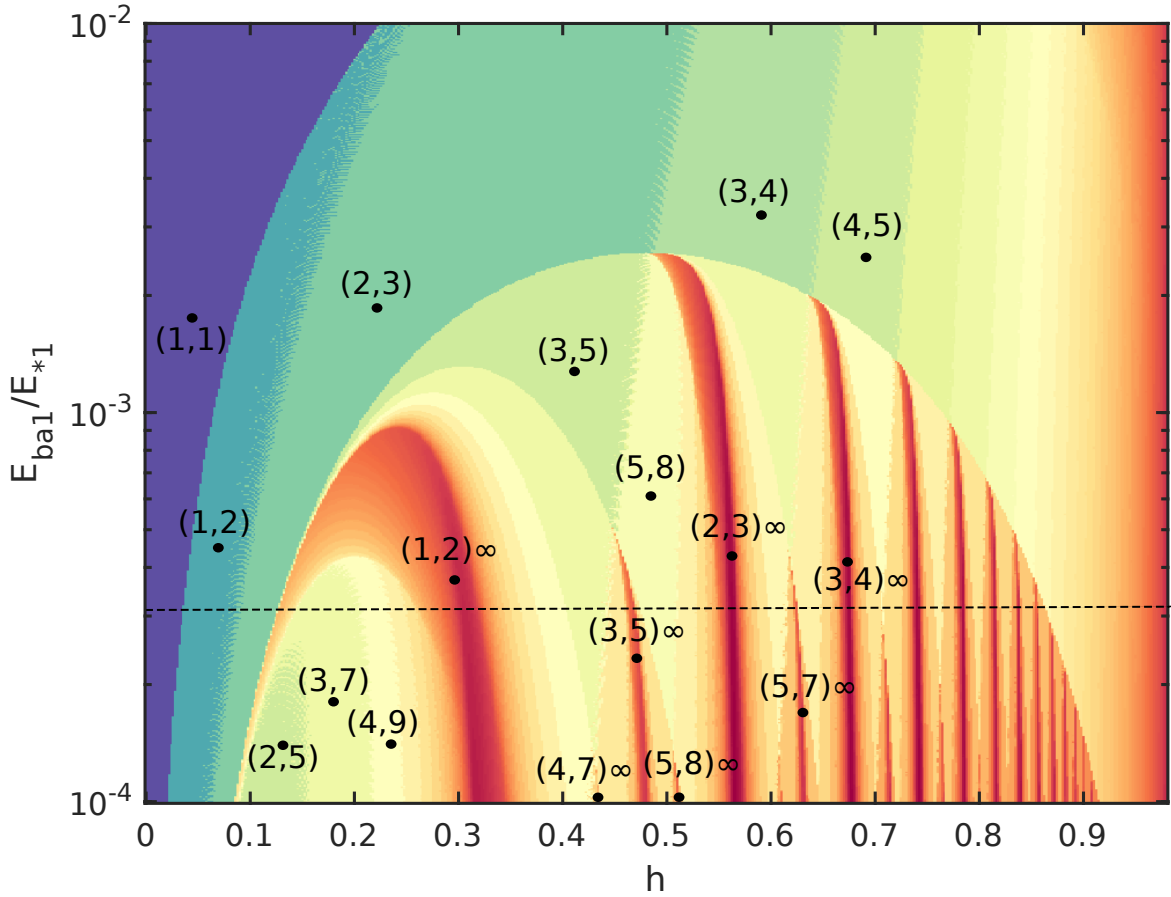


FIG. S4. Phase-locking diagram as a function of coupling strength h and E_{ba1}/E_{*1} , for fixed $E_{ba2}/E_{ba1} = 1$ and $E_{*2}/E_{*1} = 35$. The horizontal line corresponds to $E_{ba1}/E_{*1} = 3 \cdot 10^{-4}$ which was used throughout the main text.

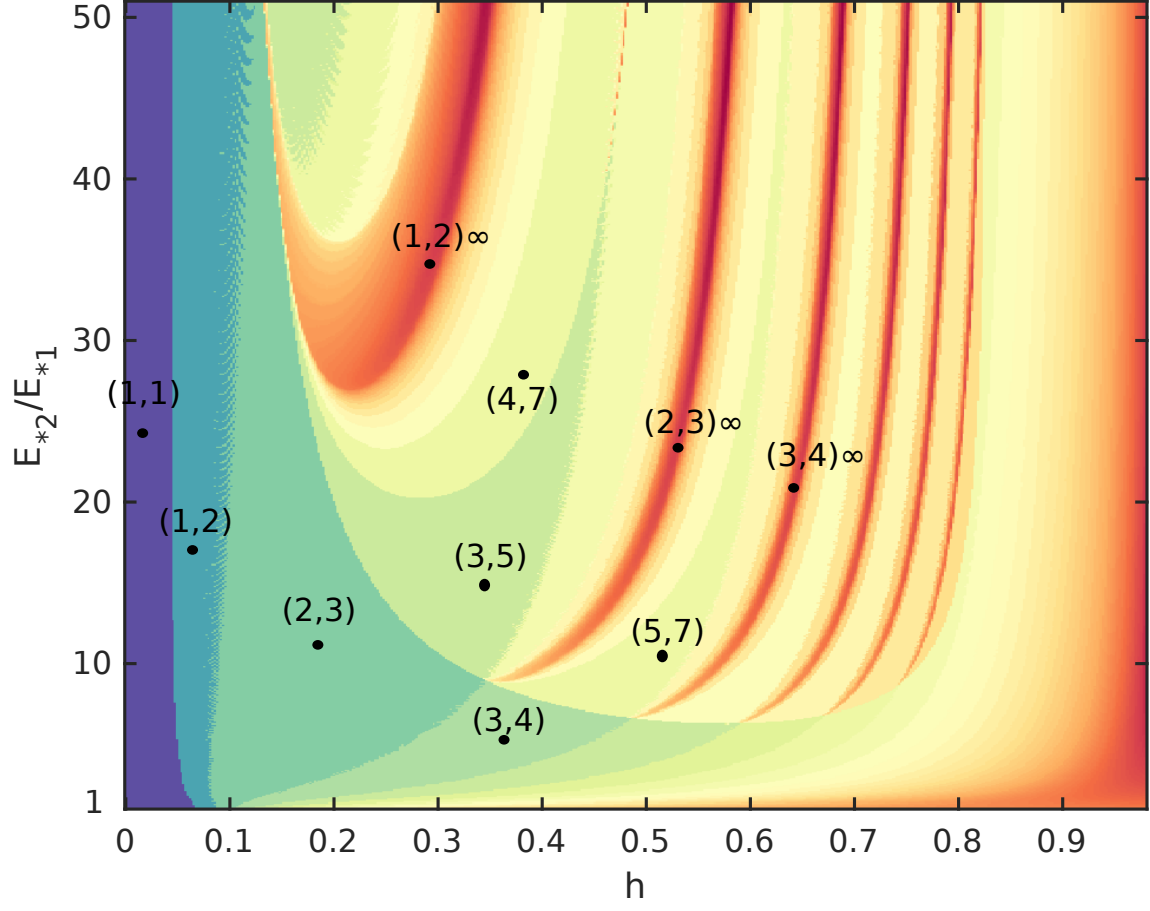


FIG. S5. Phase-locking diagram as a function of the coupling strength h and the driving force asymmetry E_{*2}/E_{*1} . In comparison with Fig. 5 in the main text, which used $E_{ba1}/E_{*1} = 3 \cdot 10^{-4}$ and $E_{ba2}/E_{ba1} = 1$, here we use $E_{ba1}/E_{*1} = 10^{-3}$ and $E_{ba2}/E_{ba1} = 0.5$.

Chapter 4

Universal mechanistic rules for de novo design of enzymes

This chapter is reproduced from a version of the preprint Chatzitofi M. et al arXiv:2408.16639 [133] which is under review in Chem Catalysis. In this work, I contributed in designing the research and in developing a numerical code to solve the Fokker-Planck and Langevin equations. I have performed numerical calculations, contributed in the analysis of the results and writing the paper.

Universal mechanistic rules for de novo design of enzymes

Michalis Chatzittofi,¹ Jaime Agudo-Canalejo,^{1,2,*} and Ramin Golestanian^{1,3,†}

¹*Max Planck Institute for Dynamics and Self-Organization (MPI-DS), D-37077 Göttingen, Germany*

²*Department of Physics and Astronomy, University College London, London WC1E 6BT, United Kingdom*

³*Rudolf Peierls Centre for Theoretical Physics, University of Oxford, Oxford OX1 3PU, United Kingdom*

(Dated: August 30, 2024)

Enzymes are nano-scale machines that have evolved to drive chemical reactions out of equilibrium in the right place at the right time. Thermodynamically favourable reactions such as ATP hydrolysis are used by the cell to convert chemical energy into useful structure, function, and mechanical work. This includes the ‘fuelled’ catalysis of chemical reactions that would otherwise be thermodynamically unfavourable. Given the complexity and specificity of enzymatic function, bottom-up design of enzymes presents a daunting task that is far more challenging than making passive molecules with specific binding affinities or building nano-scale mechanically active devices. Here, we present a thermodynamically-consistent model for the operation of such a fuelled enzyme, which uses the energy from a favourable reaction to undergo non-equilibrium conformational changes that in turn catalyze a chemical reaction on an attached substrate molecule. We show that enzymatic function can emerge through a bifurcation upon appropriate implementation of momentum conservation on the effective reaction coordinates of the low dimensional description of the enzyme, and thanks to a generically present dissipative coupling. By considering the different aspects of the dynamics, such as the interplay of the non-equilibrium drive and the geometry of the enzyme-substrate complex, we propose three golden rules that should be universally applicable for de novo design of enzymes, as they are based on generic ingredients and physical constraints. These rules lead to optimal combinations of parameters, which can vastly accelerate reactions, while at the same time decreasing the energy dissipation of the combined reaction process, or, in other words, to an efficient enzyme. Our results can complement the recently developed strategies for de novo enzyme design based on machine learning approaches.

I. INTRODUCTION

A fundamental question at the core of many areas of research is how to develop novel strategies for achieving non-equilibrium control at the nano-scale over the direction of chemical reactions [1]. While this is a challenging task from the point of view of bottom-up synthetic approaches, there are lessons to be learned from biological enzymes that have evolved to carry out such tasks with a high degree of precision and robustness despite the overwhelming buffeting by the environment in which they function. Since the pioneering work by Michaelis and Menten who elucidated some of the key phenomenological aspects of enzyme-assisted reaction kinetics [2, 3], our understanding of the underlying mechanisms behind these processes has been progressively refined [4–7]. The underlying physical picture provided by the Kramers theory of noise-activated barrier crossing has provided a key conceptual framework for a reduced low-dimensional characterization of catalytic processes along appropriately selected reaction coordinates [8, 9], while molecular dynamics (MD) simulations of enzymes have been developing rapidly with the help of increased computing power [10].

All-atom MD approaches give important insight at the microscopic level, for particular systems of interest. However, they deal with many degrees of freedom and simulation parameters (e.g. atomic force fields), which might not readily lend themselves to the goal of extracting intuitive, minimal guidelines for the de novo design and

optimization of enzymes. There is moreover still a large gap in time scales that can be computationally afforded to simulate sizeable numbers of catalytic cycles for most enzymes [11]. With the advent of machine learning approaches that are increasingly used in the design and optimization of enzymes [12–14], it is evident that such minimal design rules, which reflect the physical constraints on the conformational dynamics of proteins while driven away from equilibrium through catalytic activity, will be of great potential promise.

In recent years, fundamental insight from statistical physics has been successfully used towards experimental demonstrations of many interesting non-equilibrium phenomena [15–18]. To aim towards the development of systems that can accomplish relatively complex tasks, one can benefit from innovative ideas that build on emergent physical properties of many-body non-equilibrium systems. Recent examples of such developments include proposals to employ non-reciprocal interactions to design collective barrier-crossing strategies that could emulate enzymatic function at larger scales [19], autonomous multifarious self-organization of complex protein structures [20], as well as proposed scenarios for fast and efficient self-organization of primitive metabolic cycles at the early stages of life formation [21].

The non-equilibrium dynamics of an enzyme during catalysis simultaneously involves energy transduction and conformational changes [22, 23], i.e. displacements. This suggests that mechanical considerations should play a key role in the stochastic dynamics of an enzyme, and consequently, in its optimal design with the aim of achiev-

ing the desired catalytic cycle. In other words, the mechanical activity of enzymes that lies at the core of their function as efficient catalysts bears a strong resemblance to the dynamics of molecular motors [24–26], with the important difference that the output energy is not in the form of mechanical work. Just like in the development of synthetic nano-motors, e.g. DNA-origami-based prototypes [18, 27, 28], it would be desirable to have bottom-up strategies to build synthetic enzymes.

Here, we set out to construct a minimal model for a ‘fuelled’ enzyme, so that we can extract a set of golden rules regarding its optimal design (see below). Our theoretical framework is built upon two main pillars, namely, momentum conservation as a fundamental physical constraint on the effective reaction coordinates that span the relevant low dimensional configuration space of the system, and a generically present dissipative coupling between the different reaction coordinates, which we systematically derive from a microscopic model. The implementation of momentum conservation leads to the emergence of an effective mechanochemical coupling in the same spirit as models used in studies of stochastic nano-swimmers [29–32] and enhanced diffusion of enzymes [33, 34], while the dissipative coupling has been recently used to show how enzyme pairs can cooperate by exhibiting synchronization and enhanced catalytic activity [35]. The two ingredients described above give rise to a bifurcation in the dynamical phase-portrait of the low dimensional configuration space, which enables enzymatic activity as an emergent feature of the dynamics, via a fundamentally novel mechanism not accessible to Kramers-like energy barrier-crossing descriptions in terms of reaction coordinates. Our work complements other studies that involve minimal models for studying enzymatic behaviour, often based on colloids interacting through short-ranged interaction potentials or bead-spring networks [36–41], which have been shown to be able to describe the action of a ‘passive’ enzyme, namely, catalysts that can accelerate a process of interest in the thermodynamically favourable direction.

We consider an enzyme that undergoes conformational changes during the catalytic conversion of a fuel molecule to a waste molecule (Fig. 1(a,b) and Supplemental Videos 1 and 2). During each reaction, the enzyme undergoes an expansion and contraction cycle. We consider two types of substrate molecules: a dimer that can dissociate into two monomers (Fig. 1(c)), and a dimer that has two states, a short and a long one (Fig. 1(d) and Supplemental Video 3). In both cases, the dimer is attached at the outside of the enzyme. Through a detailed, thermodynamically consistent calculation, we show that during the fuel-induced contraction the enzyme can cause the dissociation of the dimer into monomers, or its transition from the short to the long conformation, respectively, even if these processes are not favoured thermodynamically or face a substantial energy barrier (see Supplemental Video 4). These catalyzed reactions are favourable in a large portion of the parameter space, related to the sizes and

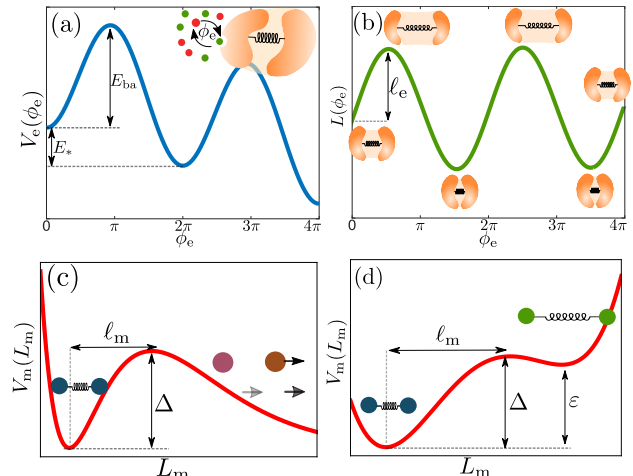


FIG. 1. (a) The free energy landscape that drives the internal (fuel-to-waste) thermodynamically favourable reaction of the enzyme, where E_{ba} is the energy barrier height and E_* the difference in the Gibbs free energy after a complete reaction. (b) The dynamics of the preferred length of the enzyme during the internal reaction, which induces conformational changes of amplitude l_e during a reaction. (c, d) Free energy landscapes for the molecule, representing the thermodynamically unfavourable substrate-to-product reaction, for two examples of reaction: (c) dissociation of a dimer molecule into two monomers (Fig. 1(c)), and a dimer that has two states, a short and a long one (Fig. 1(d) and Supplemental Video 3). In both cases, the dimer is attached at the outside of the enzyme. Through a detailed, thermodynamically consistent calculation, we show that during the fuel-induced contraction the enzyme can cause the dissociation of the dimer into monomers, or its transition from the short to the long conformation, respectively, even if these processes are not favoured thermodynamically or face a substantial energy barrier (see Supplemental Video 4). These catalyzed reactions are favourable in a large portion of the parameter space, related to the sizes and

lengths of the enzyme and the bound molecule.

Our proposed dynamical paradigm, built on appropriate implementation of the relevant physical constraints on the minimal reaction coordinates, allows us to identify the following three golden rules for the optimal function of a fuelled enzyme driven by mechanochemical coupling: (i) the enzyme and the molecule should be attached at the smaller end of each; (ii) the conformational change of the enzyme must be comparable to or larger than the conformational change required of the molecule; (iii) the conformational change of the enzyme must be fast enough so that the molecule actually stretches, rather than just following the enzyme without stretching. The rules can provide useful input to the complementary perspectives of de novo enzyme design based on machine learning and all-atom simulations.

The article is organized as follows. We first present the enzyme-molecule model. After coarse-graining, we derive the general form of the dynamical equations of the enzyme and molecule. After introducing the relevant geometric parameters and energy landscapes, we study the corresponding deterministic dynamical system. We show that the catalytic action of the enzyme can be understood as emerging, in the mathematical language of dynamical systems theory, from a novel global bifurcation in the deterministic phase-space dynamics. This bi-

furcation is a consequence of the non-equilibrium drive of the fuel-to-waste reaction and the mechanochemical coupling with the passive molecule arising from enzyme conformational changes. We confirm the latter through the analysis of the stochastic dynamics in the presence of thermodynamically consistent noise. By studying the non-equilibrium steady-state of the system, we show the existence of an optimal set of parameters. Finally, an analysis of first-passage times shows that fuelled catalysis enables a great reduction of the characteristic reaction time and thus a substantial enhancement in the reaction rate.

II. MODEL

In biological cells, many reactions are driven by enzymes that use a thermodynamically favourable reaction (fuel-to-waste) to power a thermodynamically unfavourable reaction (substrate-to-product) that would normally (spontaneously) take place in the opposite direction, in the absence of the enzyme. The most common fuel for these reactions is ATP, which is converted into useful work or motion [26, 42–45]. Here we develop a minimal model to describe the dynamics of a fuelled enzyme.

A. Geometry and deterministic dynamics

We start with the simple model for an enzyme that undergoes conformational changes during catalysis, as previously introduced in Ref. 35. In particular, the fuel-to-waste reaction is not modelled explicitly, and is instead described by an internal phase ϕ_e which moves stochastically along a downhill washboard potential $V_e(\phi_e)$; see Fig. 1(a). A noise-activated jump over one of the energy barriers (of height E_{ba}) leads to an increase of the internal phase ϕ_e by 2π , and corresponds to the conversion of fuel into waste with a free energy release given by E_* . We assume that the catalytic process is reaction-limited, which is equivalent to fuel molecules being sufficiently abundant, such that a new fuel molecule would effectively bind instantly to the enzyme after a reaction allowing the process to be repeated again.

The enzyme is represented by two sub-units, with the separation L_e between them representing the mechanical degree of freedom that is coupled to the internal chemistry. This coupling is described by the potential $U(L_e, \phi_e) = \frac{k}{2}(L_e - L(\phi_e))^2 + V_e(\phi_e)$, where the first term is a harmonic potential that couples the actual length L_e to a preferred length $L(\phi_e)$ that depends on the internal phase describing the fuel-to-waste reaction; see Fig. 1(b). As a consequence of this coupling, every time that a fuel-to-waste reaction occurs the enzyme undergoes a cyclic conformational change.

The dynamics of the dimer molecule is described by a single degree of freedom, which is the separation L_m

between its two monomers; see Fig. 1(c,d). To model the two different chemical reactions already described (dimer dissociation and short-to-long conformation switch), two different potentials $V_m(L_m)$ that govern the length of the molecule are used. For convenience and to unify the notation in both cases, we express the dimer length as $L_m = L_m^{(0)} + \ell_m \phi_m$ where $L_m^{(0)}$ is the length in the dimer state or in the transition state between short and long, respectively, and ℓ_m is the length increase necessary to reach the transition state; see Fig. 1(c,d).

We now briefly describe the dynamics governing these degrees of freedom (for the detailed derivation see Appendix A). When the substrate molecule strongly binds to the enzyme, a complex effectively made up of three sub-units is formed (Fig. 2). Each sub-unit has a hydrodynamic mobility (inverse friction): μ_e for the part of the enzyme not bound to the molecule, μ_b for the unit that is shared by the molecule and the enzyme when bound to each other, and μ_m for the part of the molecule that is not bound to the enzyme. Since the typical time scales of the catalytic activity and the associated enzyme conformational transitions are much longer than the relevant inertial time scale [32], we consider the overdamped dynamics of these three sub-units, which leads to coupled evolution equations for the two lengths. Similarly, we consider overdamped dynamics for the evolution of the internal phase of the enzyme along the chemical free energy landscape, with an associated mobility μ_ϕ . By assuming that the enzyme is stiff, one can enslave the dynamics of the enzyme length (fast variable) onto the dynamics of the internal phase (slow variable). This reduces the degrees of freedom to two, and results in coupled equations for the internal phase of the enzyme and the length of the molecule. The deterministic components of the equations take on the form

$$\dot{\phi}_\alpha = \sum_{\beta=e,m} M_{\alpha\beta}(\phi_e) [-\partial_\beta V_\beta(\phi_\beta)] \quad (1)$$

where $M_{\alpha\beta}$ is a symmetric effective mobility tensor (with $\alpha, \beta \in \{e, m\}$), and $\partial_\beta \equiv \frac{\partial}{\partial \phi_\beta}$ (note that we do not implement a summation convention). The explicit expressions for the components of the mobility tensor are given as follows

$$M_{ee} = \frac{\mu_\phi}{1 + \frac{\mu_\phi}{\mu_1} L'(\phi_e)^2}, \quad (2)$$

$$M_{em} = M_{me} = - \left(\frac{\mu_\phi}{1 + \frac{\mu_\phi}{\mu_1} L'(\phi_e)^2} \right) \frac{\mu_b}{\mu_1} \frac{L'(\phi_e)}{\ell_m}, \quad (3)$$

$$M_{mm} = \frac{1}{\ell_m^2} \left(\mu_2 - \frac{\mu_b^2}{\mu_1} \frac{1}{1 + \frac{\mu_\phi}{\mu_1} L'(\phi_e)^2} \right), \quad (4)$$

where $\mu_1 \equiv \mu_e + \mu_b$, $\mu_2 \equiv \mu_m + \mu_b$, and $L'(\phi_e) = \frac{dL(\phi_e)}{d\phi_e}$.

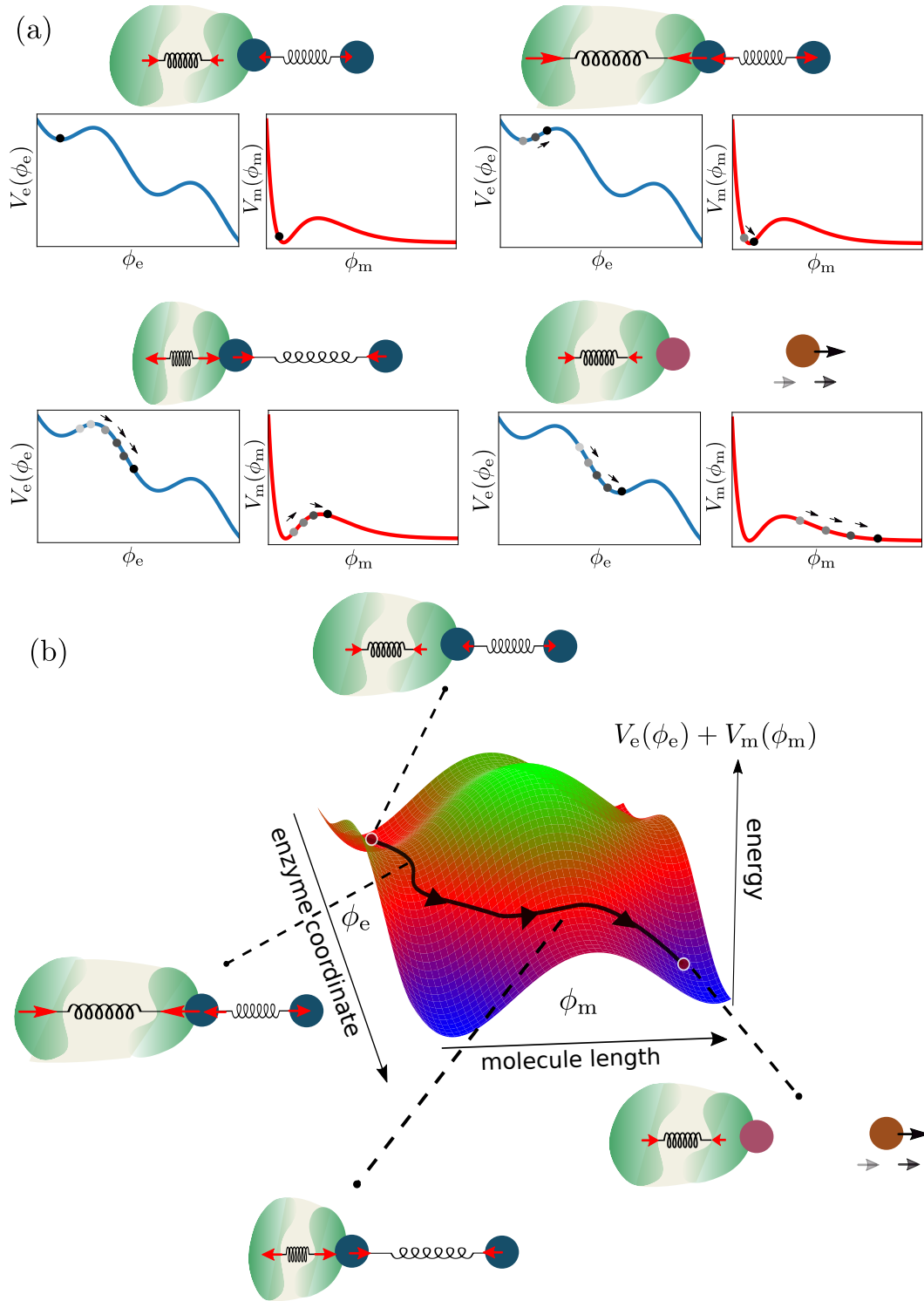


FIG. 2. (a) A visualization of a dissociation process catalyzed by a fuelled enzyme, divided into four stages. The blue and red curves correspond to the energy landscape of the internal reaction of the enzyme $V_e(\phi_e)$, and of the molecular reaction $V_m(\phi_m)$, respectively. (b) The same process visualized within the two dimensional energy landscape given by $V_e(\phi_e) + V_m(\phi_m)$, where the black line shows the evolution of the combined enzyme-molecule system. Thermal noise tends to kick the system over the enzymatic energy barrier, since it is smaller than the barrier in the energy landscape of the molecule. The coupling between the enzyme and molecule dynamics, mediated by the conformational changes of the enzyme, then causes the system to cross over the energy barrier of the molecular reaction.

B. The effect of noise in the stochastic dynamics

Since enzymes operate at the nano-scale, they are strongly affected by the thermal fluctuations of the surrounding medium. In particular, because the dynamics is dissipative, thermal noise is essential to kick the system out of local energy minima and over barriers associated with the reactions; see Fig. 1(a,c,d).

Therefore, it is essential to introduce thermal fluctuations in our description of the problem. The system is out of equilibrium due to the driving force given by the energy E_* of the fuel. In the limit of $E_* = 0$, the steady state of the system must be a state of thermodynamic equilibrium, corresponding to a Boltzmann distribution. This implies that the stochastic dynamics corresponding to the deterministic dynamics in Eq. (1) must be described by a Fokker-Planck equation describing the time evolution of the probability distribution $P(\phi_e, \phi_m, t)$ as follows

$$\partial_t P + \sum_{\alpha=e,m} \partial_\alpha J_\alpha = 0, \quad (5)$$

with the conserved probability currents given as

$$J_\alpha(\phi_e, \phi_m, t) = \sum_{\beta=e,m} M_{\alpha\beta} [P(-\partial_\beta V_\beta) - k_B T \partial_\beta P], \quad (6)$$

where k_B is the Boltzmann constant and T is the temperature. In the absence of a non-equilibrium driving force ($E_* = 0$), both probability currents J_e and J_m must vanish at the equilibrium steady state. As a result, one recovers the Boltzmann distribution $P_{\text{eq}} \propto \exp(-V_e(\phi_e)/k_B T) \exp(-V_m(\phi_m)/k_B T)$ independently of the form of the mobility matrix $M_{\alpha\beta}$, and thus of the geometric parameters describing the enzyme and the molecule.

That the equilibrium probability distribution factorizes reflects the fact that the two-dimensional energy landscape $V_e(\phi_e) + V_m(\phi_m)$ in which the phases evolve is separable, i.e. there is no coupling between ϕ_e and ϕ_m through the potential. The dynamics of ϕ_e and ϕ_m are coupled only through the off-diagonal components of the mobility tensor $M_{\alpha\beta}$, which arise due to the mechanical contact (binding) between enzyme and molecule in combination with the conformational changes of the enzyme, and represent a form of *dissipative* coupling which only plays a role in a non-equilibrium setting ($E_* > 0$), i.e. when the fuel-to-waste reaction is thermodynamically favoured. This type of coupling has been seen to emerge in models of coupled molecular machines (*via* mechanical binding or hydrodynamic interactions mediated by a viscous fluid) and enables cooperative phenomena like synchronization [35, 46] and phase-locking [47] among enzymes, of which there is suggestive experimental evidence [48, 49].

The Langevin equation associated to the Fokker-Planck equation in Eq. (5) takes the following form in

the Stratonovich convention,

$$\dot{\phi}_\alpha = \sum_{\beta=e,m} \left[M_{\alpha\beta} (-\partial_\beta V_\beta) + \sqrt{2k_B T} \sigma_{\alpha\beta} \xi_\beta + \sum_{\nu=e,m} k_B T \sigma_{\alpha\nu} \partial_\beta \sigma_{\beta\nu} \right], \quad (7)$$

where $\sum_{\nu=e,m} \sigma_{\alpha\nu} \sigma_{\beta\nu} = M_{\alpha\beta}$. The term on the second line of the right hand side is the spurious drift term arising from the multiplicative nature of the noise, due to the dependence of the mobility matrix on ϕ_e , while the last term on the first line of Eq. (7) is the thermal noise with ξ_β being a unit white noise such that $\langle \xi_\beta(t) \rangle = 0$ and $\langle \xi_\alpha(t) \xi_\beta(t') \rangle = \delta_{\alpha\beta} \delta(t - t')$. It is also worth noting that the mobility matrix must be symmetric and positive definite (which is the case here) in order for the dynamics to be thermodynamically consistent [50, 51].

C. Model parametrization

The enzyme and the molecule are embedded in a solvent under low Reynolds number conditions [51]. Therefore, we can infer that the mobilities μ_e (enzyme-only sub-unit), μ_b (bound enzyme-molecule sub-unit), and μ_m (molecule-only sub-unit) are related to their corresponding effective hydrodynamic radii a_e , a_b , and a_m , via the Stokes relation $\mu = 1/(6\pi\eta a)$, ignoring hydrodynamic interactions in this lowest order approximation. The mobilities thus directly encode information about the sizes of the enzyme and the molecule sub-units. The length scale related to the amplitude of the deformation of the molecule is ℓ_m ; see Fig. 1(c,d). For the conformational changes of the enzyme, we assume that the preferred length $L(\phi_e)$ oscillates during the enzymatic cycle as

$$L(\phi_e) = L_e^{(0)} + \ell_e \sin(\phi_e - \delta), \quad (8)$$

where $L_e^{(0)}$ is an average length which does not enter the dynamics, ℓ_e is the amplitude of the conformational change, and δ is a phase shift described below (we choose $\ell_e \geq 0$).

The washboard potential governing the dynamics of the internal phase ϕ_e is taken to be of the form $V_e(\phi_e) = -F\phi_e + v \sin(\phi_e - \delta)$ where $\delta = \arccos(F/v)$ is the value of the phase shift which guarantees that the minima of the potential are located at integer multiples of 2π . The parameters F and v can be mapped to the height of the energy barrier of the enzymatic reaction E_{ba} and the free energy released after a complete reaction E_* (see Fig. 1(a)) through $E_{\text{ba}} = [2\sqrt{1 - (F/v)^2} + 2\delta(F/v)]v$ and $E_* = 2\pi F$ [35, 47, 52]. By eliminating v and F , we find that the parameter δ is given by the solution of the transcendental equation

$$\delta + \tan \delta = \pi E_{\text{ba}}/E_*, \quad (9)$$

Parameters	Description
μ_ϕ	mobility of the internal phase ϕ_e (reaction coordinate of fuel-to-waste reaction)
μ_e	hydrodynamic mobility of the enzyme-only sub-unit
μ_m	hydrodynamic mobility of the molecule-only sub-unit
μ_b	hydrodynamic mobility of the shared (bound) sub-unit
$\mu_1 = \mu_e + \mu_b$	sum of the mobilities of the enzyme-only and shared sub-units
$\mu_2 = \mu_m + \mu_b$	sum of the mobilities of the molecule-only and shared sub-units
$h = \mu_b/(\mu_e + \mu_b)$	effective coupling strength ($0 \leq h \leq 1$)
ℓ_e	amplitude of the conformational change of the enzyme
ℓ_m	length difference between the initial and transition states of the molecule
E_{ba}	energy barrier of the fuel-to-waste reaction
E_*	Gibbs free energy released by the fuel-to-waste reaction
Δ	energy barrier of the molecule reaction
ε	unfavourable energetic bias of the short-to-long reaction
$k_B T$	thermal energy (strength of thermal fluctuations)

TABLE I. Summary of the parameters of the model.

which yields the approximate solution

$$\delta \simeq \frac{\pi}{2} \frac{E_{ba}}{E_*}, \quad (10)$$

for small values of E_{ba}/E_* .

The parameter μ_ϕ is the mobility of the internal phase ϕ_e and may have different microscopic origins depending on the particulars of the fuel-to-waste reaction. In principle, it can be related to the rate k_{cat} of the catalytic reaction and the height of the energy barrier E_{ba} through the Kramers escape rate [8, 9]

$$k_{cat} = \frac{\mu_\phi}{2\pi} \sqrt{|\lambda|\lambda^{(0)}} \exp\left(-\frac{E_{ba}}{k_B T}\right), \quad (11)$$

where $\lambda^{(0)} = V_e''|_{\min}$ and $\lambda = V_e''|_{\max}$, i.e. they correspond to the values of the second derivative (curvature) of the potential around the minimum and the maximum (energy barrier), respectively. Thus, by knowing the catalytic rate and barrier height of a reaction one can infer the value of μ_ϕ .

For the molecule, we consider two different types of reaction starting from a dimer-like substrate. For the dissociation reaction, we consider a potential with a minimum representing the stable initial state of the molecule, a maximum corresponding to an energy barrier with height Δ , and an asymptotic decrease to a constant value, which represents the fact that beyond the barrier the monomers become disconnected. We describe this with the potential $V_m(\phi_m) = \Delta\phi_m^2 \exp[2(1 - \phi_m)]$, shown in Fig. 1(c). For the conformational switch reaction where the dimer switches from a short to a long state, we choose a bistable potential, with an energy barrier Δ and an energy difference ε between the long (higher energy) and the short (lower energy) states. We model this using the potential $V_m(\phi_m) = \Delta\phi_m^2(\phi_m^2 - 2) + \varepsilon\phi_m/2$, with $\varepsilon < \Delta$; see Fig. 1(d). All the relevant model parameters are summarized in Table I.

III. RESULTS

A. Preliminary considerations

It is crucial to note that the components of the mobility tensor $M_{\alpha\beta}$ are determined by the geometric features of the enzyme and molecule, which can be tuned as to optimize the function of the enzyme. The basic principle is illustrated in Fig. 2(a), for the example of dissociation of a dimer molecule. When a catalytic reaction takes place (the internal phase ϕ_e is kicked over the chemical energy barrier by thermal noise), the coupling to the molecule length arising from the conformational changes of the enzyme drives a corresponding evolution of the molecule length, as represented by ϕ_m , and in particular can cause ϕ_m to overcome its energy barrier. The evolution along the two-dimensional energy landscape $V_e(\phi_e) + V_m(\phi_m)$ is shown in Fig. 2(b), where the black path corresponds to a catalyzed reaction.

We expect to have a strong coupling between the fuel-to-waste (ϕ_e) and substrate-to-product (ϕ_m) reactions when the off-diagonal components in the mobility tensor are non-negligible. In the limiting cases where either the middle sub-unit is large compared to the enzyme-only sub-unit, $\mu_b/\mu_1 \rightarrow 0$, or the conformational changes of the enzyme are small compared to the dissociation length of the molecule, $\ell_e/\ell_m \rightarrow 0$, the off-diagonal terms vanish, leading to a decoupling of the dynamics between the enzyme and the molecule. To achieve a strong coupling, we would aim to maximize μ_b/μ_1 and ℓ_e/ℓ_m , from which one can infer the first two golden rules [(i) and (ii)] for designing an enzyme discussed above. In the following, we define the ratio $h \equiv \mu_b/\mu_1 = \mu_b/(\mu_e + \mu_b)$ to be the ‘‘coupling strength’’, and we note that it is bounded as $0 \leq h \leq 1$. For $h < 0.5$, the mobility of the shared sub-unit is larger than that of the enzyme-only sub-unit, and the reverse is true for $h > 0.5$.

Throughout the rest of the text we will use the following parameters unless mentioned otherwise: $\mu_\phi \ell_m^2 / \mu_2 =$

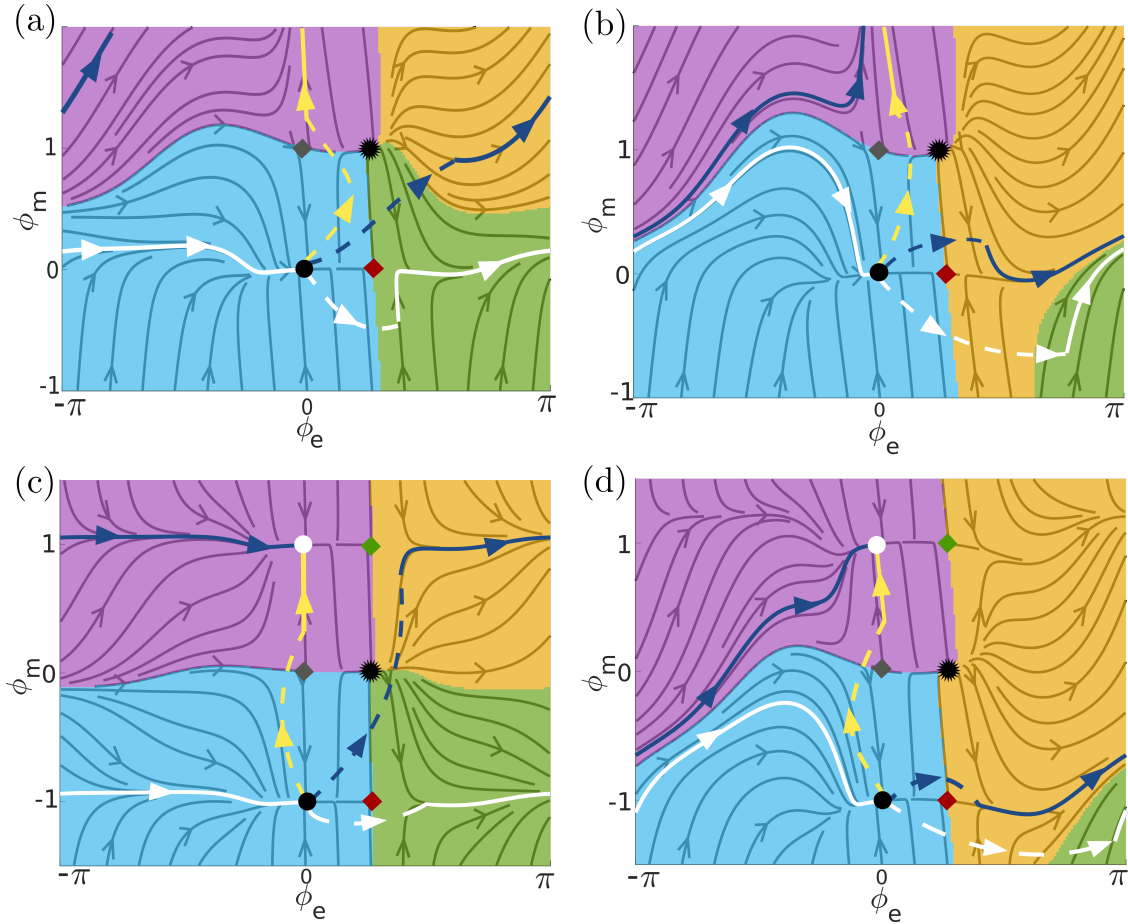


FIG. 3. Phase-portraits of the deterministic dynamics for (a,b) the dissociation reaction and (c,d) the switch reaction. A global bifurcation occurs with increasing coupling strength h , which is below the critical value in (a,c) and above it in (b,d). In all cases, stable fixed points are depicted as circles, saddle points as diamonds, and unstable fixed points as asterisks. Dashed lines depict possible scenarios in which thermal fluctuations can kick the system out of the basin of attraction of a stable fixed point. The solid flow lines show typical trajectories, and their final resting points, when starting from different basins of attraction. The different colouring of the diamonds is described in the text. The values of the coupling are (a) $h = 0.33$, (b) $h = 0.48$, (c) $h = 0.12$, and (d) $h = 0.48$.

1, $\ell_e/\ell_m = 2.5$, $\mu_1/\mu_2 = 0.88$, $E_*/\Delta = 14\pi$, $E_{ba}/\Delta = 0.4$, and (for the switch reaction) $\varepsilon/\Delta = 0.1$. The dimensionless time is defined as $\tilde{t} = (\mu_\phi \Delta)t$. The remaining dimensionless parameters that we explore in the text are the coupling strength h and the dimensionless thermal noise strength $k_B T/\Delta$.

B. Deterministic dynamics and global bifurcation

Before considering the full stochastic (noise-activated) dynamics of the system, we first study the deterministic dynamics given by Eq. (1), as we can apply tools from dynamical systems theory to obtain an intuitive understanding of the expected behaviour, particularly in the experimentally-relevant case of low noise, where $k_B T$ is smaller than all other energy scales.

In Fig. 3, phase portraits of the deterministic dynam-

ics are shown for low and high coupling strengths and both types of reaction (see Appendix C for details of the numerical calculation of phase portraits). Depending on the type of reaction, different sets of fixed points appear in the dynamics (stable fixed points are depicted as circles, saddle points as diamonds, and unstable fixed points as asterisks). For the dissociation reaction, there are four fixed points (one stable, two saddle points, one unstable) since there is no local minimum of the molecule potential after the energy barrier. The stable fixed point at $\phi_m = 0$ corresponds to the substrate (dimer) state, whereas $\phi_m \rightarrow \infty$ corresponds to the product (dissociated) state. For the switch reaction, there are six fixed points (two stable, three saddle points, one unstable). The stable fixed point at $\phi_m = -1$ corresponds to the substrate (short) state, whereas that at $\phi_m = +1$ corresponds to the product (long) state. It is worth noting that the positions of the fixed points do not depend on the

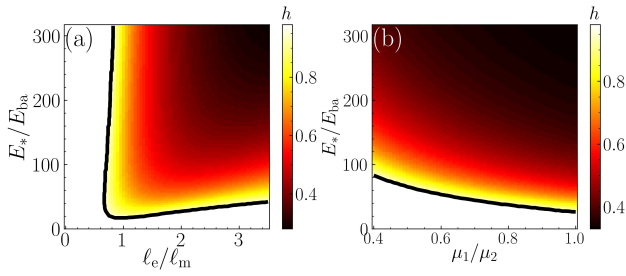


FIG. 4. Critical coupling strength at which the bifurcation occurs, as a function of (a) the geometric ratio ℓ_e/ℓ_m and the ratio E_*/E_{ba} describing the internal enzyme reaction, and (b) the mobility ratio μ_1/μ_2 and E_*/E_{ba} . In the white region outside the black solid line, a bifurcation does not occur within the physical range $0 \leq h \leq 1$.

coupling, but only on the potentials $V_e(\phi_e)$ and $V_m(\phi_m)$. Thus, changes in the geometry of the enzyme-molecule complex (and thus in the coupling strength) leave the location and nature of the fixed points unchanged. As a consequence, there cannot be any local bifurcations in the dynamical system and only global bifurcations are allowed [35]. By considering the topology of the different basins of attraction in the dynamical system, we note that global bifurcations occur between Figs. 3(a) and 3(b) for the dissociation reaction, and between Figs. 3(c) and 3(d) for the switch reaction, respectively.

The phase portraits allow us to uncover the different possibilities emerging in the full stochastic dynamics by classifying the different types of possible deterministic trajectories, depicted as solid flow lines in Fig. 3, and considering the likelihood of their stochastic activation by random thermal kicks, depicted as dashed flow lines in Fig. 3, which will take the system from an initial state around a stable fixed point to the domain of interest. Trajectories starting in the cyan region in Fig. 3 are attracted to the fixed point at $(\phi_e, \phi_m) = (0, 0)$ (for the dissociation reaction) or $(0, -1)$ (for the switch reaction). On the other hand, those starting in the green region are attracted to the fixed point at $(\phi_e, \phi_m) = (2\pi, 0)$ (dissociation) or $(2\pi, -1)$ (switch). This class of trajectories, which are depicted as solid white flow lines in Fig. 3, represent the process in which the molecule remains in the substrate state and the enzyme performs a futile cycle. Analogously, trajectories starting in the magenta region end at $(0, \infty)$ (dissociation) or $(0, 1)$ (switch), corresponding to spontaneous transition of the molecule to the product state, without an accompanying transition in the enzyme, while those in the orange region converge to $(2\pi, \infty)$ (dissociation) or $(2\pi, 1)$ (switch), representing a process in which the molecular transition coincides with the enzymatic cycle. The relative frequency of the activation of the different processes corresponding to these distinct classes will depend on the likelihood of the availability of the thermal kick of the right strength that is needed to initiate each of them.

More specifically, let us consider the case of weak coupling in Figs. 3(a,c). Thermal fluctuations can most likely kick the system over one of the two saddle points or transition states, either the one to the right of the stable fixed point shown as red diamond (white trajectory) or the one above it shown as grey diamond (yellow trajectory). When traversing the red diamond, the enzyme will complete an internal reaction ending at $\phi_e = 2\pi$, while the molecule remains in the substrate state. When traversing the grey diamond, the molecule undergoes a reaction and turns into product, while the enzyme completes no internal reaction and remains at $\phi_e = 0$. Thus, the internal (fuel-to-waste) reaction of the enzyme and the molecule (substrate-to-product) reaction are completely uncoupled in these cases. Less likely thermal fluctuations can kick the system across the unstable fixed point shown as asterisk (blue trajectory), leading to a simultaneous occurrence of both the enzyme and the molecule cycles.

We next consider the case of strong coupling, after the global bifurcation has occurred and the basins of attraction have rearranged; see Fig. 3(b,d) and Supplemental Videos 5 and 6. Thermal fluctuations kicking the system over the grey diamond (yellow trajectory) will still result in molecular reactions without associated internal reactions in the enzyme. However, if the system is activated over the red diamond, the more likely scenario will be for the enzyme to complete an internal reaction simultaneously with the molecular reaction (blue trajectory) unlike in the weak coupling case. The two reactions thus become coupled, and in particular, a fuel-to-waste reaction inside the enzyme now triggers a substrate-to-product reaction for the molecule. The futile enzyme cycle (white trajectory) is the more unlikely scenario in this case. We note that a similar bifurcation occurs for the reverse switching process, where the energetically favourable and initial state for the molecule is the long conformation; see Appendix B.

The bifurcation occurs above a critical value of the coupling h , which can be tuned by the geometric properties of the enzyme-substrate complex. Moreover, in order to have an enzyme-triggered reaction, transitions through the red diamond should be favoured over transitions through the grey diamond. This is expected to happen when the energy barrier for the internal reaction is smaller than that of the molecular reaction ($E_{ba} < \Delta$). It is also worth mentioning that, even though the dissociation and switch reactions involve rather different energy landscapes, the bifurcation takes place at the same set of parameters since in both cases the barrier for the molecular reaction is fixed to Δ .

The occurrence of the bifurcation is crucial for the coupling between the two processes to emerge, and thus for the enzyme to become active. We thus explore how the critical coupling depends on the geometric and energetic parameters of the enzyme-substrate complex. In Fig 4, we show the critical value of the coupling h as a function of the ratio E_*/E_{ba} of energies in the fuel-to-waste reac-

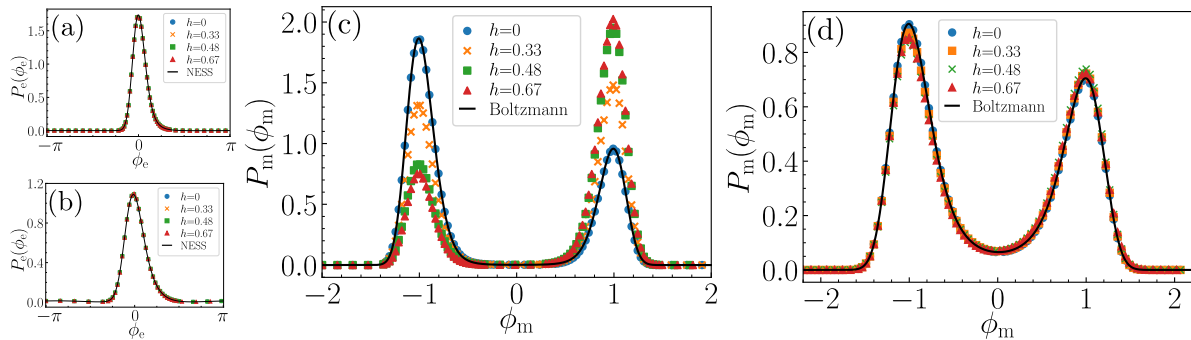


FIG. 5. Marginal steady-state distributions for the switching reaction, (a,c) at low noise $k_B T/\Delta = 0.15$, and (b,d) at high noise $k_B T/\Delta = 0.4$. The distribution for the enzyme coordinate ϕ_e is shown in (a,b), and that for the molecule coordinate ϕ_m in (c,d). In (a,b) the black line labelled “NESS” is the analytical result for an uncoupled enzyme given in Eq. (D4). In (c,d) the black line labelled “Boltzmann” is the equilibrium distribution $P_m(\phi_m) \propto \exp(-V_m/k_B T)$.

tion, and ℓ_e/ℓ_m or μ_1/μ_2 which are directly related to the geometrical properties of the complex. In Fig 4(a), it is observed that the bifurcation takes place at low coupling strengths when the driving E_* is large, which is linked to higher reaction rates [related to golden rule (iii)]. In addition, there is a non-trivial behaviour as a function of the length ratio ℓ_e/ℓ_m at a fixed value of E_*/E_{ba} , showing non-monotonic behaviour with a minimum at intermediate values. In Fig 4(b), we see that the bifurcation is favoured at higher values of the ratio μ_1/μ_2 . The results in Fig. 4 serve to highlight the different parameters that must be tuned in order to favour a bifurcation in the deterministic dynamics. Below, we show how these results translate to the full noise-activated stochastic dynamics.

C. Stochastic dynamics

1. Steady state: driving a reaction uphill

Passive enzymes can lower reaction barriers, but do not shift reaction equilibria, which are still purely governed by the free energy differences between substrate and product. Fuelled enzymes, on the other hand, can use the free energy provided by the fuel to drive the substrate-to-product reaction uphill, i.e. favouring the formation of a high free energy product from a low free energy substrate. To study whether our model enzyme is capable of driving reactions uphill, we focus on the switch reaction (Fig. 1(d)), and numerically solve the Fokker-Planck equation (Eq. (5), see Appendix C for details of the numerical solution), where we are interested in how the probability distribution evolves over time and in the form of the steady state distribution in the long time limit, where $\partial_t P_{ss} \rightarrow 0$.

In Fig. 5, the steady state marginal distributions $P_e(\phi_e) \equiv \int_{-\infty}^{\infty} d\phi_m P_{ss}(\phi_e, \phi_m)$ and $P_m(\phi_m) \equiv \int_0^{2\pi} d\phi_e P_{ss}(\phi_e, \phi_m)$ for the enzyme and molecule reaction coordinates are presented for low and high thermal noise. Both at low and at high noise, the effect of the cou-

pling h is negligible with respect to the non-equilibrium steady state (NESS) attained by the enzyme, $P_e(\phi_e)$; see Fig. 5(a,b). The form of $P_e(\phi_e)$ can be obtained analytically in the $h = 0$ case (solid black line), by extending a classical calculation [53–55] to the case with multiplicative noise, i.e. a phase-dependent mobility, as described in Appendix D. At high temperatures, the multiplicative noise causes a small maximum at intermediate values of ϕ_e that would not be present for additive noise; see Fig. 5(b).

In stark contrast, at low noise the coupling h has a substantial effect on the NESS attained by the molecule, $P_m(\phi_m)$; see Fig. 5(c). At $h = 0$, the distribution $P_m(\phi_m)$ corresponds to a Boltzmann distribution $\propto e^{-V_m(\phi_m)/k_B T}$, and thus shows two peaks (corresponding to the short and long states), with the peak corresponding to the lower energy short state being much higher. As the coupling h increases, we see this trend progressively reverse, as the fuelled action of the enzyme drives more and more probability towards the long state. This demonstrates that the fuelled action of the enzyme can indeed drive a reaction uphill, in the thermodynamically unfavourable direction. However, the action of the enzyme becomes much less effective at high noise, where deviations from the Boltzmann equilibrium are minimal; see Fig. 5(d).

To further understand this effect, we consider the time evolution of the probability of finding the molecule in the long state $P_{\text{long}}(t)$, defined as

$$P_{\text{long}}(t) = \int_0^{2\pi} d\phi_e \int_{\phi_{m,\text{max}}}^{\infty} d\phi_m P(\phi_e, \phi_m, t), \quad (12)$$

where $\phi_{m,\text{max}}$ is the location of the energy barrier of the molecular reaction along the ϕ_m coordinate. We consider an enzyme and a molecule that are initially separated from each other, and bind at time $t = 0$. We thus initialize the enzyme probability distribution as being in the steady state of an uncoupled enzyme ($h = 0$). For the molecule, we consider two cases: (i) the molecule starts in its Boltzmann equilibrium, or (ii) the molecule starts

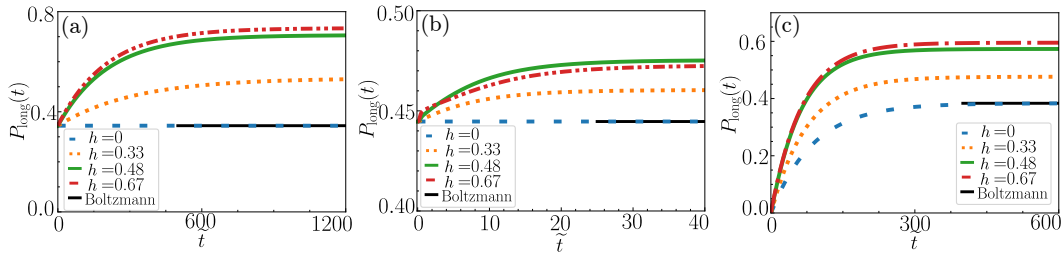


FIG. 6. Probability of finding the shape-switching molecule in the long state as a function of time, for various values of the coupling h . In (a,b) the initial state is chosen as a Boltzmann distribution, while in (c) it is chosen as a narrow Gaussian centered around the short state. The strength of the noise is (a) $k_B T / \Delta = 0.15$, (b) $k_B T / \Delta = 0.4$, and (c) $k_B T / \Delta = 0.2$. The horizontal line labelled “Boltzmann” is the long-time limit expected from an equilibrium distribution.

only in the short state (with probability distributed in a narrow Gaussian around it). Results from numerical solution of the Fokker-Planck equation (Eq. (5)) are shown in Fig. 6. For $h = 0$, P_{long} tends to the probability corresponding to the equilibrium Boltzmann distribution, as expected. However, for $h > 0$, P_{long} is consistently higher than what the Boltzmann distribution dictates. Clearly, coupling to the fuelled enzyme can drive the molecular reaction uphill. The effect is most pronounced at larger coupling strengths and lower noise.

From $P_{\text{long}}(t)$, we may calculate the probability that the molecule is in the long state once it unbinds from the enzyme, which is a quality measure for the function of the enzyme. Assuming that the molecule unbinds from the enzyme at a rate k_{off} , the probability of the molecule remaining bound at time t is $p_{\text{bo}}(t) = \exp(-k_{\text{off}}t)$. The probability of unbinding precisely between t and $t + dt$ is then $p_{\text{bo}}(t)k_{\text{off}}dt$, and thus the average probability of being in the long state when it unbinds is

$$\langle P_{\text{long}} \rangle = k_{\text{off}} \int_0^{\infty} dt' P_{\text{long}}(t') p_{\text{bo}}(t'). \quad (13)$$

The behaviour of $P_{\text{long}}(t)$ in Fig. 6 can be well approximated by an exponential relaxation $P_{\text{long}}(t) \simeq P_{\text{long}}(\infty) - [P_{\text{long}}(\infty) - P_{\text{long}}(0)] \exp(-k_{\text{cat}}t)$, where k_{cat} is the inverse timescale associated with the transient regime in Fig. 6. With this choice, Eq. (13) evaluates to

$$\langle P_{\text{long}} \rangle \simeq \frac{k_{\text{off}} P_{\text{long}}(0) + k_{\text{cat}} P_{\text{long}}(\infty)}{k_{\text{off}} + k_{\text{cat}}}. \quad (14)$$

In the limiting case in which $k_{\text{off}} \ll k_{\text{cat}}$, so that the typical timescale for unbinding is longer than the timescale of the transient regime in Fig. 6, we find $\langle P_{\text{long}} \rangle \simeq P_{\text{long}}(\infty)$.

We can also consider the energetic efficiency of the enzymatic action. In the NESS, the reaction rate of the enzyme and thus the energy dissipation (or equivalently the entropy production) rate can be used as a measure of the enzymatic activity. The enzymatic reaction rate Ω_e is given by

$$\Omega_e \equiv \frac{1}{2\pi} \int_{-\infty}^{\infty} J_e d\phi_m \quad (15)$$

and is constant in the NESS. The rate of energy dissipation is then given by $\Omega_e E_*$. In Fig. 7, we show the steady state values of P_{long} and the energy dissipation rate $\tilde{\Omega}_e E_* / k_B T$ (where $\tilde{\Omega}_e$ is the rate in dimensionless time units \tilde{t} as introduced above), as a function of the coupling h and the geometric parameter ℓ_e / ℓ_m . Interestingly, there are large regions of parameter space where the enzyme is highly functional (larger P_{long}) while the energy dissipation is much lower than the corresponding value for an uncoupled enzyme, which can be explained by a slow-down of the fuelled enzymatic reaction (smaller Ω_e) due to the coupling to the molecular reaction. It is also worth noting that P_{long} is non-monotonic as a function of ℓ_e / ℓ_m , and peaks at intermediate values of order one, i.e. when the deformation of the enzyme is comparable to the deformation required of the molecule during the course of the reaction.

2. First passage time: speeding up a slow reaction

We now focus on the early-time dynamics of the process and quantify the characteristic time that is needed for the substrate-to-product conversion to take place, i.e. the mean first passage time. We focus on the switch reaction, although analogous results are obtained for the dissociation reaction. We initialize the system in the short state ($\phi_m = -1$) at $t = 0$, and numerically solve the Langevin dynamics (Eq. (7), see Appendix C for details of the numerical solution) until the long state ($\phi_m = 1$) is reached at a time $t = \tau$ (which we then record). The ensemble average of τ (i.e. average over many simulations), which we denote as $\langle \tau \rangle$, corresponds to the mean first passage time.

In Fig. 8(a), we show the distribution of first passage times $P(\tau)$ for zero and large coupling strength h . Clearly, in the presence of dissipative coupling, the first passage times are much smaller in relative terms, while the distribution appears to be markedly narrower. Figures 8(b,c) show how the mean first passage time $\langle \tau \rangle$, relative to the value $\langle \tau_0 \rangle$ corresponding to the absence of enzyme conformational changes ($\ell_e / \ell_m = 0$), depends on the tuning parameters, namely the fuelled reaction drive

E_*/E_{ba} , the (geometric) deformation ratio ℓ_e/ℓ_m , and the coupling strength h . By comparing Fig. 8(b) with Fig. 4(a), it becomes clear that the speed-up in the reaction is directly related to the global bifurcation in the deterministic dynamics.

Some analytical progress towards a calculation of the mean first passage time is possible in the limit of small noise ($k_B T$ much smaller than the energy barriers E_{ba} and Δ). In this limit, a generalization of the Kramers escape rate to higher dimensions due to Langer [9, 56, 57] gives the rate at which the probability current crosses through a saddle point, which represents the transition state. To deal with the multiplicative nature of the noise, we evaluate the mobility tensor $M_{\alpha\beta}$ around the saddle point of interest. Moreover, we are interested in the catalyzed reaction, and thus focus on the transition state shown as the red diamond in Fig. 3. The rate then takes a similar form to the one-dimensional case (see Eq. (11)), given by

$$k_{\text{Langer}} = \frac{|\Lambda_-|}{2\pi} \sqrt{\frac{\lambda_e^{(0)}}{|\lambda_e|}} \exp\left(-\frac{E_{ba}}{k_B T}\right). \quad (16)$$

For more details see Appendix E. As shown in Fig. 8(d), Eq. (16) agrees well with numerical solution of Eq. (5) for the crossing rate over the saddle point marked as the red diamond in Fig. 3, after a brief initial transient. In the numerics, the initial probability distribution for both enzyme and molecule was chosen as a narrow Gaussian centered at the potential minimum.

IV. DISCUSSION

We have developed a minimal model for a fuelled enzyme that is able to extract energy from a thermodynamically favourable reaction to drive and speed-up a thermodynamically unfavourable reaction. The transduction is mechanical, arising from the conformational changes of the enzyme that couple to the conformational changes of the attached substrate molecule. This goes beyond previously developed minimal models for enzymes that only described passive enzymes [36–41], which can speed up energetically favourable reactions but are unable to alter the reaction equilibrium as determined by thermodynamics.

The function of our model enzyme is most prominently dictated by the geometry of the enzyme-substrate complex, and can be optimized by following three simple golden rules: (i) the enzyme and the molecule should be attached at the smaller end of each; (ii) the conformational change of the enzyme must be comparable to or larger than the conformational change required of the molecule; (iii) the conformational change of the enzyme must be fast enough. These parameters can be experimentally tuned when designing an artificial enzyme, and should be experimentally accessible when investigating

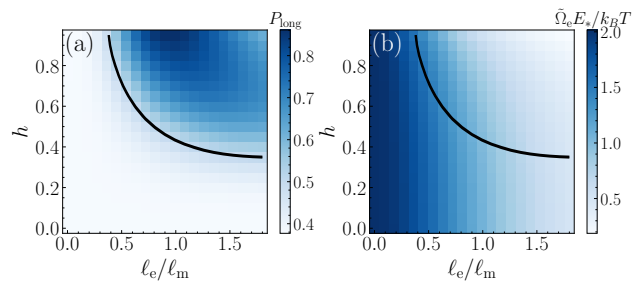


FIG. 7. (a) Probability of finding the shape-switching molecule in the long state and (b) energy dissipation rate, versus the length ratio ℓ_e/ℓ_m and the coupling strength h . The black line corresponds to $P_{\text{long}} = 0.5$. The noise strength is $k_B T/\Delta = 0.2$.

the function of biological enzymes. Interestingly, the effectiveness of the enzyme (as measured by successful catalytic action) and its energy dissipation do not follow a one-to-one relation (Fig. 7), leaving additional room for the optimization of not just the enzyme effectiveness but its energetic efficiency.

We were able to understand the emergence of a strong coupling between the thermodynamically favourable and unfavourable reactions to be a result of a global bifurcation in the deterministic dynamics of the system, of a similar nature to that causing synchronization and phase-locking among mechanically-coupled enzymes [35, 47]. Importantly, however, by adding thermodynamically-consistent fluctuations to the theory, we showed that the effect survives in the presence of noise, and we could calculate important quantities such as non-equilibrium steady states reflecting the departure from equilibrium thermodynamics in the reaction equilibrium, and first passage time distributions for the catalyzed reaction.

Our approach readily allows us to probe the energetic aspects of the non-equilibrium reaction [58], and in particular, the entropy production due to the coupling between the mechanical and the chemical degrees of freedom [59]. It can also be used to study evolutionary advantages of having mechanical control during the catalytic process via conformational changes, as opposed to simple utilization of the uncontrolled metal-based catalysis.

In conclusion, our model introduces new and important features to serve as a minimal model of a fuelled catalyst. This opens an avenue towards further progress in understanding and designing bio-inspired systems for artificial catalysis.

ACKNOWLEDGMENTS

We acknowledge discussions with Navdeep Rana regarding the numerical integrators. We acknowledge support from the Max Planck School Matter to Life and the MaxSynBio Consortium which are jointly funded by the

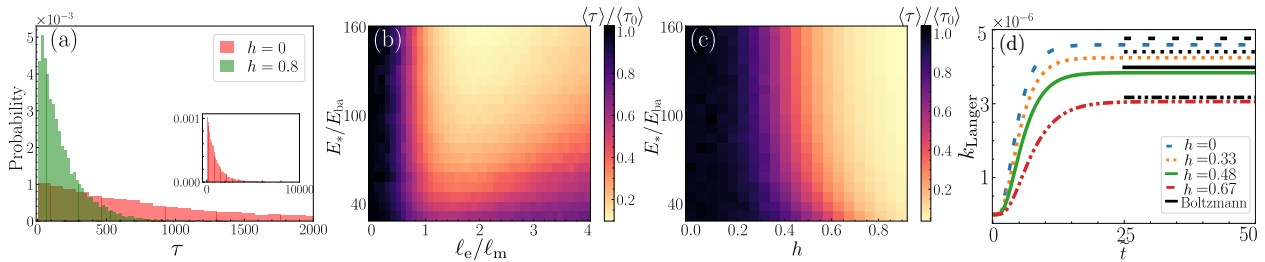


FIG. 8. (a) Distribution of first passage times τ for $\ell_e/\ell_m = 1.6$ in the absence (red) and presence (green) of dissipative coupling. (b,c) Mean first passage time $\langle\tau\rangle$, normalized by the mean first passage time in the uncoupled case where $\ell_e/\ell_m = 0$, as a function of the length ratio ℓ_e/ℓ_m and the energy ratio E_*/E_{ba} for fixed value of coupling strength $h = 0.48$ (a), and as a function of the coupling strength h and E_*/E_{ba} for fixed $\ell_e/\ell_m = 1$ in (b). In (a-c), the noise strength is $k_B T/\Delta = 0.15$. (d) The rate at which the saddle point marked as the red diamond in Fig. 3 is crossed extracted numerically (coloured lines) compared to the Langer rate given by Eq. (16) (black horizontal lines), for $E_{ba}/\Delta = 0.8$ and $k_B T/\Delta = 0.08$.

Federal Ministry of Education and Research (BMBF) of Germany and the Max Planck Society.

Appendix A: Derivation of the phase-equations

We consider an enzyme and a molecule, both assumed to be dumbbell-shaped for simplicity. Upon binding, they are considered to be tightly linked together, thus forming a complex with three sub-units. The position vectors of the three sub-units are \mathbf{r}_e , \mathbf{r}_b and \mathbf{r}_m for the enzyme-only sub-unit, the bound enzyme-substrate sub-unit, and the molecule-only sub-unit, respectively. The lengths of the enzyme and molecule are therefore $\mathbf{L}_e = \mathbf{r}_b - \mathbf{r}_e = L_e \hat{\mathbf{n}}$ and $\mathbf{L}_m = \mathbf{r}_m - \mathbf{r}_b = L_m \hat{\mathbf{n}}$ where $\hat{\mathbf{n}}$ is the unit vector along the axis of the complex. The equations of motion for the sub-units are $\dot{r}_e = -\mu_e f_e$, $\dot{r}_b = \mu_b (f_e - f_m)$ and $\dot{r}_m = \mu_m f_m$, where f_e and f_m are the internal mechanical forces (stresses) of the enzyme and molecule, respectively, which can be expressed as $f_e = -\partial_{L_e} U(L_e, \phi_e)$ and $f_m = -\partial_{L_m} V_m(L_m)$. This implies that the equations of motion for the lengths are $\dot{L}_e = \mu_1 f_e - \mu_b f_m$ and $\dot{L}_m = -\mu_b f_e + \mu_2 f_m$, with the mobilities given as $\mu_1 \equiv \mu_e + \mu_b$ and $\mu_2 \equiv \mu_m + \mu_b$.

The governing dynamical equations for the two effective geometric degrees of freedom are therefore given by

$$\dot{L}_e = -\mu_1 k [L_e - L(\phi_e)] + \mu_b \partial_{L_m} V_m(L_m), \quad (\text{A1})$$

$$\dot{L}_m = \mu_b k [L_e - L(\phi_e)] - \mu_2 \partial_{L_m} V_m(L_m). \quad (\text{A2})$$

The dynamics of the internal enzyme phase is in turn given by

$$\begin{aligned} \dot{\phi}_e &= \mu_\phi [-\partial_{\phi_e} U(L_e, \phi_e)], \\ &= -\mu_\phi [-k(L_e - L(\phi_e))L'(\phi_e) + V'_e(\phi_e)], \end{aligned} \quad (\text{A3})$$

with the prime representing a derivative with respect to ϕ_e . We define $\delta L_e \equiv L_e - L(\phi_e)$ such that $\dot{L}_e = \delta \dot{L}_e + L'(\phi_e) \dot{\phi}_e$. If the enzyme is relatively stiff with the timescale $(\mu_1 k)^{-1}$ being much shorter than the timescale of changes in the internal phase, the enzyme length will

quickly adapt to changes of the preferred length, and thus $\delta \dot{L}_e \approx 0$. From Eq. (A1), this implies

$$L'(\phi_e) \dot{\phi}_e \approx -\mu_1 k [L_e - L(\phi_e)] + \mu_b \partial_{L_m} V(L_m), \quad (\text{A4})$$

which allows us to eliminate $k[L_e - L(\phi_e)]$ between Eqs. (A2) and (A4), hence projecting the dynamics onto the slow manifold (ϕ_e, L_m) . Finally, we reexpress L_m in terms of the dimensionless reaction coordinate ϕ_m through $L_m = L_m^{(0)} + \ell_m \phi_m$. The resulting governing equations for (ϕ_e, ϕ_m) then reduce to Eq. (1).

Appendix B: Reverse switch reaction

One can observe that for the switch reaction our enzyme is equally capable of catalyzing a reverse reaction, i.e. from long to short conformational state, by choosing $\varepsilon < 0$. Exploiting the symmetries of our dynamical equations, we find that a π phase shift will be needed for ϕ_e in the conformation cycle (Eq. (8)), as in this case the enzyme will first contract and then expand during its conformational change. A phase portrait of the deterministic dynamics at strong coupling (beyond the global bifurcation) is shown in Fig. 9(a). This can be compared to the dynamics of the forward switch reaction in Fig. 3(d). Note that the bifurcation now happens near the upper saddle point, where the blue solid line represents the flow from the long state to the short state. An example of the NESS distributions for this reverse case is shown in Fig. 9(b), which may be compared to the case of the forward reaction in Fig. 5(b). It highlights how the action of the enzyme can favour the short state even if the long state is thermodynamically preferred.

Appendix C: Simulations

To generate the phase portraits in Fig. 3 and the parameter scan in Fig. 4 from the deterministic equations (Eq. (1)), we used the built-in *ode45* integrator

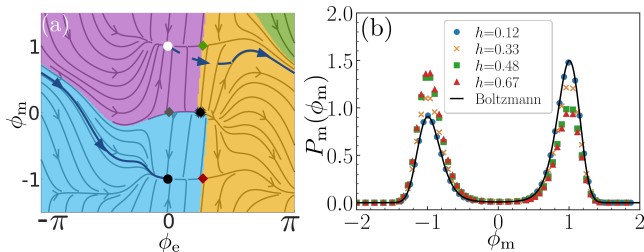


FIG. 9. Reverse switch reaction. (a) Phase-portrait for $h = 0.48$, $\ell_e/\ell_m = 2.5$, and $\varepsilon/\Delta = -0.1$. The black solid line represents a deterministic trajectory. (b) Marginal distributions of the molecule reaction coordinate in steady-state, for various values of the coupling strength. (a) and (b) can be respectively compared to Fig. 3(d) and Fig. 5(b) for the forward reaction.

of MATLAB, which uses a fourth order Runge-Kutta method [60]. A grid of 201×201 for $-\pi < \phi_e < \pi$ and $-2 < \phi_m < 2$ was used to generate the initial conditions, and the equations were integrated for a total time of $\tilde{t}_{\text{tot}} = 120$.

For the numerical integration of the Fokker-Planck equation given by Eq. (5) we used a custom code written in Python [61]. The code uses a finite difference method with fourth-order accuracy for the spatial derivatives and fourth order Runge-Kutta method for the time integration. For the enzyme coordinate ϕ_e we considered the domain $0 \leq \phi_e < 2\pi$ with periodic boundary conditions. For the molecule coordinate ϕ_m , we used Dirichlet boundary conditions in the domains $[-1.8, 1.8]$, $[-2.0, 2.0]$, $[-2.2, 2.2]$ and noise strengths $k_B T/\Delta = 0.15, 0.2, 0.4$. To discretize the domains we used a rectangular shape domain such that the finite-difference increments satisfied $\Delta\phi_e \simeq \Delta\phi_m$ and thus the integrator would be more stable. For $k_B T/\Delta = 0.15, 0.2, 0.4$ the corresponding number of points (N_1, N_2) per side were (512, 128), (400, 128), (300, 100), and the time step was $\Delta\tilde{t} = 10^{-3}, 10^{-3}, 5 \cdot 10^{-4}$.

For the numerical integration of the Langevin equations in Eq. (7), we used a custom code written in Julia [62]. The Euler-Maruyama method was used for the numerical integration. The time step used was $\Delta\tilde{t} = 10^{-3}$.

To check for consistency between the Langevin and Fokker-Planck approaches, long trajectories from the solution of the Langevin equations were binned and compared with the steady state distribution predicted by the Fokker-Planck equation. The two approaches exhibit good agreement, as depicted in Fig. 10 for the case of $h = 0.67$ and $k_B T/\Delta = 0.2$.

Appendix D: Steady state distribution for an uncoupled enzyme

In the uncoupled case with $h = 0$ or $\ell_e/\ell_m = 0$, an exact expression for the steady state probability distribution for ϕ_e can be found. In the absence of coupling,

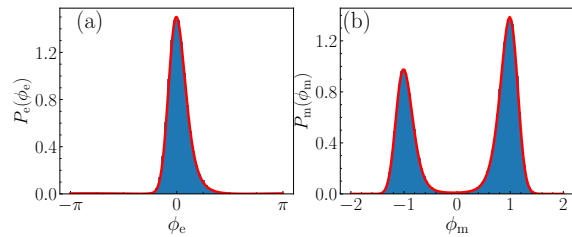


FIG. 10. Comparison of the marginal distributions obtained from the Fokker-Planck equation (red solid line) at steady state and long simulations of the Langevin equations (histogram). (a) and (b) show the distribution of the enzyme and molecule reaction coordinates, respectively. The parameters for this example are $h = 0.67$ and $k_B T/\Delta = 0.2$.

the dynamics of ϕ_e at the steady state is determined by solving the following equation for a constant flux

$$J_e = -M_{ee}(\phi_e)[V_e'(\phi_e)P_e + k_B T \partial_{\phi_e} P_e]. \quad (\text{D1})$$

Integrating this equation, we obtain

$$P_e = e^{-V_e(\phi_e)/k_B T} \left[C - J_e \int_0^{\phi_e} M_{ee}^{-1}(x) e^{V_e(x)/k_B T} dx \right], \quad (\text{D2})$$

where C and J_e are constants of integration and are determined by the boundary conditions. Note that $M_{ee}(\phi_e)$ and $V_e'(\phi_e)$ are both 2π -periodic. This implies that the probability distribution is also periodic, by following a similar derivation as in Ref. [53]. One finds that $C = \mathcal{N}I$ and $(1 - e^{-2\pi F/k_B T})\mathcal{N} = J_e$, with \mathcal{N} a normalization constant and

$$I = \int_0^{2\pi} dx M_{ee}^{-1}(x) e^{V_e(x)/k_B T}. \quad (\text{D3})$$

Hence, the full expression for the steady state marginal probability distribution for the enzyme reaction coordinate in the uncoupled case is

$$P_e(\phi_e) = \mathcal{N} \left[\int_{\phi_e}^{2\pi} dx M_{ee}^{-1}(x) \exp\left(\frac{V_e(x) - V_e(\phi_e)}{k_B T}\right) + \int_0^{\phi_e} dx M_{ee}^{-1}(x) \exp\left(\frac{V_e(x) - V_e(\phi_e) - 2\pi F}{k_B T}\right) \right]. \quad (\text{D4})$$

The form of V_e does not readily lend itself to further analytical progress, and we integrate Eq. (D4) numerically to obtain the black lines in Fig. 5(a,c). In the particular case $E_* = 0$, we find that $J_e = 0$ and thus the enzyme coordinate is in thermodynamic equilibrium described by the Boltzmann weight $P_e(\phi_e) \propto e^{-V_e(\phi_e)/k_B T}$.

Appendix E: Langer rate

Starting from the Fokker-Planck equation, one derives the Langer rate through the enzyme saddle point to be

[9, 56, 57]

$$k_{\text{Langer}} = \frac{|\Lambda_-|}{2\pi} \frac{\sqrt{\lambda_e^{(0)} \lambda_m^{(0)}}}{\sqrt{|\lambda_e| \lambda_m}} \exp\left(-\frac{E_{\text{ba}}}{k_B T}\right), \quad (\text{E1})$$

where $\lambda_\alpha^{(0)} = V''_\alpha(\phi_\alpha)|_{\text{min}}$, and $\lambda_\alpha = V''_\alpha(\phi_\alpha)|_{\text{saddle}}$, namely, the corresponding values evaluated around the saddle point. The definitions imply that $\lambda_m = \lambda_m^{(0)}$, and thus, they cancel each other in Eq. (E1). Finally, Λ_- is

the negative eigenvalue of the matrix $\lambda_\alpha M_{\alpha\beta}$ evaluated around the saddle point which is given by

$$\Lambda_- = \frac{1}{2} \left(M_{ee} \lambda_e + M_{mm} \lambda_m - \sqrt{(M_{ee} \lambda_e - M_{mm} \lambda_m)^2 + 4M_{em}^2 \lambda_e \lambda_m} \right). \quad (\text{E2})$$

-
- * j.agudo-canalejo@ucl.ac.uk
 † ramin.golestanian@ds.mpg.de
- [1] S. Borsley, D. A. Leigh, and B. M. W. Roberts, Molecular Ratchets and Kinetic Asymmetry: Giving Chemistry Direction, *Angew. Chem. Int. Ed.* **63**, e202400495 (2024).
- [2] L. Michaelis and M. L. Menten, Die kinetik der invertinwirkung, *Biochemische Zeitschrift* **49**, 333 (1913).
- [3] K. A. Johnson and R. S. Goody, The Original Michaelis Constant: Translation of the 1913 Michaelis–Menten Paper, *Biochemistry* **50**, 8264 (2011).
- [4] H. Qian, Phosphorylation energy hypothesis: Open chemical systems and their biological functions, *Annu. Rev. Phys. Chem.* **58**, 113 (2007).
- [5] H. P. Lu, Single-molecule enzymatic dynamics, *Science* **282**, 1877–1882 (1998).
- [6] B. P. English, W. Min, A. M. van Oijen, K. T. Lee, G. Luo, H. Sun, B. J. Cherayil, S. C. Kou, and X. S. Xie, Ever-fluctuating single enzyme molecules: Michaelis–Menten equation revisited, *Nat. Chem. Biol.* **2**, 87–94 (2005).
- [7] S. Kou, B. J. Cherayil, W. Min, B. P. English, and X. S. Xie, Single-molecule michaelis–menten equations, *J. Phys. Chem. B* **109**, 19068 (2005).
- [8] H. Kramers, Brownian motion in a field of force and the diffusion model of chemical reactions, *Physica* **7**, 284 (1940).
- [9] P. Hänggi, P. Talkner, and M. Borkovec, Reaction-rate theory: fifty years after Kramers, *Rev. Mod. Phys.* **62**, 251 (1990).
- [10] M. Karplus and J. A. McCammon, Molecular dynamics simulations of biomolecules, *Nat. Struct. Mol. Biol.* **9**, 646 (2002).
- [11] C. Kutzner, S. Páll, M. Fechner, A. Esztermann, B. L. de Groot, and H. Grubmüller, More bang for your buck: Improved use of GPU nodes for GROMACS 2018, *J. Comput. Chem.* **40**, 2418–2431 (2019).
- [12] S. L. Lovelock, R. Crawshaw, S. Basler, C. Levy, D. Baker, D. Hilvert, and A. P. Green, The road to fully programmable protein catalysis, *Nature* **606**, 49 (2022).
- [13] A. H.-W. Yeh, C. Norn, Y. Kipnis, D. Tischer, S. J. Pellock, D. Evans, P. Ma, G. R. Lee, J. Z. Zhang, I. Anishchenko, B. Coventry, L. Cao, J. Dauparas, S. Halabiya, M. DeWitt, L. Carter, K. N. Houk, and D. Baker, De novo design of luciferases using deep learning, *Nature* **614**, 774–780 (2023).
- [14] C. Dallago and K. K. Yang, Illuminating enzyme design using deep learning, *Nat. Chem.* **15**, 749–750 (2023).
- [15] M. Kathan, S. Crespi, N. O. Thiel, D. L. Stares, D. Morsa, J. de Boer, G. Pacella, T. van den Enk, P. Kobauri, G. Portale, C. A. Schalley, and B. L. Feringa, A light-fuelled nanoratchet shifts a coupled chemical equilibrium, *Nat. Nanotechnol.* **17**, 159–165 (2021).
- [16] S. Corra, M. T. Bakić, J. Groppi, M. Baroncini, S. Silvi, E. Penocchio, M. Esposito, and A. Credi, Kinetic and energetic insights into the dissipative non-equilibrium operation of an autonomous light-powered supramolecular pump, *Nat. Nanotechnol.* **17**, 746–751 (2022).
- [17] A. Sorrenti, J. Leira-Iglesias, A. Sato, and T. M. Hermans, Non-equilibrium steady states in supramolecular polymerization, *Nat. Commun.* **8** (2017).
- [18] A.-K. Pumm, W. Engelen, E. Kopperger, J. Isensee, M. Vogt, V. Kozina, M. Kube, M. N. Honemann, E. Bertolin, M. Langecker, R. Golestanian, F. C. Simmel, and H. Dietz, A DNA origami rotary ratchet motor, *Nature* **607**, 492–498 (2022).
- [19] S. Osat, J. Metson, M. Kardar, and R. Golestanian, Escaping kinetic traps using nonreciprocal interactions, *Phys. Rev. Lett.* **133**, 028301 (2024).
- [20] S. Osat and R. Golestanian, Non-reciprocal multifarious self-organization, *Nat. Nanotechnol.* **18**, 79 (2023).
- [21] V. Ouazan-Reboul, J. Agudo-Canalejo, and R. Golestanian, Self-organization of primitive metabolic cycles due to non-reciprocal interactions, *Nat. Commun.* **14**, 4496 (2023).
- [22] D. R. Glowacki, J. N. Harvey, and A. J. Mulholland, Taking ockham's razor to enzyme dynamics and catalysis, *Nat. Chem.* **4**, 169 (2012).
- [23] R. Callender and R. B. Dyer, The dynamical nature of enzymatic catalysis, *Acc. Chem. Res.* **48**, 407 (2014).
- [24] F. Jülicher, A. Ajdari, and J. Prost, Modeling molecular motors, *Rev. Mod. Phys.* **69**, 1269 (1997).
- [25] A. B. Kolomeisky and M. E. Fisher, Molecular motors: A theorist's perspective, *Annu. Rev. Phys. Chem.* **58**, 675–695 (2007).
- [26] M. L. Mugnai, C. Hyeon, M. Hinczewski, and D. Thirumalai, Theoretical perspectives on biological machines, *Rev. Mod. Phys.* **92**, 025001 (2020).
- [27] X. Shi, A.-K. Pumm, J. Isensee, W. Zhao, D. Verschuere, A. Martin-Gonzalez, R. Golestanian, H. Dietz, and C. Dekker, Sustained unidirectional rotation of a self-organized DNA rotor on a nanopore, *Nat. Phys.* **18**, 1105–1111 (2022).
- [28] X. Shi, A.-K. Pumm, C. Maffeo, F. Kohler, E. Feigl, W. Zhao, D. Verschuere, R. Golestanian, A. Aksimentiev, H. Dietz, and C. Dekker, A DNA turbine powered by a transmembrane potential across a nanopore, *Nat. Nanotechnol.* (2023).




- [29] R. Golestanian, Synthetic mechanochemical molecular swimmer, *Phys. Rev. Lett.* **105**, 018103 (2010).
- [30] R. Golestanian and A. Ajdari, Mechanical response of a small swimmer driven by conformational transitions, *Phys. Rev. Lett.* **100**, 038101 (2008).
- [31] R. Golestanian, Anomalous diffusion of symmetric and asymmetric active colloids, *Phys. Rev. Lett.* **102**, 188305 (2009).
- [32] R. Golestanian, Enhanced diffusion of enzymes that catalyze exothermic reactions, *Phys. Rev. Lett.* **115**, 108102 (2015).
- [33] P. Illien, T. Adeleke-Larodo, and R. Golestanian, Diffusion of an enzyme: The role of fluctuation-induced hydrodynamic coupling, *EPL* **119**, 40002 (2017).
- [34] J. Agudo-Canalejo, T. Adeleke-Larodo, P. Illien, and R. Golestanian, Enhanced diffusion and chemotaxis at the nanoscale, *Acc. Chem. Res.* **51**, 2365–2372 (2018).
- [35] J. Agudo-Canalejo, T. Adeleke-Larodo, P. Illien, and R. Golestanian, Synchronization and enhanced catalysis of mechanically coupled enzymes, *Phys. Rev. Lett.* **127**, 208103 (2021).
- [36] Z. Zeravcic and M. P. Brenner, Self-replicating colloidal clusters, *Proc. Natl. Acad. Sci. U.S.A.* **111**, 1748–1753 (2014).
- [37] Z. Zeravcic and M. P. Brenner, Spontaneous emergence of catalytic cycles with colloidal spheres, *Proc. Natl. Acad. Sci. U.S.A.* **114**, 4342–4347 (2017).
- [38] Z. Zeravcic, V. N. Manoharan, and M. P. Brenner, Colloquium: Toward living matter with colloidal particles, *Rev. Mod. Phys.* **89**, 031001 (2017).
- [39] O. Rivoire, Geometry and flexibility of optimal catalysts in a minimal elastic model, *J. Phys. Chem. B* **124**, 807–813 (2020).
- [40] M. Muñoz-Basagoiti, O. Rivoire, and Z. Zeravcic, Computational design of a minimal catalyst using colloidal particles with programmable interactions, *Soft Matter* **19**, 3933 (2023).
- [41] O. Rivoire, How flexibility can enhance catalysis, *Phys. Rev. Lett.* **131**, 088401 (2023).
- [42] B. Alberts, D. Bray, J. Lewis, M. Raff, K. Roberts, J. D. Watson, *et al.*, *Molecular biology of the cell*, Vol. 3 (Garland New York, 1994).
- [43] S. Borsley, D. A. Leigh, and B. M. W. Roberts, Chemical fuels for molecular machinery, *Nat. Chem.* **14**, 728 (2022).
- [44] R. Astumian and M. Bier, Mechanochemical coupling of the motion of molecular motors to ATP hydrolysis, *Biophys. J.* **70**, 637 (1996).
- [45] J. L. Eide, A. K. Chakraborty, and G. F. Oster, Simple models for extracting mechanical work from the ATP hydrolysis cycle, *Biophys. J.* **90**, 4281 (2006).
- [46] M. Chatzittofi, R. Golestanian, and J. Agudo-Canalejo, Collective synchronization of dissipatively-coupled noise-activated processes, *New J. Phys.* **25**, 093014 (2023).
- [47] M. Chatzittofi, R. Golestanian, and J. Agudo-Canalejo, Topological phase locking in molecular oscillators, *arXiv:2310.11788* (2023).
- [48] S. Lu, S. Li, and J. Zhang, Harnessing allostery: A novel approach to drug discovery, *Med. Res. Rev.* **34**, 1242 (2014).
- [49] M. J. Hehir, J. E. Murphy, and E. R. Kantrowitz, Characterization of heterodimeric alkaline phosphatases from *Escherichia coli*: An investigation of intragenic complementation, *J. Mol. Biol.* **304**, 645 (2000).
- [50] S. R. De Groot and P. Mazur, *Non-equilibrium thermodynamics* (Courier Corporation, 2013).
- [51] S. Kim and S. J. Karrila, *Microhydrodynamics: principles and selected applications* (Courier Corporation, 2013).
- [52] M. Chatzittofi, J. Agudo-Canalejo, and R. Golestanian, Nonlinear response theory of molecular machines, *EPL* **147**, 21002 (2024).
- [53] H. Risken, Fokker-Planck equation, in *The Fokker-Planck Equation* (Springer, 1996) pp. 63–95.
- [54] P. Reimann, C. Van den Broeck, H. Linke, P. Hänggi, J. M. Rubi, and A. Pérez-Madrid, Giant acceleration of free diffusion by use of tilted periodic potentials, *Phys. Rev. Lett.* **87**, 010602 (2001).
- [55] P. Reimann, C. Van den Broeck, H. Linke, P. Hänggi, J. M. Rubi, and A. Pérez-Madrid, Diffusion in tilted periodic potentials: Enhancement, universality, and scaling, *Phys. Rev. E* **65**, 031104 (2002).
- [56] J. S. Langer, Theory of nucleation rates, *Phys. Rev. Lett.* **21**, 973 (1968).
- [57] J. Langer, Statistical theory of the decay of metastable states, *Ann. Phys.* **54**, 258 (1969).
- [58] G. Ragazzon and L. J. Prins, Energy consumption in chemical fuel-driven self-assembly, *Nat. Nanotechnol.* **13**, 882–889 (2018).
- [59] M. Chatzittofi, J. Agudo-Canalejo, and R. Golestanian, Entropy production and thermodynamic inference for stochastic microswimmers, *Phys. Rev. Res.* **6**, L022044 (2024).
- [60] T. M. Inc., *Matlab version: 9.14.0 (r2023a)* (2023).
- [61] G. Van Rossum and F. L. Drake, *Python 3 Reference Manual* (CreateSpace, Scotts Valley, CA, 2009).
- [62] J. Bezanson, S. Karpinski, V. B. Shah, and A. Edelman, Julia: A fast dynamic language for technical computing, *arXiv:1209.5145* (2012).

Chapter 5

Thermodynamic inference of correlations in nonequilibrium collective dynamics

This chapter is reproduced from a version of the article *Phys. Rev. Research* **6**, L042012[134] which is published in Physical Review Research. In this work, I contributed in designing the research and the numerical code in Julia for the numerical calculations, and I also performed the analytical calculations. I contributed in the analysis of the results and writing/editing the paper.

Thermodynamic inference of correlations in nonequilibrium collective dynamics

Michalis Chatzittofi ¹, Ramin Golestanian ^{1,2,*}, and Jaime Agudo-Canalejo ^{1,3,†}

¹Department of Living Matter Physics, Max Planck Institute for Dynamics and Self-Organization, D-37077 Göttingen, Germany

²Rudolf Peierls Centre for Theoretical Physics, University of Oxford, Oxford OX1 3PU, United Kingdom

³Department of Physics and Astronomy, University College London, London WC1E 6BT, United Kingdom



(Received 23 August 2024; accepted 30 September 2024; published 11 October 2024)

The theory of stochastic thermodynamics has revealed many useful fluctuation relations, with the thermodynamic uncertainty relation (TUR) being a theorem of major interest. When many nonequilibrium currents interact with each other, a naive application of the TUR to an individual current can result in an apparent violation of the TUR bound. Here, we explore how such an apparent violation can be used to put a lower bound on the strength of correlations C as well as the number N of interacting currents in collective dynamics. This lower bound is a combined bound on $C(N - 1)$ if only one current is measured, or a bound on N if two currents are measured. Our proposed protocol allows for the inference of hidden correlations in experiment, for example when a team of molecular motors pulls on the same cargo but only one or a subset of them is fluorescently tagged. By solving analytically and numerically several models of many-body nonequilibrium dynamics, we ascertain under which conditions this strategy can be applied and the inferred bound on correlations becomes tight.

DOI: [10.1103/PhysRevResearch.6.L042012](https://doi.org/10.1103/PhysRevResearch.6.L042012)

Introduction. Entropy production rate (EPR) is the measure of nonequilibrium activity in a stochastic system and is tied to the existence of nonequilibrium currents in the system [1,2]. The thermodynamic uncertainty relation (TUR) [3] quantifies the tradeoff between EPR and the precision of the nonequilibrium currents, where precision is related to the ratio between the average and the standard deviation of the fluctuating currents. The TUR, which has been proven rigorously [4,5] and has been confirmed in experiments [6,7], has found its most practical application in the inference of (lower bounds for) nonequilibrium driving forces given experimental measurements of fluctuating currents [8,9]. Relevant experimental systems include active matter [10], molecular machines [11] such as motors [12] and enzymes [13], stochastic oscillators [14–17], microscopic heat engines [18], artificial nanorotors [19,20], and even in open quantum systems [21,22]. Additionally, the TUR has also inspired other important thermodynamic relations [23–25], placing bounds on, e.g., the extent of anomalous diffusion [26], the asymmetry of crosscorrelations [27], and correlation times [28].

In its original form, the TUR for a nonequilibrium system in steady state was proposed for a scalar (one dimensional) fluctuating current and can be expressed as [3]

$$\mathcal{J}^2/D_{\mathcal{J}} \leq \dot{\sigma}/k_B, \quad (1)$$

where \mathcal{J} represents the steady state average of the scalar observable current of interest, $D_{\mathcal{J}}$ the diffusion coefficient associated to the corresponding fluctuating observable, $\dot{\sigma}$ the steady state average EPR, and k_B the Boltzmann constant. An important generalization to vectorial fluctuating currents, or equivalently to several scalar currents that are simultaneously observed, is the multidimensional thermodynamic uncertainty relation (MTUR) given by [29]

$$\mathcal{J}^T \cdot \mathcal{D}^{-1} \cdot \mathcal{J} \leq \dot{\sigma}/k_B, \quad (2)$$

where \mathcal{J} is now the steady state average of the vectorial observable current and \mathcal{D} is the covariance tensor associated with the fluctuating multidimensional observable. The MTUR allows for the inference of tighter lower bounds on the entropy production in systems with multiple degrees of freedom, when more than one observable can be tracked simultaneously, for example, in interacting many-body systems [30]. Alternatively, one may use the MTUR together with known mechanistic information about the coupling between degrees of freedom to obtain tighter bounds on dissipation even when only one observable is tracked, as recently proposed for stochastic swimmers with coupled chemical and mechanical degrees of freedom [31].

In this Letter, we propose to turn the MTUR on its head and exploit it to infer the existence of hidden correlations in a system, even when only a single observable is experimentally accessible. We show that this is possible in systems satisfying two simple conditions: (i) many statistically identical processes interact with each other, and (ii) the observable quantities are tightly coupled to entropy production, with a known rate of entropy production per step. This may, for example, represent ensembles of identical molecular motors walking on the same biofilament [32,33], clustered enzymes catalyzing chemical reactions in a metabolon [34,35],

*Contact author: ramin.golestanian@ds.mpg.de

†Contact author: j.agudo-canalejo@ucl.ac.uk

Published by the American Physical Society under the terms of the [Creative Commons Attribution 4.0 International](https://creativecommons.org/licenses/by/4.0/) license. Further distribution of this work must maintain attribution to the author(s) and the published article's title, journal citation, and DOI. Open access publication funded by Max Planck Society.

clustered rotors or channels in a membrane [36,37], or driven colloids in an optical ring [38–40]. We will first introduce the general strategy, valid for any system that satisfies the two conditions just described. We will then study two toy models that are analytically solvable, and two models that we solve numerically, in order to ascertain under which conditions the proposed strategy can be applied, and when does the inferred bound on correlations become tight.

Inference of correlations. We consider N stochastic processes that are identical, in the sense that they are governed by the identical underlying stochastic dynamics, and are all to all coupled in a statistical sense, i.e., will show identical pair correlations with each other after a sufficiently long observation time (as expected in an ergodic system). Let us denote the associated scalar observables as (ϕ_1, \dots, ϕ_N) . Quantitatively, the conditions just described imply that all scalar observables have the same average current $\Omega \equiv \lim_{t \rightarrow \infty} \langle \phi_i \rangle / t$, the same diffusion coefficient $D \equiv \lim_{t \rightarrow \infty} (\langle \phi_i^2 \rangle - \langle \phi_i \rangle^2) / (2t)$, and the same pair correlation strength $C \equiv \lim_{t \rightarrow \infty} (\langle \phi_i \phi_j \rangle - \langle \phi_i \rangle \langle \phi_j \rangle) / \sqrt{(\langle \phi_i^2 \rangle - \langle \phi_i \rangle^2)(\langle \phi_j^2 \rangle - \langle \phi_j \rangle^2)}$ (for $i \neq j$). Note that C is bounded between $-1/(N-1)$ for maximally anticorrelated processes and $+1$ for perfectly correlated processes. Lastly, we assume that the observable currents are driven by energy dissipation (entropy production) through a tightly coupled mechanism [3,16,17,30,41–43] so that, for every individual current, we can write an average energy dissipation rate that is proportional to the average current $\dot{\sigma}^{(1)} T \equiv \Omega \Delta \mu$, with $\Delta \mu$ the energy dissipated per step and T the temperature of the bath. The total EPR in the system is then $\dot{\sigma} = N \dot{\sigma}^{(1)}$.

With these choices, application of the MTUR [Eq. (2)] and a rearrangement of the terms result in the inequality

$$\frac{\Omega k_B T}{D \Delta \mu} - 1 \leq C(N-1), \quad (3)$$

which puts a lower bound on the correlation strength C (and the number of interacting processes N) given a measurement of the average current Ω and the diffusion coefficient D , and provided that the dissipation per step $\Delta \mu$ is known. We note that Eq. (3) can also be obtained by applying the standard TUR [Eq. (1)] to the observable corresponding to the total sum $\sum_i \phi_i$.

To get an intuition for the meaning of Eq. (3), it is useful to note that its left hand side represents a measure of the violation of a naively applied single-current TUR. Indeed, for a single isolated or noninteracting current, the standard TUR [Eq. (1)] gives $\frac{\Omega k_B T}{D \Delta \mu} \leq 1$ [consistent with Eq. (3) with $N = 1$ or $C = 0$]. Thus, if measurement of a single observable appears to violate (outperform) this naive TUR, it implies that the left hand side of Eq. (3) is positive, and therefore that there must be positive correlations in the system ($C > 0$ and $N \geq 2$). If, on the other hand, the naive TUR is satisfied, it means that the measurement is compatible with the absence of correlations in the system, and Eq. (3) only serves to rule out negative correlations stronger than those allowed by the bound.

When a single observable is tracked, e.g., when only one molecular motor within a team is fluorescently labeled, Eq. (3) puts a combined lower bound on the correlation strength C and number of interacting processes N , see Fig. 1(a). If one

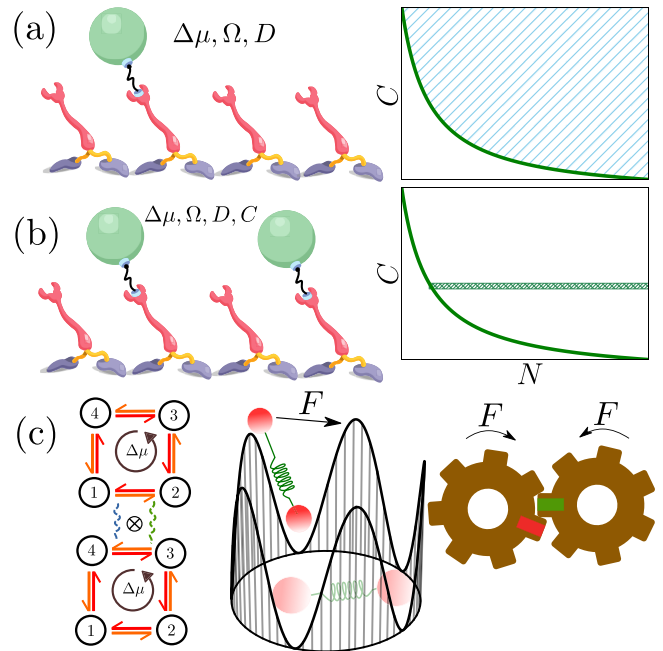


FIG. 1. (a) Measurement of a single observable (here, the position of a fluorescently-tagged molecular motor) allows for inference of a combined bound on the strength of correlations C and the number of interacting processes N . (b) Simultaneous measurement of two observables fixes the strength of correlations and places a bound on the number of interacting processes N . (c) Examples of coupled identical processes: two discrete biomolecular processes driven by a cyclic affinity $\Delta \mu$; two colloids in an optical ring driven by a constant force F ; two molecular gears driven by a constant force F .

can additionally measure the correlation strength, e.g., if two or more motors within the team are labeled, one can infer a lower bound on the number of processes N , see Fig. 1(b). In the following, we present several minimal models [Fig. 1(c)] that allow us to ascertain the conditions under which the naive TUR is broken and the proposed strategy can be applied, and those for which the inferred bound of Eq. (3) becomes tight.

Discrete coupled processes. We first consider a rather generic example of coupled discrete Markov processes, which might represent various interacting or coupled biomolecular processes such as molecular motors walking on a track, or chemical reactions catalyzed by nearby enzymes or different monomers in a multimeric enzyme. As an example, in Fig. 2(a) we show two identical one-dimensional processes where the red (orange) arrow indicates the forward (backward) rate k_+ (k_-). For local detailed balance to be satisfied, one must impose that $k_+/k_- = e^{\Delta \mu / k_B T}$, where $\Delta \mu$ represents the energy dissipated per transition. The simultaneous dynamics of the two processes can alternatively be viewed as taking place on a two-dimensional lattice of Markov states as shown in Fig. 2(b), where transitions of one process or the other correspond to hopping horizontally or vertically on the two-dimensional lattice. To include interactions between the two processes, coupling rates h_{\pm} are introduced which are represented by the green and blue squiggles in Fig. 2(a) and arrows in Fig. 2(b). These correspond to diagonal jumps in the lattice, which imply a forward or backward

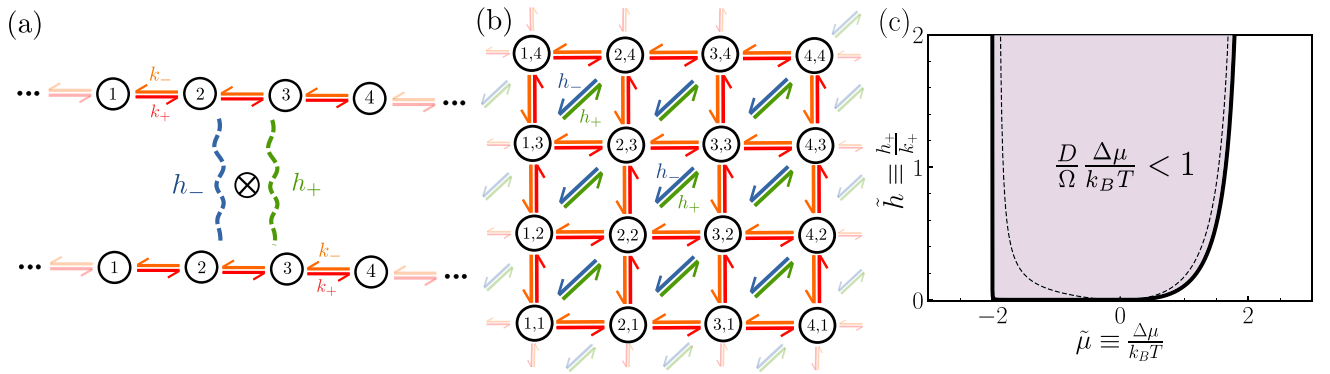


FIG. 2. (a) Two identical discrete processes modeled as biased one-dimensional random walks, with red (orange) arrows indicating forward (backward) transitions with rates k_{\pm} . Interactions between the two processes are represented by the green and blue squiggles. (b) The “outer product” of the two one-dimensional processes corresponds to a two-dimensional lattice, where the tuples indicate the internal state of the whole system. Interactions are governed by the green and blue arrows, representing simultaneous forward and backward transitions for both processes with rates h_{\pm} . (c) Parameter space spanned by the nonequilibrium driving force $\tilde{\mu} \equiv \Delta\mu/k_B T$ and the coupling strength $\tilde{h} \equiv h_+/k_+$, showing the regime in which the naive TUR is broken, and thus the existence of nonzero correlations could be inferred in experiment, for a large number of interacting processes ($N \gg 1$). The corresponding boundary for $N = 2$ is shown as the dashed line.

transition taking place simultaneously for both processes. Since two steps are performed during a coupled transition, detailed balance demands $h_+/h_- = e^{2\Delta\mu/k_B T}$.

The dynamics just illustrated for two coupled processes are straightforwardly extended to N coupled processes, where we assume an all-to-all coupling, such that with rate h_+ (h_-) all N processes undergo a simultaneous forward (backward) step. In this case, detailed balance demands $h_+/h_- = e^{N\Delta\mu/k_B T}$. Following an analytical derivation (Appendix A), we find that the correlation strength is

$$C = \frac{\tilde{h}(1 + e^{-N\tilde{\mu}})}{1 + e^{-\tilde{\mu}} + \tilde{h}(1 + e^{-N\tilde{\mu}})}, \quad (4)$$

where $\tilde{h} \equiv h_+/k_+$ is the dimensionless coupling strength and $\tilde{\mu} \equiv \Delta\mu/k_B T$. As may be expected, we find that $C \rightarrow 1$ as $\tilde{h} \rightarrow \infty$ and $C = 0$ when $\tilde{h} = 0$. In turn, the ratio of average current to diffusion coefficient can be written as

$$\frac{\Omega}{D} = 2 \frac{1 - e^{-\tilde{\mu}} + \tilde{h}(1 - e^{-N\tilde{\mu}})}{1 + e^{-\tilde{\mu}} + \tilde{h}(1 + e^{-N\tilde{\mu}})}. \quad (5)$$

Combining both expressions, we obtain an exact relation between Ω/D , C , and the energy dissipation per step $\tilde{\mu}$, with the form

$$\frac{\Omega}{D} = 2 \frac{1 - e^{-\tilde{\mu}} + 2C \frac{e^{-\tilde{\mu}} - e^{-N\tilde{\mu}}}{1 + e^{-N\tilde{\mu}}}}{1 + e^{-\tilde{\mu}}}. \quad (6)$$

This expression can be shown to always satisfy the bound in Eq. (3), which it saturates in the near-equilibrium limit $\Delta\mu \rightarrow 0$. In the case where $C = 0$ (or $N = 1$), the right hand side becomes $2 \tanh(\tilde{\mu}/2)$, and we recover the relation for the single biased random walk which was used to conjecture the original TUR [3]. Our model thus represents the minimal extension of this basic toy model to the case of many interacting processes.

Using Eq. (5), we can investigate under which conditions the naive TUR is violated and $\frac{D}{\Omega} \frac{\Delta\mu}{k_B T} < 1$. For such parameter values, the inference strategies proposed in Figs. 1(a) and 1(b) can be used to infer the existence of nonzero correlations

in the system and put a lower bound on them. We find that this is possible when the coupling \tilde{h} is larger than a critical coupling strength $\tilde{h}(\tilde{\mu})$, see Fig. 2(c). Interestingly, this is only possible if the driving forces are weak, with $|\tilde{\mu}| < \tilde{\mu}^*$ where $\tilde{\mu}^* \simeq 1.915$ for $N = 2$ and $\tilde{\mu}^* \rightarrow 2$ as $N \rightarrow \infty$. Indeed, the critical coupling strength diverges as $\tilde{\mu}$ approaches $\pm\tilde{\mu}^*$.

Even further, using Eqs. (4) and (5) we can characterize how close to saturation the bound in Eq. (3) can get, as shown in Fig. 3(a) where we plot $\frac{D}{\Omega} \frac{\Delta\mu}{k_B T}$ against $C(N - 1)$ for a range of parameter values in $0 \leq \tilde{h} \leq 1$, $-1 \leq \tilde{\mu} \leq 2$, and $2 \leq N \leq 21$. The black solid line represents the equality in Eq. (3). For all values of N , there are parameter values for which the bound in Eq. (3) is close to saturated. Parameter values that violate the naive TUR, for which the correlation inference strategy can be applied, correspond to points that fall to the left of the vertical line in Fig. 3(a).

Continuous coupled processes. We next consider several examples that involve N continuous phases ϕ_α with $\alpha = 1, \dots, N$, described by systems of coupled Langevin dynamics in the overdamped regime, with the general form

$$\dot{\phi}_\alpha = \sum_{\beta=1}^N \{M_{\alpha\beta}(-\partial_\beta \mathcal{U}) + \sqrt{2k_B T} \Sigma_{\alpha\beta} \xi_\beta\}, \quad (7)$$

with \mathcal{U} a generic potential, $M_{\alpha\beta}$ a mobility matrix with constant coefficients (i.e., independent of ϕ_α), $\Sigma_{\alpha\beta}$ the square root of the mobility matrix satisfying $\Sigma_{\alpha\nu} \Sigma_{\beta\nu} = M_{\alpha\beta}$, and ξ_β a white noise of unit strength. For the mobility matrix, we set all diagonal coefficients to $M_{\alpha\alpha} = M$ and all off-diagonal coefficients to $M_{\alpha\beta} = h/(N - 1)$ ($\alpha \neq \beta$), so that $\tilde{h} \equiv h/M$ is a dimensionless measure of the strength of coupling mediated by the mobility matrix.

We first consider a minimal model of $N = 2$ coupled phases that can be treated analytically. This model could describe two driven stochastic gears or rotors, as represented by the entrained gears in Fig. 1(c), in which case the phases ϕ_1 and ϕ_2 represent the internal state (angular position) of these rotors. The potential \mathcal{U} , is chosen as $\mathcal{U}(\phi_1, \phi_2) = -F(\phi_1 + \phi_2) - K \cos(\phi_1 - \phi_2) - v \cos(\phi_1 + \phi_2)$ where F , K , and v

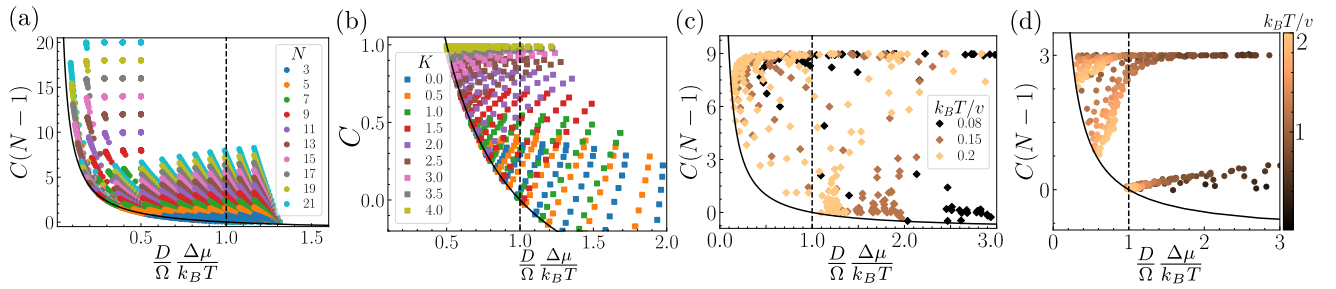


FIG. 3. Scatter plots of $\frac{D}{\Omega} \frac{\Delta\mu}{k_B T}$ against $C(N-1)$ for the four different models described in the main text, showing how the bound in Eq. (3) is satisfied and can be close to saturated. Points to the left of the vertical black dashed line correspond to parameter choices for which $\frac{D}{\Omega} \frac{\Delta\mu}{k_B T} < 1$ and thus the naive TUR is saturated, allowing for the thermodynamic inference of correlations. (a) Discrete model of Fig. 2; (b) analytically solvable continuous model; (c) thermally activated oscillators with dissipative coupling; (d) thermally activated oscillators with Kuramoto coupling. Parameter choices for each of the four models are described in the text. Simulations in (c) and (d) were performed using Euler-Maruyama integration.

are arbitrary constants. The first term is the nonequilibrium drive, with a driving force F which is related to the energy dissipation per cycle (when a phase has advanced by 2π), given by $\Delta\mu = 2\pi F$. The second term is a Kuramoto-type coupling that favors synchronization of the two phases [14]. Finally, the third term is an antisynchronizing coupling that favors opposite rotation of the phases and creates energy barriers for the synchronized advances of the two phases. The problem can be solved analytically by a change of variables to the average phase $\Theta = (\phi_1 + \phi_2)/2$ and phase difference $\Delta = \phi_1 - \phi_2$ (see Appendix B). Analytically calculated results for $0 < F/k_B T < 1$, $0 < v/k_B T < 2$, $0 < K/k_B T < 4$, and $\tilde{h} = 0.3$ are shown in Fig. 3(b).

We next consider N thermally activated oscillators that are coupled purely dissipatively, i.e., only through the off-diagonal components of the mobility matrix, with dimensionless strength \tilde{h} . The potential \mathcal{U} is set to $\mathcal{U}(\{\phi_\alpha\}) = \sum_{\alpha=1}^N V(\phi_\alpha)$ with $V(\phi) = -F\phi - v \cos(\phi)$ a washboard potential. This model has been shown to provide a description of the dynamics of mechanically coupled enzymes, which become effectively deterministic and synchronized at sufficiently high \tilde{h} [13,15,44]. The results of numerical simulations of this model for $N = 10$, $0 < \tilde{h} < 8$, $0.4 < F/v < 0.9$, and $k_B T/v = 0.08, 0.15, 0.2$ are shown in Fig. 3(c).

Finally, we consider the case of N thermally activated oscillators with Kuramoto-type coupling [14], previously studied in Ref. [45]. In this case, we set $\tilde{h} = 0$ so that the mobility matrix is diagonal, and we set $\mathcal{U}(\{\phi_\alpha\}) = \sum_{\alpha=1}^N V(\phi_\alpha) - \frac{K}{N} \sum_{\alpha=1}^N \sum_{\beta=\alpha+1}^N \cos(\phi_\alpha - \phi_\beta)$ where $V(\phi)$ is the same washboard potential as above. The results of numerical simulations of this model for $N = 4$, $0.1 < F/v < 0.9$, $0.01 < k_B T/v < 2$, and $K/v = 1, 6, 10$ are shown in Fig. 3(d).

For all three continuous models [Figs. 3(b)–3(d)], we find that there are regions of parameter space where the naive TUR is violated, i.e., $\frac{D}{\Omega} \frac{\Delta\mu}{k_B T} < 1$, and the correlation inference strategy can be applied. In all cases, saturation of the bound in Eq. (3) is facilitated when the noise strength $k_B T$ is large relatively to the energy barriers whose height is controlled by v , as in this case the dynamics become analogous to those of a particle under a constant force, which are known to saturate the TUR. However, to ensure that nonzero correlations survive, the couplings must remain sufficiently strong relative to

thermal fluctuations. A notable exception is the case of dissipatively coupled oscillators, Fig. 3(c), which can violate the naive TUR and come close to saturating the bound even at low noise strength. This can be understood as a consequence of the fact that the dissipative coupling induces quasideterministic dynamics even in the absence of noise [13,15].

Discussion. By applying the MTUR to an ensemble of statistically identical coupled processes with tight-coupling to entropy production, we have derived a bound [Eq. (3)] that allows for thermodynamic inference of the strength of correlations and the number of interacting processes in the system, even when only one or a small subset of them is experimentally accessible. In particular, when only a single current is observed, our strategy provides a lower bound on $C(N-1)$, where C is the strength of correlations and N the number of interacting processes. When two currents are observed, and thus C can be measured experimentally, our strategy provides a lower bound on N . The inference strategy is applicable when a “naive” application of the TUR to a single observable (i.e., assuming that this observable is isolated or uncorrelated to others) shows an apparent violation. By studying a number of minimal toy models that we solved analytically and numerically, we showed that the naive TUR is broken (and thus our proposed inference strategy is applicable) in large portions of parameter space.

One possible way of easily and directly testing the proposed inference strategy experimentally would be in controlled experiments using several driven colloids in an optical ring [Fig. 1(c)]. This experimental setup can produce constant driving forces [39,40] as well as washboardlike potentials [38]. When two or more colloids are present in the ring, hydrodynamic interactions between them can lead to correlations [39]. Otherwise, our proposed strategy could be applied to experiments with teams of molecular motors pulling on the same cargo [46] or clustered enzymes catalyzing chemical reactions [47].

Finally, we note that, although we have focused here on the inference of correlations provided that the energy dissipation per step ($\Delta\mu$) is known, our results also have implications for the experimental inference of $\Delta\mu$ when it is unknown. Indeed, Eq. (3) shows that, in an interacting system, individual currents behave as if they were driven by an effective energy dissipation per step $\Delta\mu_{\text{eff}} = [1 + C(N-1)]\Delta\mu$, with

$\Delta\mu_{\text{eff}} > \Delta\mu$ when $C > 0$. In the limit of strong correlations ($C = 1$), the system behaves as if every individual current was driven by the total energy dissipation in the system, i.e., $\Delta\mu_{\text{eff}} = N\Delta\mu$, as has been reported in previous studies [16,33]. An inference strategy unaware of existing correlations could therefore lead to a severe overestimation of (the lower bound on) the true $\Delta\mu$. Our results thus suggest that one must be very careful to experimentally rule out possible interactions with other processes before applying thermodynamic inference to entropy production, even when one can assume tight coupling (i.e., a fixed amount of energy dissipation per step) between the observed current and entropy production.

Acknowledgments. We acknowledge support from the Max Planck School Matter to Life and the MaxSynBio Consortium which are jointly funded by the Federal Ministry of Education and Research (BMBF) of Germany and the Max Planck Society.

Appendix A: Analytical solution of discrete model. To construct the TUR for this coupled model, we consider the number of steps ϕ_i of the i th process. This number can be split into the simultaneous steps ϕ_d that have occurred for all processes due to the diagonal transitions, and the individual steps $\phi_{s,i}$ taken by each process independently, so that $\phi_i = \phi_d + \phi_{s,i}$. Importantly, ϕ_d and all the different $\phi_{s,i}$ are governed by one-dimensional biased random walks that are statistically independent of each other. Using standard results for the biased random walk, we can write $\langle\phi_{s,i}\rangle = (k_+ - k_-)t$, $\langle\phi_d\rangle = (h_+ - h_-)t$, $\langle\phi_{s,i}^2\rangle - \langle\phi_{s,i}\rangle^2 = (k_+ + k_-)t$, and $\langle\phi_d^2\rangle - \langle\phi_d\rangle^2 = (h_+ + h_-)t$. Using the definitions of Ω , D , and C given in the main text, and exploiting the statistical independence of ϕ_d and all the different $\phi_{s,i}$, we can straightforwardly obtain $\Omega = k_+ + h_+ - k_- - h_-$, $D = (k_+ + h_+ + k_- + h_-)/2$, and $C = (h_+ + h_-)/(k_+ + k_- + h_+ + h_-)$. Together with the detailed balance conditions, these expressions are used to obtain Eqs. (4) and (5) in the main text.

Appendix B: Analytical solution of continuous model. The Langevin equations in Eq. (7) are equivalent to the Fokker-Planck equation

$$\partial_t P = \partial_\alpha [M_{\alpha\beta} ((\partial_\beta \mathcal{U})P + k_B T \partial_\beta P)], \quad (\text{B1})$$

for the probability $P(\{\phi_\alpha\}; t)$, where Einstein summation has been used. For the analytically solvable model, we

have $N = 2$ phases, $\mathcal{U}(\phi_1, \phi_2) = -F(\phi_1 + \phi_2) - K \cos(\phi_1 - \phi_2) - v \cos(\phi_1 + \phi_2)$, $M_{11} = M_{22} = M$, and $M_{12} = M_{21} = h$ as described in the main text.

By performing a linear transformation we change variables to go to the average phase $\Theta = (\phi_1 + \phi_2)/2$ and phase difference $\Delta = \phi_1 - \phi_2$. The Fokker-Planck equation becomes

$$\begin{aligned} \partial_t P = \partial_\Theta \left[\frac{M+h}{2} ((\partial_\Theta \mathcal{U})P + k_B T \partial_\Theta P) \right] \\ + \partial_\Delta [2(M-h)((\partial_\Delta \mathcal{U})P + k_B T \partial_\Delta P)], \end{aligned} \quad (\text{B2})$$

where we have $\mathcal{U}(\Theta, \Delta) = -2F\Theta - v \cos 2\Theta - K \cos \Delta$. Because the potential becomes separable in these coordinates, we can obtain separate Fokker-Planck equations for the marginal distributions

$$P_\Theta = \int d\Delta P(\Theta, \Delta), \quad P_\Delta = \int d\Theta P(\Theta, \Delta), \quad (\text{B3})$$

given by

$$\partial_t P_\Theta = \partial_\Theta \left[\frac{M+h}{2} ([\partial_\Theta V_\Theta(\Theta)]P_\Theta + k_B T \partial_\Theta P_\Theta) \right], \quad (\text{B4})$$

$$\partial_t P_\Delta = \partial_\Delta [2(M-h)([\partial_\Delta V_\Delta(\Delta)]P_\Delta + k_B T \partial_\Delta P_\Delta)], \quad (\text{B5})$$

where $V_\Theta(\Theta) = -2F\Theta - v \cos 2\Theta$ and $V_\Delta(\Delta) = -K \cos \Delta$.

Equations (B4) and (B5) each represent the stochastic dynamics of a (driven) particle in a one-dimensional periodic potential. The average velocity and long-time effective diffusion coefficient of a particle in such systems can be calculated analytically, with closed form expressions given in Refs. [48–50] which we do not reproduce here. In the case of Eq. (B4), the particle is driven by a force $2F$ and one obtains an average velocity $\langle\dot{\Theta}\rangle \neq 0$ and an effective diffusion coefficient D_Θ . In the case of Eq. (B5), the particle is not driven and thus the average velocity vanishes, $\langle\dot{\Delta}\rangle = 0$, while the effective diffusion coefficient is denoted by D_Δ .

As a final step, we note that ϕ_1 and ϕ_2 are related to Θ and Δ by the inverse transformations $\phi_1 = \Theta + \Delta/2$ and $\phi_2 = \Theta - \Delta/2$. Exploiting the fact that the dynamics of Θ and Δ are statistically independent, we can use the definitions of Ω , D , and C given in the main text to obtain $\Omega = \langle\dot{\Theta}\rangle$, $D = D_\Theta + D_\Delta/4$, and $C = (D_\Theta - D_\Delta/4)/(D_\Theta + D_\Delta/4)$.

-
- [1] U. Seifert, From stochastic thermodynamics to thermodynamic inference, *Annu. Rev. Condens. Matter Phys.* **10**, 171 (2019).
- [2] C. Nardini, E. Fodor, E. Tjhung, F. van Wijland, J. Tailleur, and M. E. Cates, Entropy production in field theories without time-reversal symmetry: Quantifying the non-equilibrium character of active matter, *Phys. Rev. X* **7**, 021007 (2017).
- [3] A. C. Barato and U. Seifert, Thermodynamic uncertainty relation for biomolecular processes, *Phys. Rev. Lett.* **114**, 158101 (2015).
- [4] T. R. Gingrich, J. M. Horowitz, N. Perunov, and J. L. England, Dissipation bounds all steady-state current fluctuations, *Phys. Rev. Lett.* **116**, 120601 (2016).
- [5] C. Dieball and A. Godec, Direct route to thermodynamic uncertainty relations and their saturation, *Phys. Rev. Lett.* **130**, 087101 (2023).
- [6] C. Maggi, F. Saglimbeni, V. C. Sosa, R. Di Leonardo, B. Nath, and A. Puglisi, Thermodynamic limits of sperm swimming precision, *PRX Life* **1**, 013003 (2023).
- [7] S. Pal, S. Saryal, D. Segal, T. S. Mahesh, and B. K. Agarwalla, Experimental study of the thermodynamic uncertainty relation, *Phys. Rev. Res.* **2**, 022044(R) (2020).
- [8] D. B. Brückner, P. Ronceray, and C. P. Broedersz, Inferring the dynamics of underdamped stochastic systems, *Phys. Rev. Lett.* **125**, 058103 (2020).

- [9] D. J. Skinner and J. Dunkel, Improved bounds on entropy production in living systems, *Proc. Natl. Acad. Sci. USA* **118**, e2024300118 (2021).
- [10] M. C. Marchetti, J. F. Joanny, S. Ramaswamy, T. B. Liverpool, J. Prost, M. Rao, and R. A. Simha, Hydrodynamics of soft active matter, *Rev. Mod. Phys.* **85**, 1143 (2013).
- [11] M. Chatzittofi, J. Agudo-Canalejo, and R. Golestanian, Non-linear response theory of molecular machines, *Europhys. Lett.* **147**, 21002 (2024).
- [12] F. Jülicher, A. Ajdari, and J. Prost, Modeling molecular motors, *Rev. Mod. Phys.* **69**, 1269 (1997).
- [13] J. Agudo-Canalejo, T. Adeleke-Larodo, P. Illien, and R. Golestanian, Synchronization and enhanced catalysis of mechanically coupled enzymes, *Phys. Rev. Lett.* **127**, 208103 (2021).
- [14] Y. Kuramoto, Chemical Turbulence, in *Chemical Oscillations, Waves, and Turbulence*, Springer Series in Synergetics, Vol. 19 (Springer, Berlin, Heidelberg, 1984), pp. 111–140.
- [15] M. Chatzittofi, R. Golestanian, and J. Agudo-Canalejo, Collective synchronization of dissipatively-coupled noise-activated processes, *New J. Phys.* **25**, 093014 (2023).
- [16] S. Lee, C. Hyeon, and J. Jo, Thermodynamic uncertainty relation of interacting oscillators in synchrony, *Phys. Rev. E* **98**, 032119 (2018).
- [17] A. C. Barato and U. Seifert, Cost and precision of brownian clocks, *Phys. Rev. X* **6**, 041053 (2016).
- [18] P. Pietzonka and U. Seifert, Universal trade-off between power, efficiency, and constancy in steady-state heat engines, *Phys. Rev. Lett.* **120**, 190602 (2018).
- [19] A.-K. Pumm, W. Engelen, E. Kopperger, J. Isensee, M. Vogt, V. Kozina, M. Kube, M. N. Honemann, E. Bertolin, M. Langecker, R. Golestanian, F. C. Simmel, and H. Dietz, A DNA origami rotary ratchet motor, *Nature (London)* **607**, 492 (2022).
- [20] X. Shi, A.-K. Pumm, C. Maffeo, F. Kohler, E. Feigl, W. Zhao, D. Verschuere, R. Golestanian, A. Aksimentiev, H. Dietz, and C. Dekker, A DNA turbine powered by a transmembrane potential across a nanopore, *Nat. Nanotechnol.* **19**, 338 (2023).
- [21] Y. Hasegawa, Thermodynamic uncertainty relation for general open quantum systems, *Phys. Rev. Lett.* **126**, 010602 (2021).
- [22] H. J. D. Miller, M. H. Mohammady, M. Perarnau-Llobet, and G. Guarneri, Thermodynamic uncertainty relation in slowly driven quantum heat engines, *Phys. Rev. Lett.* **126**, 210603 (2021).
- [23] K. Macieszczak, K. Brandner, and J. P. Garrahan, Unified thermodynamic uncertainty relations in linear response, *Phys. Rev. Lett.* **121**, 130601 (2018).
- [24] J. M. Horowitz and T. R. Gingrich, Thermodynamic uncertainty relations constrain non-equilibrium fluctuations, *Nat. Phys.* **16**, 15 (2020).
- [25] K. J. Ray, A. B. Boyd, G. Guarneri, and J. P. Crutchfield, Thermodynamic uncertainty theorem, *Phys. Rev. E* **108**, 054126 (2023).
- [26] D. Hartich and A. Godec, Thermodynamic uncertainty relation bounds the extent of anomalous diffusion, *Phys. Rev. Lett.* **127**, 080601 (2021).
- [27] N. Ohga, S. Ito, and A. Kolchinsky, Thermodynamic bound on the asymmetry of cross-correlations, *Phys. Rev. Lett.* **131**, 077101 (2023).
- [28] A. Dechant, J. Garnier-Brun, and S.-i. Sasa, Thermodynamic bounds on correlation times, *Phys. Rev. Lett.* **131**, 167101 (2023).
- [29] A. Dechant, Multidimensional thermodynamic uncertainty relations, *J. Phys. A* **52**, 035001 (2019).
- [30] T. Koyuk and U. Seifert, Thermodynamic uncertainty relation in interacting many-body systems, *Phys. Rev. Lett.* **129**, 210603 (2022).
- [31] M. Chatzittofi, J. Agudo-Canalejo, and R. Golestanian, Entropy production and thermodynamic inference for stochastic microswimmers, *Phys. Rev. Res.* **6**, L022044 (2024).
- [32] S. Klumpp and R. Lipowsky, Cooperative cargo transport by several molecular motors, *Proc. Natl. Acad. Sci. USA* **102**, 17284 (2005).
- [33] G. Costantini and A. Puglisi, Thermodynamic precision of a chain of motors: The difference between phase and noise correlation, *J. Stat. Mech.* (2024) 024003.
- [34] L. J. Sweetlove and A. R. Fernie, The role of dynamic enzyme assemblies and substrate channelling in metabolic regulation, *Nat. Commun.* **9**, 2136 (2018).
- [35] B. G. O'Flynn and T. Mittag, The role of liquid–liquid phase separation in regulating enzyme activity, *Curr. Opin. Cell Biol.* **69**, 70 (2021).
- [36] L. Jimenez, D. Laporte, S. Duvezin-Caubet, F. Courtout, and I. Sagot, Mitochondrial ATP synthases cluster as discrete domains that reorganize with the cellular demand for oxidative phosphorylation, *J. Cell Sci.* **127**, 719 (2014).
- [37] K. M. Visscher, J. Medeiros-Silva, D. Mance, J. P. Rodrigues, M. Daniëls, A. M. Bonvin, M. Baldus, and M. Weingarth, Supramolecular organization and functional implications of K⁺ channel clusters in membranes, *Angew. Chem. Int. Ed.* **56**, 13222 (2017).
- [38] S.-H. Lee and D. G. Grier, Giant colloidal diffusivity on corrugated optical vortices, *Phys. Rev. Lett.* **96**, 190601 (2006).
- [39] Y. Sokolov, D. Frydel, D. G. Grier, H. Diamant, and Y. Roichman, Hydrodynamic pair attractions between driven colloidal particles, *Phys. Rev. Lett.* **107**, 158302 (2011).
- [40] H. Nagar and Y. Roichman, Collective excitations of hydrodynamically coupled driven colloidal particles, *Phys. Rev. E* **90**, 042302 (2014).
- [41] P. Pietzonka, A. C. Barato, and U. Seifert, Universal bound on the efficiency of molecular motors, *J. Stat. Mech.* (2016) 124004.
- [42] R. Marsland, W. Cui, and J. M. Horowitz, The thermodynamic uncertainty relation in biochemical oscillations, *J. R. Soc. Interface.* **16**, 20190098 (2019).
- [43] M. P. Leighton and D. A. Sivak, Dynamic and thermodynamic bounds for collective motor-driven transport, *Phys. Rev. Lett.* **129**, 118102 (2022).
- [44] M. Chatzittofi, R. Golestanian, and J. Agudo-Canalejo, Topological phase locking in molecular oscillators, [arXiv:2310.11788](https://arxiv.org/abs/2310.11788).
- [45] S. Shinomoto and Y. Kuramoto, Phase transitions in active rotator systems, *Prog. Theor. Phys.* **75**, 1105 (1986).
- [46] G. Nettesheim, I. Nabti, C. U. Murade, G. R. Jaffe, S. J. King, and G. T. Shubeita, Macromolecular crowding acts as a physical regulator of intracellular transport, *Nat. Phys.* **16**, 1144 (2020).

Chapter 6

Entropy production and thermodynamic inference for stochastic microswimmers

This chapter is reproduced from Michalis Chatzittofi, Jaime Agudo-Canalejo, and Ramin Golestanian *Phys. Rev. Research* **6**, L022044 [135]. In this article, I contributed in designing the research. I have performed analytical calculations, contributed in the analysis of the results and writing/editing the paper.

Entropy production and thermodynamic inference for stochastic microswimmers

Michalis Chatzittofi ¹, Jaime Agudo-Canalejo ^{1,2,*} and Ramin Golestanian ^{1,3,†}

¹*Department of Living Matter Physics, Max Planck Institute for Dynamics and Self-Organization (MPI-DS), D-37077 Göttingen, Germany*

²*Department of Physics and Astronomy, University College London, London WC1E 6BT, United Kingdom*

³*Rudolf Peierls Centre for Theoretical Physics, University of Oxford, Oxford OX1 3PU, United Kingdom*



(Received 23 October 2023; accepted 9 May 2024; published 21 May 2024)

The question of characterization of the degree of nonequilibrium activity in active matter systems is studied in the context of a stochastic microswimmer model driven by a chemical cycle. The resulting dynamical properties and entropy production rate unravel a complex interplay between the chemical and the hydrodynamic degrees of freedom beyond linear response, which is not captured by conventional phenomenological approaches. By studying the precision-dissipation trade off, a new protocol is proposed in which microscopic chemical driving forces can be inferred experimentally. Our findings highlight subtleties associated with the stochastic thermodynamics of autonomous microswimmers.

DOI: [10.1103/PhysRevResearch.6.L022044](https://doi.org/10.1103/PhysRevResearch.6.L022044)

Understanding entropy production and thermodynamic inference [1] in autonomous systems [2], such as stochastic motors [3,4] and microswimmers [5], is of fundamental importance to the study of biological and synthetic active matter [6–9]. These systems typically produce net motion or mechanical work as a consequence of the dissipation of some form of locally available energy (e.g., ATP hydrolysis) [10–12]. A common assumption in the literature is that the dissipation can be quantified by representing the autonomous self-propulsion via an effective external “active force” [8,13–16].

The thermodynamic uncertainty relation (TUR) and its various generalizations quantify the trade off between the precision of a nonequilibrium current and its associated dissipation, and thus provide a powerful tool to infer the underlying driving forces of a system from experimental measurements of its trajectories [1,17–19]. However, many of the models studied until now to test the behavior of TURs have been based on the assumption of tight coupling between chemical and spatial degrees of freedom (where, e.g., a chemical reaction always corresponds to a mechanical step and vice versa) so that the dynamics is effectively one-dimensional, and, hence, rendering the spatial, chemical, and entropy production currents one and the same [17,20–25].

While convenient, these two (related) assumptions are not generally valid. Realistic autonomous swimmers and molecular motors involve at least two distinct currents (e.g., spatial and chemical) and consequently at least two distinct kinds of

driving forces. In fact, the relevant coupling in these systems is off diagonal (in the language of linear irreversible thermodynamics [26–28]), as chemical forces drive motion. This is particularly evident in the case of microswimmers, where the force-free constraint on their self-propulsion mechanisms introduces additional complexities [29–36], and has important consequences on the bounds on entropy production [37,38]. A multidimensional version of the TUR (MTUR) can, in principle, be used in multicurrent systems to obtain much-improved bounds on the entropy production, and thus better inference of the underlying driving forces [39]. However, how to exploit this bound in practice is unclear, as typically only the spatial current is measurable, while the chemical current is not. To shed light on the inner workings of autonomous swimmers and motors, we must therefore understand how spatial and chemical forces and currents couple to each other arbitrarily far from equilibrium, beyond linear response.

In this Letter, we study a stochastic three-sphere swimmer [32] as a minimal model that includes both chemical and spatial (hydrodynamic) degrees of freedom; see Fig. 1. The chemical cycle is represented by a four-state process where each state corresponds to a different conformation of the swimmer [Fig. 1(a)]. The key hydrodynamic degree of freedom corresponds to the spatial position of the swimmer, to which an external force may also be applied. The total chemical energy ε associated with a cycle and the external force F are the two affinities that drive the system out of equilibrium and cause the overall swimming [Fig. 1(b)]. From a hydrodynamic derivation (see Appendix A and [40]), we show that the entropy production rate (EPR) can be written as

$$T\dot{\sigma} = J(\varepsilon, F)\varepsilon + V(\varepsilon, F)F, \quad (1)$$

where $J(\varepsilon, F)$ is the chemical current (rate) of the internal cycle (see Fig. 1(b) and [40]) and $V(\varepsilon, F)$ is the velocity of the swimmer. Superficially, Eq. (1) appears to have the standard form of an EPR, with the chemical current J driven by the

*j.agudo-canalejo@ucl.ac.uk

†ramin.golestanian@ds.mpg.de

Published by the American Physical Society under the terms of the [Creative Commons Attribution 4.0 International](https://creativecommons.org/licenses/by/4.0/) license. Further distribution of this work must maintain attribution to the author(s) and the published article's title, journal citation, and DOI. Open access publication funded by Max Planck Society.

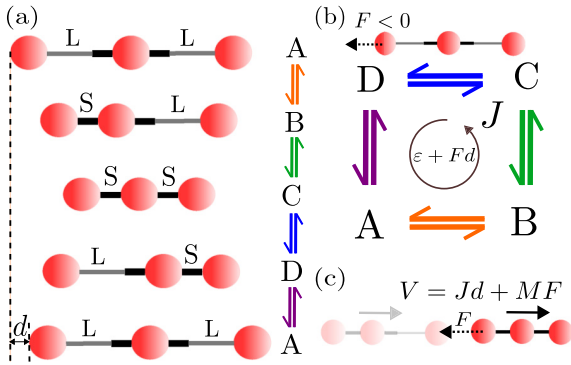


FIG. 1. (a) Full four-state cycle of the stochastic three-sphere swimmer, after which it advances a distance d . L (long) and S (short) indicate the state of the arms. (b) The current J through the cycle is driven by the total affinity $\varepsilon + Fd$, where ε is the chemical affinity and F the external force applied on the swimmer. (c) The total velocity of the swimmer V includes an active swimming contribution Jd and a passive drag MF , with M the hydrodynamic mobility.

chemical affinity ε and the spatial current V driven by the spatial affinity F . However, the hydrodynamics of the swimming mechanism leads to a coupling between the chemical and spatial degrees of freedom, such that the currents J and V do not respectively vanish when ε and F vanish. In fact, we find that the velocity of the swimmer [40] is given by

$$V(\varepsilon, F) = J(\varepsilon, F)d + MF, \quad (2)$$

where the first term represents the active swimming (with d being the distance advanced in the laboratory frame after a full conformational cycle), while the second term is the passive drag of the swimmer by the external force [Fig. 1(c)]. Here, M is the hydrodynamic mobility of the swimmer, which is related to its positional thermal diffusion coefficient through the fluctuation-dissipation relation $D_{\text{th}} = Mk_B T$, where k_B is the Boltzmann constant and T is the temperature. Introducing (2) into (1), we can rewrite the EPR as

$$T\dot{\sigma} = J(\varepsilon, F)(\varepsilon + Fd) + MF^2. \quad (3)$$

While perhaps less intuitive, (3) can be viewed as the canonical form of the EPR. Indeed, we show below that the external force influences the dynamics of the chemical cycle through the swimmer mechanics, such that the overall affinity driving the chemical current J is $\varepsilon + Fd$. The passive drag velocity MF in turn represents a hidden current that is exclusively driven by the external force. Therefore, although Eq. (1) is more practical as it involves currents that are observable (at least in principle), it is only when written in the form of Eq. (3) that the nonnegativity of the entropy production rate as required by thermodynamics becomes manifest. Below, we derive these results, and show how they strongly influence the precision-dissipation trade off for the swimmer, and how they can be used to infer the chemical driving force of the swimmer from measurements of its position only.

Model. The model is summarized in Fig. 1(a). We assume quick expansions or contractions of the arms such that their possible states are contracted ($u_\rho = 0$) or expanded ($u_\rho = \delta$), where u_ℓ and u_r represent the deformation of the left and right arms, respectively, and δ is the extension amplitude.

TABLE I. Displacement of each sphere in each transition. For the reverse transitions, $\Delta x_{i,\alpha\beta} = -\Delta x_{i,\beta\alpha}$. The constants $\alpha_{L,S}$ depend on the geometry of the swimmer and satisfy $\frac{1}{3} < \alpha_L < \alpha_S < \frac{1}{2}$. The total displacement d of the swimmer after a full cycle, obtained by summing over any of the columns, is $d = 2(\alpha_S - \alpha_L)\delta$.

Process	$\Delta x_{1,\beta\alpha}/\delta$	$\Delta x_{2,\beta\alpha}/\delta$	$\Delta x_{3,\beta\alpha}/\delta$
$A = LL \rightarrow B = SL$	$1 - \alpha_L$	$-\alpha_L$	$-\alpha_L$
$B = SL \rightarrow C = SS$	α_S	α_S	$-(1 - \alpha_S)$
$C = SS \rightarrow D = LS$	$-(1 - \alpha_S)$	α_S	α_S
$D = LS \rightarrow A = LL$	$-\alpha_L$	$-\alpha_L$	$1 - \alpha_L$

Each conformation corresponds to a state $\alpha = A, B, C, D$ of the chemical cycle. The rate for the transition $\alpha \rightarrow \beta$ is denoted as $k_{\beta\alpha}$. The states can also be named based on the arms being long (L) or short (S), e.g., state B corresponds to SL . To introduce forward propulsion (toward the right) without an external force, one must break detailed-balance such that the trajectory of the system follows closed cycles in the conformational space [30–32]. If the energy released in going from α to β is $\Delta\varepsilon_{\beta\alpha}$, local detailed balance requires $k_{\beta\alpha}/k_{\alpha\beta} = e^{\Delta\varepsilon_{\beta\alpha}/k_B T}$. Note that local detailed balance is required for a thermodynamically consistent definition of stochastic entropy [41]. The total affinity of a cycle is then given by $\varepsilon = \sum \Delta\varepsilon_{\beta\alpha} = k_B T \ln \frac{k_{BA}k_{CB}k_{DC}k_{AD}}{k_{AB}k_{BC}k_{CD}k_{DA}}$. The steady-state probability current J is given by $J = k_{BA}P_A - k_{AB}P_B$, where P_α 's are the steady-state probabilities [40]. This current can be viewed as the rate or the inverse period for completion of a chemical cycle. For $\varepsilon = 0$, equilibrium is restored and the current vanishes.

Effect of an external force. We now consider that the swimmer is pulled or pushed by a constant external force F , with the convention that negative force points toward the left (against the direction of swimming). In principle, the force could be distributed among the three spheres such that $F_1 + F_2 + F_3 = F$ where force F_i is applied on the i th sphere. Importantly, the force not only directly drags the swimmer, but also affects its conformational dynamics by modifying the transition rates $k_{\beta\alpha}$. From a hydrodynamic derivation of entropy production (Appendix A), we calculate the total dissipation per transition which includes the work done by the external forces due to the displacements of each sphere.

The displacements $\Delta x_{i,\beta\alpha}$ of the i th sphere during transition $\alpha \rightarrow \beta$ are listed in Table I (see Appendix A). Denoting the rates in the absence of the external forces (or the bare rates) as $k_{0\beta\alpha}$, local detailed balance demands that the rates be modified as

$$k_{\beta\alpha} = k_{0\beta\alpha} \exp\left(\frac{\theta_{\beta\alpha} W_{\beta\alpha}}{k_B T}\right), \quad (4)$$

where $W_{\beta\alpha} = \sum_i F_i \Delta x_{i,\beta\alpha}$ is the work done by the external forces. Since the signs of the displacements are reversed in the reverse transitions, this implies that $W_{\alpha\beta} = -W_{\beta\alpha}$. The factors $\theta_{\beta\alpha}$ are related to the location of the energy barrier between states α and β , and must satisfy $\theta_{\alpha\beta} = 1 - \theta_{\beta\alpha}$ [40,42]. Importantly, independently of the choice of $\theta_{\beta\alpha}$ and of where the force is applied, the total affinity of the cycle becomes $k_B T \ln \frac{k_{BA}k_{CB}k_{DC}k_{AD}}{k_{AB}k_{BC}k_{CD}k_{DA}} = \varepsilon + Fd$. Using these ingredients

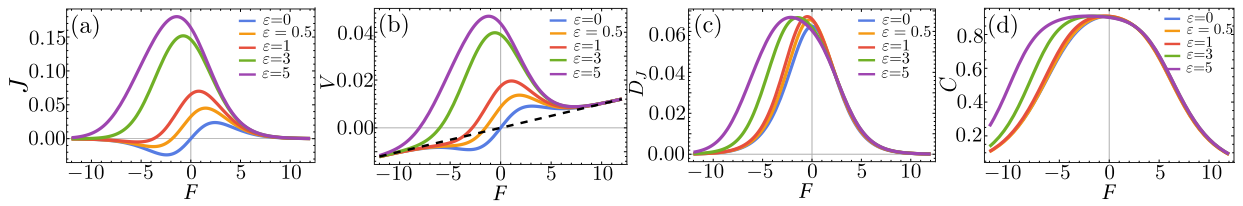


FIG. 2. Dependence on external force F , for several values of the chemical affinity ε , of (a) the chemical current J , (b) the spatial current or velocity V , (c) the chemical diffusion coefficient D_J , and (d) the correlation C between J and V . In (b), the dotted black line represents the passive drag velocity $V = MF$.

and existing results from the literature [43,44] we calculate the chemical current J and its associated diffusion coefficient D_J [40]. Because each conformational cycle results in a displacement $d = 2(\alpha_S - \alpha_L)\delta$ (see Table I), the active swimming contributes Jd to the velocity V of the swimmer, while the force F additionally contributes a passive drift; see Eq. (2). The hydrodynamic mobility M is to the leading order constant during the whole cycle, and more generally, it is an average over all conformations of the swimmer [40]. The spatial diffusion coefficient (associated to V) also includes active swimming and passive hydrodynamic contributions, and reads $D_V = D_J d^2 + D_{th}$ [40]. Using Eq. (2), we can also calculate the correlation between J and V as $C = 1/\sqrt{1 + D_{th}/(D_J d^2)}$ [40].

Swimmer dynamics. In all of the following results, we fix the geometric parameters to $\alpha_L = \frac{2.1}{6}$ and $\alpha_S = \frac{2.9}{6}$; the force is applied on the leftmost (trailing) sphere so that $F_1 = F$ and $F_2 = F_3 = 0$, and we set $\theta_{\beta\alpha} = 1/2$ for all the transitions. The bare transition rates $k_{0\beta\alpha}$ are all set to the same value k , with the exception of k_{0BA} which is set to $k_{0BA} = ke^{\varepsilon/k_B T}$. Furthermore, we focus on strong swimmers and set $D_{th}/k\delta^2 = 10^{-3}$. In all plots, quantities are nondimensionalized using k^{-1} as the timescale, δ as the length scale, and $k_B T$ and k_B as units of energy and entropy, respectively.

Figure 2 displays the behavior of several quantities of interest as a function of the applied force F , for various values of the chemical affinity ε . The chemical current, shown in Fig. 2(a), clearly manifests the mechanochemical coupling in this system, as an applied force can create a chemical current even in the absence of any chemical driving ($\varepsilon = 0$). When $\varepsilon > 0$, the current vanishes at the critical force $F_* = -\varepsilon/d$ that makes the total affinity of the cycle zero, while it is reversed for $F < F_*$. At large positive or negative force, J vanishes [45]. The behavior of the velocity V is similar to that of J [see Fig. 2(b)] except that V shows a linear dependence as $V = MF$ at large force, when it is dominated by the passive drag by the external force since J vanishes. The velocity vanishes at the stall force F_s , which can be calculated from the implicit equation $J(\varepsilon, F_s)d + MF_s = 0$ [see Eq. (2)] and satisfies $F_* < F_s < 0$ (for $\varepsilon > 0$). For sufficiently large ε , small positive forces cause the swimmer to decelerate, whereas small negative forces cause the swimmer to accelerate [32]. This phenomenon, known as negative differential mobility, has also been observed in other nonequilibrium systems [46,47]. Lastly, the force dependence of the chemical diffusion coefficient D_J (which coincides with that of the spatial diffusion D_V , except for a prefactor and a constant baseline) and the correlation C are displayed in Figs. 2(c) and

2(d). We find that both generally peak at small negative values of the applied force, independently of the magnitude of ε .

Entropy production. We can calculate the EPR from the hydrodynamic definition of dissipation, $T\dot{\sigma} = \sum_i \langle \dot{x}_i f_i \rangle$, where \dot{x}_i is the velocity of each sphere and f_i is the corresponding instantaneous force, satisfying the force balance $f_1 + f_2 + f_3 = F$. The crucial step in the derivation is to separately consider the internal and external contributions to the forces (see Appendix A). In this framework, the EPR splits into an active swimming contribution related to the conformational transitions, and a purely passive one. After averaging, these two contributions make up the result presented in Eq. (3). The coupling between chemical and hydrodynamic driving forces gives rise to a rather complicated dependence of the EPR on the forces, with local maxima and minima as shown in Fig. 3(a). For $\varepsilon = F = 0$, the system is at equilibrium. For $\varepsilon > 0$, at low force the entropy production is largely dominated by the chemical part, while at large force we recover the usual hydrodynamic energy dissipation ($\sim F^2$) of a passive object dragged by a constant force.

Thermodynamic precision. The precision of a nonequilibrium process is bounded by the EPR through the TUR [17]. More specifically, the MTUR provides the bound $\mathcal{J}^T \cdot \mathcal{D}^{-1} \cdot \mathcal{J} \leq \dot{\sigma}/k_B$ at steady state, where \mathcal{J} is any vectorial current and \mathcal{D} is the diffusion matrix describing the fluctuations of the current [39]. Applying this bound to the individual current V , we obtain the standard TUR, $V^2/D_V \leq \dot{\sigma}/k_B$. We estimate the quality of this bound using the (nonnegative) factor $Q_V \equiv (V^2/D_V)/(\dot{\sigma}/k_B)$, which equals one when the bound is saturated and is smaller otherwise. The values of Q_V for our swimmer are shown in Fig. 3(b) as a function of the force F for several values of the chemical driving ε , and in Fig. 3(c) as a function of ε for several values of F . The behavior of Q_V is rather complex, reflecting the fact that the current has two driving forces which can compete with each other.

An intriguing observation can be made by considering the behavior of Q_V near equilibrium ($\varepsilon = F = 0$). While in the limit $F \rightarrow 0$ for $\varepsilon = 0$ in Fig. 3(b) we find $Q_V \rightarrow 1$ (the bound is saturated), in the limit $\varepsilon \rightarrow 0$ for $F = 0$ in Fig. 3(c) we find $Q_V \rightarrow 0.8163$ (the bound is not saturated). The two limits do not coincide as one might have naively expected, implying that the near equilibrium limit is not uniquely defined. This generic behavior can be understood in linear response (see Appendix B), and reflects the fact that F is the direct (diagonal) driving force of the current V , whereas ε is its indirect (off-diagonal) driving force [48]. This difference between direct and indirect forces with regards to TUR saturation near equilibrium is of practical relevance, as typically (e.g., for

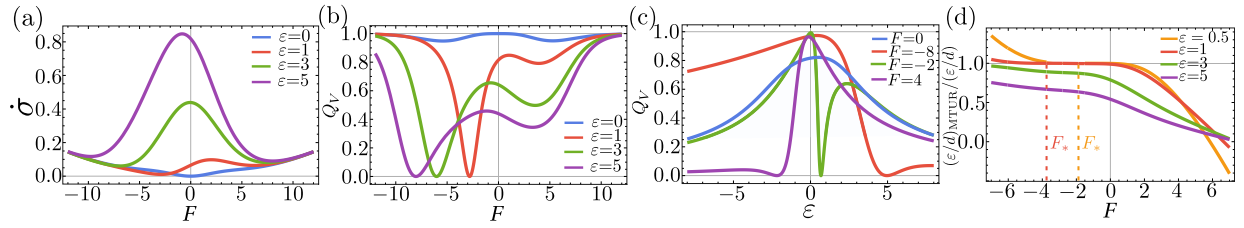


FIG. 3. (a) Entropy production rate $\dot{\sigma}$ as a function of the external force F , for several values of the chemical affinity ϵ . (b), (c) The quality factor Q_V of the precision-dissipation trade off for the spatial current V , (b) as a function of F for fixed values of ϵ , and (c) as a function of ϵ for fixed values of F . (d) Ratio of the MTUR-inferred [Eq. (6)] and true chemical force ϵ/d . F_* is the critical force at which the chemical current vanishes. For $F > F_*$ the inferred value is a lower bound, for $F < F_*$ an upper bound, and for $F = F_*$ it is exact.

molecular motors and swimmers) the affinity of interest (e.g., ATP hydrolysis) only indirectly drives the measurable current (e.g., spatial velocity).

A tighter bound on entropy production can be obtained by applying the MTUR to the two-dimensional current (J, V) , which yields

$$\frac{1}{1 - C^2} \left[\frac{J^2}{D_J} - \frac{2CJV}{\sqrt{D_J D_V}} + \frac{V^2}{D_V} \right] \leq \frac{\dot{\sigma}}{k_B}. \quad (5)$$

This bound is well behaved and saturated in the near equilibrium limit, as can be proven in the linear response regime (see Appendix B). While it may appear to be less useful in practice, as it involves J , D_J , and C , all of which are not directly observable in an experiment that only has access to the swimmer position, our knowledge of the swimmer mechanics can be exploited to obtain a much improved bound (even an equality) on the chemical energy consumption per unit distance (chemical force) of the swimmer, ϵ/d .

Thermodynamic inference. Indeed, using Eq. (2) and the expressions for D_V and C , we can write J , D_J , and C as functions of V , D_V , the passive hydrodynamic mobility M (or thermal diffusion coefficient $D_{th} = Mk_B T$), and the external force F ; substitute them into (5) together with expression (3) for the EPR; and finally rearrange the terms to obtain an inequality on ϵ/d . Defining

$$\left(\frac{\epsilon}{d} \right)_{\text{MTUR}} \equiv \frac{k_B T V / D_V - F}{1 - D_{th} / D_V}, \quad (6)$$

we find that, for $F > F_*$ (where $F_* < 0$ is the critical force at which the chemical current vanishes), the MTUR provides a lower bound $\epsilon/d \geq (\epsilon/d)_{\text{MTUR}}$, while for $F < F_*$ the MTUR provides an upper bound $\epsilon/d \leq (\epsilon/d)_{\text{MTUR}}$. By continuity, for $F = F_*$ [which implies $J = 0$ and thus $V = MF_*$ through Eq. (2)], we find the equality $\epsilon/d = (\epsilon/d)_{\text{MTUR}} = -F_*$. This result is consistent with the total affinity $\epsilon + Fd$ of the chemical current vanishing at $F = F_*$. The quality of this bound as measured by the ratio $(\epsilon/d)_{\text{MTUR}}/(\epsilon/d)$ is shown in Fig. 3(d) as a function of F , for several values of ϵ .

These results reveal several strategies for the inference of the chemical force. In passive measurements with $F = 0$, we can estimate $\epsilon/d \geq k_B T (V/D_V)(1 - D_{th}/D_V)^{-1}$. This improves the bound obtained from the standard TUR by a factor $(1 - D_{th}/D_V)^{-1}$. In active measurements with $F \neq 0$, one may measure the stall force of the swimmer $F_s < 0$ at which $V = 0$, as well as the position fluctuations giving D_V , and infer $\epsilon/d \geq -F_s(1 - D_{th}/D_V)^{-1}$. Lastly, and optimally, one may measure the critical force F_* at which the

swimmer moves precisely at the velocity that one would expect from passive hydrodynamic drag, i.e., $V = MF_*$. The chemical force is then exactly $\epsilon/d = -F_*$. In all these cases, the passive mobility M (and associated $D_{th} = Mk_B T$) may be estimated from purely hydrodynamic calculations. Alternatively, if $|J(F)|$ grows more slowly than linear, tends to a constant, or vanishes at large force (as is the case for the three-sphere swimmer), M can be measured from the asymptotic behavior of the swimmer velocity as $F \rightarrow \pm\infty$; see the force-velocity (F - V) curve in Fig. 2(b). In this case, F_* and thus ϵ/d can be inferred by measuring the F - V curve, estimating its high-force asymptote, and obtaining the intersection point of the asymptote and the F - V curve, which occurs at F_* .

Discussion. Using a stochastic three-sphere swimmer as an analytically tractable and thermodynamically-consistent model for a chemically powered autonomous microswimmer, we have explicitly calculated its swimming dynamics and its entropy production in the presence of an external force. This allowed us to study the coupling between spatial and chemical forces and currents beyond the linear response regime. We have found a number of interesting properties in the force dependence of the swimmer dynamics as well as its thermodynamic properties, such as the radically different dependence of the thermodynamic precision-dissipation trade off of the swimmer velocity on the external force (direct driving) and internal chemical affinity (indirect driving). Moreover, we have shown how the chemical affinity of the swimmer can be precisely inferred by measurements of the spatial dynamics only.

All of these properties are a consequence of the coupling between spatial and chemical forces and currents in this system, as exemplified by Eqs. (1), (2), (3), and the expressions for D_V and C . Importantly, we expect the form of these equations to remain unchanged for other autonomous swimmers (see, e.g., Ref. [49] for a derivation of equivalent expressions for self-phoretic swimmers). Only the precise functional form of the chemical current $J(\epsilon, F)$ (and associated diffusion D_J) and the distance d advanced per cycle will depend on the microscopic details. Therefore, the general lessons learned here and the thermodynamic inference strategy proposed [Eq. (6)] should be applicable to a wide range of autonomous motors and swimmers.

Acknowledgments. We acknowledge support from the Max Planck School Matter to Life and the MaxSynBio Consortium which are jointly funded by the Federal Ministry of Education and Research (BMBF) of Germany and the Max Planck Society.

Appendix A: Hydrodynamic calculation of velocity and entropy production. The force balance equation for the swimmer reads $\sum_i f_i = F$. The force on sphere i denoted as f_i can be expressed as $f_i = \tilde{f}_i + F_i$, in terms of the internal force \tilde{f}_i and the external force F_i . We have $\sum_i \tilde{f}_i = 0$ and $\sum_i F_i = F$. The internal forces can be written as $\tilde{f}_1 = -\tilde{f}_\ell$, $\tilde{f}_2 = \tilde{f}_\ell - \tilde{f}_r$, and $\tilde{f}_3 = \tilde{f}_r$, where \tilde{f}_ℓ and \tilde{f}_r are respectively the internal stresses on the left and right arms, defined to be positive when they act to expand the arm. We denote the instantaneous speeds of the arms as $\dot{u}_\ell = \dot{x}_2 - \dot{x}_1$, $\dot{u}_r = \dot{x}_3 - \dot{x}_2$. Forces and velocities are linearly related through the hydrodynamic friction tensor Z_{ij} such that $f_i = \sum_j Z_{ij} \dot{x}_j$. By summing over the forces we deduce that $\sum_i A_i \dot{x}_i = BF$, with $A_i(u_\ell, u_r) \equiv (\sum_j Z_{ij}) / (\sum_{i,j} Z_{ij})$ and $B(u_\ell, u_r) \equiv 1 / (\sum_{i,j} Z_{ij})$. From this expression, we derive equations describing the motion of each of the spheres in response to the external force as well as the changes in the lengths of the arms (active swimming) as follows:

$$\dot{x}_1 = BF - (1 - A_1)\dot{u}_\ell - A_3\dot{u}_r, \quad (\text{A1})$$

$$\dot{x}_2 = BF + A_1\dot{u}_\ell - A_3\dot{u}_r, \quad (\text{A2})$$

$$\dot{x}_3 = BF + A_1\dot{u}_\ell + (1 - A_3)\dot{u}_r. \quad (\text{A3})$$

The average velocity V of the swimmer is given by $\langle \dot{x}_2 \rangle$, where the average is taken at steady state and any sphere i may be considered without loss of generality. Choosing $i = 2$, we can write

$$V = \langle \dot{x}_2 \rangle = MF + \langle A_1\dot{u}_\ell - A_3\dot{u}_r \rangle, \quad (\text{A4})$$

where we have defined $M \equiv \langle B \rangle$, which is independent of ε or F to leading order in the hydrodynamic interactions [40]. The first term represents the passive drag, whereas the second term represents the active swimming. The latter results in finite contributions for each conformational change, so that

$$\begin{aligned} \langle A_1\dot{u}_\ell - A_3\dot{u}_r \rangle &= \frac{1}{\mathcal{T}} \int_0^{\mathcal{T}} (A_1\dot{u}_\ell - A_3\dot{u}_r) dt, \\ &= J \sum_{\{\beta\alpha\}} \left[\int_\alpha^\beta A_1 du_\ell - \int_\alpha^\beta A_3 du_r \right], \\ &= J \sum_{\{\beta\alpha\}} \Delta x_{2,\beta\alpha} = Jd, \end{aligned} \quad (\text{A5})$$

where $\mathcal{T} = J^{-1}$ is the period of a cycle in steady state, and the sums run over the forward transitions $\{\beta\alpha\} = \{BA, CB, DC, AD\}$. Equations (A4) and (A5) together result in Eq. (2).

The displacement in each transition $\Delta x_{2,\beta\alpha}$ is calculated by performing the associated integral in the second line of Eq. (A5). For instance, in the transition $A \rightarrow B$ the left arm shrinks and the right arm stays fixed at $u_r = \delta$, so that we find

$$\Delta x_{2,BA} = \int_A^B A_1 du_\ell = \int_\delta^0 A_1(u_\ell, \delta) du_\ell = -\alpha_L \delta, \quad (\text{A6})$$

where we have defined

$$\alpha_L \equiv \frac{1}{\delta} \int_0^\delta A_1(u_\ell, \delta) du_\ell. \quad (\text{A7})$$

Conversely, in the transition $B \rightarrow C$, the right arm shrinks while the left arm stays fixed at $u_\ell = 0$. We thus find

$$\Delta x_{2,CB} = - \int_B^C A_3 du_r = - \int_\delta^0 A_3(0, u_r) du_r = \alpha_S \delta, \quad (\text{A8})$$

with the definition

$$\alpha_S \equiv \frac{1}{\delta} \int_0^\delta A_3(0, u_r) du_r. \quad (\text{A9})$$

Repeating this procedure for all transitions and calculating the corresponding displacement of the first and third sphere, we obtain the results in Table I, which are valid for a swimmer with symmetric geometry as in Fig. 1. The calculations for a more general asymmetric swimmer, their explicit integration using the Oseen approximation, and the estimation of the bound $1/3 < \alpha_L < \alpha_S < 1/2$ are performed in Ref. [40]. These recover the known results relating the velocity of the swimmer to the area swept by cycles in conformational space [31,32].

To calculate the EPR at steady state, we start from the hydrodynamic dissipation $T\dot{\sigma} = \sum_i \langle \dot{x}_i f_i \rangle$. Using (A1)–(A3), the EPR becomes

$$\begin{aligned} T\dot{\sigma} &= MF^2 + \langle \dot{u}_\ell [\tilde{f}_\ell - (1 - A_1)F_1 + A_1(F_2 + F_3)] \\ &\quad + \dot{u}_r [\tilde{f}_r - A_3(F_1 + F_2) + (1 - A_3)F_3] \rangle. \end{aligned} \quad (\text{A10})$$

Here, analogously to the calculation of the velocity, the first term represents the dissipation due to passive drag, whereas the second term represents dissipation due to the active swimming, which gives a finite contribution for each conformational transition.

Indeed, following the same procedure used to derive Eq. (A5), we may write

$$T\dot{\sigma} = MF^2 + J \sum_{\{\beta\alpha\}} T \Delta \sigma_{\beta\alpha}, \quad (\text{A11})$$

where $T \Delta \sigma_{\beta\alpha}$ gives the dissipation occurring during the transition $\alpha \rightarrow \beta$. As an example, we consider again the transition $A \rightarrow B$. In this transition, u_ℓ shrinks whereas u_r remains constant and fixed to δ . Thus, the discrete dissipation during this transition is

$$\begin{aligned} T \Delta \sigma_{BA} &= \int_\delta^0 [\tilde{f}_\ell - (1 - A_1)F_1 + A_1(F_2 + F_3)] du_\ell \\ &= \Delta \varepsilon_{BA} + F_1 \Delta x_{1,BA} + F_2 \Delta x_{2,BA} + F_3 \Delta x_{3,BA}. \end{aligned} \quad (\text{A12})$$

Here, the first term results from the definition

$$\Delta \varepsilon_{BA} \equiv \int_\delta^0 \tilde{f}_\ell du_\ell, \quad (\text{A13})$$

and gives the dissipation due to the internal active mechanism of the swimmer, while the remaining terms result from the displacements of the spheres previously calculated and give the dissipation by the external force during a conformational change.

An analogous result $T \Delta \sigma_{\beta\alpha} = \Delta \varepsilon_{\beta\alpha} + \sum_i F_i \Delta x_{i,\beta\alpha}$ is obtained for all other transitions [40]. The transition-induced dissipation obtained in this way must be used to enforce local detailed balance in the stochastic transitions, leading to

Eq. (4). Finally, using this result in Eq. (A11), and noting that $\sum_{\{\beta\alpha\}} \Delta \varepsilon_{\beta\alpha} = \varepsilon$ and $\sum_{\{\beta\alpha\},i} F_i \Delta x_{i,\beta\alpha} = Fd$, leads to the expression for the EPR in Eq. (3), which gives Eq. (1) when combined with Eq. (2).

Appendix B: Linear response regime. In the linear-response regime ($\varepsilon, Fd \ll k_B T$), the currents can be written as $J = L_{\varepsilon\varepsilon}\varepsilon + L_{\varepsilon F}F$ and $V = L_{F\varepsilon}\varepsilon + L_{FF}F$, with $L_{\varepsilon\varepsilon} = \tilde{\kappa}$, $L_{FF} = \tilde{\kappa}d^2 + M$, and $L_{\varepsilon F} = L_{F\varepsilon} = \tilde{\kappa}d$, where $\tilde{\kappa} = \kappa_0/(k_B T)$ and κ_0 is an inverse timescale that depends only on the force-free rates $k_{0\beta\alpha}$ [40]. Thus, affinities couple to the currents through $\mathcal{J}_a = \sum_b L_{ab} \mathcal{A}_b$, where $\mathcal{J}_a = (J, V)$ is a vector of currents, $\mathcal{A}_a = (\varepsilon, F)$ is a vector of affinities, and L_{ab} is a symmetric Onsager matrix. The EPR can then be expressed in the usual bilinear form $T\dot{\sigma} = \sum_{ab} L_{ab} \mathcal{A}_a \mathcal{A}_b$ [26–28].

It is straightforward to show that the MTUR ($\mathcal{J}^T \cdot \mathcal{D}^{-1} \cdot \mathcal{J} \leq \dot{\sigma}/k_B$) is saturated in linear regime. Indeed, the diffusion matrix \mathcal{D} relates to the Onsager mobility matrix L through the fluctuation-dissipation theorem $\mathcal{D} = k_B T L$, and using this together with $\mathcal{J} = L \cdot \mathcal{A}$ directly results in $\mathcal{J}^T \cdot \mathcal{D}^{-1} \cdot \mathcal{J} = \dot{\sigma}/k_B$. The behavior of the standard single-current TUR, $Q_a \equiv$

$(\mathcal{J}_a^2/D_a)/(\dot{\sigma}/k_B) \leq 1$ for current \mathcal{J}_a , is more surprising. In general, for a current \mathcal{J}_a driven by N affinities \mathcal{A}_b with $b = 1, \dots, N$, the quality factor Q_a can be written as

$$Q_a = \frac{\sum_{b,c} L_{ab} L_{ac} \mathcal{A}_b \mathcal{A}_c}{L_{aa} \sum_{b,c} L_{bc} \mathcal{A}_b \mathcal{A}_c}, \quad (\text{B1})$$

where we have used the fluctuation-dissipation relation $D_a = \mathcal{D}_{aa} = k_B T L_{aa}$. There are two distinct cases with regards to how the system behaves when only one of the affinities is nonzero: (i) If $\mathcal{A}_b = 0$ for all $b \neq a$ and $\mathcal{A}_a \neq 0$ (weak direct driving), we find $Q_a = 1$, i.e., the bound saturates; (ii) If $\mathcal{A}_b = 0$ for all $b \neq c$ and $\mathcal{A}_c \neq 0$ for some $c \neq a$ (weak indirect driving), we find $Q_a = L_{ac}^2/(L_{aa}L_{cc})$ [48]. The latter value is guaranteed to be smaller than or equal to one due to the positive semidefiniteness of the Onsager matrix. Typically, it is smaller than one, implying that the TUR bound is not saturated. For our swimmer, we thus have $Q_V \rightarrow L_{F\varepsilon}^2/(L_{FF}L_{\varepsilon\varepsilon})$ when $F = 0$ and $\varepsilon \rightarrow 0$, which for the parameters used in Fig. 3 gives $Q_V \rightarrow 0.8163$.

-
- [1] U. Seifert, From stochastic thermodynamics to thermodynamic inference, *Annu. Rev. Condens. Matter Phys.* **10**, 171 (2019).
 - [2] G. Gompper, R. G. Winkler, T. Speck, A. Solon, C. Nardini, F. Peruani, H. Löwen, R. Golestanian, U. B. Kaupp, L. Alvarez, T. Kiørboe, E. Lauga, W. C. K. Poon, A. DeSimone, S. Muiños-Landin, A. Fischer, N. A. Söker, F. Cichos, R. Kapral, P. Gaspard *et al.*, The 2020 motile active matter roadmap, *J. Phys.: Condens. Matter* **32**, 193001 (2020).
 - [3] F. Jülicher, A. Ajdari, and J. Prost, Modeling molecular motors, *Rev. Mod. Phys.* **69**, 1269 (1997).
 - [4] A.-K. Pumm, W. Engelen, E. Kopperger, J. Isensee, M. Vogt, V. Kozina, M. Kube, M. N. Honemann, E. Bertosin, M. Langecker, R. Golestanian, F. C. Simmel, and H. Dietz, A DNA origami rotary ratchet motor, *Nature (London)* **607**, 492 (2022).
 - [5] R. Golestanian and A. Ajdari, Stochastic low reynolds number swimmers, *J. Phys.: Condens. Matter* **21**, 204104 (2009).
 - [6] C. Nardini, E. Fodor, E. Tjhung, F. van Wijland, J. Tailleur, and M. E. Cates, Entropy production in field theories without time-reversal symmetry: Quantifying the non-equilibrium character of active matter, *Phys. Rev. X* **7**, 021007 (2017).
 - [7] P. Pietzonka and U. Seifert, Entropy production of active particles and for particles in active baths, *J. Phys. A: Math. Theor.* **51**, 01LT01 (2018).
 - [8] S. Shankar and M. C. Marchetti, Hidden entropy production and work fluctuations in an ideal active gas, *Phys. Rev. E* **98**, 020604(R) (2018).
 - [9] C. Battle, C. P. Broedersz, N. Fakhri, V. F. Geyer, J. Howard, C. F. Schmidt, and F. C. MacKintosh, Broken detailed balance at mesoscopic scales in active biological systems, *Science* **352**, 604 (2016).
 - [10] M. L. Mugnai, C. Hyeon, M. Hinczewski, and D. Thirumalai, Theoretical perspectives on biological machines, *Rev. Mod. Phys.* **92**, 025001 (2020).
 - [11] S. Borsley, D. A. Leigh, and B. M. W. Roberts, Chemical fuels for molecular machinery, *Nat. Chem.* **14**, 728 (2022).
 - [12] R. Golestanian, Phoretic active matter, in *Active Matter and Nonequilibrium Statistical Physics: Lecture Notes of the Les Houches Summer School: Volume 112, September 2018* (Oxford University Press, Oxford, UK, 2022).
 - [13] T. Speck, Stochastic thermodynamics for active matter, *Europhys. Lett.* **114**, 30006 (2016).
 - [14] G. Szamel, Stochastic thermodynamics for self-propelled particles, *Phys. Rev. E* **100**, 050603(R) (2019).
 - [15] L. Tociu, E. Fodor, T. Nemoto, and S. Vaikuntanathan, How dissipation constrains fluctuations in nonequilibrium liquids: Diffusion, structure, and biased interactions, *Phys. Rev. X* **9**, 041026 (2019).
 - [16] L. Dabelow, S. Bo, and R. Eichhorn, Irreversibility in active matter systems: Fluctuation theorem and mutual information, *Phys. Rev. X* **9**, 021009 (2019).
 - [17] A. C. Barato and U. Seifert, Thermodynamic uncertainty relation for biomolecular processes, *Phys. Rev. Lett.* **114**, 158101 (2015).
 - [18] T. R. Gingrich, J. M. Horowitz, N. Perunov, and J. L. England, Dissipation bounds all steady-state current fluctuations, *Phys. Rev. Lett.* **116**, 120601 (2016).
 - [19] C. Dieball and A. Godec, Direct route to thermodynamic uncertainty relations and their saturation, *Phys. Rev. Lett.* **130**, 087101 (2023).
 - [20] P. Pietzonka, A. C. Barato, and U. Seifert, Universal bound on the efficiency of molecular motors, *J. Stat. Mech.* (2016) 124004.
 - [21] A. C. Barato and U. Seifert, Cost and precision of brownian clocks, *Phys. Rev. X* **6**, 041053 (2016).
 - [22] S. Lee, C. Hyeon, and J. Jo, Thermodynamic uncertainty relation of interacting oscillators in synchrony, *Phys. Rev. E* **98**, 032119 (2018).
 - [23] R. Marsland III, W. Cui, and J. M. Horowitz, The thermodynamic uncertainty relation in biochemical oscillations, *J. R. Soc. Interface* **16**, 20190098 (2019).

- [24] T. Koyuk and U. Seifert, Thermodynamic uncertainty relation in interacting many-body systems, *Phys. Rev. Lett.* **129**, 210603 (2022).
- [25] M. P. Leighton and D. A. Sivak, Dynamic and thermodynamic bounds for collective motor-driven transport, *Phys. Rev. Lett.* **129**, 118102 (2022).
- [26] L. Onsager, Reciprocal relations in irreversible processes. I, *Phys. Rev.* **37**, 405 (1931).
- [27] L. Onsager, Reciprocal relations in irreversible processes. II, *Phys. Rev.* **38**, 2265 (1931).
- [28] S. R. De Groot and P. Mazur, *Non-Equilibrium Thermodynamics* (Courier Corporation, North Chelmsford, MA, 2013).
- [29] E. M. Purcell, Life at low Reynolds number, *Am. J. Phys.* **45**, 3 (1977).
- [30] A. Najafi and R. Golestanian, Simple swimmer at low Reynolds number: Three linked spheres, *Phys. Rev. E* **69**, 062901 (2004).
- [31] R. Golestanian and A. Ajdari, Analytic results for the three-sphere swimmer at low Reynolds number, *Phys. Rev. E* **77**, 036308 (2008).
- [32] R. Golestanian and A. Ajdari, Mechanical response of a small swimmer driven by conformational transitions, *Phys. Rev. Lett.* **100**, 038101 (2008).
- [33] E. Lauga and T. R. Powers, The hydrodynamics of swimming microorganisms, *Rep. Prog. Phys.* **72**, 096601 (2009).
- [34] R. Golestanian, T. B. Liverpool, and A. Ajdari, Propulsion of a molecular machine by asymmetric distribution of reaction products, *Phys. Rev. Lett.* **94**, 220801 (2005).
- [35] F. Jülicher and J. Prost, Generic theory of colloidal transport, *Eur. Phys. J. E* **29**, 27 (2009).
- [36] P. Gaspard and R. Kapral, Fluctuating chemohydrodynamics and the stochastic motion of self-diffusiophoretic particles, *J. Chem. Phys.* **148** (2018).
- [37] B. Nasouri, A. Vilfan, and R. Golestanian, Minimum dissipation theorem for microswimmers, *Phys. Rev. Lett.* **126**, 034503 (2021).
- [38] A. Daddi-Moussa-Ider, R. Golestanian, and A. Vilfan, Minimum entropy production by microswimmers with internal dissipation, *Nat. Commun.* **14**, 6060 (2023).
- [39] A. Dechant, Multidimensional thermodynamic uncertainty relations, *J. Phys. A: Math. Theor.* **52**, 035001 (2018).
- [40] See Supplemental Material at <http://link.aps.org/supplemental/10.1103/PhysRevResearch.6.L022044> for details on the calculation of currents, diffusion coefficients, and correlation; the linear response regime; the full hydrodynamic calculations; the intuitive meaning of $\theta_{\beta\alpha}$; and results for negative chemical affinity.
- [41] U. Seifert, Stochastic thermodynamics, fluctuation theorems and molecular machines, *Rep. Prog. Phys.* **75**, 126001 (2012).
- [42] P. Hänggi, P. Talkner, and M. Borkovec, Reaction-rate theory: fifty years after Kramers, *Rev. Mod. Phys.* **62**, 251 (1990).
- [43] B. Derrida, Velocity and diffusion constant of a periodic one-dimensional hopping model, *J. Stat. Phys.* **31**, 433 (1983).
- [44] Z. Koza, General technique of calculating the drift velocity and diffusion coefficient in arbitrary periodic systems, *J. Phys. A: Math. Gen.* **32**, 7637 (1999).
- [45] The vanishing of J at large force can be understood mechanistically in the context of the three-sphere microswimmer. This feature is caused by the swimmer stalling into one of its four internal states: no matter on which sphere and in which direction the external force is applied, there is always a state transitioning out of which (both toward the next or the previous state in the cycle) requires that the sphere move against the external force acting on it.
- [46] R. K. P. Zia, E. L. Praestgaard, and O. G. Mouritsen, Getting more from pushing less: Negative specific heat and conductivity in nonequilibrium steady states, *Am. J. Phys.* **70**, 384 (2002).
- [47] O. Bénichou, P. Illien, G. Oshanin, A. Sarracino, and R. Voituriez, Microscopic theory for negative differential mobility in crowded environments, *Phys. Rev. Lett.* **113**, 268002 (2014).
- [48] While the full expression of the TUR in linear response was derived in the seminal Ref. [17], this particular consequence appears to have been overlooked.
- [49] R. Bebon, J. F. Robinson, and T. Speck, Thermodynamics of active matter: Tracking dissipation across scales, [arXiv:2401.02252](https://arxiv.org/abs/2401.02252).

Entropy production and thermodynamic inference for a stochastic microswimmer

Supplemental Material

Michalis Chatzittofi,¹ Jaime Agudo-Canalejo,^{1,2,*} and Ramin Golestanian^{1,3,†}

¹*Max Planck Institute for Dynamics and Self-Organization (MPI-DS), D-37077 Göttingen, Germany*

²*Department of Physics and Astronomy, University College London, London WC1E 6BT, United Kingdom*

³*Rudolf Peierls Centre for Theoretical Physics, University of Oxford, Oxford OX1 3PU, United Kingdom*

CONTENTS

I. Currents, diffusion coefficients, and correlation	1
II. Linear response theory	2
III. Hydrodynamic calculations	3
A. Swimming velocity	3
B. Perturbative expansion	5
C. Hydrodynamic mobility	6
D. Entropy production rate	6
IV. Intuitive meaning of $\theta_{\beta\alpha}$	7
V. Results for negative chemical affinity	8
References	9

I. CURRENTS, DIFFUSION COEFFICIENTS, AND CORRELATION

To derive the expressions for the currents, diffusion coefficients, and the correlation, we define the observables n , which counts the number of cycles completed by the internal process, and y , the displacement due to the passive drag by the force. The total displacement of the swimmer is given by $x = nd + y$, where $d = 2(\alpha_S - \alpha_L)\delta$ as derived in the main text. At steady-state, we have

$$\lim_{t \rightarrow \infty} \langle n \rangle / t = J, \quad (\text{S1})$$

$$\lim_{t \rightarrow \infty} \langle y \rangle / t = MF, \quad (\text{S2})$$

$$\lim_{t \rightarrow \infty} \langle x \rangle / t = Jd + MF = V, \quad (\text{S3})$$

where the hydrodynamic mobility M of the swimmer is related to its thermal diffusion coefficient through $M = D_{\text{th}}/k_B T$. We show (below) through a comprehensive hydrodynamic calculation that the mobility is constant to lowest order, and thus independent of the cyclic process n . To calculate J , we need to solve the master equation

$$\frac{dp_\alpha}{dt} = \sum_{\beta} (k_{\alpha\beta} p_\beta - k_{\beta\alpha} p_\alpha), \quad (\text{S4})$$

which governs the dynamics of the probability distribution p_β . At steady-state we denote $p_\beta \rightarrow P_\beta$, and write the probability current as $J = k_{\beta\alpha} P_\alpha - k_{\alpha\beta} P_\beta$. We find [1]

$$J = \frac{k_{AD}k_{DC}k_{CB}k_{BA} - k_{AB}k_{BC}k_{CD}k_{DA}}{\sum_{\text{cycl.perm. of } A,B,C,D} (k_{AD}k_{DC}k_{CB} + k_{AB}k_{BC}k_{CD} + k_{AB}k_{AD}k_{DC} + k_{AD}k_{AB}k_{BC})}. \quad (\text{S5})$$

* j.agudo-canalejo@ucl.ac.uk

† ramin.golestanian@ds.mpg.de

The diffusion coefficients are defined as

$$\lim_{t \rightarrow \infty} \langle (n - \langle n \rangle)^2 \rangle / (2t) = D_J, \quad (\text{S6})$$

$$\lim_{t \rightarrow \infty} \langle (y - \langle y \rangle)^2 \rangle / (2t) = D_{\text{th}}, \quad (\text{S7})$$

$$\lim_{t \rightarrow \infty} \langle (x - \langle x \rangle)^2 \rangle / (2t) = D_V. \quad (\text{S8})$$

The explicit expression for calculating the diffusion coefficient D_J can be found in [2]. Using the above equations and the definition of x , the spatial diffusion coefficient can be found as

$$\lim_{t \rightarrow \infty} \langle (x - \langle x \rangle)^2 \rangle / (2t) = D_J d^2 + D_{\text{th}} = D_V, \quad (\text{S9})$$

since $\langle ny \rangle - \langle n \rangle \langle y \rangle = 0$. The correlation C between the processes x and n and is defined as

$$C = \lim_{t \rightarrow \infty} \frac{\langle (x - \langle x \rangle)(n - \langle n \rangle) \rangle}{\sqrt{\langle (x - \langle x \rangle)^2 \rangle \langle (n - \langle n \rangle)^2 \rangle}}, \quad (\text{S10})$$

and can be straightforwardly calculated as

$$C = \frac{1}{\sqrt{1 + \frac{D_{\text{th}}}{D_J d^2}}}. \quad (\text{S11})$$

II. LINEAR RESPONSE THEORY

Expanding the currents J and V around the equilibrium state ($\varepsilon = F = 0$), we find

$$J(\varepsilon, F) = \left. \frac{\partial J}{\partial \varepsilon} \right|_{\varepsilon=F=0} \varepsilon + \left. \frac{\partial J}{\partial F} \right|_{\varepsilon=F=0} F, \quad (\text{S12})$$

$$V(\varepsilon, F) = d \left. \frac{\partial J}{\partial \varepsilon} \right|_{\varepsilon=F=0} \varepsilon + \left(M + d \left. \frac{\partial J}{\partial F} \right|_{\varepsilon=F=0} \right) F. \quad (\text{S13})$$

To verify the Onsager reciprocity condition, we need to show that $\frac{\partial J}{\partial F} = d \frac{\partial J}{\partial \varepsilon}$ is satisfied.

To this end, we note that

$$J = \kappa \left(1 - \Pi \frac{k_{\beta\alpha}^{\leftarrow}}{k_{\alpha\beta}^{\rightarrow}} \right) = \kappa \left(1 - \exp(-\mathcal{A}/k_B T) \right), \quad (\text{S14})$$

where

$$\kappa = \frac{k_{AD} k_{DC} k_{CB} k_{BA}}{\sum_{\text{cycl.perm. of } A,B,C,D} (k_{AD} k_{DC} k_{CB} + k_{AB} k_{BC} k_{CD} + k_{AB} k_{AD} k_{DC} + k_{AD} k_{AB} k_{BC})}. \quad (\text{S15})$$

and the cycle affinity \mathcal{A} is defined as

$$\frac{\mathcal{A}}{k_B T} = \ln \left(\frac{k_{AD} k_{DC} k_{CB} k_{BA}}{k_{AB} k_{BC} k_{CD} k_{DA}} \right). \quad (\text{S16})$$

Thus, close to equilibrium we find

$$J \simeq \kappa_0 \frac{\mathcal{A}}{k_B T} = \kappa_0 \frac{(\varepsilon + Fd)}{k_B T}, \quad (\text{S17})$$

where $\kappa_0 = \kappa(\varepsilon = F = 0)$ and $\mathcal{A} = \varepsilon + Fd$ is the affinity. Therefore, we deduce that Onsager reciprocity is satisfied, and the Onsager coefficients are as given in the main text. Moreover, one can easily check that in the linear regime the entropy production is given as $T\dot{\sigma} = J\varepsilon + VF$.

III. HYDRODYNAMIC CALCULATIONS

The equations for the velocities of each sphere are given in terms of the hydrodynamic mobility tensor M_{ij} , such that $\dot{x}_i = \sum_j M_{ij} f_j$. In what follows we assume arbitrary sizes of the three spheres and also different length of the arms where u_ℓ and u_r can take maximum expansions of δ_ℓ and δ_r , respectively.

As describe in Appendix A, it is useful to consider the inverse problem $f_i = \sum_j Z_{ij} \dot{x}_j$, with the friction matrix $Z = M^{-1}$,

$$Z = \frac{1}{\det M} \begin{bmatrix} M_{22}M_{33} - M_{23}^2 & M_{13}M_{23} - M_{33}M_{12} & M_{12}M_{23} - M_{13}M_{22} \\ M_{13}M_{23} - M_{33}M_{12} & M_{11}M_{33} - M_{13}^2 & M_{12}M_{13} - M_{11}M_{23} \\ M_{12}M_{23} - M_{13}M_{22} & M_{12}M_{13} - M_{11}M_{23} & M_{11}M_{22} - M_{12}^2 \end{bmatrix}, \quad (\text{S18})$$

where

$$\det M = M_{11}M_{22}M_{33} - M_{11}M_{23}^2 - M_{22}M_{13}^2 - M_{33}M_{12}^2 + 2M_{12}M_{13}M_{23}, \quad (\text{S19})$$

is the determinant of M_{ij} . We thus obtain that

$$\sum_{ij} Z_{ij} \dot{x}_j = \sum_i f_i = \sum_i F_i = F \quad (\text{S20})$$

since $\sum f_i = \sum F_i = F$ and $\sum \tilde{f}_i = 0$ as explained in the main letter. Thus, by dividing both sides with $\sum_{ij} Z_{ij}$, and defining

$$B \equiv \frac{1}{\sum_{ij} Z_{ij}}, \quad (\text{S21})$$

and

$$A_i \equiv \frac{\sum_j Z_{ij}}{\sum_{ij} Z_{ij}}, \quad (\text{S22})$$

we obtain $\sum_i A_i \dot{x}_i = BF$. Using $\dot{u}_\ell = \dot{x}_2 - \dot{x}_1$ and $\dot{u}_r = \dot{x}_3 - \dot{x}_2$ in this expression, we find

$$\dot{x}_1 = BF - (1 - A_1)\dot{u}_\ell - A_3\dot{u}_r, \quad (\text{S23})$$

$$\dot{x}_2 = BF + A_1\dot{u}_\ell - A_3\dot{u}_r, \quad (\text{S24})$$

$$\dot{x}_3 = BF + A_1\dot{u}_\ell + (1 - A_3)\dot{u}_r, \quad (\text{S25})$$

where the explicit expressions are given as follows

$$A_1(u_\ell, u_r) = \frac{1}{N} (M_{22}M_{33} - M_{33}M_{12} - M_{22}M_{13} + M_{13}M_{23} + M_{12}M_{23} - M_{23}^2), \quad (\text{S26})$$

$$A_2(u_\ell, u_r) = \frac{1}{N} (M_{11}M_{33} - M_{33}M_{12} - M_{11}M_{23} + M_{12}M_{13} + M_{13}M_{23} - M_{13}^2), \quad (\text{S27})$$

$$A_3(u_\ell, u_r) = \frac{1}{N} (M_{11}M_{22} - M_{11}M_{23} - M_{22}M_{13} + M_{12}M_{23} + M_{12}M_{13} - M_{12}^2). \quad (\text{S28})$$

Here N is determined by $A_1 + A_2 + A_3 = 1$. The expression for B is

$$B(u_\ell, u_r) = \frac{1}{N} \det M. \quad (\text{S29})$$

A. Swimming velocity

The average swimming velocity V is given by $V = \langle \dot{x}_i \rangle$ where without loss of generality we choose $\langle \dot{x}_2 \rangle$ with

$$\langle \dot{x}_2 \rangle = \langle B \rangle F + \langle A_1 \dot{u}_\ell - A_3 \dot{u}_r \rangle = MF + \langle A_1 \dot{u}_\ell - A_3 \dot{u}_r \rangle \quad (\text{S30})$$

Process	$\Delta x_{1,\beta\alpha}$	$\Delta x_{2,\beta\alpha}$	$\Delta x_{3,\beta\alpha}$
$A = LL \rightarrow B = SL$	$(1 - \alpha_{L,\ell})\delta_\ell$	$-\alpha_{L,\ell}\delta_\ell$	$-\alpha_{L,\ell}\delta_\ell$
$B = SL \rightarrow C = SS$	$\alpha_{S,r}\delta_r$	$\alpha_{S,r}\delta_r$	$-(1 - \alpha_{S,r})\delta_r$
$C = SS \rightarrow D = LS$	$-(1 - \alpha_{S,\ell})\delta_\ell$	$\alpha_{S,\ell}\delta_\ell$	$\alpha_{S,\ell}\delta_\ell$
$D = LS \rightarrow A = LL$	$-\alpha_{L,r}\delta_r$	$-\alpha_{L,r}\delta_r$	$(1 - \alpha_{L,r})\delta_r$

TABLE SI. The displacement of each sphere in each transition for a general asymmetric swimmer. For the reverse transitions, $\Delta x_{i,\alpha\beta} = -\Delta x_{i,\beta\alpha}$ as in the main text. The first index of α coefficients stands for whether the other (fixed) arm is in the long or short and the second one is for the arm that is changing.

where in the steady-state

$$M \equiv \langle B \rangle = B(\delta_\ell, \delta_r)P_A + B(0, \delta_r)P_B + B(0, 0)P_C + B(\delta_\ell, 0)P_D, \quad (\text{S31})$$

with the brackets indicating the state of B . For the second term we have,

$$\begin{aligned} \langle A_1 \dot{u}_\ell - A_3 \dot{u}_r \rangle &= \frac{1}{\mathcal{T}} \int_0^{\mathcal{T}} (A_1 \dot{u}_\ell - A_3 \dot{u}_r) dt = J \sum_{\{\beta\alpha\}} \left[\int_\alpha^\beta A_1 du_\ell - \int_\alpha^\beta A_3 du_r \right], \\ &= J(\Delta x_{2,BA} + \Delta x_{2,CB} + \Delta x_{2,DC} + \Delta x_{2,DA}) = Jd, \end{aligned} \quad (\text{S32})$$

where after integrating over each step we obtain the displacement during each transition, and we have used the fact that in the steady-state $J(\varepsilon, F) = \frac{1}{\mathcal{T}}$.

Performing the individual integrals for each transition we find that for the transition $A = LL \rightarrow B = SL$ the following result holds

$$\Delta x_{2,BA} = \int_{\delta_\ell}^0 A_1(u_\ell, \delta_\ell) du_\ell = -\alpha_{L,\ell}\delta_\ell \quad \text{with} \quad \alpha_{L,\ell} \equiv \frac{1}{\delta_\ell} \int_0^{\delta_\ell} A_1(u_\ell, \delta_r) du_\ell. \quad (\text{S33})$$

Due to the constraint of $\dot{u}_r = 0$, we find that $\Delta x_{3,BA} = -\delta_\ell \alpha_{L,\ell}$, and since $-\delta_\ell = \Delta x_{2,BA} - \Delta x_{1,BA}$, then $\Delta x_{1,BA} = (1 - \alpha_{L,\ell})\delta_\ell$.

For the transition $B = SL \rightarrow C = SS$, we find

$$\Delta x_{2,CB} = - \int_{\delta_r}^0 A_3(0, u_r) du_r = \alpha_{S,r}\delta_r \quad \text{with} \quad \alpha_{S,r} \equiv \frac{1}{\delta_r} \int_0^{\delta_r} A_3(0, u_r) du_r, \quad (\text{S34})$$

where $\Delta x_{1,CB} = \delta_r \alpha_{S,r}$ and $\Delta x_{3,CB} = -(1 - \alpha_{S,r})\delta_r$.

For the transition $C = SS \rightarrow D = LS$, we find

$$\Delta x_{2,DC} = \int_0^{\delta_\ell} A_1(u_\ell, 0) du_\ell = \alpha_{S,\ell}\delta_\ell \quad \text{with} \quad \alpha_{S,\ell} \equiv \frac{1}{\delta_\ell} \int_0^{\delta_\ell} A_1(u_\ell, 0) du_\ell, \quad (\text{S35})$$

where $\Delta x_{1,DC} = -(1 - \alpha_{S,\ell})\delta_\ell$ and $\Delta x_{3,DC} = \delta_\ell \alpha_{S,\ell}$.

Finally, for the transition $D = LS \rightarrow A = LL$, we find

$$\Delta x_{2,AD} = - \int_0^{\delta_r} A_3(\delta_\ell, u_r) du_r = -\alpha_{L,r}\delta_r \quad \text{with} \quad \alpha_{L,r} \equiv \frac{1}{\delta_r} \int_0^{\delta_r} A_3(\delta_\ell, u_r) du_r, \quad (\text{S36})$$

where $\Delta x_{1,AD} = -\alpha_{L,r}\delta_r$ and $\Delta x_{3,DC} = (1 - \alpha_{L,r})\delta_r$.

The above results are all summarized in Table SI. By summing any column of the table, we find that the total displacement due to swimming after a full cycle is

$$d = (\alpha_{S,\ell} - \alpha_{L,\ell})\delta_\ell + (\alpha_{S,r} - \alpha_{L,r})\delta_r. \quad (\text{S37})$$

In the special case of a symmetric swimmer like in the main text with all spheres identical and thus $M_{11} = M_{22} = M_{33} = \mu$ as well as $\delta_\ell = \delta_r = \delta$, we find $\alpha_{S,\ell} = \alpha_{S,r} = \alpha_S$ and $\alpha_{L,\ell} = \alpha_{L,r} = \alpha_L$ and the table in the main text is recovered, which implies that $d = 2(\alpha_S - \alpha_L)\delta$. Bounds on the possible values of α_S and α_L can be obtained by considering two extreme cases. If in the L state the spheres are very far from each other, hydrodynamic interactions are negligible and then $A_1 = A_2 = A_3 = 1/3$, giving a lower bound of $\alpha_L = 1/3$. If in the S state the spheres are so

close to each other as to be overlapping, we can transform the three-sphere problem into a two-sphere problem. We take the $C \rightarrow D$ transition as an example. The internal active force of the left arm is denoted \tilde{f} (positive if it acts to contract the arm). The positions of the spheres then evolve according to $\dot{x}_1 = (-\mu + M_{12})\tilde{f}$ and $\dot{x}_2 = (\mu_S - M_{12})\tilde{f}$ with μ_S defined as the effective mobility of the rigid block. Therefore, we can express α_S as

$$\alpha_S = \frac{\mu_S - M_{12}}{\mu + \mu_S - 2M_{12}}. \quad (\text{S38})$$

For the upper bound one can assume that the effective block with mobility μ_S becomes a sphere of mobility μ . Hence, in this limit $\alpha_S = 1/2$. With these two bounds, we find that overall $1/3 < \alpha_L < \alpha_S < 1/2$ as stated in the main text.

B. Perturbative expansion

We proceed further to find a perturbative expression for the values of the α -coefficients, displacement after a full cycle, and average velocity. We use the Stokes law for the friction coefficient and the expression for the Oseen tensor. For simplicity, we take all spheres to be equal. We assume that $M_{11} = M_{22} = M_{33} \equiv \mu = \frac{1}{6\pi\eta a}$ where a is the radius of the spheres and η is the viscosity of the medium. For the off-diagonal components the expressions are, $M_{12} = \frac{1}{4\pi\eta s_\ell}$, $M_{23} = \frac{1}{4\pi\eta s_r}$ and $M_{13} = \frac{1}{4\pi\eta(s_\ell + s_r)}$, where s_i is the distance between the corresponding spheres. We define, $s_\rho = L_\rho + u_\rho$ with L_ρ being a constant length with $u_\rho \ll L_\rho$. By Taylor expanding, the two integrals in Eq. (S32) become

$$\int_{\text{cycle}} A_1 du_\ell = \frac{1}{3} \int_{\text{cycle}} du_\ell + \frac{a}{3} \int_{\text{cycle}} (K_{0,\ell r} + K_{1,\ell r} u_\ell - K_{2,\ell r} u_r) du_\ell + \mathcal{O}\left(\frac{au_\rho^2}{L_\rho^3}\right), \quad (\text{S39})$$

$$- \int_{\text{cycle}} A_3 du_r = -\frac{1}{3} \int_{\text{cycle}} du_r - \frac{a}{3} \int_{\text{cycle}} (K_{0,r\ell} - K_{2,r\ell} u_\ell + K_{1,r\ell} u_r) du_r + \mathcal{O}\left(\frac{au_\rho^2}{L_\rho^3}\right), \quad (\text{S40})$$

where

$$K_{0,\rho\nu} = \frac{L_\rho}{L_\nu(L_\rho + L_\nu)} - \frac{L_\nu}{2L_\rho(L_\rho + L_\nu)}, \quad (\text{S41})$$

$$K_{1,\rho\nu} = \frac{1}{(L_\rho + L_\nu)^2} + \frac{L_\nu}{L_\rho(L_\rho + L_\nu)^2} + \frac{L_\nu^2}{2L_\rho^2(L_\rho + L_\nu)^2}, \quad (\text{S42})$$

$$K_{2,\rho\nu} = \frac{1}{2(L_\rho + L_\nu)^2} + \frac{2L_\rho}{L_\nu(L_\rho + L_\nu)^2} + \frac{L_\rho^2}{L_\nu^2(L_\rho + L_\nu)^2}. \quad (\text{S43})$$

This allows us to calculate the perturbative expressions for α coefficients as follows

$$\alpha_{L,\ell} = \frac{1}{3} + \frac{a}{3} \left(K_{0,\ell r} + \frac{1}{2} K_{1,\ell r} \delta_\ell - K_{2,\ell r} \delta_r \right), \quad (\text{S44})$$

$$\alpha_{S,r} = \frac{1}{3} + \frac{a}{3} \left(K_{0,r\ell} + \frac{1}{2} K_{1,r\ell} \delta_r \right), \quad (\text{S45})$$

$$\alpha_{S,\ell} = \frac{1}{3} + \frac{a}{3} \left(K_{0,r\ell} + \frac{1}{2} K_{1,\ell r} \delta_\ell \right), \quad (\text{S46})$$

$$\alpha_{L,r} = \frac{1}{3} + \frac{a}{3} \left(K_{0,r\ell} + \frac{1}{2} K_{1,r\ell} \delta_r - K_{2,r\ell} \delta_\ell \right), \quad (\text{S47})$$

which implies

$$d = \frac{a}{3} (K_{2,\ell r} + K_{2,r\ell}) \delta_\ell \delta_r = \frac{a}{3} \left(\frac{1}{L_\ell^2} + \frac{1}{L_r^2} - \frac{1}{(L_\ell + L_r)^2} \right) \delta_\ell \delta_r. \quad (\text{S48})$$

This recovers the expected result [1]

$$V(F=0) = Jd = \frac{a}{3} \left(\frac{1}{L_\ell^2} + \frac{1}{L_r^2} - \frac{1}{(L_\ell + L_r)^2} \right) J \delta_\ell \delta_r = \frac{a}{3} \left(\frac{1}{L_\ell^2} + \frac{1}{L_r^2} - \frac{1}{(L_\ell + L_r)^2} \right) \left\langle \frac{d\mathcal{A}}{dt} \right\rangle, \quad (\text{S49})$$

for the propulsion of a swimmer in the absence of an external force being proportional to the area \mathcal{A} enclosed by its trajectory in conformation space.

In the special case of $L_\ell = L_r \equiv L_0$, one obtains

$$\alpha_{L,\ell} = \frac{1}{3} + \frac{a}{12L_0^2} \left(L_0 + \frac{5}{4}\delta_\ell - \frac{7}{2}\delta_r \right), \quad (\text{S50})$$

$$\alpha_{S,r} = \frac{1}{3} + \frac{a}{12L_0^2} \left(L_0 + \frac{5}{4}\delta_r \right), \quad (\text{S51})$$

$$\alpha_{S,\ell} = \frac{1}{3} + \frac{a}{12L_0^2} \left(L_0 + \frac{5}{4}\delta_\ell \right), \quad (\text{S52})$$

$$\alpha_{L,r} = \frac{1}{3} + \frac{a}{12L_0^2} \left(L_0 + \frac{5}{4}\delta_r - \frac{7}{2}\delta_\ell \right), \quad (\text{S53})$$

which implies

$$d = \frac{7a}{12L_0^2} \delta_\ell \delta_r. \quad (\text{S54})$$

If we further assume that $\delta_\ell = \delta_r \equiv \delta$ as in the main text, we find

$$\alpha_{L,\ell} = \alpha_{L,r} \equiv \alpha_L = \frac{1}{3} + \frac{a}{12L_0^2} \left(L_0 - \frac{9}{4}\delta \right), \quad (\text{S55})$$

$$\alpha_{S,\ell} = \alpha_{S,r} \equiv \alpha_S = \frac{1}{3} + \frac{a}{12L_0^2} \left(L_0 + \frac{5}{4}\delta \right). \quad (\text{S56})$$

As stated in the main text, we observe that we generically have $\alpha_L < \alpha_S$. The lower bound of 1/3 corresponds to the limit $L_0 \gg a$. The total displacement after a full cycle is then

$$d = \frac{7a}{12L_0^2} \delta^2. \quad (\text{S57})$$

C. Hydrodynamic mobility

As derived above, the average mobility M describing the passive drag of the particle by the external force is given in Eq. (S31).

In general, M therefore depends on the chemical affinities and external forces through the probabilities P_α , and is not purely geometric. However, to the first order in the hydrodynamic interactions $\mathcal{O}(M_{ij}/M_{ii})$, the instantaneous mobility B can be written as

$$B = (M_{11}^{-1} + M_{22}^{-1} + M_{33}^{-1})^{-1} \left(1 + 2 \frac{M_{11}M_{23} + M_{22}M_{13} + M_{33}M_{12}}{M_{11}M_{22} + M_{11}M_{33} + M_{22}M_{33}} + \mathcal{O}\left(\frac{M_{ij}^2}{M_{ii}^2}\right) \right), \quad (\text{S58})$$

where the dependence on (u_ℓ, u_r) is only contained in the cross-mobilities M_{ij} with $i \neq j$, which are of higher order. Therefore, the average mobility M is independent of the chemical affinities and external forces to the lowest order and reads

$$M = (M_{11}^{-1} + M_{22}^{-1} + M_{33}^{-1})^{-1} + \langle \mathcal{O}(M_{ij}/M_{ii}) \rangle. \quad (\text{S59})$$

In particular, for equal-sized spheres with mobility μ we find $M \approx \mu/3$.

D. Entropy production rate

As described in Appendix A, starting for the expression of the EPR $T\dot{\sigma} = \sum_i \langle \dot{x}_i f_i \rangle$, splitting the forces into internal and external, and using Eqs. (S23)–(S25), the EPR becomes

$$T\dot{\sigma} = \langle BF^2 + \dot{u}_\ell [\tilde{f}_\ell - (1 - A_1)F_1 + A_1(F_2 + F_3)] + \dot{u}_r [\tilde{f}_r - A_3(F_1 + F_2) + (1 - A_3)F_3] \rangle. \quad (\text{S60})$$

As explained in the main text the contributions to entropy production from each stochastic transition can be calculated as was done explicitly for the displacements in Eq. (S32). By following the procedure per step and averaging over the steady-state limit, one easily finds

$$T\dot{\sigma} = MF^2 + J(\varepsilon, F) \sum_{\{\beta\alpha\}} T\Delta\sigma_{\beta\alpha}, \quad (\text{S61})$$

where the contributions to dissipation in each transition are given by the following expressions

$$T\Delta\sigma_{BA} = \int_{\delta_\ell}^0 [\tilde{f}_\ell - (1 - A_1)F_1 + A_1(F_2 + F_3)]du_\ell = \Delta\varepsilon_{BA} + \sum_i F_i\Delta x_{i,BA} \text{ with } \Delta\varepsilon_{BA} \equiv \int_{\delta_\ell}^0 \tilde{f}_\ell du_\ell, \quad (\text{S62})$$

$$T\Delta\sigma_{CB} = \int_{\delta_r}^0 [\tilde{f}_r - A_3(F_1 + F_2) + (1 - A_3)F_3]du_r = \Delta\varepsilon_{CB} + \sum_i F_i\Delta x_{i,CB} \text{ with } \Delta\varepsilon_{CB} \equiv \int_{\delta_r}^0 \tilde{f}_r du_r, \quad (\text{S63})$$

$$T\Delta\sigma_{DC} = \int_0^{\delta_\ell} [\tilde{f}_\ell - (1 - A_1)F_1 + A_1(F_2 + F_3)]du_\ell = \Delta\varepsilon_{DC} + \sum_i F_i\Delta x_{i,DC} \text{ with } \Delta\varepsilon_{DC} \equiv \int_0^{\delta_\ell} \tilde{f}_\ell du_\ell, \quad (\text{S64})$$

$$T\Delta\sigma_{AD} = \int_0^{\delta_r} [\tilde{f}_r - A_3(F_1 + F_2) + (1 - A_3)F_3]du_r = \Delta\varepsilon_{AD} + \sum_i F_i\Delta x_{i,AD} \text{ with } \Delta\varepsilon_{AD} \equiv \int_0^{\delta_r} \tilde{f}_r du_r. \quad (\text{S65})$$

By summing the chemical energies $\Delta\varepsilon_{\beta\alpha}$ over all four transitions we recover (by definition) the total chemical affinity ε . In turn, the sum of $\sum_i F_i\Delta x_{i,\beta\alpha}$ over all four transitions gives Fd , as the sum of displacements for any of the spheres leads to the swimming distance d , and the sum of the forces F_i correspond to the total external force F . Therefore,

$$T\dot{\sigma} = MF^2 + J(\varepsilon, F)(\varepsilon + Fd) = V(\varepsilon, F)F + J(\varepsilon, F)\varepsilon, \quad (\text{S66})$$

as stated in the main text.

The local detailed balance between forward and backward rates requires that we account for the dissipation associated with each transition [3], so that

$$\frac{k_{\beta\alpha}}{k_{\alpha\beta}} = \exp\left[\frac{T\Delta\sigma_{\beta\alpha}}{k_B T}\right] = \exp\left[\frac{\Delta\varepsilon_{\beta\alpha} + W_{\beta\alpha}}{k_B T}\right] = \frac{k_{0\beta\alpha}}{k_{0\alpha\beta}} \exp\left(\frac{W_{\beta\alpha}}{k_B T}\right), \quad (\text{S67})$$

where we have defined the work done by the external forces during the transition $\alpha \rightarrow \beta$ as $W_{\beta\alpha} \equiv \sum_i F_i\Delta x_{i,\beta\alpha}$. This gives the modification of the rates due to the external forces as stated in the main text.

IV. INTUITIVE MEANING OF $\theta_{\beta\alpha}$

The parameter $\theta_{\beta\alpha}$ can be related to the position of the energy barrier between states α and β along a continuous reaction coordinate, in the context of a Kramers escape problem [4]. Without loss of generality, let us focus on a reaction involving the expansion of an arm from $u = 0$ (state α) to $u = \delta$ (state β), where u acts as the reaction coordinate. Consider a bistable potential $U(u)$ which, in the absence of any additional forces, has one minimum at $u = 0$, one minimum at $u = \delta$, and an energy barrier between them located at the transition state $u = u_{ba} = \theta_{\beta\alpha}\delta$.

Now consider an additional constant force $f_{\beta\alpha}$ acting on the arm (in our model, this corresponds to the internal stress in the arm that is caused by the presence of the external force). The total potential including the effect of the force is then $U_{\text{tot}}(u) = U(u) - f_{\beta\alpha}u$. The total energy of state α remains $U_{\text{tot}}(0) = 0$, while that of state β becomes $U_{\text{tot}}(\delta) = U(\delta) - f_{\beta\alpha}\delta$. Assuming that the energy barrier is sharply peaked, so that its location remains unchanged, the energy of the transition state becomes $U_{\text{tot}}(u_{ba}) = U(u_{ba}) - f_{\beta\alpha}\theta_{\beta\alpha}\delta$.

Using Kramers rate theory [4], the transition rate from α to β is related to the height of the transition energy barrier as seen from α , with

$$\begin{aligned} k_{\beta\alpha} &\propto \exp\left\{-\frac{U_{\text{tot}}(u_{ba}) - U_{\text{tot}}(0)}{k_B T}\right\} = \exp\left\{-\frac{U(u_{ba}) - f_{\beta\alpha}\theta_{\beta\alpha}\delta - U(0)}{k_B T}\right\} \\ &= \exp\left\{-\frac{U(u_{ba}) - U(0)}{k_B T}\right\} \exp\left\{\frac{f_{\beta\alpha}\theta_{\beta\alpha}\delta}{k_B T}\right\}, \end{aligned}$$

while the transition rate from β to α is related to the height of the transition energy barrier as seen from β , with

$$\begin{aligned} k_{\alpha\beta} &\propto \exp\left\{-\frac{U_{\text{tot}}(u_{\text{ba}}) - U_{\text{tot}}(\delta)}{k_B T}\right\} = \exp\left\{-\frac{U(u_{\text{ba}}) - f_{\beta\alpha}\theta_{\beta\alpha}\delta - U(0) + f_{\beta\alpha}\delta}{k_B T}\right\} \\ &= \exp\left\{-\frac{U(u_{\text{ba}}) - U(\delta)}{k_B T}\right\} \exp\left\{-\frac{f_{\beta\alpha}(1 - \theta_{\beta\alpha})\delta}{k_B T}\right\}. \end{aligned}$$

If, again, we assume the energy barrier to be sharply peaked, the force does not significantly alter the curvature of the energy barrier, so that the prefactor of Kramers' rate (omitted in the proportionality relations given above) remains unchanged in presence of the force. We can then write

$$k_{\beta\alpha} = k_{0\beta\alpha} \exp\left\{\frac{\theta_{\beta\alpha} f_{\beta\alpha} \delta}{k_B T}\right\}, \quad (\text{S68})$$

$$k_{\alpha\beta} = k_{0\alpha\beta} \exp\left\{-\frac{(1 - \theta_{\beta\alpha}) f_{\beta\alpha} \delta}{k_B T}\right\}. \quad (\text{S69})$$

Identifying the work done by the force in the $\alpha \rightarrow \beta$ transition as $W_{\beta\alpha} = f_{\beta\alpha}\delta$, from Eq. (S68) we immediately recover Eq. (4) in the main text. On the other hand, self-consistency with Eq. (S69) implies the requirements $\theta_{\alpha\beta} = 1 - \theta_{\beta\alpha}$ and $W_{\alpha\beta} = -W_{\beta\alpha}$ already stated in the main text.

In summary, $\theta_{\beta\alpha} = 0$ corresponds to the limit in which the energy barrier is close to the ‘‘origin’’ state α , whereas $\theta_{\beta\alpha} = 1$ corresponds to the opposite limit in which the energy barrier is close to the ‘‘destination’’ state β .

V. RESULTS FOR NEGATIVE CHEMICAL AFFINITY

In this section, we report results for negative values of cycle affinity ε ; see Figs. S1, S2, and S3. This implies, that the cycle will run in reverse in the absence of the force, and the swimmer will swim backwards (towards the left). The force F still remains exerted on the first sphere (which now becomes the front of the swimmer). The sign convention for the force is still such that positive forces point towards the right, so positive forces F in this case oppose the self-propulsion of the swimmer.

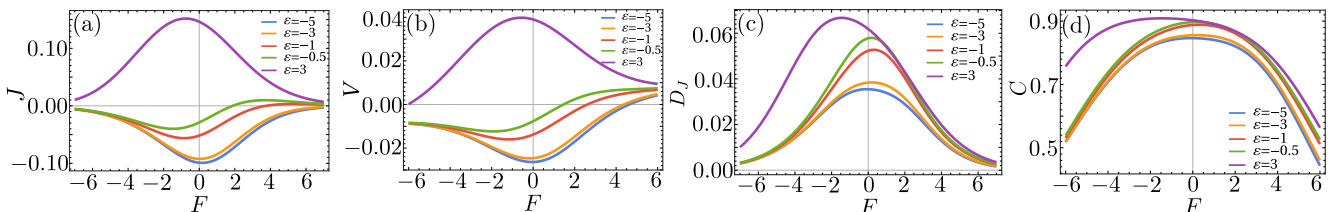


FIG. S1. Dependence on the external force F , for several values of the chemical affinity ε , of (a) the chemical current J , (b) the spatial current or velocity V , (c) the chemical diffusion coefficient D_J , and (d) the correlation C between J and V .

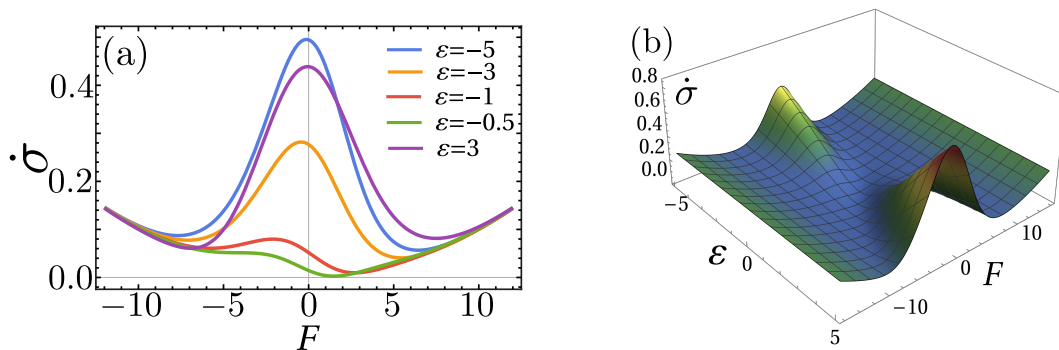


FIG. S2. (a) Entropy production rate $\dot{\sigma}$ as a function of the external force F , for several values of the chemical affinity ε , and (b) as a function of both the external force and ε .

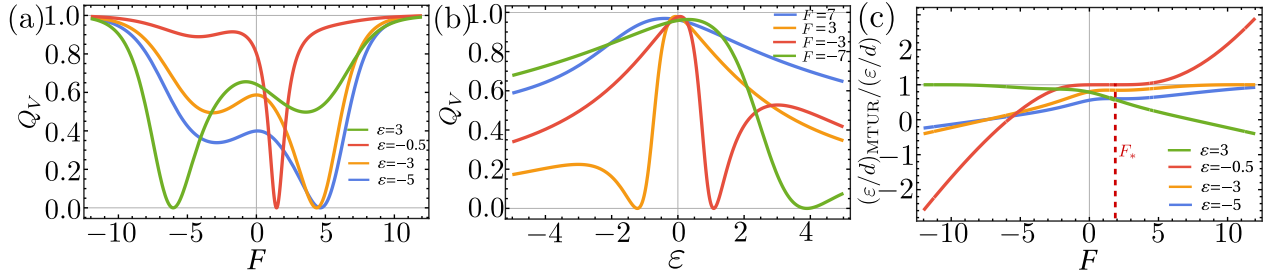


FIG. S3. (a,b) The quality factor Q_V of the precision-dissipation tradeoff for the spatial current V , (a) as a function of F for fixed values of ϵ , (b) as a function of ϵ for fixed values of F . (c) Ratio of the MTUR-inferred [Eq. (8) of the main text] and true chemical force ϵ/d . F_* is the critical force at which the chemical current vanishes. For $F < F_*$ the inferred value is a lower bound, for $F > F_*$ an upper bound, for $F = F_*$ it is exact.

-
- [1] R. Golestanian and A. Ajdari, Mechanical response of a small swimmer driven by conformational transitions, *Phys. Rev. Lett.* **100**, 038101 (2008).
 [2] Z. Koza, General technique of calculating the drift velocity and diffusion coefficient in arbitrary periodic systems, *J. Phys. A: Math* **32**, 7637 (1999).
 [3] U. Seifert, Stochastic thermodynamics, fluctuation theorems and molecular machines, *Rep. Prog. Phys.* **75**, 126001 (2012).
 [4] P. Hänggi, P. Talkner, and M. Borkovec, Reaction-rate theory: fifty years after kramers, *Rev. Mod. Phys.* **62**, 251 (1990).

Chapter 7

Nonlinear response theory of molecular machines

This chapter is reproduced from the Letter Michalis Chatzittofi, Jaime Agudo-Canalejo, and Ramin Golestanian, *EPL* 147 21002 [\[136\]](#).

In this article, I contributed in designing the research and deriving the equations of motion. I performed the analytical calculations and contributed in writing the paper.

Nonlinear response theory of molecular machines

MICHALIS CHATZITTOFI¹ , JAIME AGUDO-CANALEJO^{1,2} and RAMIN GOLESTANIAN^{1,3(a)} 

¹ *Max Planck Institute for Dynamics and Self-Organization (MPI-DS) - D-37077 Göttingen, Germany*

² *Department of Physics and Astronomy, University College London - London WC1E 6BT, UK*

³ *Rudolf Peierls Centre for Theoretical Physics, University of Oxford - Oxford OX1 3PU, UK*

received 22 May 2024; accepted in final form 2 August 2024

published online 21 August 2024

Abstract – Chemical affinities are responsible for driving active matter systems out of equilibrium. At the nano-scale, molecular machines interact with the surrounding environment and are subjected to external forces. The mechano-chemical coupling which arises naturally in these systems reveals a complex interplay between chemical and mechanical degrees of freedom with strong impact on their active mechanism. By considering various models far from equilibrium, we show that the tuning of applied forces gives rise to a nonlinear response that causes a non-monotonic behaviour in the machines' activity. Our findings have implications in understanding, designing, and triggering such processes by controlled application of external fields, including the collective dynamics of larger non-equilibrium systems where the total dissipation and performance might be affected by internal and inter-particle interactions.



Copyright © 2024 The author(s)

Published by the EPLA under the terms of the [Creative Commons Attribution 4.0 International License](https://creativecommons.org/licenses/by/4.0/) (CC BY). Further distribution of this work must maintain attribution to the author(s) and the published article's title, journal citation, and DOI.

Active matter systems [1] convert chemical energy into motion or useful work. In the biological context, the chemical energy typically comes from ATP hydrolysis [2]. In general, such systems may be enzymes, molecular motors [3,4], stochastic micro-swimmers [5–8], rotors [9–11], and even synthetic active matter [12–14]. When modeling the motion or the activity of such active matter systems, especially in the case of self-propelled particles, the existence of an “active force” that creates propulsion or motion is typically assumed [15].

In reality, the mechanism that generates the useful work is some non-equilibrium cyclic process that is driven by some *chemical affinity* which is the free energy dissipated per cycle [16]. This affinity generates an out-of-equilibrium current associated to the reaction velocity of the specific process, and the product of the current and the affinity is related to the total entropy production rate [17]. Any external forces (conservative or otherwise) must be treated carefully due to the mechano-chemical coupling of the internal mechanism of the nano-machines with the external, spatial, or hydrodynamic degrees of freedom which determine the extraction of work or power [18–21].

In the past, theoretical models for how internal energy dissipation is transduced into actuation of external degrees of freedom have been used successfully to explain the enhanced diffusion [22], chemotaxis [23], and synchronization [24] of enzymes, the motion of rotors by using flashing ratchets [12], or the steps of molecular motors [3,25]. On the other hand, these models often lack an important missing piece: how applied forces or other experimentally controlled triggers feed back on the dynamics of the internal degrees of freedom via the mechano-chemical coupling, beyond what linear response theory can predict [26,27].

In this letter, we focus on the activity of enzymes (see fig. 1(a)), rotors (fig. 1(b)), and force-free micro-swimmers (fig. 1(f)) in the presence of external forces. The key ingredient for activity is a chemical affinity $\Delta\mu$ which drives the system out of equilibrium and induces motion or performs work, depending on the system. To model discrete chemical reactions that dissipate an energy $\Delta\mu$, we assume that nano-machines carry an internal reaction coordinate ϕ which is subject to a washboard potential, see fig. 1(c), where a reaction corresponds to the phase ϕ advancing by 2π . We show that an applied force effectively modifies either the energy barriers of the energy free landscape that governs the dynamics of the internal process or reaction coordinate (fig. 1(d)), the chemical driving force (fig. 1(e)),

^(a)E-mail: ramin.golestanian@ds.mpg.de (corresponding author)

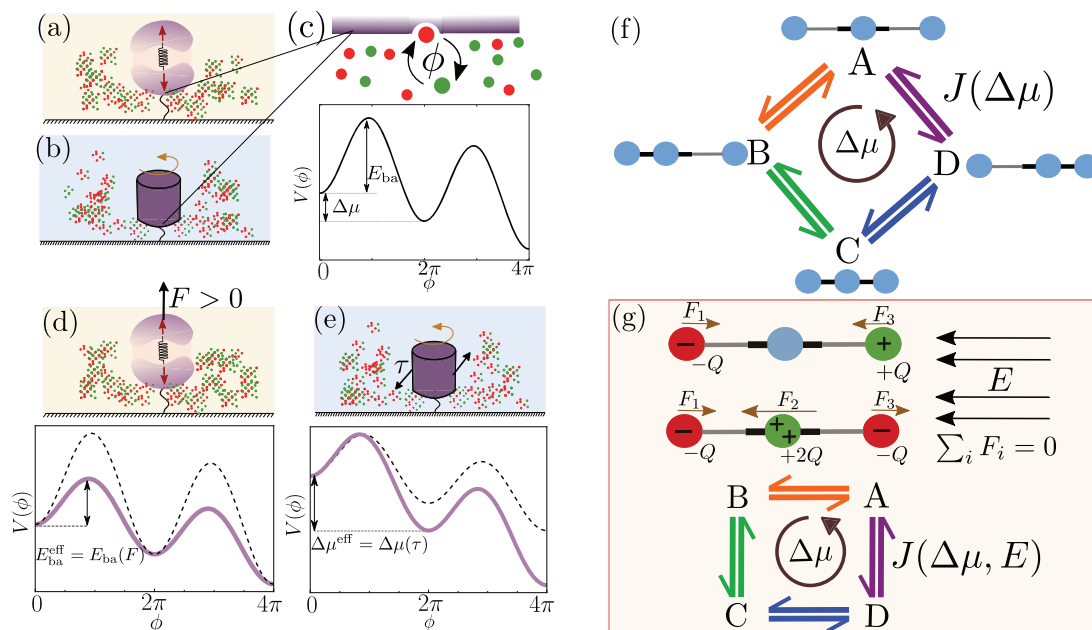


Fig. 1: Examples of molecular machines: (a) an enzyme that undergoes conformational changes attached to a surface, (b) a molecular rotor surrounded by a fluid medium. (c) The internal dynamics of the molecular machine involves the conversion of a “fuel” or “substrate” molecule into a lower-energy “waste” or “product” molecule. The reaction is here described by a phase ϕ that advances by 2π in each step along a potential $V(\phi)$ that represents the free energy landscape of the chemical reaction, with $\Delta\mu$ being the free energy difference or driving force, and E_{ba} being the energy barrier of the process. (d) For an enzyme, an applied force F effectively changes the energy barrier of the internal process. (e) For a rotor, an applied torque τ effectively changes the driving force of the internal process. (f) A stochastic three-sphere swimmer model with four possible conformations [5]. Transitions between the states happen along a cycle driven by the affinity $\Delta\mu$, which generates a current $J(\Delta\mu)$. (g) The electric dipole $(-Q, 0, +Q)$ and the electric quadrupole $(-Q, +2Q, -Q)$ models for micro-swimmers with overall charge neutrality. The arrows show the influence of the external electric field E that generates electrostatic forces with vanishing net sum. The cycle affinity is still equal to $\Delta\mu$, but the current now depends also on the strength of the electric field E .

or both. This can be used to tune the catalytic activity of enzymes and motors in both directions, from enhancement to stalling. Experimentally, such manipulations might arise from ultrasound irradiation, electromagnetic fields, and other methods [28,29]. Various experiments have reported a non-monotonic behaviour of the enzymatic activity due to such external manipulations [28].

In the case of micro-swimmers, to emphasize how a mechano-chemical coupling cannot generally be modelled as an active force, we consider examples of neutrally charged swimmers with spatially non-uniform charge distributions subjected to an external electric field (fig. 1(g)) which applies different forces on the different sub-units of the complex. These serve as examples where applied forces do not cause any net drift or direct hydrodynamic dissipation. In particular, this simple consideration highlights how, for force-free micro-swimmers, external fields affect the activity and the total chemical energy dissipation in a non-trivial way.

Enzymes. –

Model. To model an enzyme that can undergo conformational changes, we consider a minimal model in which the enzyme is represented with two sub-units reflecting its softest mode, as shown in fig. 1(a) [22]. We denote with

x_1 and x_2 the positions of the two sub-units. To model its catalytic cycle (*e.g.*, ATP hydrolysis in the biological case), we use a cyclic coordinate ϕ , with $\Delta\mu$ being the difference in Gibbs free energy catalyzed in every reaction; see fig. 1(c). The non-equilibrium potential $U(x_1, x_2, \phi)$, which governs the coupled dynamics of the two spatial coordinates and the internal coordinate, reads [24]

$$U(x_1, x_2, \phi) = \tilde{V}(\phi) - f\phi + \frac{k}{2}(x_1 - x_2 - L(\phi))^2 - Fx_1. \quad (1)$$

Here, $\tilde{V}(\phi)$ is a 2π -periodic function that represents the conservative part of the chemical dynamics—that is related to the energy barriers of the washboard potential—and the second term is the non-equilibrium contribution with f being the chemical driving force related to $\Delta\mu$ through $\Delta\mu = 2\pi f$. The third term in eq. (1) corresponds to a harmonic potential governing the conformation (elongation) of the enzyme. The rest length $L(\phi)$ (with $L(\phi)$ being a 2π -periodic function) depends on the internal reaction coordinate ϕ , and is responsible for the reaction-induced conformational changes of the enzyme. The last term of eq. (1) represents the external force F that is applied on one of the sub-units (here sub-unit 1, without loss of generality).

The overdamped dynamics of this system is

$$\dot{x}_1 = -m_1 \partial_1 U, \quad (2)$$

$$\dot{x}_2 = -m_2 \partial_2 U, \quad (3)$$

$$\dot{\phi} = -m_\phi \partial_\phi U, \quad (4)$$

where m_1 , m_2 , and m_ϕ are the corresponding mobilities of the coordinates. To proceed further we assume that subunit 2 is rigidly attached to a substrate (see figs. 1(a), (d)). This implies that x_2 is constant (as $m_2 \rightarrow 0$), and can thus be absorbed in the definition of the rest length $L(\phi)$. Moreover, we assume that the enzyme is relatively stiff, *i.e.*, $m_1 k \gg m_\phi \Delta\mu$, and therefore the length relaxes relatively more quickly, as compared to the dynamics of the phase ϕ . This is equivalent to assuming a strong mechano-chemical coupling of the internal cycle and the spatial conformation. We define $\delta x_1 \equiv x_1 - L(\phi)$, which yields $\delta \dot{x}_1 = \dot{x}_1 - L'(\phi) \dot{\phi}$. This allows us to enslave x_1 to the dynamics of ϕ via the stiff enzyme assumption, which implies that $\delta \dot{x}_1 \simeq 0$ and the actual enzyme elongation closely trails behind the rest length $L(\phi)$. This projection reduces the deterministic dynamics of the internal phase ϕ to a single, closed equation of motion given by

$$\dot{\phi} = -M(\phi) \partial_\phi V(\phi), \quad (5)$$

with a modified effective potential $V(\phi)$ and mobility $M(\phi)$ for the phase given by

$$V(\phi) = -f\phi - \tilde{V}(\phi) - FL(\phi), \quad (6)$$

$$M(\phi) = \frac{m_\phi}{1 + m_\phi (\partial_\phi L)^2 / m_1}. \quad (7)$$

Because enzymatic systems operate at the nano-scale, the thermal fluctuations that help the system overcome the free energy barriers in the potential $V(\phi)$ must be included in a thermodynamically consistent way that respects the fluctuation-dissipation theorem. The Langevin equation for the stochastic dynamics, to be interpreted in the Stratonovich convention, takes the form

$$\dot{\phi} = -M(\phi) \partial_\phi V(\phi) + \frac{k_B T}{2} \partial_\phi M(\phi) + \sqrt{2k_B T M(\phi)} \xi, \quad (8)$$

where k_B is the Boltzmann constant, T the temperature, and ξ is a Gaussian white noise with $\langle \xi(t) \rangle = 0$ and $\langle \xi(t) \xi(t') \rangle = \delta(t-t')$. The second term is the spurious drift which guarantees that in the absence of non-equilibrium driving ($f \rightarrow 0$) the phase ϕ will reach a Boltzmann equilibrium distribution [24,30]. It is worth noting that for a free enzyme (not bound to a substrate) a similar derivation can be carried out leading to the same phase dynamics, eq. (8). This coarse-graining procedure has also been recently used to derive a model to study synchronization for coupled enzymes [24].

For concreteness, we now make a choice for the form of the scalar functions $\tilde{V}(\phi)$ and $L(\phi)$. To describe the dynamics of a chemical reaction two key energetic scales are needed. One is the chemical driving or Gibbs free energy of the reaction, which is captured by the parameter $\Delta\mu$. The second is the height of the energy barrier E_{ba} that must be

overcome, which defines a characteristic rate (inverse time scale) of the reaction, namely, the Kramers rate $r_K \propto e^{-E_{\text{ba}}/k_B T}$. Choosing $\tilde{V}(\phi) = -v \cos(\phi + \arcsin(f/v))$ leads to the standard form of a washboard potential shown in fig. 1(c), given by

$$V_{\text{ch}}(\phi) = -f\phi - v \cos(\phi + \arcsin(f/v)), \quad (9)$$

where the phase shift $\arcsin(f/v)$ is introduced as a convention such that the minima of the chemical potential are located at multiples of 2π . The mapping between (f, v) and $(\Delta\mu, E_{\text{ba}})$ is given by $\Delta\mu = 2\pi f$ and $E_{\text{ba}} = [2\sqrt{1 - (f/v)^2} - (f/v)\pi]v$ [24,30].

The rest length $L(\phi)$ must be a 2π -periodic function, so that after a full reaction the rest length remains unchanged. At the leading harmonic order, the function $L(\phi)$ can be described by $L = L^{(0)} + \ell \cos(\phi + \delta)$, where $L^{(0)}$ is the average length of the enzyme, ℓ is the amplitude of expansion and contraction, and δ is an arbitrary phase shift. The choice of only the first harmonic implies that, during a catalytic reaction, the enzyme will expand and contract once. For example, if $\delta = 0$ ($= \pi$) then the enzyme is initially in a fully expanded (contracted) state and undergoes one contraction (expansion) during the reaction. As we show in what follows, the phase δ strongly affects the response to the applied force F .

Results. We have managed to reduce the problem to the dynamics of a single degree of freedom. This allows us to use analytical tools from the literature to calculate the average reaction rate J and the diffusion D of the number of reactions at steady state, defined as

$$J \equiv \lim_{t \rightarrow \infty} \frac{\langle \phi \rangle_t}{2\pi t}, \quad (10)$$

$$D \equiv \lim_{t \rightarrow \infty} \frac{\langle \phi^2 \rangle_t - \langle \phi \rangle_t^2}{(2\pi)^2 \cdot 2t}, \quad (11)$$

where $\langle \dots \rangle$ stands for the time average.

As eq. (7) shows, the projection on the slow manifold gives rise to multiplicative noise. Both J and D have been calculated analytically in the case of additive [31] and multiplicative [32] noise. The general expressions for the case with multiplicative noise are

$$J = k_B T \frac{1 - e^{-2\pi f/k_B T}}{\int_0^{2\pi} dx I_+(x)}, \quad (12)$$

$$D = m_\phi k_B T \frac{\int_0^{2\pi} dx [I_+(x)]^2 I_-(x)}{\left[\int_0^{2\pi} dx I_+(x) \right]^3}, \quad (13)$$

where we define

$$I_+(x) \equiv \frac{1}{M(x)} e^{V(x)/k_B T} \int_{x-2\pi}^x dy e^{-V(y)/k_B T}, \quad (14)$$

$$I_-(x) \equiv e^{-V(x)/k_B T} \int_x^{x+2\pi} dy \frac{1}{M(y)} e^{V(y)/k_B T}. \quad (15)$$

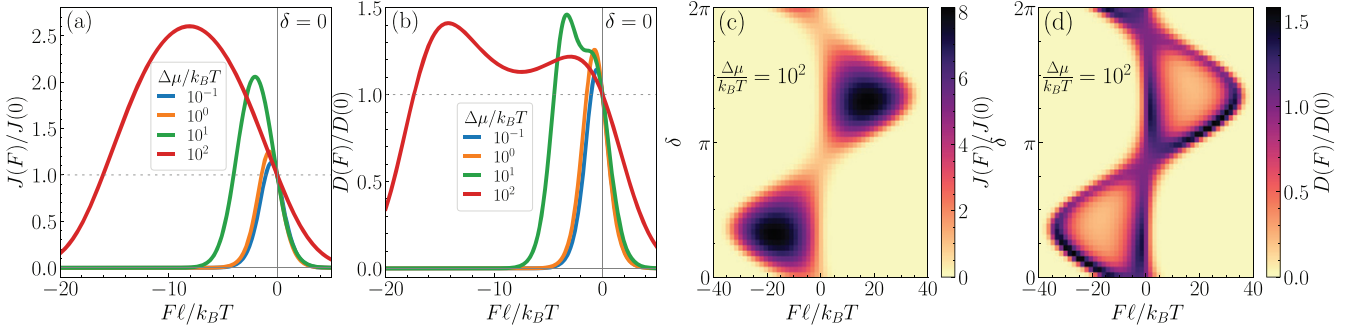


Fig. 2: (a), (b): the internal current (a), and the diffusion of the current (b) for an enzyme that undergoes catalysis-induced conformational changes, as a function of the dimensionless applied force $F\ell/(k_B T)$ for different chemical forces for the case of $\delta = 0$. (c), (d): heat maps for the current (c) and the diffusion (d) as functions of δ and the external force for fixed $\Delta\mu/k_B T = 10^2$.

In the following, we focus on different values of $\Delta\mu/k_B T$, $F\ell/k_B T$, and δ , while we fix the dimensionless mobility ratio as $m_\phi \ell^2/m_1 = 1$ and noise strength as $k_B T/E_{ba} = 1$. Our results for the effect of an external force F on the catalytic dynamics of an enzyme are summarized in fig. 2. More specifically, figs. 2(a) and (b) display the average reaction rate and diffusion for $\delta = 0$ as functions of the applied force, for several values of the chemical driving $\Delta\mu$. For all choices of $\Delta\mu$, we observe stalling of both the reaction rate and the diffusion at high forces (independently of the sign, *i.e.*, $|F| \rightarrow \infty$). The reaction rate typically shows a maximum at a finite force value, whereas the diffusion typically shows two peaks.

The stalling as $|F| \rightarrow \infty$ can be understood as coming from the last term in eq. (6), as the energy barrier in the effective potential goes as $F\ell$ that becomes much larger than $k_B T$, which implies that $J(F) \rightarrow 0$ and $D(F) \rightarrow 0$. The maxima of the reaction rate and the diffusion at finite force can be understood as coming from a delicate interplay between all three terms in eq. (6), or more specifically, between F , δ , f , and v . As a particularly striking illustration, let us consider the special case where $\delta = \arcsin(f/v)$ and the elongation $L(\phi)$ is in (anti-) phase with $\tilde{V}(\phi)$. When the external force reaches the critical value $F = -v/\ell$, the second and third terms in eq. (6) cancel each other, and the internal phase experiences only the constant force f . This special case corresponds to the global maximum of $J(F)$ of the heat map (dark region) in fig. 2(c) and local minimum of $D(F)$ (light region) in fig. 2(d). On the other hand, when $F = (\pm f - v)/\ell$, the effective potential develops an inflection point which leads to the phenomenon known as giant diffusion [31,33] and explains the two peaks in $D(F)$.

Rotors. –

Model. With a similar kind of model as used for an enzyme, we can derive the equations of motion for a rotor (fig. 1(b)), representing, *e.g.*, F1-ATPase [10,11]. The rotor is described by two coordinates: ϕ , which represents an internal reaction coordinate, and θ which is the actual

angular state of the rotor [34]. The potential describing their coupling in this case is

$$U_{\text{rot}}(\theta, \phi) = \tilde{V}(\phi) - f\phi - k_\theta \cos(\phi - n\theta) - \tau\theta, \quad (16)$$

where the first two terms are the same as in eq. (6) and describe the chemical free energy. The third term is a “toothed gear” coupling with strength k_θ between the angle θ and the internal phase ϕ . The integer n describes how many reactions it takes to complete a full turn of the rotor (in the case of ATP-synthase, the motor rotates by 120° per reaction and therefore $n = 3$ [10,11]). The last term corresponds to an externally applied torque.

The over-damped deterministic equations of motion are given as

$$\dot{\theta} = -m_\theta \partial_\theta U_{\text{rot}}, \quad (17)$$

$$\dot{\phi} = -m_\phi \partial_\phi U_{\text{rot}}, \quad (18)$$

where m_θ is the angular mobility. For strong coupling, *i.e.*, $m_\theta k_\theta \gg m_\phi \Delta\mu$, the dynamics of θ is fast relative to the dynamics of ϕ , and therefore, enslaved to it, such that $\dot{\theta} \simeq \dot{\phi}/n$. After further coarse graining and inclusion of the appropriate noise as above, we find that the stochastic evolution of the internal phase is given by

$$\dot{\phi} = -M_{\text{rot}} \partial_\phi V_{\text{rot}}(\phi) + \sqrt{2k_B T M_{\text{rot}}} \xi, \quad (19)$$

to be interpreted in the Stratonovich convention, where

$$V_{\text{rot}}(\phi) = -\phi(f + \tau/n) - v \cos(\phi + \arcsin(f/v)), \quad (20)$$

$$M_{\text{rot}} = \frac{m_\phi}{1 + m_\phi/(m_\theta n^2)}. \quad (21)$$

Notice that there is no spurious drift term in eq. (19) since M_{rot} is constant and, thus, the thermal noise is additive.

Results. As eq. (20) shows, external torques on rotors have a very different effect compared to external forces on enzyme: instead of affecting the energy barriers, the torque τ now effectively changes the driving force f and thus the chemical affinity $\Delta\mu$ (see fig. 1(e)).

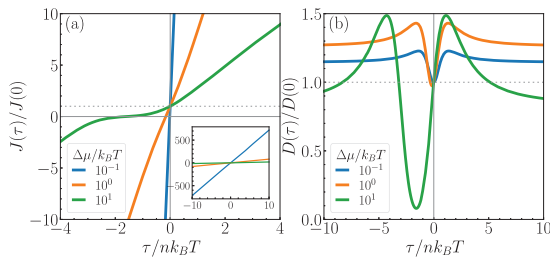


Fig. 3: (a) The internal current and (b) the diffusion of the current as functions of the external torque for several values of the chemical driving force, for a chemically driven rotor.

Figure 3 summarizes our results for the rotor model. For negative values of the torque τ , which oppose the chemically driven motion of the rotor, the reaction rate vanishes and switches sign (fig. 3(a)), implying that the reaction now happens in the reverse direction, *e.g.*, ATP synthesis instead of hydrolysis.

From eq. (20), we see that this reversal occurs at the stall torque $\tau = -nf$ where the effective driving force becomes zero. At high torques, we expect the dynamics to be mostly deterministic, since the energy barriers of the effective potential disappear when $|f + \tau/n| > v$, as shown in fig. 3(a) (see also the inset) where the current depends linearly on the torque as $\tau \rightarrow \pm\infty$. At the stall torque, the diffusion coefficient reaches a minimum since diffusion is lower for a non-driven system (fig. 3(b)). On either side of this local minimum, we find two peaks in the diffusion, corresponding to giant diffusion occurring at the values of the torque for which the effective potential develops inflection points, $\tau = n(-f \pm v)$. At large values of the torque, the dynamics is effectively reduced to that of a particle under the influence of a constant force, and hence, the diffusion plateaus towards a constant value of $M_{\text{rot}}k_B T$, as expected (the Einstein relation).

Stochastic micro-swimmers. –

Model. In this last example, we consider the Najafi-Golestanian micro-swimmer model [35], which is made up of three spheres that are linked together by two arms (see fig. 1(f)), in its stochastic form [5,18,36]. The motion of the mechanical arms is assumed to be due to an internal non-equilibrium mechanism that dissipates some energy $\Delta\mu$ after a full chemical cycle and drives the non-equilibrium current J as shown in fig. 1(f). This coordinated expansion-contraction of the arms ultimately leads to a net displacement of the swimmer after a full cycle, and thus to active swimming. In the absence of a driving affinity $\Delta\mu$, there would be no net current in the chemical cycle, and the micro-swimmer would show no net swimming. Generally speaking, the number of states needed to generate swimming can vary depending on the model, with the minimum number needed to form a cycle being three [6].

Here, we consider four possible conformations for the swimmer, which are associated with four states in a

Table 1: Displacement of each sphere during each transition step. For the reverse transitions, $\Delta x_{i,\alpha\beta} = -\Delta x_{i,\beta\alpha}$.

Process	$\Delta x_{1,\beta\alpha}/\ell$	$\Delta x_{2,\beta\alpha}/\ell$	$\Delta x_{3,\beta\alpha}/\ell$
$A \rightarrow B$	$1 - \alpha_L$	$-\alpha_L$	$-\alpha_L$
$B \rightarrow C$	α_S	α_S	$-(1 - \alpha_S)$
$C \rightarrow D$	$-(1 - \alpha_S)$	α_S	α_S
$D \rightarrow A$	$-\alpha_L$	$-\alpha_L$	$1 - \alpha_L$

discrete Markovian stochastic dynamics [5]. The states of the arms are described by the deformations of the left and right arms, u_{left} and u_{right} , respectively, where we assume that the expansions and contractions take place relatively fast. During a conformational transition, one of the two arms expands or contracts by a distance ℓ . As an example, state B corresponds to $(u_{\text{left}}, u_{\text{right}}) = (0, \ell)$. The transition from α to β happens with rate $k_{\beta\alpha}$. For a thermodynamically consistent description we must require local detailed balance, given by

$$\frac{k_{\beta\alpha}}{k_{\alpha\beta}} = \exp(\Delta\sigma_{\beta\alpha}/k_B), \quad (22)$$

where $\Delta\sigma_{\beta\alpha}$ is the entropy production during the transition $\alpha \rightarrow \beta$ [37]. In the absence of external forces on the micro-swimmer, the entropy production is purely due to the chemical and the internal processes. Hence, $T\Delta\sigma_{\beta\alpha} = \Delta\mu_{\beta\alpha}$ and the transition rates satisfy $k_{0,\beta\alpha}/k_{0,\alpha\beta} = \exp(\Delta\mu_{\beta\alpha}/k_B T)$. The total energy dissipation after a complete cycle in the absence of external forces is then $\sum_{\{\beta\alpha\}} T\Delta\sigma_{\beta\alpha} = \sum_{\{\beta\alpha\}} \Delta\mu_{\beta\alpha} = \Delta\mu$.

To examine the effect of external forces, let us now consider a micro-swimmer with charged components, in the presence of an external electric field, as generalizations of the model presented in ref. [36]. We will consider two different classes of micro-swimmers (see fig. 1(g)). The first one, namely the “dipole model”, has two charged sub-units: the left sphere is negatively charged ($-Q$), the middle one is neutral, and the right sphere is positively charged ($+Q$). The second one, namely the “quadrupole model” has the left and right spheres with negative charge $-Q$, while the central one has positive charge $+2Q$. In both cases, the micro-swimmer is overall neutrally charged. As a consequence, the external field E (parallel to the axis of the micro-swimmer) generates external forces on the charged spheres but does not cause an extra net drift since the net force on the micro-swimmer is zero, *i.e.*, $\sum_i F_i = 0$ where F_i denotes the force on sphere i , with $i = 1, 2, 3$. The forces on the spheres, however, modify the work done by the arms during the conformational transitions and thus the dissipation during each step. To calculate this dissipation, we need to know the displacements of each sphere in every transition. These displacements have been calculated in ref. [18] through a full hydrodynamic derivation, and are summarized in table 1. The parameters α_L and α_S depend purely on the geometry of the swimmer and satisfy the constraint,

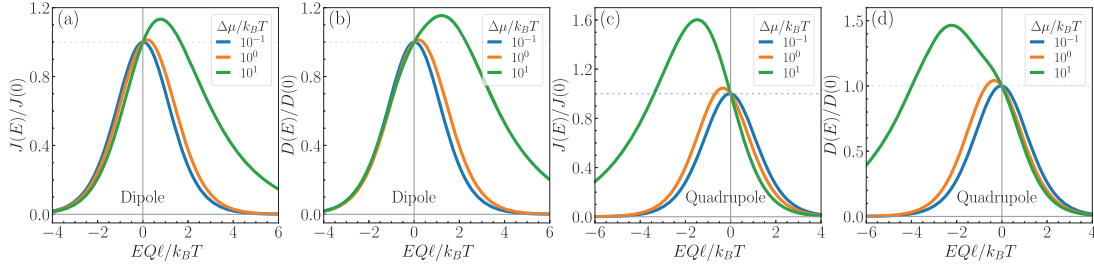


Fig. 4: (a), (c) The internal current and (b), (d) the diffusion of the current as functions of an externally applied electric field, for the dipole model micro-swimmer (a), (b) and the quadrupole model micro-swimmer (c), (d); see fig. 1(g).

$1/3 < \alpha_L < \alpha_S < 1/2$ with the lower bound occurring in the limit of no hydrodynamic interactions (when the spheres remain very far away from each other in all conformations).

The work done by the external field on the spheres in the case of the dipole model is

$$W_{\beta\alpha} = EQ(\Delta x_{1,\beta\alpha} - \Delta x_{3,\beta\alpha}), \quad (23)$$

whereas, for the quadrupole model, it is

$$W_{\beta\alpha} = EQ(\Delta x_{1,\beta\alpha} - 2\Delta x_{2,\beta\alpha} + \Delta x_{3,\beta\alpha}). \quad (24)$$

Importantly, because the displacement of every sphere is the same across a full cycle, *i.e.*, $\sum_{\{\beta\alpha\}} \Delta x_{1,\beta\alpha} = \sum_{\{\beta\alpha\}} \Delta x_{2,\beta\alpha} = \sum_{\{\beta\alpha\}} \Delta x_{3,\beta\alpha}$, we find that there is no net work done by the field after a full cycle, *i.e.*, $\sum_{\{\beta\alpha\}} W_{\beta\alpha} = 0$. Thus, the external field does not contribute to the total affinity driving the cycle, which is still $\Delta\mu$ (see fig. 1(g)). However, it still affects the dynamics by modifying the individual transition rates.

To determine the form of the transition rates, we use the expression

$$k_{\beta\alpha} = k_{0,\beta\alpha} \exp(\theta_{\beta\alpha} W_{\beta\alpha}/k_B), \quad (25)$$

where $k_{0,\beta\alpha}$ are the rates in the absence of external forces. Since we must maintain local detailed balance (eq. (22)), the parameters $\theta_{\beta\alpha}$ satisfy $\theta_{\beta\alpha} = 1 - \theta_{\alpha\beta}$, and are related to the location of the energy barrier between states α and β [18].

Results. For the stochastic dynamics of the three-sphere swimmer we consider the master equation

$$\frac{dP_\alpha}{dt} = \sum_{\beta} (k_{\alpha\beta} P_\beta - k_{\beta\alpha} P_\alpha). \quad (26)$$

At steady state (where we have $dP_\alpha^{\text{ss}}/dt = 0$), the current J is constant, and is given by $J = k_{BA} P_A^{\text{ss}} - k_{AB} P_B^{\text{ss}}$ (or any other pair of neighbouring states may be used). An explicit expression for J and the diffusion coefficient D associated with this stochastic current can be found in refs. [38,39]. It is worth noting that the self-propulsion speed of the micro-swimmer is proportional to J while its spatial diffusion is closely related to D [18].

In the following, we assume $\Delta\mu_{\beta\alpha} = 0$ for all transitions except for $\Delta\mu_{DC} = \Delta\mu$. For the displacements, we fix the geometric parameters as $\alpha_L = 2.1/6$ and $\alpha_S = 2.2/6$ (which implies weak hydrodynamic interactions). We further assume $\theta_{\beta\alpha} = 1/2$ for all transitions. The remaining dimensionless parameters are $\Delta\mu/k_B T$ and $EQl/k_B T$. Figure 4 summarizes the results for the chemical current $J(E)$ and the corresponding diffusion coefficient $D(E)$ as functions of the applied electric field. Note that we consider $E > 0$ to correspond to the electric field pointing towards the left (fig. 1(g)), *i.e.*, against the direction of self-propulsion (whereas for $E < 0$ the field points towards the right). The different charge distributions in the two examples give rise to different internal forces during the cycle. Indeed, for the dipole model swimmer we observe that both $J(E)$ and $D(E)$ peak at positive values of E , whereas they peak at negative values for the quadrupole model swimmer. The enhancement is similar to that observed for our model enzyme above, where the phase shift δ controlled the optimal force.

In summary, the chemical current, which controls the self-propulsion of the micro-swimmer [5,18], exhibits a nonlinear dependence on the applied external field, depending on the charge distribution of the micro-swimmer.

Concluding remarks. – In this work, we have studied three minimal models describing the stochastic, non-equilibrium dynamics of biological and synthetic nano-machines: an enzyme, a rotor, and a micro-swimmer. We focused, in particular, on the nonlinear response of the internal (chemical) dynamics of these nano-machines to externally applied (spatial) forces. Our results indicate that the average currents and diffusion coefficients describing the reaction dynamics inside these nano-machines exhibit a strongly non-monotonic behaviour in terms of the dependence on the external forces, and typically peak at intermediate values of the applied forces. Interestingly, such non-monotonic behaviour has been reported experimentally for a variety of enzymes, in response to multiple external stimuli [28]. While we developed proof-of-concept models, more elaborate models based on similar principles may be able to quantitatively capture the results of these experiments.

The observed behaviour can be ascribed to several nonlinear mechanisms. For enzymes that undergo

conformational changes during catalysis, external forces can effectively reduce the energy barrier in the reaction free energy. In the case of the rotors, an external mechanical torque can effectively increase (or decrease) the driving force of the internal reaction. Lastly, an external electric field can affect the performance of a micro-swimmer even if the latter is neutrally charged overall, by affecting the energy dissipation and thus the local detailed balance in individual stochastic transitions between conformations of the micro-swimmer.

The various systems considered here unravel a rich interplay between chemical and mechanical degrees of freedom, which emerges when the mechano-chemical coupling is accounted for in a thermodynamically consistent manner. In the particular case of force-free micro-swimmers, these are subtle but important effects that are lost in models where the swimming is considered to come simply from an “active force”. We hope that the nonlinear response framework developed here will prove useful in modelling other molecular-scale non-equilibrium systems where a precise formulation of the mechano-chemical coupling is of utmost importance.

* * *

We acknowledge support from the Max Planck School Matter to Life and the MaxSynBio Consortium which are jointly funded by the Federal Ministry of Education and Research (BMBF) of Germany and the Max Planck Society.

Data availability statement: All data that support the findings of this study are included within the article (and any supplementary files).

REFERENCES

- [1] GOMPPER G., WINKLER R. G., SPECK T., SOLON A., NARDINI C., PERUANI F., LÖWEN H., GOLESTANIAN R., KAUPP U. B., ALVAREZ L., KIØRBOE T., LAUGA E., POON W. C. K., DESIMONE A., MUIÑOS-LANDIN S., FISCHER A., SÖKER N. A., CICHOS F., KAPRAL R., GASPARD P., RIPOLL M., SAGUES F., DOOSTMOHAMMADI A., YEOMANS J. M., ARANSON I. S., BECHINGER C., STARK H., HEMELRIJK C. K., NEDELEC F. J., SARKAR T., ARYAKSAMA T., LACROIX M., DUCLOS G., YASHUNSKY V., SILBERZAN P., ARROYO M. and KALE S., *J. Phys.: Condens. Matter*, **32** (2020) 193001.
- [2] BORSLEY S., LEIGH D. A. and ROBERTS B. M., *Nat. Chem.*, **14** (2022) 728.
- [3] JÜLICHER F., AJDARI A. and PROST J., *Rev. Mod. Phys.*, **69** (1997) 1269.
- [4] MAGNASCO M. O., *Phys. Rev. Lett.*, **72** (1994) 2656.
- [5] GOLESTANIAN R. and AJDARI A., *Phys. Rev. Lett.*, **100** (2008) 038101.
- [6] GOLESTANIAN R. and AJDARI A., *J. Phys.: Condens. Matter*, **21** (2009) 204104.
- [7] GOLESTANIAN R., *Phys. Rev. Lett.*, **102** (2009) 188305.
- [8] GOLESTANIAN R., LIVERPOOL T. B. and AJDARI A., *Phys. Rev. Lett.*, **94** (2005) 220801.
- [9] NOJI H., YASUDA R., YOSHIDA M. and KINOSITA K. jr., *Nature*, **386** (1997) 299.
- [10] JUNGE W. and NELSON N., *Annu. Rev. Biochem.*, **84** (2015) 631.
- [11] YASUDA R., NOJI H., KINOSITA K. and YOSHIDA M., *Cell*, **93** (1998) 1117.
- [12] PUMM A.-K., ENGELEN W., KOPPERGER E., ISENSEE J., VOGT M., KOZINA V., KUBE M., HONEMANN M. N., BERTOSIN E., LANGECKER M. *et al.*, *Nature*, **607** (2022) 492.
- [13] SHI X., PUMM A.-K., MAFFEO C., KOHLER F., FEIGL E., ZHAO W., VERSCHUEREN D., GOLESTANIAN R., AKSIMENTIEV A., DIETZ H. *et al.*, *Nat. Nanotechnol.*, **19** (2024) 338.
- [14] KLUMPP S., LEFÈVRE C. T., BENNET M. and FAIVRE D., *Phys. Rep.*, **789** (2019) 1.
- [15] SPECK T., *EPL*, **114** (2016) 30006.
- [16] SEIFERT U., *Phys. A: Stat. Mech. Appl.*, **504** (2018) 176.
- [17] SEIFERT U., *Eur. Phys. J. B*, **64** (2008) 423.
- [18] CHATZITTOFI M., AGUDO-CANALEJO J. and GOLESTANIAN R., *Phys. Rev. Res.*, **6** (2024) L022044.
- [19] DADDI-MOUSSA-IDER A., GOLESTANIAN R. and VILFAN A., *Nat. Commun.*, **14** (2023) 6060.
- [20] BEBON R., ROBINSON J. F. and SPECK T., arXiv:2401.02252 (2024).
- [21] FRITZ J. H. and SEIFERT U., *J. Stat. Mech.: Theory Exp.*, **2023** (2023) 093204.
- [22] ILLIEN P., ADELEKE-LARODO T. and GOLESTANIAN R., *EPL*, **119** (2017) 40002.
- [23] AGUDO-CANALEJO J., ILLIEN P. and GOLESTANIAN R., *Nano Lett.*, **18** (2018) 2711.
- [24] AGUDO-CANALEJO J., ADELEKE-LARODO T., ILLIEN P. and GOLESTANIAN R., *Phys. Rev. Lett.*, **127** (2021) 208103.
- [25] LIPOWSKY R. and KLUMPP S., *Phys. A: Stat. Mech. Appl.*, **352** (2005) 53.
- [26] ONSAGER L., *Phys. Rev.*, **37** (1931) 405.
- [27] DE GROOT S. R. and MAZUR P., *Non-equilibrium Thermodynamics* (Courier Corporation) 2013.
- [28] DIK G., BAKAR B., ULU A. and ATEŞ B., *Ind. Eng. Chem. Res.*, **62** (2023) 14111.
- [29] GUMPP H., PUCHNER E. M., ZIMMERMANN J. L., GERLAND U., GAUB H. E. and BLANK K., *Nano Lett.*, **9** (2009) 3290.
- [30] CHATZITTOFI M., GOLESTANIAN R. and AGUDO-CANALEJO J., *New J. Phys.*, **25** (2023) 093014.
- [31] REIMANN P., VAN DEN BROECK C., LINKE H., HÄNGGI P., RUBI J. M. and PÉREZ-MADRID A., *Phys. Rev. Lett.*, **87** (2001) 010602.
- [32] DAN D. and JAYANNAVAR A. M., *Phys. Rev. E*, **66** (2002) 041106.
- [33] REIMANN P., VAN DEN BROECK C., LINKE H., HÄNGGI P., RUBI J. M. and PÉREZ-MADRID A., *Phys. Rev. E*, **65** (2002) 031104.
- [34] CHATZITTOFI M., GOLESTANIAN R. and AGUDO-CANALEJO J., arXiv:2310.11788 (2023).
- [35] NAJAFI A. and GOLESTANIAN R., *Phys. Rev. E*, **69** (2004) 062901.
- [36] GOLESTANIAN R., *Phys. Rev. Lett.*, **105** (2010) 018103.
- [37] SEIFERT U., *Rep. Prog. Phys.*, **75** (2012) 126001.
- [38] DERRIDA B., *J. Stat. Phys.*, **31** (1983) 433.
- [39] KOZA Z., *J. Phys. A: Math*, **32** (1999) 7637.

Chapter 8

Discussion and conclusions

In this thesis we explored various scenarios related to stochastic non-equilibrium processes linked to molecular systems. This led us in developing new and interesting results towards different directions.

Extending the work related to the synchronization of two mechanically coupled enzymes, we have shown in Chapter 2 that synchronization occurs in a system of arbitrary oscillators in the presence of an all-to-all coupling. This is a new model of synchronization with different dynamical structure compared to the classical models in the literature. The crucial difference is the dissipative coupling $M_{\alpha\beta}$ which couples the oscillators through a velocity force relation and it serves as a potential mechanism for cooperation at small scales.

To further demonstrate the importance of the dissipative coupling, we have generalized the idea to non-identical processes. Particularly, in Chapter 3, we work on examples of two asymmetric processes, which might demonstrate examples of molecular oscillators. By considering two molecular rotors that hydrodynamically interact with each other, we explicitly show how one can derive the phase equations coupled through the dissipative mobility matrix. By tuning the free energy landscapes and off-diagonal coupling of the mobility a rich phenomenology of phase locked dynamics emerges. The oscillators in the presence of the coupling become phase-locked with different coprime ratios depending on the asymmetry in their free energy landscapes. At certain combinations there is also the emergence of topological phase locking (TPL).

These two models introduce novel mechanisms for coordination and enhancement in the activity at the molecular scale. Along these lines, it has been observed that oligomeric structures of enzymes operate at higher activity compared to isolated monomers [137]. Moreover, this intriguing result suggests that the slow process might get boosted by the fast one. The TPL and the effects of the dissipative coupling potentially might be achieved experimentally in designed systems with molecular rotors [138] or turbines [139], optomechan-

ical oscillators [140] and others. Another aspect that might be explored in the future are systems of phase oscillators with local interactions and various topologies, e.g one dimensional ring or higher-dimensional lattices [141]. The nearest-neighbour interactions could potentially generate a chemical wave propagation along a chain of oscillators. Furthermore, it would be possible to study this problem from the point of view of disordered systems, by including disorder in the coupling (off-diagonal terms of the mobility tensor) and how it could affect the performance and the synchronization [142, 143]. Different combinations of these ideas would be interesting for exploration. For instance, the dynamics of three or more asymmetric driven coupled phase oscillators governed by the presented dynamical system might lead to unexpected results like for instance chimera states [144, 145].

A system of an enzyme mechanically coupled to a passive molecule was introduced in Chapter 4. This mechanistic description of an enzyme allowed us to propose three rules for designing an enzyme. These are linked to the arising dissipative coupling which is controlled by the geometry of the complex and leads to a global bifurcation in the dynamical system of equations. Our results can be important for designing and understanding synthetic catalysts and complement developed machine learning strategies for the design of enzymes.

In Chapter 5 we proposed a method for inferring correlations that is applicable to many-body non-equilibrium systems. To demonstrate the application of the uncertainty relation, we have included various different models (both analytically and numerically solvable) where a single current measurement can apparently outperform the classical TUR. A possible experimental realisation of this idea is the motion of two hydrodynamically interacting colloids inside an optical ring [146].

In Chapter 6, we use an analytically tractable model and we fully determine the dissipation of a stochastic swimmer far from the linear response regime [135]. Assuming that the active swimming arises from a non-equilibrium cyclic process and not from an active force we calculate the entropy production rate. Our calculation unravels the complex interplay of systems far-from equilibrium and the effect of external fields in the total dissipation. This is essential for the collective dissipation of active matter systems where interactions between the various agents might affect the dissipation. For instance, density fluctuations around an active particle exert different forces on it which should be taken into

account to properly quantify dissipation.

Finally in, Chapter 7, we studied the effect of external forces on chemically driven machines and showed that these typically display a non-monotonic behavior in their activity as a function of the applied forces [136]. These forces could arise from electromagnetic fields, light irradiation, optical tweezers and others. A direct extension of this problem is considering time-dependent forces, i.e forces generated by an alternate electric field. There is ongoing research about controlling the chemical activity of chemical reactions with forces, which sometimes can effectively lower the energy barrier [147], in agreement with our theory.